THE DEVELOPMENT OF A DETAILED ABUNDANCE ANALYSIS METHOD INTENDED FOR THE INTEGRATED LIGHT SPECTRA OF EXTRAGALACTIC GLOBULAR CLUSTERS

by

Scott A. Cameron

A dissertation submitted in partial fulfillment
of the requirements for the degree of
Doctor of Philosophy
(Astronomy and Astrophysics)
in The University of Michigan
2009

Doctoral Committee:

Associate Professor Rebecca A. Bernstein, Co-Chair,
University of California
Professor Mario L. Mateo, Co-Chair
Professor August Evrard
Associate Professor Marion S. Oey
Associate Professor Mary E. Putman, Columbia University

To my mother and father,

patrons of my endeavors

ACKNOWLEDGMENTS

I thank the University of Michigan Astronomy department for their financial and moral support during my time as one of their graduate students. I also thank the department's office staff for their administrative expertise, which saved me more time, money, and headaches than I myself even realize. Finally, I thank the department for giving me meaningful teaching opportunities. These teaching opportunities broadened my outlook on the role of science and have probably shaped the future direction of my life more so than any other experience in graduate school.

Lastly, I thank my dissertation committee for keeping me on track towards this dissertation and for improving its final form. I also thank Rebecca for allowing me to participate as an equal in her research and for her support and mentorship along the way.

CONTENTS

LIST OF FIGURES

Figure

LIST OF TABLES

Table

LIST OF APPENDICES

Appendix

CHAPTER 1

Introduction

Globular clusters are stellar systems that possess an astrophysically rare combination of theoretical and observational simplicity. The origin of this simplicity can be traced back to their relatively simple composition, geometry, and kinematics. In terms of composition, a globular cluster (GC) closely approximates a simple stellar population (SSP) composed of $10^4 - 10^6$ stars that share the same age and chemical make-up. Because SSPs are largely understood from principles of stellar evolution (e.g. Gallart, Zoccali, & Aparicio 2005), they can be modelled for any arbitrary combination of GC age and chemical make-up. In terms of geometry, GC stars fill a roughly spherical volume ($r_{tidal} \sim 30\ pc$, $e_{mean} \lesssim 0.1$) (White & Shawl 1987) and demonstrate a radial density distribution that is centrally concentrated ($r_{half-light} \sim 4\ pc$). This combination of spherical symmetry and radial density distribution greatly simplifies the mathematical modelling of GCs because it permits the use of purely analytical methods (e.g. King 1966; Spitzer 1987). These properties also ensure that GCs have observationally advantageous surface-brightnesses and luminosities ($M_V = -10$ to $-4\ mag$, $M_{V,mean} \sim -7\ mag$). In terms of internal kinematics, GC stars have dynamically hot orbits that are bound within each cluster's own gravitational potential, which may be modified by the tidal field of the cluster's host galaxy. Under these quiescent conditions, the stellar kinematics of a GC can be directly modelled using stellar N-body simulations (e.g. Heggie & Hut 2003). However, over cosmological timescales, the stellar membership of a cluster may become altered due to internal stellar evaporation (Spitzer & Thuan 1972), external disk shocking (Ostriker, Spitzer, & Chevalier 1972) and dynamical friction (Binney & Tremaine 1987). For these external dynamical processes, a GC must be

modelled using more sophisticated considerations (e.g. Fall & Zhang 2001; Gnedin et al. 1999; Gnedin & Ostriker 1997; Elson et al. 1987). Lastly, in terms of external kinematics, GCs themselves have dynamically hot orbits that are bound within the gravitational potential of their host galaxy, where they tend to form "bulge" and "halo" populations. The large orbital radii attained by these halo populations largely remove them from the observational interference of their host galaxy, which allows them to be cleanly observed in both Galactic and extragalactic systems. Altogether, these theoretical and observational simplicities make GCs ideal diagnostic tracers of astrophysical processes in both space and time.

This chapter is organized as follows. In § 1.1 the use of GCs as diagnostic tracers of astrophysical processes is discussed. In particular, the processes reviewed are the ones most pertinent to this dissertation's topic of deriving detailed chemical abundances from extragalactic GCs. These processes include both stellar evolution and stellar nucleosynthesis within GCs, and the more contemporary use of GCs to trace galaxy formation. In § 1.2, the concepts relating to how chemical compositions are derived from stellar spectra are discussed. This section begins with the standard process of deriving chemical abundances from the spectra of single stars, and then discusses the current method used to derive integrated chemical abundances from the integrated-light spectra of GCs. This section then concludes with an introduction to this dissertation's improved method for deriving detailed chemical abundances from the integrated-light spectra of extragalactic GCs. Chapters 2 through 5 then discuss this dissertation's method and results.

1.1 GCs as Diagnostic Tracers of Astrophysical Processes

When theory is applied to GCs, knowledge is frequently gained. This profitable relationship was particularly true throughout twentieth century astronomy and continues to be true today. During much of the twentieth century, GCs were used as Rosetta stones to help develop the fields of stellar evolution, stellar nucleosynthesis, stellar dynamics, and Milky Way formation theory. Towards the end of that century, GCs continued to play roles in these fields, but these roles progressively dealt with more

subtle and refined issues, largely due to decades of accumulated progress. As astronomy entered the twenty-first century, this situation began to change as the utility of GCs for studying cosmological issues became more widely recognized. This shift in focus was largely due to the discovery that the ubiquitous GC systems observed around galaxies almost universally possess distinctly bimodal populations of metal-poor and metal-rich GCs. This discovery naturally led to various hypotheses that attempted to explain the bimodal distribution in terms of various modes of galaxy formation. This section encapsulates the most important concepts from the classical GC research areas of stellar evolution and stellar nucleosynthesis along with the more contemporary GC research area of galaxy formation as they relate to this dissertation.

This section is organized as follows. § 1.1.1 discusses GCs from the standpoint of stellar evolution theory. In particular, the section begins by giving a basic overview of the observationally important stellar phases found in GCs, and then concludes by discussing some of the known difficulties that exist in modelling these stellar phases. § 1.1.2 discusses stellar chemical composition and nucleosynthesis from the standpoint of GCs. In particular, the section first defines useful terms and relations that interlink theoretical chemical compositions with observed chemical compositions. The section then reviews the observationally important Fe-peak elements, α-elements, neutron-capture elements, and light-elements. This review includes their basic formation processes and their observed trends in GCs.

1.1.1 Laboratories of Stellar Evolution

GCs are useful laboratories for investigating stellar evolution. This status can be attributed to four of their basic characteristics. First, because the stars in a GC share homogeneous initial conditions in both age and chemical composition, the only meaningful parameter in which they initially differed was their initial mass. Therefore, any differences observed between the stars in a GC today must have originated from initial mass differences. Second, because the stars in a GC are located at a heliocentric distance that is much larger than their cluster's radius, every star in a cluster is essentially located at exactly the same heliocentric distance. This unifor-

mity in distance allows an observer to directly compare the apparent brightnesses of a GC's stars, and interpret any brightness differences as differences in intrinsic stellar luminosity. Third, the vast number of stars within a GC statistically ensures that almost every stage of stellar evolution is represented somewhere within that GC's collection of stars. Lastly, because the stars in a GC all formed at the same time and in the same volume of space, their distribution in mass represents the present-day mass function of their cluster's past formation event. If this realization is combined with the assumption that most stars born within a GC remain gravitationally bound to the cluster, then a GC's current family of stars closely approximates the initial mass function (IMF) for that cluster. The main implication from combining all four of these characteristics is that by simply observing physically meaningful observables from a sample of GC stars, an observer can obtain a snapshot that depicts the current state of stellar evolution for those stars, which must have been dictated by the cluster's IMF and the passage of time.

Color-Magnitude Diagrams

The most practical and physically meaningful observables used to characterize a star's current state of evolution is the star's apparent brightness (i.e. observed flux) and color (i.e. indirectly observed surface temperature). When these observables are plotted for numerous stars, with apparent brightness on the plot's *y-axis* and color on its *x-axis*, the plot is called a color-magnitude diagram (CMD). The logic behind such a diagram is that stars behave approximately like thermal "black body" radiators; therefore, a star's luminosity (L) and effective temperature (T_{eff}) are related through Stefan-Boltzmann's law

$$L = 4\pi\sigma R^2 T_{eff}^4 \tag{1.1}$$

where σ is Stefan-Boltzmann's constant and R is the radius of the star at the star's photosphere (i.e. surface). Because apparent brightness and color serve as observable proxies for L and T_{eff}, a CMD is an observable statement of Stefan-Boltzmann's law. More importantly, because a star's T_{eff} and R change as a function of time due to stellar evolution, a star's location in a CMD is a statement of its current

evolutionary state. Therefore, a GC's CMD can be used to test stellar evolution theory by modelling the evolution of L and T_{eff} for a collection of stars of different initial masses in the form of an *isochrone*, converting those parameters to apparent brightness and color, and then comparing the isochrone with the cluster's observed CMD (e.g. Gallart et al. 2005; Salaris & Cassisi 2005; Chiosi et al. 1992; Renzini & Fusi Pecci 1988). By correlating the isochrone's stars with their counterparts in the observed CMD, the physical conditions of the observed stars can be deduced by simply assigning them the physical conditions of the matching theoretical stars. Any anomalies in these comparisons indicate that something is most likely incorrect with the applied assumptions or with the stellar evolution model itself. Thus, each comparison between an isochrone and an observed CMD is a test of stellar evolution theory, and as the theory improves, it can be applied to observed CMDs with greater accuracy and precision.

After many decades of constructing and investigating stellar evolution models (e.g. Iben 1967, 1974; Iben & Renzini 1983), most of the features in a GC's CMD are now understood in terms of their underlying, physical conditions (e.g. Gallart et al. 2005). Figure 1.1 shows a schematic GC CMD overlade on an observed CMD of the Galactic GC, NGC 104. The most stable and recognizable feature of a CMD corresponds to its stars' stable configuration of hydrostatic equilibrium, regulated by the release of nuclear energy through the fusion, or "burning", of hydrogen into helium inside a star's central core. This configuration appears in Figure 1.1 as the red line that roughly spans between the color-magnitude locations $[(B-V) \sim 1,\, M_V \sim 8]$ and $[(B-V) \sim 0.5,\, M_V \sim 4]$. This feature is called the main sequence (MS), and all the black dots along this sequence correspond to MS stars in NGC 104. Note that the scatter along the color coordinate for these data, and the scatter's progressive broadening as the brightness of the MS decreases, are artifacts of photometric errors for the measured magnitudes. If these errors were eliminated, the MS would form a one-dimensional line that is smooth and slightly curved. The placement of a star on this one-dimensional sequence is dictated by the star's initial mass, where the most massive stars "live" on the MS as hot and bright stars located on the upper left

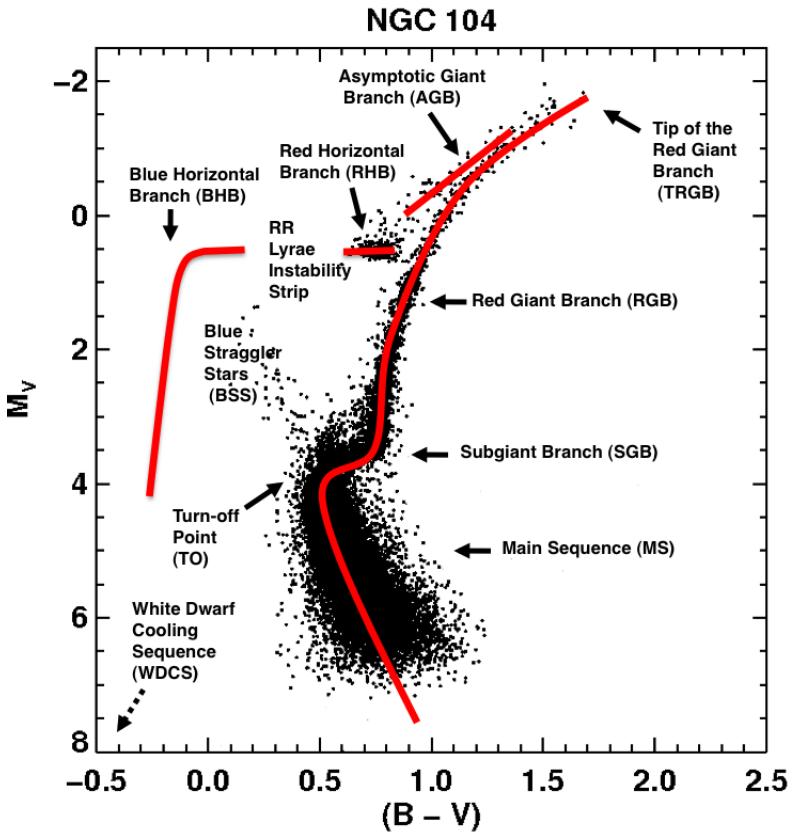

Figure 1.1. Schematic color-magnitude diagram using NGC 104. See the text for descriptions of the figure's labeled CMD features. The photometry data (black dots) are from Piotto et al. (2002).

segment of the sequence, while the lower mass stars live at progressively dimmer and cooler MS locations that are a monotonic function of their initial masses.

Once a MS star depletes all of the H inside of its core, it can no-longer generate enough energy to maintain hydrostatic equilibrium. To regain equilibrium, the star must reconfigure itself. This reconfiguration involves burning H inside of a thin shell of material located around the star's inert He core. Because the star's new source of energy is located outside the core, the core begins to gravitationally contract, which forces the shell to start moving outward in an attempt to re-establish equilibrium. Observationally, this stage of core-H depletion is located at the MS turn-off point (TO), which is located in Figure 1.1 approximately at $[(B-V) \sim 0.5,\ M_V \sim 4]$. An important feature of the TO involves the relationship between the initial mass of a cluster star located at the TO and the cluster's age. Because the rate of core

H-burning is a strong function of a star's initial mass, the most massive stars in a cluster will deplete their core-H faster and reach the TO sooner than the less massive stars in the cluster. Therefore, all cluster stars still located on the MS must have masses smaller than the mass of a cluster star located at the TO, and all cluster stars that have already evolved off the MS must have initial masses larger than the mass of a star located at the TO. If the location of this unique TO mass can be calculated as a function of cluster age using stellar evolution models (e.g. isochrones), then the location of a cluster's TO within a CMD can be used to determine the age of the cluster (e.g. Vandenberg, Bolte, & Stetson 1996). For example, the TO for NGC 104 in Figure 1.1 roughly corresponds to a stellar initial mass of $0.8 - 0.9\mathcal{M}_{\odot}$ and an isochrone of age of $\sim 10 - 13\ Gyrs$. This example also reveals the important fact that even though a CMD of an "old" (age $\sim 10 - 13\ Gyrs$) GC has stars that represent almost ever stage of stellar evolution, they do not have MS stars of "intermediate" mass ($2\ \mathcal{M}_{\odot} \lesssim \mathcal{M} \lesssim 8\ \mathcal{M}_{\odot}$) or "high" mass ($8\ \mathcal{M}_{\odot} \lesssim \mathcal{M} \lesssim 150\ \mathcal{M}_{\odot}$). Therefore, the majority of the discussion that follows implicitly pertains to "low" mass ($0.08\ \mathcal{M}_{\odot} \lesssim \mathcal{M} \lesssim 2\ \mathcal{M}_{\odot}$) stars, although, most of their evolutionary stages are qualitatively similar to intermediate mass stars.

As the core of a TO star continues to slowly contract, the star evolves to cooler temperatures, while maintaining an approximately constant luminosity. This relatively short stage of evolution is called the subgiant branch (SGB) stage, and is shown in Figure 1.1 as the short line segment immediately to the right of the TO. Ideally, a SGB star would maintain this temperature trend, but in reality it eventually approaches the Hayashi track, which separates the temperature-luminosity plane into a high-temperature region that permits hydrodynamical equilibrium, and a low-temperature region that forbids hydrodynamical equilibrium. Therefore, to maintain equilibrium, a SGB star cannot cross the Hayashi track, and is forced to increase its luminosity and travel up along this boundary instead. This attempt at stability is called the red giant branch (RGB) stage, which curves roughly from $[(B-V) \sim 0.75,\ M_V \sim 3.5]$ to $[(B-V) \sim 1.7,\ M_V \sim -1.5]$ in Figure 1.1. Note that from Equation 1.1 the large increase in brightness and approximately constant temperature maintained

during the RGB stage implies that RGB stars must drastically increase their radii. As their radii increase, their atmospheres become tenuous and begin to lose mass. Meanwhile, as the star continues to evolve up the RGB, its He core continues to contract and slowly increases in temperature. Eventually, the star's core becomes hot enough to fuse He into carbon and oxygen at the tip of the RGB (TRGB). This ignition of He occurs in a very rapid He "flash", which causes the star to rapidly change its structure and achieve a new equilibrium. This new equilibrium consists of the star fusing He inside of its core, while maintaining H fusion in a shell around the core. Depending on the new equilibrium temperature reached by the star, this new configuration is called the horizontal branch (HB) stage or the RR Lyrae stage, which are shown in Figure 1.1 as the blue and red HBs (BHB, RHB) and the RR Lyrae instability strip. Note that NGC 104 has only a RHB and that none of the stars sampled by the CMD are located in the RR Lyrae instability strip.

While fusing core-He and shell-H during the HB or RR Lyrae stage, a star achieves a short period of stability ($\sim$ 100 $Myrs$) that is qualitatively similar to the MS stage. One important observational feature of this stability is the relatively constant brightness ($M_V \sim 0.5\ mag$) achieved by these stars. This property allows these stars to be used as standard candles to determine their distances (e.g. Sandage & Tammann 2006). Once the core-He is depleted, the star now has an inert C-O core that is surrounded by a He-burning shell. This configuration is unstable, and the star once again begins to move towards the Hayashi track, where it will asymptotically join the RGB. This stage is called the asymptotic giant branch (AGB) stage and it is shown in Figure 1.1 as the line segment between the RHB and the TRGB. During this stage, an AGB star's C-O core continues to gravitationally contract until it is halted by electron degeneracy pressure. While this contraction occurs, the star's He-shell moves outward, and after $\sim 10^7\ yr$ the star ignites a new H-burning shell around its He-burning shell. This new configuration, called the thermally pulsating AGB (TPAGB) stage, results in unstable shell burning where the star's He- and H-burning shells rapidly take turns being the the star's main energy source. This shell-driven oscillation becomes extremely unstable and soon ($\sim 10^6\ yr$) it becomes violent enough

to remove the star's entire outer atmosphere, which essentially leaves behind only the star's inert C-O core. This final stage is called the white dwarf (WD) stage and it signals the end of stellar life for any low-mass star that is not a member of a binary system. Because a WD is no-longer generating energy from fusion, its luminosity rapidly decreases and its residual temperature begins to cool. Eventually, all solitary WDs settle on the WD cooling sequence (WDCS), which is located beyond the lower left-hand-side of Figure 1.1. Here, WDs slowly move towards lower luminosities and cooler temperatures as their remnant energies are radiated into space.

Stellar Evolution Model Deficiencies

While standard stellar evolution models are largely successful at predicting the broad stellar evolution stages mentioned above, they do suffer from known deficiencies (e.g. Gallart et al. 2005). These deficiencies can be categorized into both "large-scale" and "small-scale" deficiencies. The large-scale deficiencies are attributable to the neglect of real hydrodynamics, which forces the models to apply simple, hydrodynamical approximations instead. These hydrodynamical approximations are applied during treatments of convective radiation, convective overshooting, and mass-loss. The small-scale deficiencies in stellar evolution models are attributable to a wide variety of different physical processes and assumptions. Two of the most important small-scale deficiencies in stellar models include their assumed chemical compositions and the opacities they use for cool stars.

Hydrodynamical deficiencies in standard stellar evolution models stem from their lack of three-dimensional hydrodynamics. As originally outlined by Eddington (1926), standard stellar evolution models are "simply" the application of a set of four, one-dimensional differential equations that are combined with detailed applications of microphysics. These four equations are mathematical statements of mass conservation, energy conservation, momentum conservation, and energy transport, all under the assumption of spherical symmetry (Cox 2000, Chap. 20). The applied microphysics take the form of very detailed computations of energy generation, equation of state, opacity, entropy, and adiabaticity, where each is a function of a star's density,

temperature, and composition.

The most important consequence of stellar hydrodynamics is convection. Convection results in both the transfer of internal energy towards a star's surface, and the mixture of stellar material within or near a convection zone. Of these two processes, the first process, called "convective radiation", must be treated wherever interior stellar conditions warrant it, while the second process is most frequently treated for stars with convective cores using a mathematical formalism called "overshooting". Of the four stellar evolution equations, convective radiation directly affects the energy transport equation. In order to account for this effect, models must first determine which regions inside a star experience energy transport from convection. The classic method to determine these locations is to test each region inside a star for convective stability using the Schwarzschild criterion (1906), which simply checks too see if a test parcel of gas with a higher temperature than its surrounding material could adiabatically cool itself faster or slower than the surrounding material as it tries to rise towards the surface. For regions where convection is found to be important, the energy transport equation must account for any energy contributed to the surrounding material from rising parcels of gas as they "mix" themselves into their surroundings. This convective "radiation" process is estimated using a phenomenological model called mixing length theory (Prandtl 1952; Böhm-Vitense 1958). This theory parametrizes the efficiency of convective radiation using a single free-parameter called the "mixing length" that characterizes the distance that a convective parcel can travel before it completely mixes itself into its surroundings.

Following the discussion found in Gallart et al. (2005), the application of mixing length theory is one of the largest uncertainties in stellar evolution models. Because mixing length theory controls the efficiency of convection, the selection of its single free parameter affects all stars that are predominantly convective, such as low-mass MS stars and all RGB stars. For example, if the mixing length is changed by 30%, the $(B-V)$ colors of a cluster's MS and RGB will change by approximately 0.017 *mags* and 0.045 *mags*, respectively (Cariulo, Degl'Innocenti, & Castellani 2004). This 30% difference covers the range of mixing lengths adopted by modern stellar evolution

models (see Gallart et al., *Table 1*). In an attempt to empirically calibrate the mixing length, the mixing length of the Sun has been determined by choosing various values until a stellar model of the Sun reproduces the Sun's radius (e.g. Mazzitelli 1979; Sweigart 1983; Vandenberg 1983). The range in these empirical measurements largely account for the range found in modern stellar evolution models. Perhaps more importantly, even if the Solar value is known exactly, there is no known reason why it should be the same value for RGB stars (Robinson et al. 2004) or stars with non-Solar chemical composition, although this seems to be the case (Ferraro et al. 2006; Palmieri et al. 2002; Freytag & Salaris 1999).

The other important convective process is convective mixing. When a hot convective parcel rises, it can lift nuclearly processed material towards a star's surface, which can both affect the opacities and surface abundances of a star. Meanwhile, when the material in a convective parcel cools, it can sink and carry some of the upper, unprocessed material down towards a star's core. This second case of convective sinking is particularly important for stars that have convective cores, because any unprocessed material that sinks into a core adds to the core's reservoir of nuclear fuel, which will then allow the star to stay on the MS longer and reach higher luminosities. Therefore, if a model does not account for convective core mixing, it will predict that clusters have younger ages than they really have. Because of this significance, attempts at adding secondary mechanisms to the application of mixing length theory for convective cores are attempted. These finer level modifications usually involve considerations of "overshooting", which corresponds to convective parcels moving slightly above or below the official convective boundary defined by the Schwarzschild criterion. The physical motivation for this violation is that the Schwarzschild criterion merely marks where convective parcels stop experiencing buoyant acceleration; therefore, the parcels must still possess coasting velocities that allow them to overshoot above or below the official convective boundary before they come to rest. Unlike mixing length theory, overshooting is usually parametrized differently between various models, though it is frequently parametrized using an overshooting length parameter that is similar in concept to the mixing length parameter.

Following Gallart et al. (2005), a universal formulation of overshooting is hard to design and calibrate simultaneously for all stellar evolution models. This difficulty is because all stellar evolution models, to varying degrees, use different microphysical formulations, which affect the intrinsic size and conditions of their Schwarzschild criterion defined convective cores. Therefore, any calibration of a universal overshooting formulation is subject to various systematic offsets between models. Despite this difficulty, various observational tests using features that are sensitive to overshooting (Maeder & Meynet 1989; Stothers 1991) have provided some constraints. Using Galactic open clusters, various groups have agreed that some amount of overshooting is needed for young stars close to Solar metallicity (Maeder & Mermilliod 1981; Stothers & Chin 1991; Carraro et al. 1993; Daniel et al. 1994; Demarque et al. 1994; Kozhurina-Platais et al. 1997; Nordstroem et al. 1997). Similar investigations of intermediate-age LMC clusters (Gallart et al. 2003; Woo et al. 2003; Bertelli et al. 2003) found that the overshooting formulations in the models they tested agreed reasonably well with their observations. Observations of field stars in the LMC and SMC by Cordier et al. (2002) may indicate that overshooting increases indirectly with metallicity. Observations of detached eclipsing binaries suggest that overshooting increases with stellar mass (Schroder et al. 1997; Ribas et al. 2000). Observations of bump Cepheids (Bono et al. 2002; Keller & Wood 2002) indicate that overshooting is needed. Finally, astroseismology observations (Aerts et al. 2003; Dupret et al. 2004) also indicate that overshooting is needed for massive stars. In summary, overshooting corrections appear to be necessary but the level of these corrections is not well known.

The third important consequence of stellar hydrodynamics is mass-loss. Mass-loss is a crucial evolutionary process for RGB and AGB stars (e.g. Habing 1996; Willson 2000). As a star moves up the RGB, its radius expands and its luminosity increases. These changes lead to a combination of lower surface gravity and higher radiative pressure, which favor mass-loss all along the RGB. When a low-mass RGB stars reaches the TRGB, its rapid establishment of core He-burning may also lead to massive amounts of mass-loss, although the level to which this is true is debated (Willson 2000). The situation for AGB stars is similar to that of RGB stars, except

the amount of mass-loss is significantly greater (Habing 1996). As a star moves off the HB, it expands its radius and increases its luminosity, thus lowering its surface gravity and increasing its radiative pressure. This once again leads to mass-loss throughout the AGB stage. More importantly, when an AGB star eventually establishes a H-burning shell, the star enters the TPAGB stage, and its rapid thermal pulsations dramatically expel most of the star's atmosphere until only its $\sim 0.6 - 1.4\ \mathcal{M}_{\odot}$ WD core remains (Habing 1996).

Despite the obvious importance of mass-loss during stellar evolution, its treatment in stellar evolution models is largely phenomenological. For RGB stars, the empirically motivated mass-loss formula of Reimers (1975) is frequently used in stellar evolution models. This formula is a function of a star's mass, luminosity, and radius, but also includes a free-parameter coefficient that is used to fine-tune a star's mass-loss efficiency. The chosen value for this parameter usually falls between 0.3 and 3 (Habing 1996), though the lower values are usually used for RGB stars. For AGB stars, several different mass-loss prescriptions are in use (e.g. Bowen & Willson 1991; Vassiliadis & Wood 1993; Bloecker 1995). For a review of the merits of these AGB mass-loss prescriptions, see Habing (1996).

Unlike the large-scale hydrodynamical deficiencies, small-scale deficiencies in stellar evolution models can take many forms. One of the most important small-scale deficiencies for a model is its assumed chemical composition. The wrong choice of chemical composition will drastically affect a model's energy generation rate and opacity. The most influential chemical composition parameters for a model are its initial metallicity, initial He abundance, and relative abundance distribution. Of these parameters, metallicity is the most important parameter and is usually the most sought after physical parameter for observed stars or clusters. For example, the results of most stellar evolution models, produced in the form of stellar tracks and isochrones, are provided in relatively fine grids of metallicities that range from super-Solar to extremely metal-poor. Therefore, a model's assumed metallicity is usually not a practical deficiency because it can be easily changed. This situation is frequently not true for a model's assumed He abundance and overall abundance

distribution, because they are usually implicitly treated as constants, regardless of the observed star or cluster.

The way He is accounted for in stellar evolution models introduces two potential sources of error (Gallart et al. 2005). First, a model needs to assume an initial He abundance in which to begin its stellar evolution. Second, the model needs to determine how a star's He abundance will increase with time. These two problems are usually parametrized in the form of an He enrichment law

$$Y = Y_P + \left(\frac{\Delta Y}{\Delta Z}\right) Z \tag{1.2}$$

where Y is the current He mass-fraction of the star; Y_P is the universe's primordial He mass-fraction from big bang nucleosynthesis; Z is the current mass-fraction of all elements heavier than He in the star; and $\frac{\Delta Y}{\Delta Z}$ is the slope between two (Y,Z) reference points. The two reference points used to compute the slope are the universe's primordial He and metal mass-fractions and the Sun's current He and metal mass-fractions. As Gallart et al. (2005) point out, the Solar mass-fraction values are actually the biggest source of error in the calibration. The observed primordial He mass-fraction obtained from HII regions (Olive et al. 1997; Luridiana et al. 2003; Izotov & Thuan 2004) fall within the range $0.239 - 0.242$, which agrees within the errors of the 0.2479 value obtained from big bang nucleosynthesis calculations (Coc et al. 2004). Recent observation's of the Sun (Asplund et al. 2004; Meléndez 2004) indicate that its current He and metal mass-fractions are approximately 0.2486 and 0.0122 (Basu & Antia 2004), respectively, while the canonical values used in most stellar models are approximately 0.28 and 0.018, respectively. These sizable discrepancies prove to be important because the amount of He assumed for a model greatly affects both the luminosity and MS lifetime of the model.

Besides He, the relative distribution of heavy element abundances assumed for a stellar evolution model can also affect the model (e.g. Salaris & Cassisi 2005). The simplest method used to distribute elemental abundances for a model is to first assume the Sun's abundance distribution and then rescale this entire distribution

using the abundance of Fe as a single reference point. For example, as a model's metallicity is changed within a metallicity grid, the model's abundance distribution gets proportionally rescaled up or down in unison with Fe. These "Solar-scaled" abundance distributions usually provide sensible results, but there is no *a priori* reason why every observed star should have exactly the same relative abundance distribution. In fact, it is known that low metallicity stars in the Galaxy are enriched with α-elements relative to the Sun (see § 1.1.2). These enrichments are important because they affect the shape of a model's isochrones because they increase the opacity of the model and potentially even the model's energy generation rates (Gallart et al. 2005).

The last example of a small-scale deficiency in stellar evolution models that will be mentioned here relates to the opacities of cool stars. In order to compare a stellar model to observations, the model's luminosity and temperature must be converted to magnitudes and colors. To do this conversion, a synthetic spectrum corresponding to the model star must be convolved through filters that correspond to the magnitude system of interest. To create a realistic synthetic spectrum, the line opacities for the model star must be known and applied. For model stars with effective temperatures between $4,500K \lesssim T_{eff} \lesssim 50,000\ K$, atomic lines comprise the vast majority of their spectral line opacities, and these line opacities are known in great detail (Gallart et al. 2005). For hot stars with $T_{eff} \gtrsim 50,000K$, their spectra are almost completely free of absorption lines, so these stars' spectra can be treated as black-body spectra (Gallart et al. 2005). For cool stars with $4,500K \lesssim T_{eff}$, their spectra are dominated by molecular bands. Because these molecular spectra are very detailed and complicated, there currently does not exist any molecular opacity distribution functions for cool stars that are capable of producing realistic spectra (Gallart et al. 2005). Therefore, converting the models of cool stars to magnitudes and colors must use less accurate methods, such as applying empirical bolometric corrections and empirical temperature-color relations.

In summary, while it is true that stellar evolution models have known deficiencies, it is equally true that they are largely successful. Where these successes and

deficiencies lie within models must be understood though, so that their application to real observed CMDs do not result in incorrect interpretations.

1.1.2 Laboratories of Nucleosynthesis

A star's chemical composition is perhaps the richest set of physical parameters that can be measured from a star. GC stars, in particular, provide useful chemical composition benchmarks because they provide a large number of stars with nearly identical compositions from which statistically precise, mean cluster abundances can be determined (e.g. Gratton et al. 2004). Furthermore, the chemical compositions of GCs are cosmologically interesting because GCs represent some of the oldest self-contained stellar systems in the universe; therefore, their stars preserve many of the chemical signatures present in the early universe (e.g. Freeman & Bland-Hawthorn 2002). The chemical composition concepts important for this dissertation are discussed in this section. These concepts include the relations that interlink theoretical chemical compositions with observed chemical compositions, along with the origins and observational trends of the important Fe-peak elements, α-elements, neutron-capture elements, and light-elements.

Defining Chemical Composition

There are several ways to parametrize the chemical composition of a star. One common method quotes a star's composition in terms of *mass-fractions*, which measure, by mass, the quantity of H, He, and everything heavier than He contained within a star. Mathematically, mass-fractions are simply

$$X \equiv \frac{\mathcal{M}_H}{\mathcal{M}_{Total}} \tag{1.3}$$

$$Y \equiv \frac{\mathcal{M}_{He}}{\mathcal{M}_{Total}} \tag{1.4}$$

$$Z \equiv \frac{\mathcal{M}_{Heavy}}{\mathcal{M}_{Total}} \tag{1.5}$$

where X, Y, and Z are the H, He, and heavy element mass-fractions, respectively; $\mathcal{M}_H$, $\mathcal{M}_{He}$, and $\mathcal{M}_{Heavy}$ are the total masses of H, He, and heavy elements inside

the star, respectively; and $\mathcal{M}_{Total}$ is the total mass of the star. Mass-fractions are primarily used within the confines of theoretical stellar modelling. For example, once a particular Z value is chosen for a model, the model's Y value can be estimated using Equation 1.2, and its X value then follows from the identity $1 = X + Y + Z$. Note that even though Z is simply a single number, it actually hides an assumed mixture of heavy elements for the model. This mixture of heavy elements takes the form of an *abundance distribution*, which specifies the relative chemical composition for a star on an element-by-element basis. Given an assumed abundance distribution, Z is computed by summing over the distribution in terms of how much mass each element contributes to $\mathcal{M}_{Heavy}$.

Ideally, a similar system could be used to describe the chemical compositions of real stars. To do so would require the measurement of a star's H and He mass fractions and the star's heavy element abundance distribution. Unfortunately, most stars are too cool to emit observable He abundance indicators, and only a small subset of their heavy elements are easily observable. Furthermore, almost every observationally accessible feature of a star's composition originates from the star's thin, upper photosphere; therefore, these indicators may not perfectly represent a star's true composition. Regardless, large quantities of information concerning a star's chemical composition can be obtained from these clues.

When a star's elemental abundances are measured, they are conventionally quoted relative to H in the logarithmic form

$$log\,\epsilon(X) \equiv \log\left(\frac{N_X}{N_H}\right) + 12.0\,dex \tag{1.6}$$

where the abundance notation, $log\,\epsilon(X)$[1], symbolizes the the mathematical quantity on the right-hand-side of its definition; N_X/N_H is the ratio of the number of atoms and ions of element "X" to the number of atoms and ions of H; and the extra $12.0\,dex$[2]

[1]Note that other symbolic notations are sometimes used, such as A_X.

[2]The unit *dex* simply indicates that the preceding number is in units of log_{10}. Therefore, the linear quantity that corresponds to a number in units of *dex* is computed using the "decimal exponent" 10^x.

term normalizes $log\,\epsilon(X)$ so that it equals the logarithm of the number of atoms and ions of element "X" that correspond to every 1×10^{12} atoms and ions of H. This normalization can be better understood if the definition for $log\,\epsilon(X)$ is rewritten as $log(1 \times 10^{12}(N_X/N_H))$, and N_X/N_H is interpreted as a fractional pure number that equals the number of atoms and ions of "X" per every one atom and ion of H. The reference point of 1×10^{12} atoms and ions of H was chosen to prevent $log\,\epsilon(X)$ values from becoming negative.

The reason that abundances are referenced to H is because it is the dominant element in most stars (i.e. MS, RGB, AGB), and because it is normally the main source of a star's continuous opacity, which defines the continuum level of a star's spectrum (Asplund, Grevesse, & Sauval 2005). By measuring the strength of an absorption line, induced from the line opacity of a particular element, relative to this continuum level, $log\,\epsilon(X)$ can be determined for that element (see § 1.2). For most stars, photospheric $log\,\epsilon(X)$ values can be accurately measured for approximately a dozen elements, while, for the Sun, approximately 64 elements can be measured with an accuracy of $\sim 0.5 - 0.10\ dex$ (e.g. Grevesse, Asplund, & Sauval 2007). Note that because stellar abundances cover a range of $\sim 12\,dex$, abundance errors at the level of $\sim 0.5 - 0.10\,dex$ are generally not a practical concern.

Besides having numerous elemental abundances measurable from its photosphere, the Sun also has the distinct advantage that several elemental abundances not accessible from its photosphere can be measured from other sources. In terms of non-photospheric solar sources, a handful of inaccessible elements (e.g. Ne and Ar) can be measured from the Sun's sunspots, chromosphere, corona, solar wind, and solar energetic particles. More importantly, most solar abundances can be indirectly verified using very accurate abundance measurements from type CI carbonaceous chondrite meteorites (e.g. Lodders 2003; Anders & Ebihara 1982). Because these meteorites are believed to consist of unprocessed, remnant material from which the Sun formed, direct laboratory measurements of their chemical composition provide a wealth of abundance information for elements that are completely inaccessible from the Sun, and corroboration for the abundance measurements that are observed from the Sun.

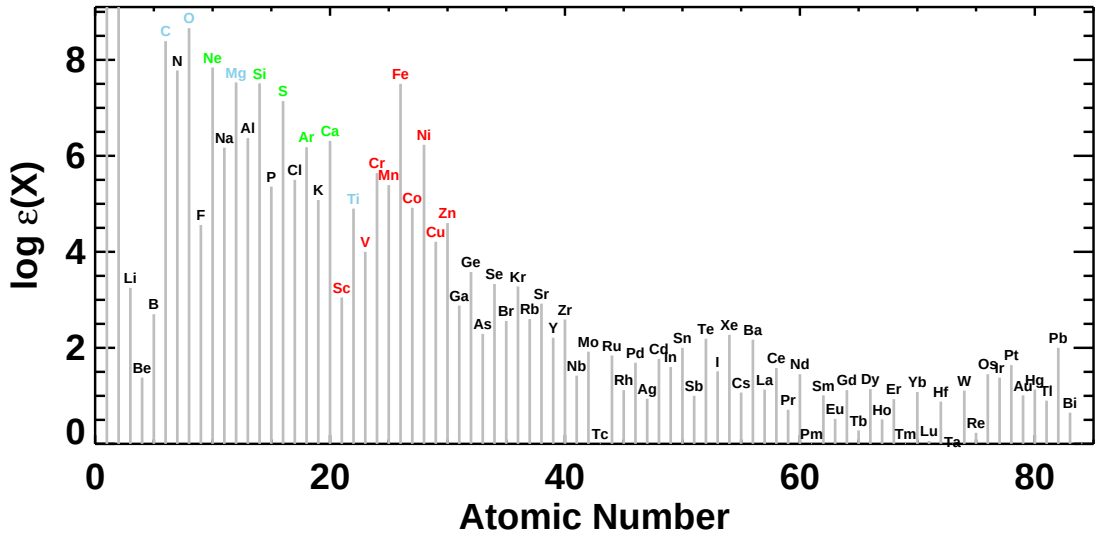

Figure 1.2. Solar abundance distribution. Data comes from Asplund et al. (2005). The color coding conventions are referred to in the text.

As noted by Lodders (2003), of the naturally occurring elements, 56 of them have both solar and meteoritic abundance measurements that can be compared. Of these 56 common elements, 31 of them have abundance values that agree to within 10% of their photospheric and meteoritic values, and 41 of them agree to within 15%. When all of the above sources for solar abundances are assembled, they reveal a detailed picture of the Sun's chemical abundance distribution (e.g. Grevesse et al. 2007; Asplund et al. 2005; Grevesse & Sauval 1998; Grevesse & Noels 1993; Anders & Grevesse 1989). A plot of the Sun's abundance distribution using the compiled data of Asplund et al. (2005) is shown in Figure 1.2.

Unlike the Sun's well studied abundance distribution, the abundance distributions for most stars cannot be reconstructed. This limitation mainly stems from the fact that distant stars are observationally too faint to allow an observer to obtain their spectra at arbitrarily high levels of signal-to-noise. To deal with this limitation, observational astronomers conventionally use only a star's Fe abundance, $log\,\epsilon(Fe)$, to track a star's heavy element abundance distribution. The reason for choosing Fe is because Fe is an abundant component of all heavy element distributions (see Figure 1.2), but mainly because Fe provides a vast number of observable absorption

lines in optical spectra from which its abundance can be derived.

A star's Fe abundance is conventionally quoted relative to the Sun's Fe abundance. This logarithmic comparison takes the form

$$[Fe/H] \equiv log\left(\frac{N_{Fe}}{N_H}\right)_\star - log\left(\frac{N_{Fe}}{N_H}\right)_\odot \tag{1.7}$$

where the notation $[Fe/H]$ is called a star's *metallicity*[3] and is mathematically defined on right-hand-side of the definition. Note that this definition is equivalent to the Sun's $log\,\epsilon(Fe)$ subtracted from a star's $log\,\epsilon(Fe)$. Therefore, stars with $[Fe/H] > 0\ dex$ are more *metal-rich* than the Sun, while stars $[Fe/H] < 0\ dex$ are more *metal-poor* than the Sun. The main reason for quoting stellar Fe abundances relative to the Sun's Fe abundance is because, if they are both measured using the same spectroscopic analysis methods and assumptions, then various systematic errors in the assumptions differentially cancel out (e.g. Gray 2008). Frequently, though, the solar Fe abundance used in Equation 1.7 is merely adopted from a high quality, published data set, which largely negates the benefit of the differential calibration.

Equation 1.7 can also be generalized for any two elements. Mathematically, this generalization takes the form

$$[a/b] \equiv log\left(\frac{N_a}{N_b}\right)_\star - log\left(\frac{N_a}{N_b}\right)_\odot \tag{1.8}$$

where a and b can represent any element. Equation 1.8 is frequently used to express abundance ratios with respect to Fe, where b is equal to Fe and a is any other element. Note that this equation is equivalent to $[\log\epsilon(a)_\star - \log\epsilon(a)_\odot] - [\log\epsilon(b)_\star - \log\epsilon(b)_\odot]$, which once again allows for differential calibration.

Ideally, a star's single $[Fe/H]$ measurement could be used to compute its theoretical Z value, and vice-versa. Under various assumptions regarding a star's abundance distribution, such a relationship can be written. For example, if a star's abundance distribution is assumed to be a *scaled solar* distribution, which is simply the Sun's

[3]Note that Z is also frequently called metallicity.

abundance distribution after it has been uniformly rescaled by a constant factor, then a star's $[Fe/H]$ and Z are related by

$$[Fe/H] = log\left(\frac{Z}{X}\right)_{\star} - log\left(\frac{Z}{X}\right)_{\odot}. \tag{1.9}$$

Here, the common trends in the abundance distributions for the two stars cancel out, leaving behind the scale factor, which is now represented by [Fe/H] (Salaris & Cassisi 2005). While scaled solar distributions are usually good approximations for many stars, some stellar populations are known to deviate from them. In these cases, Equation 1.9 no-longer applies. Instead, Equation 1.9 becomes

$$[M/H] = log\left(\frac{Z}{X}\right)_{\star} - log\left(\frac{Z}{X}\right)_{\odot} \tag{1.10}$$

where $[M/H]$ is the total abundance of the star's heavy elements relative to the Sun (Salaris & Cassisi 2005). Because $[M/H]$ is not usually a direct observable, Equation 1.10 does not usefully connect observations with Z.

The most common source of deviations from a scaled solar abundance distribution is from differences in a star's α-*element* distribution. Metal-poor stars ($[Fe/H] \lesssim -0.6\ dex$) in galaxy halos and GCs tend to have α-element abundances that are enriched with respect to their Fe abundances ($[\alpha/Fe] \sim 0.2 - 0.4\ dex$) as compared to a simple scaled solar distribution (Salaris & Cassisi 2005). When a constant α-element enrichment is applied to a scaled solar distribution, the $[M/H]$ and $[Fe/H]$ values for a star are related by

$$[M/H] \cong [Fe/H] + log(0.694 \times 10^{[\alpha/Fe]} + 0.306) \tag{1.11}$$

where $[\alpha/Fe]$ is equal to

$$[\alpha/Fe] \equiv log\left(\frac{\langle N_{\alpha}\rangle}{N_{Fe}}\right)_{\star} - log\left(\frac{\langle N_{\alpha}\rangle}{N_{Fe}}\right)_{\odot} \tag{1.12}$$

and where $\langle N_{\alpha}\rangle/N_{Fe}$ is the mean number of α-element atoms and ions divided by

the number of Fe atoms and ions within the stellar material (Salaris & Cassisi 2005; Salaris et al. 1993). Equation 1.11 is extremely useful because when it is substituted into Equation 1.10, it allows an α-enriched star's observed $[Fe/H]$ to once again be related to its theoretical Z.

Another complication that is occasionally encountered when attempting to interpret a star's metallicity involves the fact that there is actually more than one *metallicity scale* in use for GCs. Because [Fe/H] is technically not a direct observable, in the sense that various stellar models and assumptions must be applied when conducting abundance analysis, each analysis method used to determine a star's [Fe/H] has its own internal set of accuracies and systematic errors. Good discussions of these metallicity scales and their limitations are presented by Gratton, Sneden, & Carretta (2004) and Harris (2001). The first widely adopted metallicity scale for GCs was the Zinn-West metallicity scale (Zinn & West 1984). This scale assigned a metallicity to most of the Galaxy's GCs using a heterogeneous collection of metallicity indicators, which were then calibrated to a common scale using photographic spectra. These metallicity indicators included integrated cluster spectral indices, individual stellar spectra, cluster CMDs, and integrated cluster colors (Harris 2001). With the advent of modern CCD spectroscopy, the Zinn-West scale was shown to suffer from nonlinearities in its calibration (Carretta & Gratton 1997; Rutledge et al. 1997). For low metallicity GCs ([Fe/H] $\lesssim -0.8\,dex$), the Zinn-West scale's metallicity errors are $\sim \pm 0.2\,dex$, while for high metallicity clusters the scale may overestimate metallicities by up to $\sim 0.5\,dex$ (Harris 2001). Because of these inaccuracies, two new metallicity scales were introduced using modern spectroscopy and line synthesis methods. The first new scale introduced was the Carretta-Gratton scale (Carretta & Gratton 1997). This scale uses only high-quality CCD spectra from individual GC stars and then applies standard spectral line synthesis on a spectrum's Fe absorption lines in order to determine each star's metallicity. This scale also formalizes which Fe absorption lines should be measured, and what line transition parameters should be used for the line synthesis. The second new metallicity scale introduced was the Kraft-Ivans scale (Kraft & Ivans 2003). This scale is very similar to the Carretta-Gratton scale in

Fusion Process	Main Reactions	Reaction Temperature (K)	Cooling Mechanism	Main Products
H-burning	pp-chain	2×10^7	photons	He
	CNO-cycle	3×10^7	photons	He, N, Na
He-burning	$3\alpha \rightarrow {}^{12}\mathrm{C}$	2×10^8	photons	C
	${}^{12}\mathrm{C}(\alpha,\gamma){}^{16}\mathrm{O}$			O
C-burning	${}^{12}\mathrm{C}+{}^{12}\mathrm{C}$	9×10^8	neutrinos	Ne, Na, Mg, Al
Ne-burning	${}^{20}\mathrm{Ne}(\gamma,\alpha){}^{16}\mathrm{O}$	1.5×10^9	neutrinos	O, Mg, Al
O-burning	${}^{16}\mathrm{O}+{}^{16}\mathrm{O}$	2×10^9	neutrinos	Si, S, Ar, Ca
Si-burning	${}^{28}\mathrm{Si}(\gamma,\alpha)$	3.5×10^9	neutrinos	Fe

Table 1.1. Stellar fusion processes. Adapted from Arnett (2004).

that it uses high-quality spectra and provides a recommended Fe transition line list, but unlike the Carretta-Gratton scale, the Kraft-Ivans scale favors the use of singly-ionized Fe transition lines as the basis for a star's metallicity. Despite the efforts of these two groups, neither of these two metallicity scales has been widely adopted, largely because modern spectroscopy and abundance analysis methods have proven to produce fairly robust abundance determinations regardless of what particular line synthesis method and Fe line list is used. As pointed out by Gratton et al. (2004), Kraft & Ivans (2003) themselves conclude that modern metallicity determinations are internally limited by systematic errors on the level of at least $0.02 - 0.05\,dex$.

While a star's observed [Fe/H] is a very useful physical quantity to known about a star when comparing stellar observations with theory, many other elemental abundances can also be observed and used. The next few subsections discuss Fe-peak elements, α-elements, neutron-capture elements, and light-elements from the standpoint of their origins and their observed trends in GCs. For these subsections, a useful reference table (Arnett 2004) that schematically lists the main stellar nucleosynthesis processes responsible for many of these elements is shown in Table 1.1.

Fe-peak Elements

Elements that have atomic numbers (Z_{atom}) in the range $21 \leq Z_{atom} \leq 30$ are Fe-peak elements, except Ti ($Z_{atom} = 22$), which is usually considered to be an α-element (Sneden, Ivans, & Fulbright 2004). Therefore, the Fe-peak elements are Sc, V, Cr, Mn, Fe, Co, Ni, Cu, and Zn. These elements are marked in red within Figure 1.2.

Largely due to their large and symmetric abundance distribution around Fe, it has long been known (e.g. Hoyle 1946; Burbidge et al. 1957) that Fe-peak elements must form in hot, dense environments that achieve *nuclear statistical equilibrium* (Wallerstein et al. 1997). Simply speaking, nuclear statistical equilibrium is the state of a nuclear system where all possible nuclear reactions are balanced by their inverse reactions (Wallerstein et al. 1997). Because the Fe-peak elements have the strongest binding energies per nucleon of all the elements, nuclear statistical equilibrium favors the production of large quantities of Fe-peak abundances, and when the equilibrium conditions come to an end, this Fe-peak abundance distribution "freezes-out" (Arnett 1996). This characteristic distribution can be seen in Figure 1.2.

The astrophysical sites responsible for producing Fe-peak elements are within the cores of massive stars and within stellar material that experiences explosive Si-burning during a supernova. For massive stars ($\mathcal{M} \gtrsim 8\ \mathcal{M}_{\odot}$), Fe-peak elements are produced both inside their cores, by means of normal hydrostatic nucleosynthesis, and within their inner layers during their deaths as core-collapse supernovae (Type II) (e.g. Smartt 2009). Of these two modes of production, only the supernova mode contributes Fe-peak elements to the interstellar medium (ISM). The origin of this asymmetry can be seen by following the steps of a core-collapse supernova.

When a massive star's core becomes mostly Fe, it becomes gravitationally unstable. This instability stems from the fact that nuclear fusion beyond Fe[4] cannot release excess energy to support the star against gravity. Without a source of energy, the core begins to collapse. As the core collapses, its temperature rises until its Fe pho-

[4]Technically, nuclear fusion releases excess energy up through the creation of Ni. Because the most abundant isotope of Ni produced, ^{56}Ni, is radioactively unstable ($\tau_{half-life} \sim 6\ days$)(Baum, Knox, & Miller 2002), it quickly decays to radioactive ^{56}Co ($\tau_{half-life} \sim 77\ days$)(Baum et al. 2002), which finally decays to stable ^{56}Fe. These decay steps are usually implicitly ignored.

todisintegrates, which robs the core of its remnant energy and forces the collapse to become a free-fall. As the pressure increases, the free particles from the disintegrated Fe combine into neutrons, and these neutrons exert a degeneracy pressure that halts the collapse[5]. This near instantaneous halt to the collapse creates a supernova shock wave that propagates away from the newly created neutron core. The temperatures achieved by the outward moving shock ($T \approx 5 \times 10^9\ K$) produce nuclear statistical equilibrium conditions up through the star's original Si-, O-, and Ne-burning central layers, which triggers explosive Si-, O-, and Ne-burning throughout this material. This explosive Si-burning is responsible for producing a core-collapse supernova's Fe-peak elements. Meanwhile, the massive star's large outer layers of lighter elements do not experience explosive nucleosynthesis because the shock wave loses too much energy by the time it reaches them. As the star continues to explode outwards, these outer layers of light elements and the inner layers' newly generated Fe-peak elements are ejected into the ISM, most likely with the aid of neutrino pressure. Once exposed, the original star's neutron core remains as a neutron star surrounded by supernova ejecta.

The production and dispersal of Fe-peak elements is even more efficient for less massive stars ($1\ \mathcal{M}_\odot \lesssim \mathcal{M} \lesssim 8\ \mathcal{M}_\odot$) when they end their lives as accretion induced supernovae (Type Ia) (e.g. Hillebrandt & Niemeyer 2000). The physical ingredients for an accretion induced supernova involves a binary system composed of a WD star and a companion star that is at an earlier stage of evolution (e.g. RGB or AGB stage). These stars must also be separated by a distance that is small enough for the WD to accrete material from the tenuous upper layers of its companion. When the WD accretes enough mass to surpass the ability of its electron degeneracy pressure to support its core against gravity ($\mathcal{M}_{WD} \approx 1.4\ \mathcal{M}_\odot$), the WD's core begins to collapse. This collapse increases the core's temperature until C-burning is ignited. This C-burning creates a subsonic, *deflagration wave* that burns away from the center

[5]Note, though, that stars more massive than $\sim 40\ \mathcal{M}_\odot$ (Wallerstein et al. 1997), cannot stop their collapse with neutron degeneracy pressure, and thus continue to collapse until they become black holes.

of the star. Because electron degeneracy pressure is independent of temperature, the star cannot cool down through adiabatic expansion; therefore, a runaway process of explosive fusion occurs within the star, all the way up to the Fe-peak producing stage of explosive Si-burning. At this point, the star disrupts and explodes, possibly due to a supersonic *detonation wave*.

A more detailed list of the astrophysical mechanisms responsible for producing the Fe-peak elements are listed in Table 1.2, which is based on *Table III* of Woosley, Heger, & Weaver (2002) and the isotope fraction data compiled by Baum et al. (2002). As qualitatively mentioned above, note that these mechanisms predominately take place in supernovae, particularly Type Ia supernovae. Sc is mainly produced from nuclear statistical equilibrium freeze-outs that are rich in α-particles (Woosley, Arnett, & Clayton 1973), and partly from normal hydrostatic C- and Ne-burning. V is mainly produced from α-rich freeze-outs, and partly from explosive Si- and O-burning. Cr is mainly produced from explosive Si-burning, and partly from α-rich freeze-outs. Mn and Fe are mainly produced from explosive Si-burning. Co is mainly produced from the s-process during He-burning in high-mass stars ($\mathcal{M} \gtrsim 8\ \mathcal{M}_{\odot}$), and partly from α-rich freeze-outs. Ni is mainly produced from α-rich freeze-outs. Cu is mainly produced from the s-process during He-burning in high-mass stars, and partly from hydrostatic C- and Ne-burning. Zn is most likely produced from the r-process within neutron-rich winds emanating from young neutron stars (Duncan, Shapiro, & Wasserman 1986), and partly from α-rich freeze-outs and the s-process during He-burning in high-mass stars.

Typical abundance yields from Type II and Type Ia supernovae are shown in Figure 1.3 for elements within the range $6 \leq Z_{atom} \leq 30$. These yields are taken from the supernovae models of Iwamoto et al. (1999). Note that all mass fractions are normalized to the total mass ejected from their corresponding supernova, while ignoring any mass contributions from elements outside the range $6 \leq Z_{atom} \leq 30$ (e.g. any quantities of H and He ejected from the Type II supernova are ignored). Upon comparing the yields of the two supernovae, it becomes immediately apparent that a Type Ia supernova mainly contributes Fe to the ISM, while a Type II supernova

Species	Origin	Iso. Fraction (% by number)
^{45}Sc	**α, C, Ne, ν(r)**	**100.0**
^{50}V	C, Ne, xNe, xO	0.25
^{51}V	**α, Ia, xSi, xO, ν(r)**	**99.75**
^{50}Cr	xSi, xO, α, Ia	4.34
^{52}Cr	**xSi, α, Ia**	**83.79**
^{53}Cr	xO, xSi	9.50
^{54}Cr	Ia	2.36
^{55}Mn	**Ia, xSi, ν(r)**	**100.0**
^{54}Fe	Ia, xSi	5.84
^{56}Fe	**xSi, Ia**	**91.75**
^{57}Fe	xSi, Ia	2.12
^{58}Fe	He(s), Ia	0.28
^{59}Co	**He(s), α, Ia, ν(r)**	**100.0**
^{58}Ni	α	**68.08**
^{60}Ni	α, He(s)	26.22
^{61}Ni	He(s), α, Ia	1.14
^{62}Ni	He(s), α	3.63
^{64}Ni	He(s)	0.92
^{63}Cu	**He(s), C, Ne**	**69.17**
^{65}Cu	He(s)	30.83
^{64}Zn	**ν(r), α, He(s)**	**48.63**
^{66}Zn	He(s), α, Ia	27.90
^{67}Zn	He(s)	4.10
^{68}Zn	He(s)	18.75

Table 1.2. The astrophysical mechanisms responsible for producing the Fe-peak elements. Adapted from *Table III* of Woosley, Heger, & Weaver (2002). The "Origin" column lists the most likely production mechanism(s) for each isotope according to Woosley et al.. The "Iso. Fraction" column lists the measured isotope fractions for terrestrial material as compiled by Baum et al. (2002) in terms of a percentage by number. The "Origin" column's mechanism symbols and meanings are: "L" $\equiv$ isotope is produced in low and intermediate-mass stars ($\mathcal{M} \lesssim 8\mathcal{M}_{\odot}$); "H", "He", "C", "Ne", "O", and "Si"$\equiv$ isotope is produced from hydrostatic H-burning, He-burning, C-burning, Ne-burning, O-burning, and Si-burning, respectively; prefix "x" $\equiv$ isotope is produced from the explosive version of its nuclear burning process; "Ia" $\equiv$ isotope is predominantly produced from Type Ia supernova; "α" $\equiv$ isotope is produced in an α-particle rich freeze-out after nuclear statistical equilibrium (Woosley et al. 1973); "He(s)" $\equiv$ isotope is produced from the s-process during He-burning in high-mass stars; ν(r) $\equiv$ isotope is produced from the r-process in a nucleon-wind powered by neutrinos emanating from a young neutron star (Duncan et al. 1986); and "novae" $\equiv$ isotope is produced from classical novae.

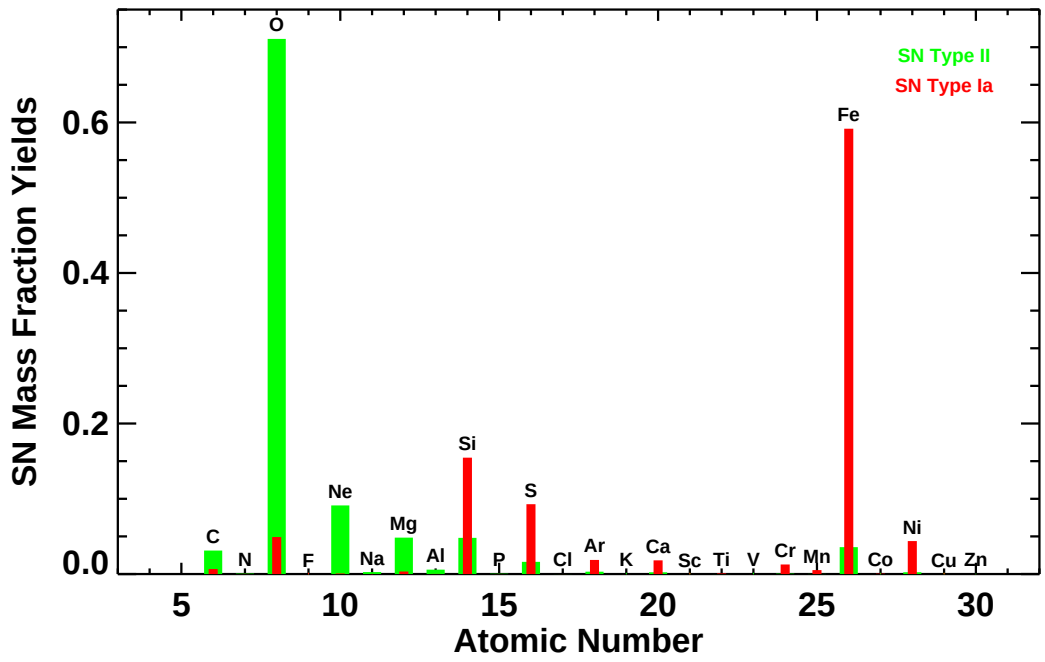

Figure 1.3. Typical mass fraction yields from core-collapse and accretion induced supernovae. The core-collapse and accretion induced supernovae data respectively come from the "Type II" and "WDD2" models of Iwamoto et al. (1999), found in their *Table 3*. Note that the data assume that all radioactive isotopes have decayed to their stable daughter products.

mainly contributes O. The O-rich ejecta from a Type II supernova predominantly originates from its progenitor star's thick outer layers that experienced hydrostatic He-burning. Meanwhile, the Fe-rich ejecta from a Type Ia supernova originates from the explosive Si-buring that occurs during its supernova process. Because this Si-burning occurs in the relatively small and confined volume of a WD, it can approach levels of complete Si-burning.

These two very different yield distributions have direct implications for the abundance patterns seen in stars as a function of their metallicities. This metallicity dependence is due to the different characteristic time scales required for Type II and Type Ia supernovae to occur (see, e.g., McWilliam 1997 and references therein). Because the time scale for core-collapse supernovae is dictated by the rapid evolution of high-mass stars, they can occur a few $Myrs$ after a star formation event. However, because an accretion induced supernova requires a binary star to evolve to a WD, and the companion star to evolve to an RGB or AGB star, accretion induced supernovae

occur on a time scale of $0.1 - 5.0\,Gyrs$ after a star formation event (Matteucci & Recchi 2001). These two different time scales imply that when the early metal-poor ISM was generating stars, the ISM was being enriched predominantly by Type II supernovae. Therefore, stars with low metallicity are predicted to have abundance distributions that reflect the O-rich and Fe-poor abundance distribution of Type II supernovae. As time progressed, Type Ia supernovae eventually began to enrich the ISM with Fe-rich material. Therefore, stars that formed later are predicted to reflect the O-poor and Fe-rich abundance distribution of Type Ia supernovae.

This metallicity dependence is shown schematically in Figure 1.4, which is adapted from *Figure 1* of McWilliam (1997). Figure 1.4 plots [O/Fe] abundance ratios for stars in a hypothetical stellar system as a function of the stars' metallicities. Note that the horizontal line at $[\mathrm{O/Fe}] = 0.0\,dex$ corresponds, by definition, to the Sun's [O/Fe] value. The basic trend that occurs comprises a super-solar, $[\mathrm{O/Fe}] \sim +0.35\,dex$ "plateau" for metal-poor stars ($[\mathrm{Fe/H}] < -1.0\,dex$), a gradual decrease in [O/Fe] for less metal-poor stars ($-1.0\,dex < [\mathrm{Fe/H}] < -0.2\,dex$), and a solar [O/Fe] value for stars near solar metallicity. Physically, the O-rich plateau corresponds to old, metal-poor stars that formed out of the ISM when only Type II supernovae were enriching the ISM. The plateau's "turnover" at $[\mathrm{Fe/H}] \sim -1.0\,dex$ corresponds to stars that formed out of the ISM when Type Ia supernovae were just beginning to enrich the ISM with Fe. As more-and-more Type Ia supernovae enriched the ISM after the turnover, the ISM's [O/Fe] value gradually decreased, and any stars that formed during this time period locked-in these [O/Fe] values. The exact height of the O-rich plateau and the metallicity location of its turnover are respectively a function of the stellar system's characteristic IMF and star formation rate (SFR) (McWilliam 1997). Because O production increases with stellar mass (e.g. Woosley & Weaver 1995), "top-heavy" IMFs create higher [O/Fe] plateaus. Meanwhile, the plateau's turnover moves to higher metallicities as a stellar system's SFR increases because a higher SFR produces more Type II supernovae, which enrich the stellar system's metallicity before the Type Ia supernovae timescale is reached.

The diagnostic utility that comes from plotting stellar abundance ratios as a

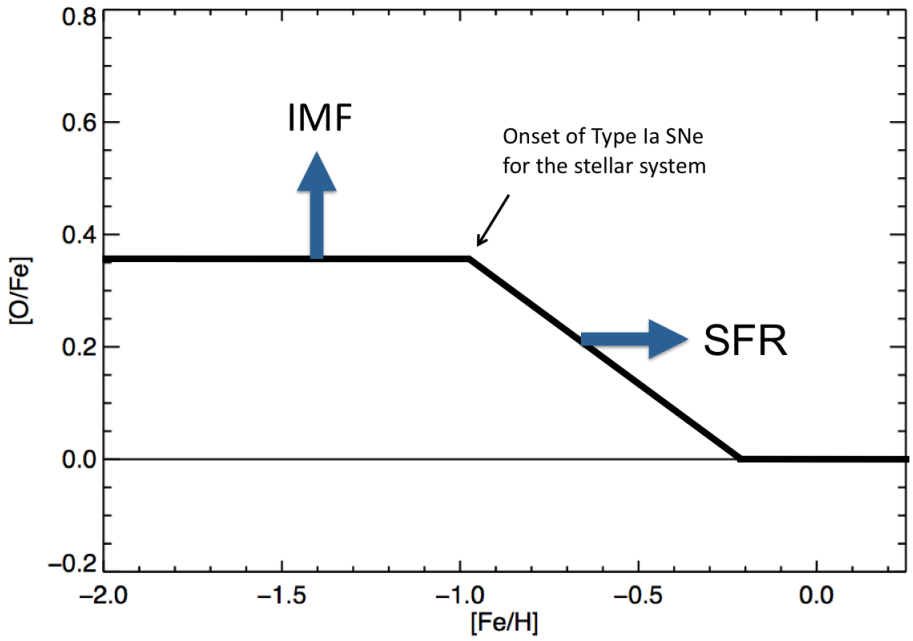

Figure 1.4. Schematic plot of [O/Fe] abundance ratio trend with metallicity. Adopted from *Figure 1* of McWilliam (1997).

function of metallicity is not limited to [O/Fe]. As can be intuitively deduced from the supernovae yields in Figure 1.3, several other elements should demonstrate strong metallicity trends. Perhaps less intuitively, this is also true for the Fe-peak elements. These Fe-peak metallicity trends are seen throughout the Milky Way's GCs and field stars.

As noted by Gratton et al. (2004), the most practical Fe-peak elements to observe in GC stars are Fe, Mn, Ni and Cu. This selection is mainly due to signal-to-noise considerations. Because Galactic GCs are old and metal poor, their stellar spectra peak in the "yellow-red" wavelength region (5100 Å$\lesssim \lambda \lesssim$ 7500 Å); therefore, the application of high signal-to-noise abundance analysis on GC stars rely heavily on this wavelength region. Within this region, numerous Fe and Ni absorption lines are available, several Mn lines are available, and a few high quality Cu lines are available. Meanwhile, the less practical Fe-peak elements of Sc, Cr, Co, and Zn have absorption lines predominantly in the "violet-blue" wavelength region. Because GC stars contribute little flux to this region, the absorption lines of these elements suffer

from low signal-to-noise, which both increases the amount of line blending that they suffer from, and makes it more difficult to identify their line profiles. Furthermore, because most observed GC stars are bright and cool RGB stars, their spectra in this region suffers from line blanketing due to numerous molecular and atomic transition lines. Finally, the last potential Fe-peak element, V, is uniquely impractical because its abundance determination is extremely sensitive to the T_{eff} used in its abundance analysis (Gratton et al. 2004).

The easily accessible Fe-peak elements in GC spectra (i.e. Mn, Ni and Cu) all demonstrate abundance trends with metallicity. These trends are shown schematically in Figure 1.5 using the GC abundance data compiled by Sneden et al. (2004) and Gratton et al. (2004) as templates. Of the three abundance ratios, [Ni/Fe] shows the most intuitive trend with metallicity. Because the production of Ni and Fe are closely related, their abundance ratio remains essentially constant for all metallicities. This implies that the characteristic [Ni/Fe] values from Type II and Type Ia supernovae have been roughly equal throughout Galactic history. The abundance ratios of [Cu/Fe] and [Mn/Fe] are less intuitive and have not been thoroughly explained from theory (see, e.g., Kobayashi et al. 2006). At low metallicities, [Cu/Fe] and [Mn/Fe] are both noticeably sub-solar. The gradual increase in [Mn/Fe] once [Fe/H] $\sim -1\,dex$ is reached is once again attributable to the initiation of Type Ia supernovae (Kobayashi et al. 2006). The transition of [Cu/Fe] towards solar values, though, begins before Type Ia supernovae have a chance to enrich the ISM. Therefore, the production of Cu in Type II supernovae must be a function of metallicity. As it turns-out, the production of the odd-Z elements Na, Al, and Cu increase when there is more ^{14}N present in a star (Kobayashi et al. 2006). Because ^{14}N tracks with metallicity, so does the abundances of Na, Al, and Cu.

The less easily accessible Fe-peak elements in the spectra of GC stars (i.e. Sc, Cr, Co, Zn, and V) have been extensively studied in Galactic field stars. Such studies demonstrate that these elements also have abundance trends with metallicity. These trends are shown schematically in Figure 1.6 using the Milky Way field star abundance data compiled by Kobayashi et al. (2006) as templates. Note that be-

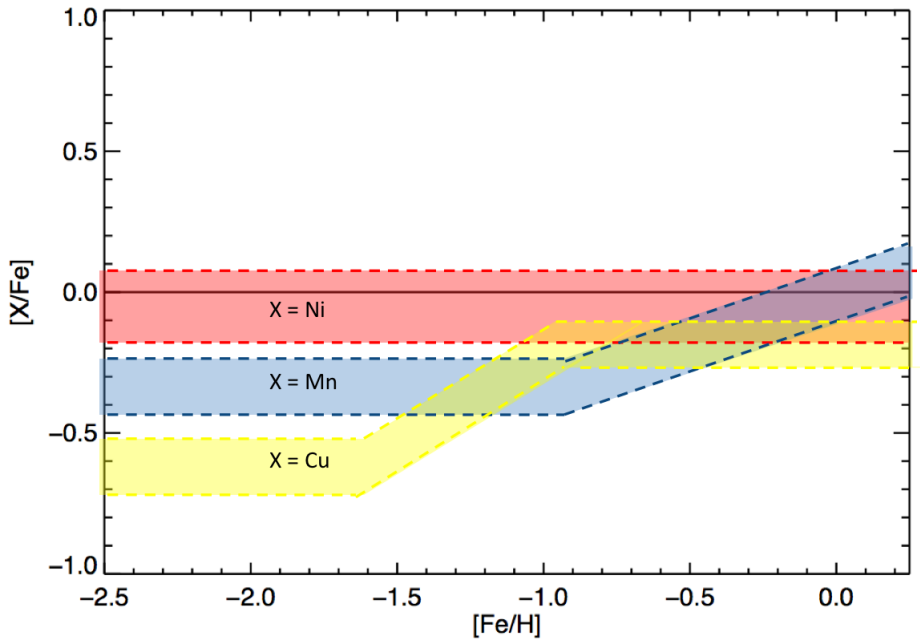

Figure 1.5. Schematic abundance ratio trends for the Fe-peak elements Mn, Ni, and Cu in Galactic GCs.

cause Galactic halo stars probe metallicities beyond the $\sim -2.5\,dex$ value reached by Galactic GCs, Figure 1.6 extends to lower metallicities than Figure 1.5. The simplest trend in the figure is for [Sc/Fe], which demonstrates that [Sc/Fe] is roughly constant for both Type II and Type Ia supernovae. The [Co/Fe] trend is perhaps the most unusual. For very low metallicities ([Fe/H] $\lesssim -3.0\,dex$), Type II supernovae initially overproduce [Co/Fe], and then begin to lower their production when the ISM reaches [Fe/H] $\sim -3\,dex$. Two proposed solutions for this trend (Umeda & Nomoto 2005; Nakamura et al. 1999) attribute it to very high-mass stars that are somehow able to overproduce [Co/Fe] compared to normal high-mass stars. Because very high-mass stars are the first to explode as Type II supernovae, they have the opportunity to increase the ISM's [Co/Fe] to super-solar levels before the normal high-mass stars get a chance to contribute their lower levels of [Co/Fe]. Nakamura et al.'s (1999) proposed mechanisms for this [Co/Fe] overproduction is that very high-mass stars might eject deeper layers of their material into the ISM, which are more rich in Co. Umeda & Nomoto's (2005) proposed mechanism is that very high-mass stars might have higher explosive energies, which produce more Co due to more complete Si-burning. The

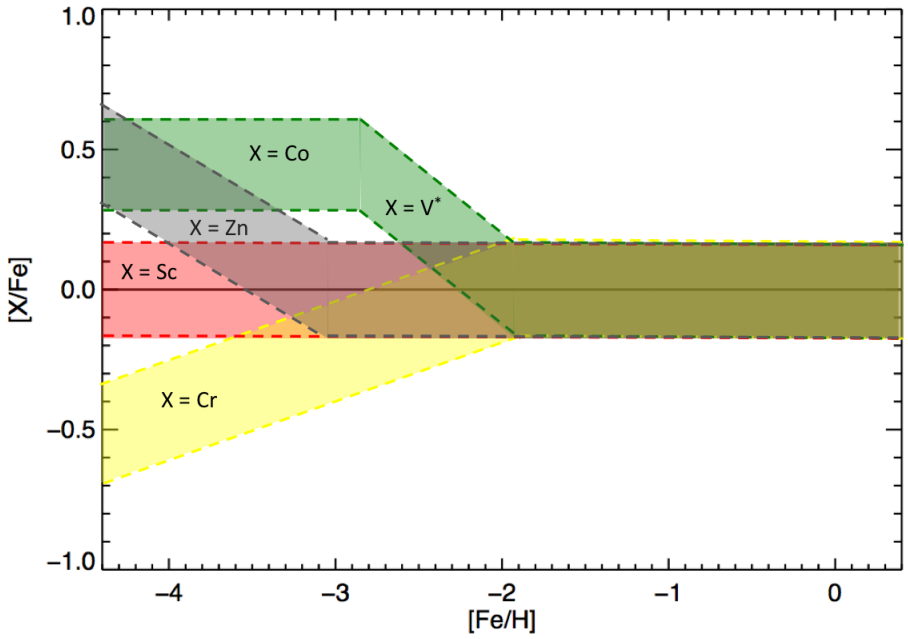

Figure 1.6. Schematic abundance ratio trends for the Fe-peak elements Sc, Cr, Co, Zn, and V in Galactic field stars.

Umeda & Nomoto model also potentially explains the gradual decrease of [Cr/Fe] that begins at [Fe/H] $\sim -2\,dex$ and continues towards lower metallacities, and the gradual increase of [Zn/Fe] that begins at [Fe/H] $\sim -3\,dex$ and continues towards lower metallicities. The reason, once again, is that if very high-mass stars explode with higher than average energies, they could achieve higher explosive energies that favor Zn production and hinder Cr production. The final trend of [V/Fe] is based only on stellar data down to [Fe/H] $\sim -3\,dex$; therefore, it is unclear if it exactly follows the [Co/Fe] plateau at lower metallicities.

α-elements

Elements that have even atomic numbers in the range $6 \leq Z_{atom} \leq 22$, and whose dominant isotopes are integer multiples of He nuclei (i.e. α-particles) are called α-elements (Sneden et al. 2004). Based purely on this definition, the α-elements are C, O, Ne, Mg, Si, S, Ar, Ca, and Ti. Various additional constraints are usually applied, which frequently results in disputes over which of these elements are "pure" α-elements (see, e.g., Jordi et al. 2002). Because C, O, and Mg abundances can be-

come altered from proton-capture reactions, they are sometimes excluded from the list of pure α-elements (Gratton et al. 2004). Meanwhile, even though Ti is usually considered to be an α-element, its pure α-element isotope, ^{44}Ti, is radioactively unstable ($t_{half-life} \sim 60\ yrs$)(Baum et al. 2002) and cannot be observed in stars. Instead, Ti's dominant isotope, ^{48}Ti, is observed and is usually implicitly considered to be the α-element ^{44}Ti. The α-elements are marked in blue and green within Figure 1.2, where the colors identify the potentially impure and pure α-elements, respectively.

The astrophysical mechanisms responsible for producing the α-elements are numerous, but their contributions to the ISM are dominated by Type II supernovae. Table 1.3 lists the most likely production mechanisms for the α-elements based on *Table III* of Woosley et al. (2002) and the isotope fraction data compiled by Baum et al. (2002). C is mainly produced in low and intermediate-mass stars ($\mathcal{M} \lesssim 8\ \mathcal{M}_{\odot}$) during hydrostatic He-burning, and is primarily contributed to the ISM from the mass-loss of RGB and AGB stars (e.g. Marigo 2001; van den Hoek & Groenewegen 1997; Renzini & Voli 1981). O is mainly produced during hydrostatic He-burning, and is primarily contributed to the ISM from Type II supernovae. Ne is mainly produced during hydrostatic C-burning, and is primarily contributed to the ISM from Type II supernovae. Mg is mainly produced during hydrostatic C- and Ne-burning, and is primarily contributed to the ISM from Type II supernovae. Si, S, and Ca are mainly produced during explosive and hydrostatic O-burning, and are primarily contributed to the ISM from Type II and Type Ia supernovae, where these supernovae respectively contribute roughly two-thirds and one-third of the Galactic Si, S, and Ca abundances (Thielemann 2001). Ar is mainly produced from the s-process during He-burning in high-mass stars ($\mathcal{M} \gtrsim 8\ \mathcal{M}_{\odot}$), and from hydrostatic C- and Ne-burning. Ar is primarily contributed to the ISM from Type II and Type Ia supernovae, where they respectively contribute roughly two-thirds and one-third of the Galactic Ar abundance (Thielemann 2001). Finally, Ti is mainly produced during explosive Si-burning, and is primarily contributed to the ISM from Type Ia supernovae.

As with the Fe-peak elements, plotting abundance ratios of the α-elements as a

Species	Origin	Iso. Fraction (% by number)
^{12}**C**	**L, He**	**98.93**
^{13}C	L, H	1.07
^{16}**O**	**He**	**99.76**
^{17}O	novae, L	0.04
^{18}O	He	0.20
^{20}**Ne**	**C**	**90.48**
^{21}Ne	C	0.27
^{22}Ne	He	9.25
^{24}**Mg**	**C, Ne**	**78.99**
^{25}Mg	C, Ne	10.00
^{26}Mg	C, Ne	11.01
^{28}**Si**	**xO, O**	**92.23**
^{29}Si	C, Ne	4.68
^{30}Si	C, Ne	3.09
^{32}**S**	**xO, O**	**94.93**
^{33}S	xO, xNe	0.76
^{34}S	xO, O	4.29
^{36}S	He(s), C, Ne	0.02
^{36}Ar	xO, O	0.34
^{38}Ar	xO, O	0.06
^{40}**Ar**	**He(s), C, Ne**	**99.60**
^{40}**Ca**	**xO, O**	**96.94**
^{42}Ca	xO	0.65
^{43}Ca	C, Ne, α	0.14
^{44}Ca	α, Ia	2.09
^{46}Ca	C, Ne	0.004
^{48}Ca	Ia	0.19
^{46}Ti	xO, Ia	8.25
^{47}Ti	Ia, xO, xSi	7.44
^{48}**Ti**	**xSi, Ia**	**73.72**
^{49}Ti	xSi	5.41
^{50}Ti	Ia, He(s)	5.18

Table 1.3. The astrophysical mechanisms responsible for producing the α-elements. Adapted from *Table III* of Woosley et al. (2002). See Table 1.2 for further details.

function of stellar metallicity is a powerful diagnostic for investigating stellar populations. This utility was previously demonstrated schematically for the α-element O in Figure 1.4. Similar plots for the rest of the α-elements can also be constructed. Unlike the Fe-peak elements, though, all α-element abundance ratio plots demonstrate essentially the same metallicity trend that is seen in Figure 1.4's schematic plot for [O/Fe]. This uniform metallicity dependence greatly simplifies the interpretation of the α-element abundance ratio diagnostics.

As noted by Gratton et al. (2004), the best, pure α-elements to observe and analyze in GC stars are Ca and Si. As previously mentioned, the α-elements C, O, and Mg have abundances that can be altered from proton-capture reactions, while the isotope of Ti that is actually observed in a star's spectrum is technically not an α-element. Meanwhile, the α-elements Ne and Ar are noble gas elements, and, therefore, cannot be observed in cool stars. Finally, S has only weak absorption lines in the near infrared that fall outside the usual wavelength range observed for most stellar abundance analysis. Therefore, Ca and Si are the only α-elements that are both pure and easily observed.

The abundance ratio trends for Ca and Si versus metallicity are shown schematically in Figure 1.7 using the GC abundance data compiled by Sneden et al. (2004) and Yong et al. (2005) as templates. Both [Ca/Fe] and [Si/Fe] have plateaus near $\sim +0.3\,dex$ for low metallicities ([Fe/H] $\lesssim -1.0\,dex$), and then gradually decrease to solar values within the metallicity range $-1.0\,dex \lesssim$ [Fe/H] $\lesssim 0.0\,dex$. The slight difference between the scatter in the two trends is most likely because Si has fewer observable transition lines than Ca within optical spectra. As with the [O/Fe] example, the Ca and Si trends are due to Type II supernovae polluting the ISM with α-element rich ejecta before Type Ia supernovae had a chance to explode and increase the metallicity of ISM. Note that Type Ia supernovae also contribute roughly one-third of the ISM's Ca and Si abundances (Thielemann 2001), but their contributions to the ISM's Fe abundance is much larger, which allows the ISM's [Ca/Fe] and [Si/Fe] abundance ratios to still decrease with increasing metallicity.

The average abundance ratio trend for O, Mg, S, and Ti is shown schematically in

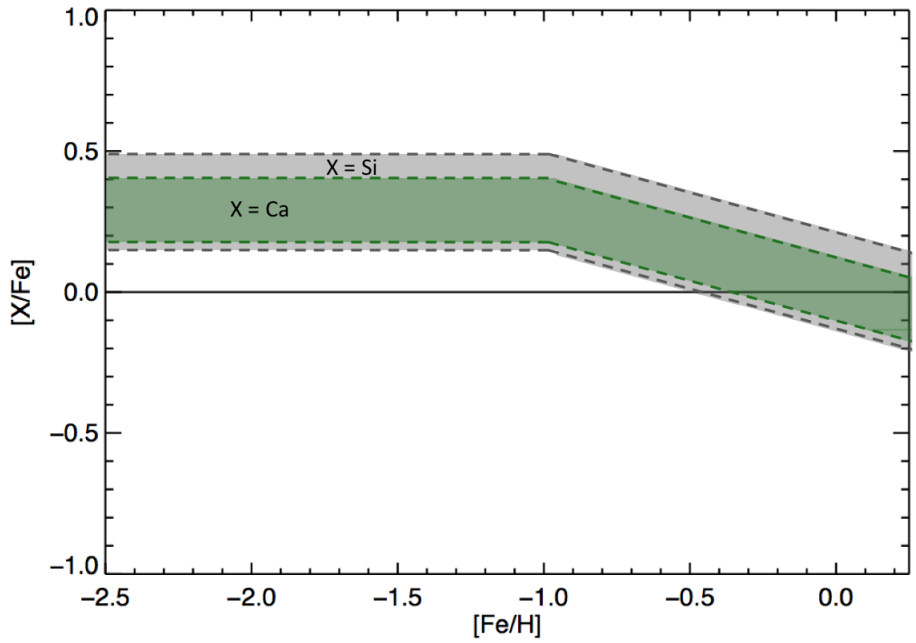

Figure 1.7. Schematic abundance ratio trends for the α-elements Ca and Si in Galactic GCs.

Figure 1.8 using the Galactic field star abundance data compiled by Kobayashi et al. (2006) as templates. All four trends are shown as a single trendline because they are intrinsically similar and because the scatter in the stellar data makes it difficult to distinguish any low-level differences between them. This average trend plateaus roughly at $\sim +0.4\,dex$ for low metallicities, and then gradually decreases to a solar value within the metallicity range $-1.0\,dex \lesssim$ [Fe/H] $\lesssim 0.0\,dex$. Within errors, this trend matches the metallicity dependence shown in Figure 1.7 for [Ca/Fe] and [Si/Fe] in GCs, and its physical interpretation is also the same.

Neutron-Capture Elements

Elements beyond the Fe-peak are not created by thermonuclear fusion, but are instead created by *neutron-capture* reactions. Because a neutron is electrically neutral, it can collide and merge with a *seed nucleus* if the relative energy of the collision and the composition of the seed nucleus correspond to a favorable neutron-capture cross section. Each time a seed nucleus absorbs a neutron, the nucleus becomes a heavier isotope of the element that it represents. If this new isotope is unstable, it can convert

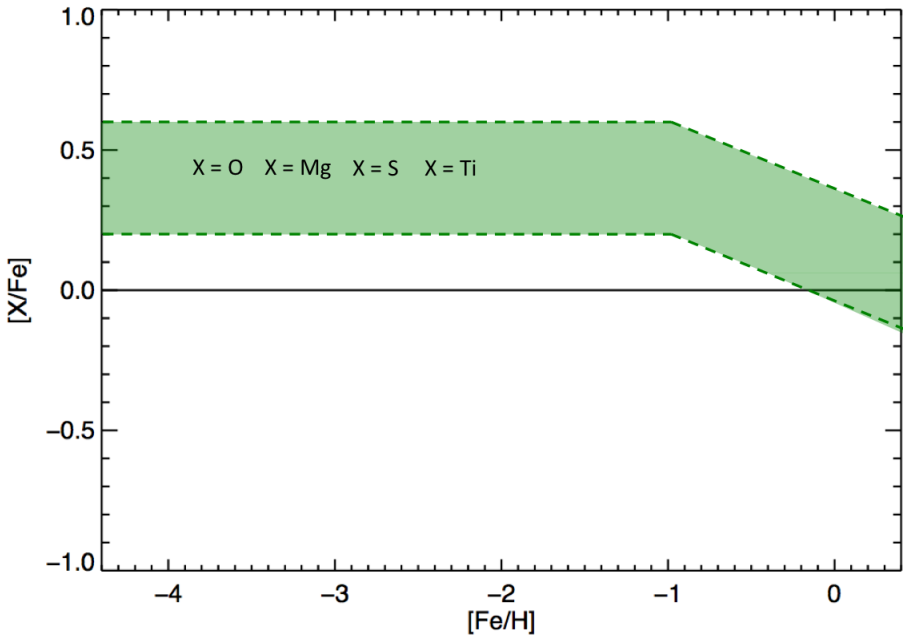

Figure 1.8. Schematic abundance ratio trends for the α-element O, Mg, S, and Ti in Galactic field stars.

one of its neutrons into a proton by means of a β^--decay, which transforms the isotope into the next element in the periodic table. Many repetitions of this process can thus create the naturally occurring elements beyond the Fe-peak.

The transformation of seed nuclei to heavier elements beyond the Fe-peak can follow two general pathways. These pathways are a function of the rate at which neutrons are captured. If sequential neutron-captures occur on a time scale that is much shorter than the time scale for a seed nucleus to β^--decay, the seed nucleus can become very neutron-rich without decaying. As the nucleus becomes more neutron-rich, it becomes increasingly unstable until either its time scale for β^--decay or photodisintegration becomes smaller than its neutron-capture time scale (Wallerstein et al. 1997). If the condition for β^--decay is reached, the seed nucleus will transform itself into a heavier element and then begin to capture neutrons again. If the condition for β^--decay is not reached, the seed nucleus will continue to capture neutrons until it reaches a balance between neutron-capture and neutron emission by way of photodisintegration until the source of incoming neutrons stops, at which

point the nucleus will rapidly β^--decay to a stable isotope (Pagel 1997). This rapid neutron-capture process is called the r-process (Burbidge et al. 1957).

If the sequential capture of neutrons occurs on a time scale that is longer than the time scale for a seed nucleus to β^--decay, the seed nucleus can slowly gain neutrons until it reaches its first available unstable isotope, at which point it will β^--decay to the next element in the periodic table. In this manner, a seed nucleus can march across the periodic table towards heavier elements. This slow neutron-capture process is called the s-process (Burbidge et al. 1957).

Because the s-process is a linear progression towards heavier elements, it suffers from bottlenecks when it reaches isotopes that have very small neutron-capture cross sections. These small cross sections physically correspond to stable isotopes that have closed neutron shells (Goeppert-Mayer & Jensen 1955), which occur for isotopes that have 50, 82, and 126 neutrons. Elements that satisfy these conditions include Sr ($Z_{atom} = 38$), Ba ($Z_{atom} = 56$), and Pb ($Z_{atom} = 82$), respectively. Therefore, the s-process preferentially creates elements centered around Sr, Ba, and Pb. The ultimate bottleneck encountered by the s-process occurs at Bi ($Z_{atom} = 83$) because elements beyond Bi α-decay faster than they can absorb the slowly arriving neutrons (Baum et al. 2002).

The r-process tends to produce the elements located in between the s-process abundance peaks. This can be seen in Figure 1.9, which plots the fractional abundances attributable to the r-process for the solar system's neutron-capture elements. This plot is adapted from Wallerstein et al. (1997) and uses neutron-capture abundance data from Sneden et al. (1996). If r- and s-process elements are arbitrarily defined to be elements that have at least 75% of their abundances attributable to either the r- or s-process, then Figure 1.9 shows that the r-process elements peak near Br ($Z_{atom} = 35$), Rh ($Z_{atom} = 45$), I ($Z_{atom} = 53$), Eu ($Z_{atom} = 63$), Ir ($Z_{atom} = 77$), and Th ($Z_{atom} = 90$). Meanwhile, the s-process abundance peaks correspond to the troughs near Sr, Ba, and Pb. Note that the r-process elements outnumber the s-process elements and that many elements have abundances that are attributable to both the r- and s-process. Also, note that all elements beyond Bi up through U

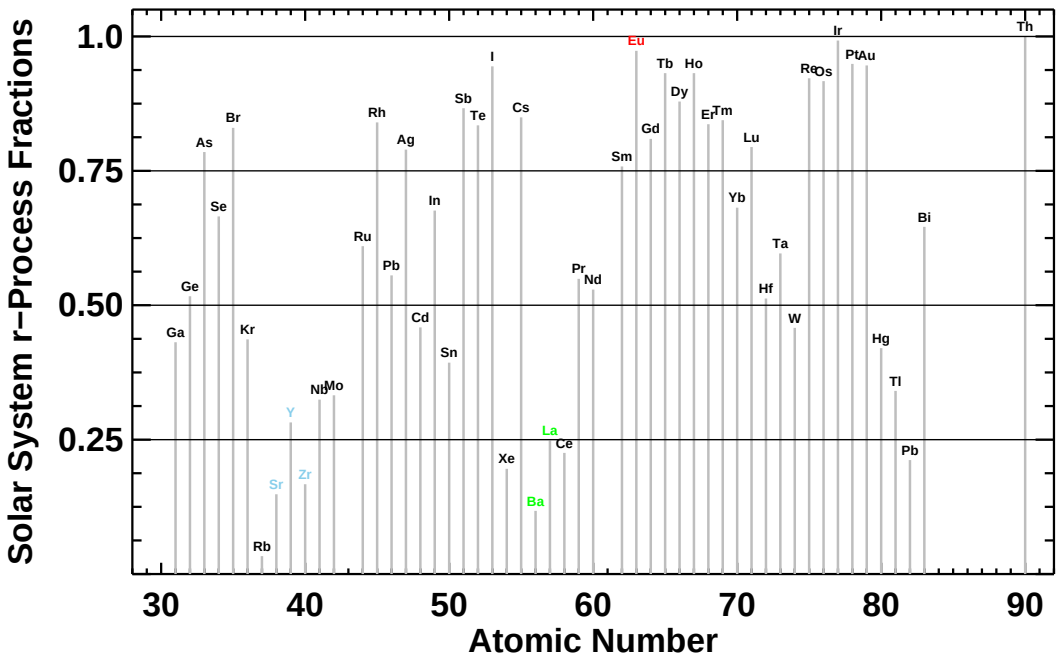

Figure 1.9. The r-process fractions for the solar system's abundances. Adapted from Wallerstein et al. (1997), using data from Sneden et al. (1996).

($Z_{atom} = 92$) are produced by the r-process. Because most of these elements, with the exceptions of Th ($Z_{atom} = 90$) and U, have short half-lives, they are not shown in the figure.

The astrophysical sites responsible for the s-process can be separated into two environments. The *weak component* of the s-process occurs during the core He-burning stage in massive stars (see, e.g., Wallerstein et al. 1997 and references therein). During this stage, free neutrons are provided by low-levels of Ne-burning. This weak component produces most of the s-process abundances below the Sr abundance peak. The canonical, *main component* of the s-process occurs for low mass stars ($\mathcal{M} \lesssim 3\ \mathcal{M}_{\odot}$) during the AGB stage of evolution (see, e.g., Wallerstein et al. 1997 and references therein). During this stage, free neutrons are provided by low-levels of C-burning that occur in between an AGB star's thermally pulsating shell H- and He-burning (Thielemann 2001; Straniero et al. 1995; Iben & Renzini 1983; Hollowell & Iben 1989). This main component produces the s-process abundances from the Sr abundance peak to the Pb abundance peak.

The astrophysical sites responsible for the r-process have never been satisfactorily proven, but almost certainly involve supernovae. Following Woosley et al. (2002), three possible astrophysical sites for the r-process are the most promising. The least likely of the three sites involves the merger of two neutron stars (see, e.g., Freiburghaus, Rosswog, & Thielemann 1999 and references therein) or the tidal disruption of a neutron star by a black hole (Lattimer & Schramm 1974). Here, neutron-rich ejecta from one of these energetic disruptions could easily produce r-process material. In fact, the production of r-process material from this mechanism seems to be too large, while the estimated neutron star disruption rates seem to be too small (Qian 2000). The second mechanism involves asymmetric core collapse supernovae that have outflow jets (LeBlanc & Wilson 1970; Symbalisty et al. 1985; Cameron 2001). In this model, neutron-rich winds are funneled away from an accretion disk that is falling into a newly formed black hole or neutron star. The third, and currently favored, mechanism involves a neutrino powered wind that emanates from a newly formed neutron star (Duncan et al. 1986). This neutrino-wind would eject free nucleons from the neutron star, which could then reassemble into a mix of seed nuclei and free neutrons as the nucleon material cools. Because this material would be neutron-rich, the excess neutrons could then merge with the newly created seed nuclei by means of the r-process.

Following the discussion of Gratton et al. (2004), the best studied s-process element in GC stars is Ba, although La, Sr, Y, and Zr are also occasionally studied, while Eu is essentially the only r-process element studied. The reason for this relatively small list of observationally targeted neutron-capture elements is because most neutron-capture elements have their transition lines below 5000Å, where high signal-to-noise spectra are difficult to obtain for GC stars. Meanwhile, the Ba and Eu transition lines that are accessible are also limited in number because they tend to be very strong and very weak, respectively. Furthermore, the abundance analysis of these lines are affected by hyperfine-structure splitting and non-LTE effects (e.g. James et al. 2004b; Mashonkina & Gehren 2001, 2000; Mashonkina et al. 1999). With these limitations in mind, the abundances of Ba and Eu can be used as observable

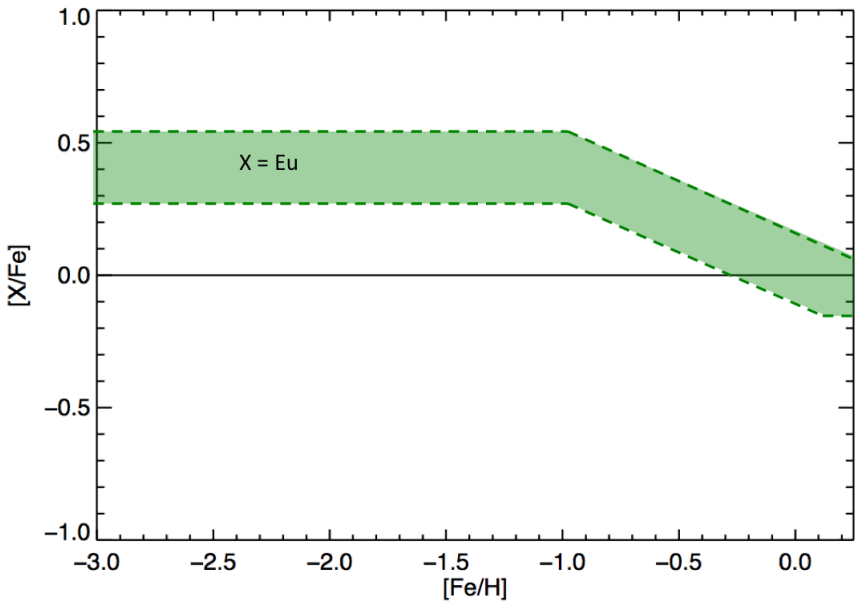

Figure 1.10. Schematic abundance ratio trend for the r-process element Eu in Galactic GCs.

proxies for the s- and r-process in GC stars.

Using the abundance data compiled by Sneden et al. (2004) and James et al. (2004b) as templates, Figure 1.10 shows a schematic plot of [Eu/Fe] versus [Fe/H] for Galactic GCs. Here, the trend for the r-process element Eu is remarkably similar to the trend seen for the α-elements in Figures 1.7 and 1.8. Like the α-elements, [Eu/Fe] starts out with a super-solar plateau with a height of [Eu/Fe] $\sim +0.4\,dex$ for low metallicities and then transitions towards a solar value once [Fe/H] $\sim -1.0\,dex$ is reached. If this plateau is interpreted as a result of Type II supernovae polluting the ISM with r-process rich material before Type Ia supernovae have a chance to pollute the ISM with Fe, then the [Eu/Fe] trend supports the belief that r-process elements are produced in Type II supernovae. This [Eu/Fe] trend for GCs is also seen in Galactic field stars, but the star-to-star scatter in their trend becomes extremely large ([Eu/Fe] ~ -0.5 to $+2.0\,dex$) as the stellar metallicities become extremely small ([Fe/H] $\lesssim -2.5\,dex$) (Gratton et al. 2004).

Again using the abundance data compiled by Sneden et al. (2004) and James et al. (2004b) as templates, Figure 1.11 shows a schematic plot of [Ba/Fe] and [La/Fe]

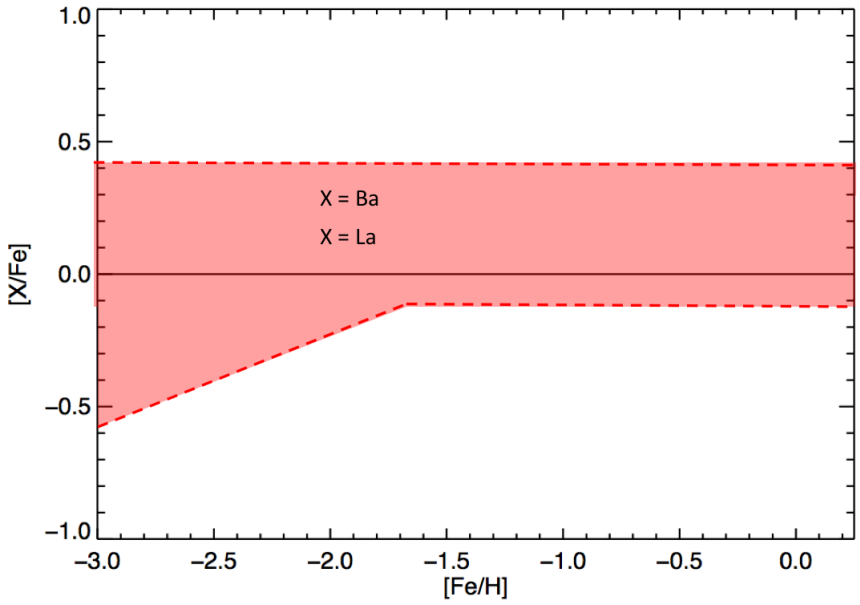

Figure 1.11. Schematic abundance ratio trends for the s-process elements Ba and La in Galactic GCs.

versus [Fe/H] for Galactic GCs. Here, the trend seen for these s-process elements has a large amount of scatter, though its running-average remains super-solar for [Fe/H] $\gtrsim -1.7\,dex$. This preference for super-solar [Ba/Fe] and [La/Fe] may imply that AGB stars are capable of polluting the ISM with enough s-process material to balance the Fe contributed to the ISM by supernovae. The apparent downward trend for [Ba/Fe] and [La/Fe] that begins at [Fe/H] $\lesssim -1.7\,dex$ may be an artifact of larger scatter in the data (James et al. 2004b), or may indicate a gradual decline, which is seen in metal-poor field stars (e.g. Gratton & Sneden 1994; Fulbright 2002).

Besides investigating the r- and s-process separately, their relative contribution to the ISM can be investigated simultaneously by plotting [Eu/Ba] versus [Fe/H]. When plotted in this format, stars with [Eu/Ba] $\sim +1.0\,dex$ are considered r-process rich, while stars with [Eu/Ba] $\sim -1.0\,dex$ are considered s-process rich (Gratton et al. 2004). Galactic field stars that are extremely metal poor ([Fe/H] $\lesssim -2.5\,dex$) scatter between these two limits (e.g. Cowan et al. 2002; Hill et al. 2002; Sneden et al. 2003; Aoki et al. 2002; Lucatello et al. 2003; Van Eck et al. 2003). Using the abundance data compiled by Gratton et al. (2004) and James et al. (2004b) as templates, Figure 1.12

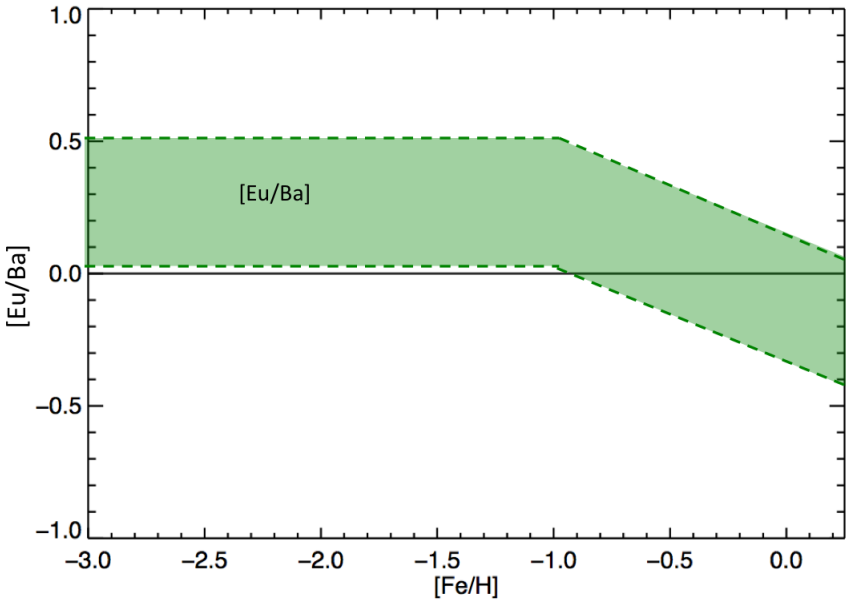

Figure 1.12. Schematic [Eu/Ba] trend with metallicity.

shows a schematic plot of [Eu/Ba] for Galactic GCs. Here, it is apparent that metal-poor GCs are mildly r-process rich when Type II supernovae dominant, while the more metal-rich GCs begin to become mildly s-process rich after the time scale for Type Ia supernovae is reached. This relation to the Type Ia time scale may be due to AGB stars reaching their peak mass-loss at a similar time scale.

Light Elements

Here, the *light elements* are defined to be C, N, O, Na, Mg, and Al. This particular group of elements is singled out because their abundances demonstrate star-to-star C-N, Na-O and Mg-Al anti-correlations in Galactic GCs. Note that C, O, and Mg are α-elements, which were discussed previously, while N, Na, and Al are three odd-Z_{atom} elements that do not belong to any of the previously discussed element groups. The main production mechanisms for N, Na, and Al are listed in Table 1.4.

Because transition lines from C and N are not available in cool stars, molecular bands from CH and CN are, respectively, used as proxies. The investigation of these band strengths led to the discovery that GC stars demonstrate a C-N anti-correlation (Osborn 1971; Norris et al. 1981). The fact that this relation is not seen in Galactic

Species	Origin	Iso. Fraction (% by number)
^{14}**N**	**L, H**	**99.63**
^{15}N	novae, ν(r)	0.37
^{23}**Na**	**C, Ne, H**	**100.0**
^{27}**Al**	**C, Ne**	**100.0**

Table 1.4. The astrophysical mechanisms responsible for producing the light odd-Z_{atom} elements. Adapted from *Table III* of Woosley et al. (2002). See Table 1.2 for further details.

field stars (Carbon et al. 1982; Langer et al. 1992) may indicate that its origin is related to the dense stellar environments found inside GCs (see, e.g., Gratton et al. 2004; Kraft 1994; Smith 1987).

Following Gratton et al. (2004), the most popular explanation for the C-N anti-correlation is that it is due to an unexplained mixing mechanism that brings up partially processed CNO-cycle material into an RGB star's upper atmosphere. As a star evolves up the RGB, its convective layer deepens and begins to "dredge-up" nuclearly processed material to its surface. This process may be able to explain some of the C-N anti-correlation features (Iben & Renzini 1984), but because the deepness of the dredge-up is a function of metallicity, it is not able to reach the CNO-cycle material in low-metallicity stars (Day et al. 1973; Cottrell & Sneden 1986; Sneden et al. 1986; Gilroy & Brown 1991). Therefore, an unexplained, second mixing mechanism is most likely at work in GC RGB stars.

The Na-O and Mg-Al anti-correlations were later discovered in GC stars using Na, O, Mg, and Al abundances derived from standard abundance analysis techniques. Like the C-N anti-correlations, these anti-correlations are not seen in Galactic field stars. Schematics of these anti-correlations are shown in Figures 1.13 and 1.14 using Kraft et al.'s (1997) abundance data for GC M13. Based on the natural tendency for α-elements to be enriched for metal-poor stars, the expected [O/Fe] value in Figure 1.13 should be $\sim 0.3 - 0.4\,dex$, while the expected [Mg/Fe] value in Figure 1.14 should be $\sim 0.3\,dex$. The decrease of [O/Fe] and [Mg/Fe] from their natural values provide clues about the depletion mechanism responsible. These depletions

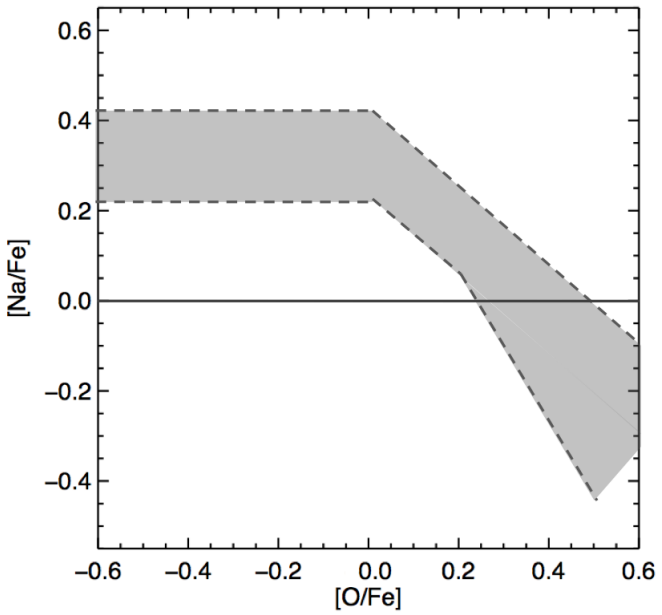

Figure 1.13. Schematic Na-O anti-correlation for GC stars.

also demonstrate why O and Mg are generally considered to be impure tracers of α-elements in GC stars.

Following Gratton et al. (2004), the origin for the Na-O and Mg-Al anti-correlations are believed to be from proton-capture reactions near or within the H-burning shells in cluster RGB and AGB stars. In these regions, O can become depleted due to the ON-cycle, while Na can become enriched by the NeNa-cycle (Langer et al. 1993; Denissenkov & Denissenkova 1990). This depletion of O and enhancement of Na would naturally explain the Na-O anti-correlation. Meanwhile, in slightly hotter regions, Mg can be converted into Al due to the MgAl-cycle, which would explain the Mg-Al anti-correlations (Langer et al. 1993).

Despite the basic agreement regarding the nucleosynthesis mechanisms responsible for the Na-O and Mg-Al anti-correlations, the mechanisms responsible for polluting the upper atmospheres of GC stars with these nucleosynthesis products is still debated. This debate is divided into two scenarios. Under the "evolutionary mixing scenario," cluster RGB and AGB stars are believed to experience an unexplained mixing mechanism that lifts up some of their altered Na, O, Mg, and Al products to

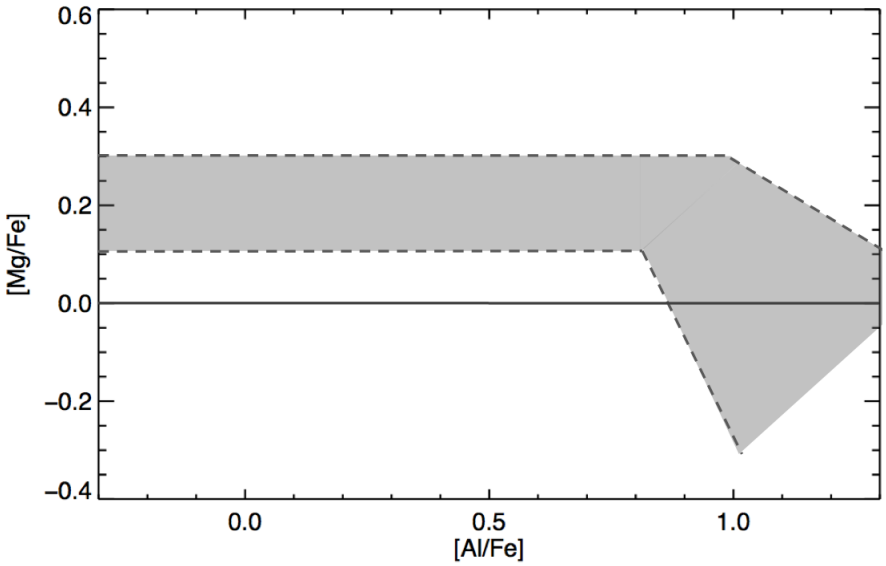

Figure 1.14. Schematic Mg-Al anti-correlation for GC stars.

their surfaces (e.g. Denissenkov & VandenBerg 2003). Under the "primordial enrichment scenario," mass-loss from AGB stars early in a GC's history pollutes the entire GC with processed material, which is then accreted onto the cluster's other stars (e.g. D'Antona et al. 1983; Cannon et al. 1998; Ventura et al. 2001; Thoul et al. 2002).

1.1.3 GC and Galaxy Formation

Because of their cosmological ages, SSP composition, and ubiquity, GCs are potentially useful tracers of galaxy formation and evolution (e.g. Brodie & Strader 2006; West et al. 2004). The major problem with using GCs in such a way, though, is that the theoretical connection between GC formation and galaxy formation is not currently understood well enough to convert GC observations into direct statements about galaxy formation. Current attempts at deriving this link between GC-galaxy formation are discussed in this section.

Star cluster formation appears to be a universal process (e.g. Elmegreen & Efremov 1997; Harris & Pudritz 1994; McLaughlin & Pudritz 1996); therefore, GCs are simply star clusters that sample the statistically rare, high-mass end of a universal

star cluster mass function. This cluster mass function takes the form

$$n(\mathcal{M})d\mathcal{M} = A\mathcal{M}^{\alpha}d\mathcal{M} \tag{1.13}$$

where $n(\mathcal{M})$ is the star cluster frequency distribution per unit mass, $\mathcal{M}$ is the star cluster mass, α is the characteristic power-law slope for the mass function, and A is a normalization coefficient that depends on the star formation rate (SFR) within the particular star forming region of interest (Elmegreen 2004). The exponent α in Equation 1.13 is approximately equal to -2, which indicates that the cluster mass distribution is a power-law with a slope roughly equal to -2 when displayed in a $\log - \log$ plot that uses linear intervals in mass (e.g. Elmegreen 2009; Lada & Lada 2003). The production of this continuous distribution requires that star formation takes place at roughly constant efficiency throughout gaseous environments that have a universal hierarchy of scale-invariant structure (Elmegreen & Efremov 1997). This structure may result from gravitational fragmentation (e.g. de Vega, Sánchez, & Combes 1996), collisional agglomeration (e.g. McLaughlin & Pudritz 1996), or turbulence (e.g. Elmegreen & Scalo 2004; Falgarone & Phillips 1991).

The reason high-mass star clusters, like GCs, are rare is because their formation requires a combination of high gas density and extremely high gas pressure. Following the scaling relations of Elmegreen (2004), the mass of a star cluster is roughly related to its formation density and pressure through the expression

$$\mathcal{M} \sim 6 \times 10^3 \left(\frac{P}{10^8\, K\, cm^{-3}}\right)^{3/2} \left(\frac{n}{10^5\, cm^{-3}}\right)^{-2} \tag{1.14}$$

where $\mathcal{M}$ is the mass of the star cluster, P is the cluster's formation gas pressure normalized to the Boltzmann constant, and n is the cluster's formation gas density normalized to the mass of molecular hydrogen (Elmegreen & Elmegreen 2001). The characteristic central mass density of present-day Galactic GCs ($\rho \sim 10^4\, \mathcal{M}_{\odot}\, pc^{-3}$) corresponds to $n \sim 10^5\, cm^{-3}$, which can be used as an estimate for a GC's formation density (Elmegreen 2004). Combining this formation density with the present-day

mass of a GC ($\sim 1 \times 10^6 \, \mathcal{M}_\odot$) yields an estimate for a GC's formation pressure, which equals $\sim 1 \times 10^9 \, K \, cm^{-3}$. Because the equilibrium pressure in the Galactic disk is only $\sim 1 \times 10^4 \, K \, cm^{-3}$ (e.g. Kasparova & Zasov 2008), the formation of GCs requires very high, large scale compression in order to achieve the high formation pressures needed (Elmegreen 2004).

The high pressures needed to form a GC also have implications for the SFR that takes place during a GC's formation process. The observed SFR per unit area of a galaxy scales likes

$$\Sigma_{SFR} = A \Sigma_{gas}^{1.4} \tag{1.15}$$

where Σ_{SFR} is a galaxy's SFR per unit area, Σ_{gas} is the column density of gas observed in the galaxy, and A is a normalization coefficient specific to the galaxy (Kennicutt 1998; Schmidt 1959). The fact that gas pressure is proportional to the square of its density implies that $P \propto \Sigma_{gas}^2$. Substituting this relation into Equation 1.15 yields $\Sigma_{SFR} \propto P^{1.4/2}$. Therefore, the extremely high gas pressures needed to form a GC will also produce intense bursts of star formation.

Direct confirmation that GCs can form under extreme environmental conditions, and that they are indeed the high-mass end of a universal mass function, has been observed in many galaxies in the local universe that are undergoing intense star formation. As reviewed by Whitmore (2000; 2003), young clusters (age $\sim$ 1 to 500 $Myrs$) with masses similar to Galactic GCs ($\mathcal{M} \sim 10^4$ to $10^7 \, M_\odot$) have been found in galaxy mergers (e.g. Holtzman et al. 1992, 1996; Whitmore et al. 1993; Whitmore & Schweizer 1995; Whitmore et al. 1999; Zepf et al. 1999), starburst galaxies (e.g. Meurer et al. 1992, 1995; Conti & Vacca 1994; O'Connell et al. 1994; Watson et al. 1996), spiral bars (e.g. Barth et al. 1995), irregular galaxies (e.g. LMC), and regular spiral galaxies (e.g. Larsen & Richtler 1999). Table 1.5 lists some of the properties of these *young massive clusters* (YMCs). Note that the *luminosity* functions for these YMCs have a mean power-law slope equal to -1.9, which supports the notion that massive star clusters form from a universal cluster mass function. When aged to $\sim 12 \, Gyrs$, these YMCs will have properties similar to GCs, and based on the den-

Galaxy	Region	N	$M_{V,max}$ (mag)	R_{eff} (pc)	$\mathcal{M}$ $(\mathcal{M}_\odot)$	Age (Myr)	α	Ref.
NGC 1741	I	314	-15	$\cdots$	$10^4 - 10^6$	4	-1.85	10
NGC 4038/39	I	800	-15.8	4	$10^3 - 10^7$	$1 - 500$	-2.1	3, 12, 14, 15
NGC 3256	I	1000	-15	$5 - 10$	$\cdots$	$\cdots$	-1.8	11
NGC 3597	I	700	-13.2	$\cdots$	$\cdots$	$\cdots$	-2.0	5, 13
NGC 7252	I	500	-16.2	5	$10^4 - 10^8$	600	-1.8	2, 7
NGC 1275	I	800	-15.8	$\cdots$	$10^4 - 10^8$	$0.1 - 10^3$	-1.9	1, 4, 8, 9
NGC 3921	I	102	-14	< 5	$\cdots$	500	-2.1	6
LMC	S	8	-11.3	2.6	$\cdots$	3	$\cdots$	17
M82	S	100	-14.5	3.5	$\cdots$	100	$\cdots$	21, 26, 28
HE 2-10	S	76	-12.7	3	$10^3 - 10^5$	$\cdots$	-1.7	19, 27
ESO 338-IG04	S	112	-15.5	$\cdots$	$10^3 - 10^7$	$10 - 10^4$	$\cdots$	25
NGC 1569	S	7	-13.9	2.2	$\cdots$	15	$\cdots$	16, 20, 22
NGC 5253	S	6	-11.1	$\cdots$	10^6	2.5	$\cdots$	24
NGC 1705	S	36	-13.7	3.4	$\cdots$	15	$\cdots$	18, 20, 23
ESO 565-11	B	700	-13.4	$\cdots$	$\cdots$	$4 - 6$	-2.2	30
NGC 1097	B	88	-13.8	2.5	$\cdots$	$\cdots$	$\cdots$	29

Table 1.5. Properties of young massive star clusters. Adapted from *Table I* of Whitmore (2000). N is the number of young clusters, complete to around $M_{V,max} \sim -9\,mag$. Note that the YMCs represent only a small subset of N. "Region" is the type of star forming region in which the clusters are observed, where I, S, and B stand for interacting, starburst, and barred galaxies, respectively. $M_{V,max}$ is the absolute V-band magnitude of the brightest cluster. R_{eff} is the mean effective radius of the clusters. $\mathcal{M}$ is the estimated mass of the clusters. "Age" is the estimated age of the clusters. α is the power-law slope of the clusters' luminosity function. The references for the data are: [1] Holtzman et al. (1992); [2] Whitmore et al. (1993); [3] Whitmore & Schweizer (1995); [4] Zepf et al. (1995); [5] Holtzman et al. (1996); [6] Schweizer et al. (1996); [7] Miller et al. (1997); [8] Brodie et al. (1998); [9] Carlson et al. (1998); [10] Johnson et al. (1999); [11] Zepf et al. (1999); [12] Whitmore et al. (1999); [13] Forbes & Hau (2000); [14] Gilbert et al. (2000); [15] Mengel et al. (2000); [16] Arp & Sandage (1985); [17] Kennicutt & Chu (1988); [18] Meurer et al. (1992); [19] Conti & Vacca (1994); [20] O'Connell et al. (1994); [21] O'Connell et al. (1995); [22] de Marchi et al. (1997); [23] Ho & Filippenko (1996); [24] Calzetti et al. (1997); [25] Oestlin et al. (1998); [26] de Grijs et al. (2000); [27] Johnson & Conti (2000); [28] Smith & Gallagher (2000); [29] Barth et al. (1995); [30] Buta et al. (1999)

sities of the most massive YMCs ($\rho \sim 10^5\,\mathcal{M}_\odot\,pc^{-3}$), they should be able to survive for tens of $Gyrs$ (Whitmore 2003).

While some proto-GCs are seen currently forming in the local universe, the specific formation details of the more numerous, "classical" GCs (i.e. old and metal-poor GCs) remain largely unknown. One major observational clue for the formation histories of these classical GCs comes in the form of their *metallicity distributions*. A metallicity distribution is simply a histogram of a galaxy's entire GC system (GCS) binned by [Fe/H] (e.g. Zinn 1985; Armandroff & Zinn 1988). An example metallicity distribution for the Galaxy's own GCS is shown in Figure 1.15 using the compiled

data of Harris (1996). Because the measurement of metallicities in extragalactic GCs has only become feasible relatively recently, most metallicity distributions are actually observed as *color distributions*. As noted by Harris (2001), plotting GC colors as proxies for [Fe/H] produces similar distributions because GC colors and metallicities are linearly related over the metallicity range [Fe/H] $\lesssim -0.5\,dex$ (Couture et al. 1990; Geisler & Forte 1990), where metal-rich GCs are redder than metal-poor GCs. Metallicity (or color) distributions are important because their histogram structure provides information about any potential GC subpopulations within a single GCS and the formation times and conditions for these potential subpopulations (Ashman & Zepf 1992; Zepf & Ashman 1993). The defining feature that has emerged from studying the histogram structures of metallicity distributions is that most galaxies have a *bimodal distribution* of GCs, composed of a metal-rich population and a metal-poor population (e.g. Gebhardt & Kissler-Patig 1999; Forbes & Forte 2001; Kundu & Whitmore 2001; Larsen et al. 2001). These metallicity subpopulations also tend to have different kinematic and spatial distributions (e.g. Ashman & Bird 1993; Zepf et al. 2000; Côté et al. 2001; Schroder et al. 2002; Côté et al. 2003; Perrett et al. 2003). For example, the bimodality of the Galaxy's GCS is clearly seen in Figure 1.15, which shows the Galaxy's metal-poor, halo population (Zinn 1985) that peaks at [Fe/H] $\sim -1.6\,dex$ and its more metal-rich, bulge population (Minniti 1995) that peaks at [Fe/H] $\sim -0.6\,dex$. Explaining this characteristic bimodality in terms of galaxy formation theory has been a key goal of GC research for more than a decade.

The successful linkage of GC and galaxy formation theories will allow GCs to be used as easily observable "fossil" tracers of galaxy formation. Because of this importance, numerous attempts at deriving this linkage have been undertaken over the years (see, e.g., Harris 2001; Ashman & Zepf 1998 and references therein). More recently, several models have been put forth that try to derive the GC-galaxy connection by explaining the characteristic bimodal metallicity distribution seen in GCSs. Following the discussions of Brodie & Strader (2006) and Harris (2001), these models can be separated into "major merger models," "in situ models," and "accretion models."

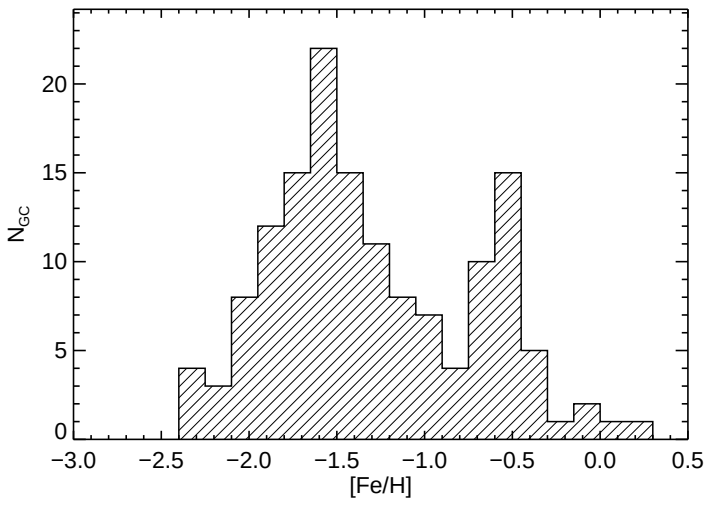

Figure 1.15. The bimodal metallicity distribution of the Galactic GC system. All metallicities are from the compilation of Harris (1996).

Major merger models postulate that a GCS' metal-poor subpopulation formed during its host galaxy's initial formation process, while its metal-rich subpopulation formed during a later gas-rich merger between the host galaxy and another large galaxy. The most influential major merger model is the model of Ashman & Zepf (1992) and Zepf & Ashman (1993), largely because their model is quantitative and has made some successful predictions. As outlined in Brodie & Strader (2006), this specific model grew out of the major merger models for elliptical galaxy formation Toomre & Toomre (1972) and the suggestions that this formation mechanism should also produce many GCs (Schweizer 1987; Burstein 1987). Successes for their model include the fact that it predicted that GCSs should have bimodal metallicity distributions, before it was known, and that proto-GCs should be seen forming in galaxy mergers, before YMCs were fully understood to be proto-GCs. After its initial successes, the major merger model lost favor as a *universal* mode for GCS formation because it fails to account for the high number of GCs seen per unit luminosity in rich elliptical galaxies (see, e.g., Harris 2001) and it also predicts larger ratios of metal-rich to metal-poor GCs in elliptical galaxies than are actually seen (Forbes, Brodie, & Grillmair 1997).

In situ models postulate that galaxies predominantly form out of local overdensities of gas that dissipatively collapse (e.g. Eggen, Lynden-Bell, & Sandage 1962), and that the GCSs of these galaxies form during this process. To account for the bimodal metallicity distributions seen in GCSs, in situ models must further postulate that the dissipative collapse occurs in at least two stages. This specific type of in situ model is called a multiphase dissipative collapse model, and the most influential version is that of Forbes, Brodie, & Grillmair (1997). Forbes et al. speculate that there are three phases of dissipative collapse, which they call the "pre-galaxy," "galaxy," and "disk" phases. During the pre-galaxy phase, a small fraction of a proto-galaxy's collapsing gas cloud experiences intense star formation, predominately in the form of colliding clumps of gas, which form GCs. An unknown mechanism then truncates the star formation for a period of time, which allows the first generation of metal-poor stars to enrich the gas. Forbes et al. speculate that this truncation may be a result of supernovae feedback that reheats the gas and prevents it from collapsing for another few Gyrs (e.g. Burkert & Ruiz-Lapuente 1997). More recently, Santos (2003) invoked cosmic reionization to explain the truncation. After the truncation period is over, a second generation of more metal-rich stars are formed, which predominantly contribute to the galaxy's field star population, but also creates metal-rich GCs. If this second phase of star formation is inefficient, then the galaxy experiences a third phase of dissipative collapse as it incorporates its leftover gas into a spiral disk. The main difficulties with this model are that it is not quantitative and that it requires fine tuning in the form of truncation.

Accretion models postulate that galaxies gain some of their GCs by accreting them from other galaxies (e.g. Searle & Zinn 1978). The most influential accretion model is that of Côté, Marzke, & West (1998). Their model postulates that metal-rich GCs correspond to GCs that form during a galaxy's in situ formation process, while a galaxy's metal-poor GCs are latter gained from tidally disrupted and accreted low-mass galaxies. This model relies on the observationally determined correlation between GC metallicity and host galaxy mass, where lower-mass galaxies tend to have lower-metallicity GCSs (Brodie & Huchra 1991). The model also assumes that the

accreted low-mass galaxies are relatively gas-poor in order to prevent their accretions from forming metal-rich halo stars. The model of Côté et al. has been built into a Monte Carlo simulation framework, which allows it to make quantitative predictions. This quantitative framework gives the model the ability to calculate a galaxy's metal-poor GC subpopulation by sampling them from donor galaxies that are defined by a variable slope, Schechter luminosity function (Schechter 1976). This model also has the advantage that accretions of GCs from dwarf galaxies are observed in the Milky Way. The best example of this is the Sagittarius dwarf galaxy (Ibata, Gilmore, & Irwin 1994) and the handful of accreted GCs associated with it. These GCs include M54, Terzan 7, Terzan 8, Arp 2 (Da Costa & Armandroff 1995), Pal 12 (Cohen 2004), and Whiting 1 (Carraro, Zinn, & Moni Bidin 2007). The main difficulties with the model are that it requires many more low-mass donor galaxies then are actually observed (e.g. Klypin et al. 1999; Moore et al. 1999, although also see Simon & Geha 2007), that the colors (i.e. metallicties) seen from the halo stars of some galaxies do not correspond to stars accreted from dwarf galaxies (Harris 2001), and that some proto-GCs are seen forming in the local universe do to galaxy mergers.

As many authors have now pointed out (see e.g. Harris 2001; Brodie & Strader 2006), the three GC-galaxy formation models mentioned above are too simple. Based on expectations gained from hierarchical galaxy assembly theory (e.g. White & Rees 1978; White & Frenk 1991; Navarro et al. 1997), all three simple GC-galaxy models should occur, to some degree, during galaxy formation. Therefore, selecting any one of the models as the *only* mechanism linking GCs and galaxies is an arbitrary constraint. Instead, it is better to think of the three models as limiting cases of hierarchical galaxy assembly.

Seizing on this realization, Beasley et al. (2002) were one of the first groups to model and follow GC formation inside of a modern hierarchical galaxy assembly simulation. To accomplish this modelling, Beasley et al. used the semi-analytic galaxy assembly code GALFORM (Cole et al. 2000). As initial conditions, GALFORM requires the user to specify a set of ΛCDM cosmological parameters and a power spectrum for the desired density fluctuations. GALFORM then computes the merger

history of dark matter (DM) halos for the supplied initial conditions using a Monte Carlo routine. GALFORM then computes and follows the history of galaxy formation throughout the DM halo merger tree using semi-analytic recipes for the gas and stellar physics. Generic galaxy formation histories obtained from GALFORM begin with small, roughly dwarf galaxy size, overdensities of gas that collapse into disks, which then generate large bursts of star formation. Later, these proto-galaxy fragments begin to merge into larger, spheroidal distributions, which re-trigger bursts of star formation during the mergers. Elliptical galaxies result from the large spheroids, while spiral galaxies result from the accretion of gas-rich proto-galaxy fragments onto the smaller spheroids, which correspond to the spiral bulges. Because GALFORM does not model GC formation, Beasley et al. applied various assumptions to the star formation within GALFORM. In particular, they assumed that metal-poor GCs form within the disks of the proto-galaxy fragments as they undergo star formation, and they assumed that the metal-rich GCs form within the later mergers. To produce the GCs, they adopted GC formation efficiencies, which simply express how much mass goes into GCs and how much mass goes into field stars during a star formation event. To select the efficiencies, they calibrated them until they replicated the number of metal-poor and metal-rich GCs seen in the GCS of NGC 4472. The results from the simulation are that bimodal metallicity distributions for GCSs could only be produced if the metal-poor GC formation is truncated at $z \gtrsim 5$. As with the truncation invoked in the in situ model of Forbes et al. (1997), the mechanism for Beasley et al.'s truncation is unknown, though the suppression of star formation due to re-ionization continues to be a favorite hypothesis (e.g. Susa & Umemura 2004). Despite this difficulty, Beasley et al.'s hierarchical model proves to be largely successful at replicating the colors and metallicities of real GCSs.

Because pure semi-analytic models are limited to estimating only the bulk properties of galaxies, real hydrodynamical N-body simulations are required to follow the actual physics, kinematics, and distributions of baryons inside of galaxies. The advantage of using this approach for studying GC formation is that, unlike the model of Beasley et al. (2002), no assumptions have to be made about where GCs should

form; instead, GCs ideally will naturally form wherever and whenever the temperature, density, and pressure conditions favor their formation. The difficulty with this approach, though, is that these simulations need to have dynamic ranges that are capable of resolving the very small spatial, mass, and time scales of star formation throughout the much vaster spatial, mass, and time scales of galaxy formation (e.g. Bekki et al. 2008). Despite these computational challenges, GC formation is now beginning to be simulated using these methods (e.g. Kravtsov & Gnedin 2005; Bekki et al. 2008). For example, the hydrodynamical N-body simulations of Kravtsov & Gnedin (2005) are capable of resolving the formation of GCs up to the creation of high redshift, supergiant molecular clouds, which correspond to the sites where GC should form (e.g. Harris & Pudritz 1994; McLaughlin & Pudritz 1996; Nakasato et al. 2000). These molecular clouds are seen forming within the spiral arms of high redshift proto-galaxies, and the GCs that form within these molecular clouds should correspond to metal-poor GCs. When these gaseous disks begin to merge, metal-rich GCs should form. The simulations of Bekki et al. (2008), however, sacrificed the modelling of real baryon particles in favor of gaining better resolution. The cost of this sacrifice was that Bekki et al.'s simulations had to numerically insert gas within the DM halos and then use semi-analytic models to calculate the properties of the gas. Unlike the model of Beasley et al. (2002), though, the DM components of Bekki et al.'s simulations were directly simulated using real N-body methods, whereas Beasley et al. used semi-analytic methods for both the DM mergers and the gas physics. The results of Bekki et al.'s simulations and assumptions find that both metal-rich and metal-poor GCs form in the early universe, and that their bimodal distributions could be due to a variable GC formation efficiency, where metal-poor GCs form more efficiently in slightly earlier, gas-rich proto-galaxies and the metal-rich GCs form more efficiently in slightly later mergers.

As computational power continues to improve, higher resolution hydrodynamical N-body simulations will continue to play a major role in connecting the formation of GCs and galaxies into a unified theory. Note that these attempts at unification can be viewed as a mutually beneficial process, whereby galaxy formation simulations help

develop GC formation theory, while GC data can help constrain galaxy formation theory. Once unified, GCs can be used as local tracers of primordial cosmological events.

1.2 Spectroscopic Abundance Analysis

As demonstrated in § 1.1.3, the acquisition of accurate metallicity distributions for extragalactic GCSs has proven to be very useful for investigating GC-galaxy formation theories. But, as demonstrated in § 1.1.2, the acquisition of detailed abundance ratios from GC stars also yields another extremely rich dataset for determining the formation and evolution histories of GCs. Therefore, both metallicity distributions *and* detailed abundance ratios should ideally be used when investigating GC-galaxy formation theories. The primary reason why extragalactic GC abundance ratios are not used is because standard abundance analysis methods are designed to analyze the spectra of individual stars, and GC stars located outside the Local Group are too far away to obtain their individual stellar spectra. Fortunately, as demonstrated in § 1.1.1, GCs have the unique property that they can be modeled as SSPs (i.e. single age, single chemical composition) stellar systems. This simplification permits the opportunity to study a GC's *integrated light spectrum* (ILS) as if it is a single bright "star," composed of the integrated spectra coming from the cluster's IMF distribution of spatially unresolved, real stars. The current abundance analysis method that relies on this simplification is called the *Lick index system*, and this dissertation introduces a new, independent ILS analysis method that offers various improvements over the Lick index system.

The outline for this section is as follows. In § 1.2.1, the standard method of abundance analysis for single stars is outlined. In § 1.2.2, the Lick index system is reviewed. And, in § 1.2.2, this dissertation's new abundance analysis method for GCs is introduced.

1.2.1 Standard Stellar Abundance Analysis

The premise behind standard stellar abundance analysis is that absorption lines observed in stellar spectra can be modeled by applying radiative transfer through model stellar atmospheres, and that the elemental abundances responsible for these absorption lines can be determined by iteratively assuming different abundances until the model absorption lines match the observed absorption lines. In practice, there are two general approaches for this iterative comparison. The first approach chooses to simultaneously model all the transition lines observed within a spectral region, and then compares this synthesized spectrum with the observed spectrum. This approach is called *spectrum synthesis*. The second approach calculates the line strengths of individually synthesized absorption lines, and then compares each synthesized line strength to its observed line strength. This approach is called *equivalent width analysis*, which quantifies line strengths in terms of *equivalent widths* (EWs). An absorption line's EW is defined as

$$EW \equiv \frac{1}{F_c} \int_{-\infty}^{+\infty} (F_c - F(\lambda)) d\lambda \tag{1.16}$$

where F_c is the continuum flux around the absorption line and $F(\lambda)$ is the flux profile of the absorption line as a function of wavelength. Note that F_c is assumed to be constant with wavelength because EW analysis is usually applied to spectra that have been continuum normalized to unity. Also, the limits of the integration assume that the absorption line is completely isolated, but for real absorption lines, the limits of the integration only extend to small offsets in wavelength away from the line's center. Note that an EW is actually equal to the area of its absorption line, A_{line}, divided by its continuum flux level

$$EW = \frac{1}{F_c} A_{line}. \tag{1.17}$$

therefore, its units are quoted in lengths measured in wavelengths.

Generally, full spectrum synthesis is reserved for analyzing small spectral regions that are observed at very high spectral resolutions ($R \sim 100,000$) and signal-to-

noise ratios, because under these conditions observed absorption lines have useful information embedded in both their line strengths and line profiles. Meanwhile, EW analysis is generally used for analyzing large spectral regions that are observed at intermediate spectral resolutions ($R \sim 30,000$) and signal-to-noise ratios, because under these conditions most of the detailed information in absorption line profiles are inaccessible.

In order to model a specific absorption line, the line opacity function responsible for the absorption line must be known. Because of its clarity, the following discussion on computing line opacities closely follows the discussion found in Leckrone (2001). Mathematically, the line opacity function for an arbitrary transition line can be written as

$$l_\lambda(x, \Delta\lambda) = C \left(\frac{n_{el,r,s}(x)}{N_{el}} \right) \left(\frac{N_{el}}{N_H} \right) N_H f \phi_\lambda(x, \Delta\lambda)(1 - e^{-hc/\lambda kT}) \tag{1.18}$$

where $l_\lambda(x, \Delta\lambda)$ is the line opacity in units of $cm^2\ g^{-1}$ and its independent variables x and $\Delta\lambda$ refer to the fact that the opacity is a function of atmospheric depth, x, and wavelength relative to the line's center, $\Delta\lambda$. The factor N_{el}/N_H in Equation 1.18 is the ratio of the total number of atoms and ions of the element responsible for the absorption line, to the total number of atoms and ions of hydrogen. Note that this ratio corresponds to the abundance of the element as defined by Equation 1.6. Therefore, the fundamental basis of both spectrum synthesis and EW abundance analysis involves iterating on this factor until the radiative transfer through a model atmosphere produces an absorption line that matches the element's observed absorption line. Meanwhile, the factor $n_{el,r,s}(x)/N_{el}$ is the ratio of the number of atoms or ions of the element in excitation state s and ionization state r that are responsible for the line absorption, to the total number of atoms and ions of the element. This factor reduces the element's total abundance to just its abundance responsible for the line transition. When working under the assumption of local thermodynamic equilibrium (LTE), the element's excitation state population is calculated using the Boltzmann equation and its ionization state population is calculated using the Saha equation.

The factor f is the transition probability for the line transition, which is measured from laboratory observations. Typically, these transition probabilities are quoted logarithmically as $log(gf)$ values, where the extra factor of g is the transition's lower level statistical weight used in the Boltzmann equation (see, e.g., Rutten 2003). The factor $(1 - e^{-hc/\lambda kT})$ is a correction factor that accounts for radiatively stimulated emission. The factor $\phi_\lambda(x, \Delta\lambda)$ incorporates all the microscopic mechanisms that control the line profile of the absorption line. These mechanisms include natural broadening, Doppler broadening, pressure broadening, and hyperfine structure splitting. The factor C is just a collection of constants. The factor N_H is the number of atoms and ions of hydrogen per gram of atmospheric material, which is determined from the adopted abundance distribution.

In order to determine the continuum flux level at which an absorption line forms, knowledge of a star's continuous opacity is also needed. Unlike line opacities, which are due to *bound-bound* electronic transitions, continuous opacities are due to *bound-free* and *free-free* processes (see, e.g., Gray 2008). These *bound-free* and *free-free* processes are, respectively, due to ionizations and collisional charge accelerations. Because the vast majority of a star's atmosphere is composed of hydrogen, most of a star's continuous opacity is produced directly or indirectly from hydrogen (e.g. H, H^-, H_2, and free electrons). Metals (e.g. C, Si, Al, Mg, Fe) can also contribute important bound-free opacities in the ultraviolet region of stellar spectra (Gray 2008). Altogether, the total continuous opacity in a star's spectrum is the summation of each individual opacity source. This can be schematically written as

$$\kappa_\lambda \propto \kappa(H_{bf}) + \kappa(H_{ff}) + \kappa(H^-_{bf}) + \kappa(H^-_{ff}) + \kappa(metals) + \kappa(e^-) + ... \qquad (1.19)$$

where κ_λ is the total continuum opacity, the other κ terms are specific continuum opacities denoted by the descriptions inside their parentheses, and the subscripts bf and ff denote bound-free and free-free processes (Gray 2008).

Once the functional forms of both the line and continuum opacities are known, they can be used to apply radiative transfer through model atmospheres in order to

determine theoretical stellar spectra. Because the thickness of a star's photosphere is much smaller than the radius of a star, most stellar atmospheres are approximated as one-dimensional, *plane parallel* slabs that have spherical symmetry. As discussed in Rutten (2003), several further assumptions are applied to these plane parallel atmospheres, which include: homogeneous composition with depth; hydrostatic equilibrium; time independence; small mass compared to the rest of the star; no energy sources or sinks; energy transport is only from radiation and convection; and, all particles have Maxwellian velocity distributions that are defined by the kinetic temperature at each atmospheric depth.

With these assumptions, the physical properties of a plane parallel atmosphere are fully determined by their star's luminosity, radius, abundance distribution, and microturbulence velocity (ξ_v) (Rutten 2003). In practice, stellar luminosity and radius are replaced by the star's effective temperature (T_{eff} from Equation 1.1) and *surface gravity* ($g_\star$) (Rutten 2003). Surface gravity is simply the gravitational acceleration of a star at its surface, which is equal to

$$g_\star = \frac{G\mathcal{M}_\star}{R_\star^2} \tag{1.20}$$

where $M_\star$ is the total mass of the star, $R_\star$ is the radius of the star (which is where the model atmosphere is located), and G is the gravitational constant. Surface gravities are usually quoted logarithmically as $log(g_\star)$ in *cgs* units. Also, the abundance distribution for an atmosphere is usually just a scaled solar abundance distribution, which is quoted using the distribution's total heavy element abundance value, $[M/H]$ (see § 1.1.2).

Altogether, the four atmosphere defining parameters of T_{eff}, $log(g_\star)$, $[M/H]$, and ξ_v determine the physical parameters needed at each depth x in an atmosphere. The depth dependent parameters required for radiative transfer are kinetic temperature ($T_{kin}(x)$), gas pressure ($P_{gas}(x)$), electron density ($n_e(x)$), and total mass density ($\rho(x)$). Because radiative transfer through these parameters takes place using finite integration steps in x, plane parallel atmospheres are usually provided as a "stack" of

many atmospheric layers, where each layer represents one specific depth x_i. Each of these layers has fully determined physical parameters $T_{kin}(x_i)$, $P_{gas}(x_i)$, $n_e(x_i)$, and $\rho(x_i)$. For example, the model atmospheres of Kurucz[6], consist of 72 layers, where each layer has a properly calculated set of parameters.

With the line opacities, continuum opacities, and model atmospheres determined, model stellar spectra can finally be produced through radiative transfer. The equations of radiative transfer compute the flux of light emitted at the surface of a model atmosphere after it has traveled through each model atmosphere layer. The first equation required simply computes the magnitude of the line and continuum opacities as a function of depth. This equation is

$$\tau_\lambda = \int_0^x (l_\lambda + \kappa_\lambda)\rho(x)dx \tag{1.21}$$

where τ_λ is called the *optical depth*, l_λ is the line opacity from Equation 1.18, κ_λ is the continuum opacity schematically defined in Equation 1.19, $\rho(x)$ is the atmosphere's mass density, and the integration is from atmospheric depth x to the atmosphere's surface at $x = 0$ (Leckrone 2001).

The next equation used in radiative transfer computes the intensity of light that emerges from the surface of a model atmosphere. This equation takes the form

$$I_\lambda(x = 0, \theta) = \int_0^\infty B_\lambda(T(\tau_\lambda))\, e^{-\tau_\lambda sec(\theta)} sec(\theta) d\tau_\lambda \tag{1.22}$$

where $I_\lambda(x = 0, \theta)$ is the emergent intensity (Leckrone 2001). Note that the intensity is a function of the observation angle θ, which is defined normal to the atmosphere's surface. The factor $B_\lambda(T(\tau_\lambda))$ in Equation 1.22 is the Planck function, which is valid under the assumption of LTE. Because the Planck function is a function of temperature, it is a function of the atmosphere's depth dependent temperature, where x has been redefined in terms of τ_λ using Equation 1.21. The factor $e^{-\tau_\lambda sec(\theta)}$ is a τ_λ and θ dependent attenuation factor for the intensity. The factor $sec(\theta)$ corrects the

[6]Available at http://kurucz.harvard.edu/grids.html

optical depth $d\tau_\lambda$ for the observation angle.

The last equation used in radiative transfer computes the flux of light that emerges from the surface of a model atmosphere by integrating Equation 1.22 over the observation angle. This equation takes the form

$$f_\lambda = C \int_0^\pi I_\lambda(x = 0, \theta) \cos(\theta) sin(\theta) d\theta \tag{1.23}$$

where f_λ is the emergent flux and C is a normalization constant that depends of the star's radius and distance (Leckrone 2001). Note that the physical value of C is not needed for spectrum synthesis and EW analysis because the flux continuum levels for observed and synthetic spectra can be normalized to unity.

Altogether, Equations 1.21, 1.22, and 1.23 form a nested set of equations that must be solved sequentially in order to determine the flux that emerges from a model atmosphere. Furthermore, because each solution depends on a chosen wavelength through Equation 1.21, the equations must be evaluated for many wavelengths in order to construct an entire flux spectrum. The absorption features in this synthetic flux spectrum can then be used in comparisons against absorption features in observed flux spectra.

One major subtlety that goes into comparing synthetic spectra with observed spectra involves the fact that the model atmosphere used must appropriately match the atmosphere of the observed star before any physically meaningful comparisons can be made. Because a model atmosphere is determined by its parameters T_{eff}, $log(g_\star)$, $[M/H]$, and ξ_v, these parameters must be chosen to match their respective counterparts within the atmosphere of the observed star. There are several variations on how to determine these parameters, but all of them essentially rely on iteratively converging on the correct set of parameters by minimizing various properties of a star's synthesized, Fe-line abundances (see, e.g., Bensby, Feltzing, & Lundström 2003).

The first step of atmosphere convergence is to guess the atmosphere's T_{eff}, $log(g_\star)$, $[M/H]$, and ξ_v values. Various clues can be used to pick order-of-magnitude estimates for these initial values. For example, the color of the observed star can be used to

estimate an initial T_{eff} value using a color-temperature relation (e.g. Alonso, Arribas, & Martínez-Roger 1999). The initial $log(g_\star)$ and ξ_v values can be estimated using the observed star's spectral type. The initial $[M/H]$ value can be estimated using the relative line strengths in the observed spectrum or the star's stellar population, if known.

After the initial parameter values are estimated, a model atmosphere corresponding to those values is interpolated from a grid of model atmospheres (e.g. Kurucz). Next, all the Fe-line EWs measured from the observed star's spectrum are synthesized using the model atmosphere. Each synthesis of an Fe-line EW involves iteratively guessing an Fe abundance for the line, $log\ \epsilon(Fe)$ (see Equation 1.18), until the line's synthesized EW equals the line's observed EW. The end result is a $log\ \epsilon(Fe)$ value for each observed Fe-line.

Next, the set of $log\ \epsilon(Fe)$ values implied from the guessed model atmosphere are used to improve the atmosphere's parameter values. For example, T_{eff} can be improved by plotting the neutral Fe-line abundances, $log\ \epsilon(Fe)_I$, versus their corresponding *excitation potentials* (EPs). If a positive $log\ \epsilon(Fe)_I - EP$ slope is present, then T_{eff} should be increased, and vice-versa for a negative slope. The atmosphere's ξ_v value can be improved by plotting $log\ \epsilon(Fe)_I$ versus their corresponding *reduced EWs* ($log(EW/\lambda)$). If a positive $\xi_v - log(EW/\lambda)$ slope is present, then ξ_v should be increased, and vice-versa for a negative slope. The $log(g_\star)$ value can be improved by requiring that the star's mean $log\ \epsilon(Fe)_I$ abundance equals the star's mean $log\ \epsilon(Fe)_{II}$ abundance, where $log\ \epsilon(Fe)_{II}$ is the Fe abundance determined from the singularly-ionized Fe-lines. Finally, $[M/H]$ can be improved by always setting it equal to the $[M/H]$ value implied by the $[Fe/H]$ value derived from the model atmosphere's mean $log\ \epsilon(Fe)_I$ abundance (see Equation 1.11).

After several iterations of this process, the model atmosphere parameters will converge on values appropriate for the observed star. Once this model atmosphere is obtained, either spectrum synthesis or EW analysis for the observed spectrum can proceed. For EW analysis, the abundance implied by each absorption line's EW can be determined by iteratively guessing the line's abundance until its synthesized EW

matches its observed EW. The final abundance for each element is then the mean of all of that element's individual line abundances. For spectrum synthesis, each element's abundance is iterated until the entire synthesized spectrum matches the observed spectrum.

1.2.2 GC Integrated-Light Spectra Abundance Analysis

Because standard stellar abundance analysis requires spatially resolved stars, its use is limited to the local neighborhood in and around the Milky Way. Ideally, this abundance analysis method could be generalized for spatially unresolved stellar populations, such as extragalactic GCs. The concepts necessary for this generalization are discussed in this section.

An absorption line observed within a stellar population's IL spectrum is equal to the flux-weighted average of all the individual absorption lines emitted by that stellar population's individual stars. This can be more intuitively understood when thinking in terms of EWs. The total area taken up by an absorption line in an IL spectrum is equal to the sum of all the areas taken up by the individual absorption lines that form the line. This total area, A_{tot}, can be written as

$$A_{tot} = \sum_{i=1}^{N} A_i \tag{1.24}$$

where A_i is the absorption line area emitted by the stellar population's i^{th} star and the summation sums over all N absorption line areas from the stellar population's N stars. From Equation 1.17, the areas in Equation 1.24 can be rewritten in terms of EWs like

$$EW_{tot} F_{c,tot} = \sum_{i=1}^{N} EW_i F_{c,\,i} \tag{1.25}$$

where EW_{tot} is the EW of the IL spectrum's absorption line, $F_{c,tot}$ is the continuum flux level of the IL spectrum around the absorption line, EW_i is the EW of the stellar population's i^{th} star, and $F_{c,\,i}$ is the continuum flux level around that i^{th} star's

absorption line. Dividing by $F_{c,tot}$ and replacing it with its summation notation yields

$$EW_{tot} = \frac{\sum_{i=1}^{N} EW_i F_{c,\,i}}{\sum_{i=1}^{N} F_{c,\,i}}. \tag{1.26}$$

Therefore, an EW measured from a stellar population's IL spectrum is mathematically equivalent to the flux-weighted average EW from the ensemble of stars in the stellar population.

Equation 1.26 proves to be extremely useful for conducting abundance analysis on GC IL spectra. Essentially, if the correct mixture of model stellar atmospheres are chosen to represent the GC's actual stellar population, each model atmosphere can then be used to synthesize an EW for a stellar absorption line until the combined EW_{tot} equals the observed EW. When this condition is true, not only is the line abundance determined, but the stellar population age and $[M/H]$ is also determined for the GC. The key simplifying assumption that makes guessing a GC's stellar population possible is the assumption that the GC is a SSP defined by a single age and $[M/H]$. This assumption readily allows GC stellar populations to be modeled using theoretical isochrone models, which define all the stellar types contained inside a generic SSP as a function of the SSP's age and $[M/H]$. Therefore, by iterating over all possible age and $[M/H]$ combinations, the correct SSP can be determined for a GC, which then can be used to determine all the GC's abundances.

Lick Indices

The Lick index system (Burstein et al. 1984; Worthey et al. 1994; Trager et al. 1998) was developed to measure absorption features in *galaxy* IL spectra in order to estimate galactic stellar populations and chemical compositions. Despite this galaxy-centric origin, the Lick system is general enough to be used on any stellar population, and, therefore, it has been adopted and applied to extragalactic GC analysis (see, e.g., Brodie & Strader 2006 and references therein). The idea behind the Lick index system is that absorption features sensitive to stellar population age and $[M/H]$ can be isolated in IL spectra, and that these measured absorption features can then be compared against calibrated SSP models for which the features are known *a priori* as

a function of SSP age and $[M/H]$. By comparing the observed absorption features to a grid of SSP absorption features, the characteristic age and $[M/H]$ of the observed stellar population can be estimated.

Measuring a Lick absorption feature, called an *index*, is very similar to measuring an EW. Some major differences, though, include the fact that the index measurement process is highly systematized, the spectra must be observed at low spectral resolution, and the absorption features may or may not represent a single, pure transition line. Mathematically, an index is calculated using

$$I \equiv \int_{\lambda_1}^{\lambda_2} \frac{F_c(\lambda) - F_I(\lambda)}{F_c(\lambda)} d\lambda \tag{1.27}$$

where I is the index in units of Å, $F_c(\lambda)$ is the interpolated continuum flux level across the absorption feature, $F_I(\lambda)$ is the flux of the absorption feature, and the integration interval from λ_1 to λ_2 equals the bandpass over which the absorption feature is defined. The continuum level, $F_c(\lambda)$, is determined by first computing the average continuum flux inside the index's two sidebands, placing each average flux value at the center of its sideband, then linearly interpolating the flux between the two sideband midpoints.

The central bandpasses and sidebands that define the Lick system's 25 indices are listed in Table 1.6. This table provides the exact integration interval to use in Equation 1.27, and also the exact continuum sideband regions to use when interpolating each index's continuum level. Note that these bandpasses and sidebands are fairly wide, which means that most indices are actually blends of many different elemental and/or molecular absorption features. More interestingly, the table lists what element(s) each index is sensitive to. These elements are listed in order of which elements the index is most sensitive, where the elements in parentheses decrease the index's strength, while the other elements increase the index's strength. Note that most of the indices are sensitive to more than one element, and that most of these indices, in turn, have strengths that are both directly proportional and inversely proportional to the various handful of elements that they are sensitive to. Therefore,

Index	Feature Bandpass (Å)	Blue Sideband (Å)	Red Sideband (Å)	Measures	Age-Z Sensitivity $\left(\frac{dlog(age)}{dlog(Z)}\right)$
CN_1	4142.125-4177.125	4080.125-4117.625	4244.125-4284.125	C,N,(O)	1.9
CN_2	4142.125-4177.125	4083.875-4096.375	4244.125-4284.125	C,N,(O)	2.1
Ca4227	4222.250-4234.750	4211.000-4219.750	4241.000-4251.000	Ca,(C)	1.5
G4300	4281.375-4316.375	4266.375-4282.625	4318.875-4335.125	C,(O)	1.0
Fe4383	4369.125-4420.375	4359.125-4370.375	4442.875-4455.375	Fe,C,(Mg)	1.9
Ca4455	4452.125-4474.625	4445.875-4454.625	4477.125-4492.125	(Fe),(C),Cr	2.0
Fe4531	4514.250-4559.250	4504.250-4514.250	4560.500-4579.250	Ti,(Si)	1.9
Ca_24668	4634.000-4720.250	4611.500-4630.250	4742.750-4756.500	C,(O),(Si)	4.9
$H\beta$	4847.875-4876.625	4827.875-4847.875	4876.625-4891.625	$H\beta$,(Mg)	0.6
Fe5015	4977.750-5054.000	4946.500-4977.750	5054.000-5065.250	(Mg),Ti,Fe	4.0
Mg_1	5069.125-5134.125	4895.125-4957.625	5301.125-5366.125	C,Mg,(O),(Fe)	1.8
Mg_2	5154.125-5196.625	4895.125-4957.625	5301.125-5366.125	Mg,C,(Fe),(O)	1.8
Mgb	5160.125-5192.625	5142.625-5161.375	5191.375-5206.375	Mg,(C),(Cr)	1.7
Fe5270	5245.650-5285.650	5233.150-5248.150	5285.650-5318.150	Fe,C,(Mg)	2.3
Fe5335	5312.125-5352.125	5304.625-5315.875	5353.375-5363.375	Fe,(C),(Mg),Cr	2.8
Fe5406	5387.500-5415.000	5376.250-5387.500	5415.000-5425.000	Fe	2.5
Fe5709	5696.625-5720.375	5672.875-5696.625	5722.875-5736.625	(C),Fe	6.5
Fe5782	5776.625-5796.625	5765.375-5775.375	5797.875-5811.625	Cr	5.1
Na D	5876.875-5909.375	5860.625-5875.625	5922.125-5948.125	Na,C,(Mg)	2.1
TiO_1	5936.625-5994.125	5816.625-5849.125	6038.625-6103.625	C	1.5
TiO_2	6189.625-6272.125	6066.625-6141.625	6372.625-6415.125	C,V,Sc	2.5
$H\delta_A$	4083.500-4122.250	4041.600-4079.750	4128.500-4161.000	$H\delta$	1.1
$H\gamma_A$	4319.750-4363.500	4283.500-4319.750	4367.250-4419.750	$H\gamma$	1.0
$H\delta_F$	4091.000-4112.250	4057.250-4088.500	4114.750-4137.250	$H\delta$	0.9
$H\gamma_F$	4331.250-4352.250	4283.500-4319.750	4354.750-4384.750	$H\gamma$	0.8

Table 1.6. The Lick index definitions. All data comes from Trager et al. (1998), Worthey (1994), and Worthey & Ottaviani (1997). The"Index" column lists the name of the Lick index. The "Feature Bandpass" column lists the wavelength interval over which each Lick index is defined. The "Blue Sideband" column lists the wavelength interval over which the blue continuum level is calculated for each Lick index. The "Red Sideband" column lists the wavelength interval over which the red continuum level is calculated for each Lick index. The "Measures" column lists what elements each Lick index actually measures, in order of the most to least dominant element. Note that the elements in parentheses are inversely related to the strength of the index, in the sense that the index grows weaker as the abundances of those elements become larger. The "Age-Z Sensitivity" column lists each Lick index's sensitivity to SSP age and metallicity. Larger sensitivity numbers mean that the index is more sensitive to metallicity, and small numbers mean that the index is more sensitive to age.

disentangling all of these sensitivity relations in order to derive detailed chemical abundances is extremely complex (e.g. Tripicco & Bell 1995).

Instead, the Lick indices are primarily used to estimate a stellar system's metallicity (Z) and age. The metallicity and age sensitivity of an index is estimated by using SSP models to see how much the index strength changes as the SSP's metallicity or age changes (Worthey 1994). This is quoted in Table 1.6 as the ratio of the index strength's change due to a change in SSP age over its change due to a change in SSP metallicity (i.e. $\frac{dlog(age)}{dlog(Z)}$). The indices with the larger ratio values are more sensitive to metallicity, while the indices with the smaller ratios are more sensitive to age. Because Balmer absorption lines roughly measure the mean temperature of

an SSP's TO stars, the Balmer line indices prove to be the most sensitive to age (Worthey & Ottaviani 1997). Several Lick indices (e.g. $C_2$4668, Fe5015, Fe5709, and Fe5782) are also predominantly sensitive to metallicity. Therefore, by comparing an IL spectrum's metallicity and age sensitive indices to model SSP indices, the observed stellar population's metallicity and age can be estimated.

The model SSPs used in Lick index comparisons are usually constructed by populating theoretical isochrones with stars using an assumed IMF, assigning empirically determined Lick indices to those stars, and then calculating the SSPs' predicted Lick index strengths using an equation similar to Equation 1.26. For example, Worthey (1994) constructed a large set of model SSPs using isochrones, populated them with a Salpeter IMF (Salpeter 1955) normalized to $10^6 \mathcal{M}_\odot$, and then assigned index strengths to each star using the *fitting function* method of Worthey et al. (1994). These fitting functions are polynomial functions that predict a Lick index's strength as a function of stellar T_{eff}, $[Fe/H]$, and $log(g_\star)$. These fitting functions are based purely on the empirical relationship between index strength, T_{eff}, $[Fe/H]$, and $log(g_\star)$ taken from a large database of calibration stars (Worthey et al. 1994). Because the final predicted index strength is the flux-weighted average of all the stellar indices in a SSP, Worthey (1994) interpolated fluxes for each SSP star using the flux models of Kurucz (1992, private communication) and Bessell et al. (1989, 1991). Once the predicted Lick index strengths for numerous age and metallicity SSP models were created, they could be used in comparisons against observed Lick indices. This comparison usually involves selecting an age sensitive index and a metallicity sensitive index, plotting their predicted SSP values in the form of an index-index grid, plotting the observed index-index value inside this grid, and then assigning the observed stellar population the age-metallicity values of the location where its index-index data point falls within the grid.

In principle, the application of the Lick index system on GCs should be more useful than for galaxies because GCs actually do approximate SSPs, whereas galaxies are composed of multiple stellar populations. Despite being more natural targets, the Lick system is somewhat handicapped when it comes to analyzing GC IL spectra because

the system was designed and optimized for studying galaxy IL spectra. This handicap stems from the fact that galaxy IL spectra have intrinsically poor spectral resolutions due to their high velocity dispersions ($\sigma_v \sim 200\ km\ s^{-1}$), which induce large Doppler broadenings ($\Delta\lambda \sim 8 - 10$ Å). Because the Lick system was calibrated exclusively for these low spectral resolutions, GC IL spectra must be artificially degraded to these galaxy spectral resolutions, even though their much smaller velocity dispersions ($\sigma_v \sim 10\ km\ s^{-1}$, Pryor & Meylan 1993) allow for IL spectra with high spectral resolutions ($\Delta\lambda \sim 0.4$ Å). These low spectral resolutions, in turn, are largely responsible for the Lick system's inability to isolate single elemental abundances, because the low resolutions force each index to simultaneously integrate over many elemental transition lines.

Dissertation's Method

While the Lick index system is a fairly mature system for estimating the metallicities and ages of extragalactic GCs, its inability to measure true detailed abundances from solitary transition lines limits the usefulness of the system. As mentioned above, this limitation is actually an artificial limitation imposed on the system due to its reliance on low spectral resolution IL spectra, which originates from its galaxy-centric origins. Ideally, a similar system should be developed that takes advantage of the intrinsically high spectral resolutions obtainable for GC IL spectra, in order to derive detailed abundances from every transition line embedded within GC IL spectra. The development and demonstration of such a system is the purpose of this dissertation.

The premise behind this dissertation's extragalactic GC abundance analysis method is that the precise and accurate techniques used for single star abundance analysis discussed in § 1.2.1 can be combined with Equation 1.26 and theoretical SSP models to derive detailed abundances from GC IL spectra. The first step in this method is to create an age-metallicity grid of theoretical SSPs for each observed GC. These SSPs can be easily created by populating theoretical isochrones with stars using an IMF normalized to the amount of flux observed from the targeted GC of interest. This SSP creation stage is similar to the method applied to create the SSPs used in the

Lick index system. Next, model stellar atmospheres are created for the stars in each theoretical SSP. Because the theoretical SSPs, by definition, completely define the stellar parameters of their stars, the atmospheric parameters needed to convert these stars into model atmospheres are fully provided by the SSPs. Next, the Fe line EWs measured in the IL spectra of the observed GC are synthesized, one-by-one, through all the model atmospheres for a selected SSP until each line's iterated Fe abundance produces a light-weighted EW (Equation 1.26) that equals the line's observed EW. This line abundance determination algorithm is schematically shown in Figure 1.16. When all the Fe lines have their abundances determined for the SSP, their mean metallicity is computed and compared with the metallicity of the theoretical SSP. If the computed metallicity from the Fe line abundances and the metallicity of the SSP have the same value, then that theoretical SSP potentially matches the observed GC's real stellar population. Once all the SSPs in the grid are processed through this Fe line analysis, approximately only eight potentially matching SSPs usually remain. To determine the single best matching theoretical SSP, further physical constraints are applied based on the quality of the Fe line abundance solutions (e.g. $log\epsilon(Fe)$ versus EP, EW, and wavelength), just as they are applied in single star abundance analysis (see § 1.2.1). Once the single best matching SSP is determined, all the non-Fe line EWs can be synthesized through that SSP's model atmospheres to determine the detailed abundances of those elements. Thus, the IL spectra abundance analysis method concludes with abundances calculated for all the elemental absorption lines observed in a GC's IL spectrum.

The rest of this dissertation develops and demonstrates this abundance analysis method using a "training set" of seven Milky Way GCs, which were observed in such a way that their IL spectra mimic extragalactic GC IL spectra. In Chapter 2, the observation and data reduction of these training set clusters are discussed. The construction of a transition line list for Fe lines and non-Fe lines, and the measurement of these lines' EWs are also discussed. In Chapter 3, a proof-of-concept for the dissertation's abundance analysis method is demonstrated using *a priori* knowledge of the training set cluster's stellar populations in the form of photometric CMDs.

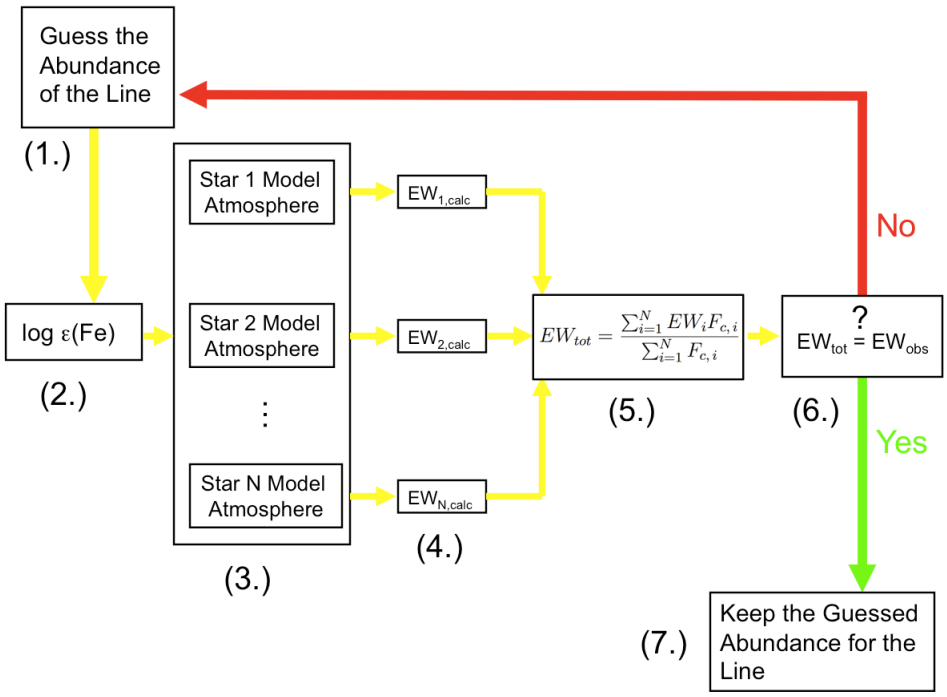

Figure 1.16. Line abundance determination algorithm for IL spectra.

Because real extragalactic GCs are spatially unresolved, their CMDs will not be known *a priori*; therefore, this chapter serves to demonstrate the basic concepts of the abundance analysis method without invoking any complications that could potentially stem from theoretical SSP modelling. In Chapter 4, the dissertation's full abundance analysis method is demonstrated using grids of theoretical SSPs. This chapter develops and demonstrates the actual abundance analysis method intended for real extragalactic GCs, and its systematic and statistical errors are explored. Finally, Chapter 5 offers conclusions.

CHAPTER 2

The Milky Way GC Training Set

This dissertation's abundance analysis method for GC IL spectra is developed and demonstrated using a training set of seven Milky Way GCs. Spatially resolved Milky Way (MW) GCs were chosen as the training set because their stellar populations are observationally known, and many of their stars have standard stellar abundances available from a large number of groups throughout the literature. These observationally determined stellar populations can be used to define model atmospheres that represent the training set clusters. The use of these model atmospheres in the abundance analysis method can serve to test the feasibility of the method without encountering any of the potential complications that may stem from using grids of theoretical SSPs. Also, the observationally determined stellar abundances can critically serve as fiducial abundances against which the dissertation's abundance results are tested.

The outline for this chapter is as follows. In § 2.1, the training set clusters are introduced and their physical properties are discussed. Particular attention is paid to physical properties that are observationally meaningful for IL spectra. § 2.2 discusses the observations conducted to obtain IL spectra for the the training set clusters. In § 2.3, the data reduction procedure used to convert the raw science data into one-dimensional, wavelength calibrated spectra are discussed. Finally, in § 2.4, the line lists used to search the IL spectra for elemental absorption lines are discussed, along with the EW measurement process itself. The line parameters used for the EW synthesis of these lines are also given, along with their final synthesized line abundances. Note that the determination of these line abundances are fully discussed in Chapters 3 and 4, but are presented here so that they remain centrally located

with their corresponding line parameters and EWs.

2.1 Training Set Properties

The training set used to develop the abundance analysis method consists of seven MW clusters (NGC 104, NGC 362, NGC 2808, NGC 6093, NGC 6388, NGC 6397, and NGC 6752) and 7 LMC clusters. The Milky Way clusters cover as wide a range of GC parameter space as is represented in the MW GC system: $-1.95\ dex \lesssim$ [Fe/H] $\lesssim -0.60\ dex$ in metallicity, $3.3\ km\ s^{-1} < \sigma_v < 18.9\ km\ s^{-1}$ in velocity dispersion, and horizontal branch morphologies that range from quite blue to quite red, quantified by horizontal branch ratios[1] (HBR) over the range $-0.99 - 1.00$ (see Figure 2.1). As all GCs in the MW are thought to be older than $\sim 10\ Gyrs$ in age (Krauss & Chaboyer 2003), the MW sample only provides clusters that are uniformly old. The LMC clusters, therefore, represent a critical addition to the training set as they include young ($< 1\ Gyr$), intermediate ($\sim 3 - 5\ Gyrs$), and old clusters ($\sim 10\ Gyrs$), with a range of elemental abundances. In order to concentrate on the fundamental techniques of the abundance analysis method, this dissertation focuses on the analysis of the MW clusters. The analysis of the LMC clusters has proven to be more complex and provides a wealth of new abundance results for the younger LMC clusters. As these results are beyond the scope of the training set's original purpose, the LMC training set clusters have been deferred to a later publishable paper. The characteristics of the MW training set are listed in Table 2.1.

The goals of this dissertation are to demonstrate both the strategy developed for the abundance analysis method and also the accuracy of its results for GCs that may be encountered in other galaxies. As such, it is important that the clusters cover the full range of cluster properties. For the purposes of analyzing integrated-light, some of the clusters with more extreme properties pose particular challenges. On average, the very high abundance clusters (NGC 104 and NGC 6388) have IL spectra with

[1]HB ratios classify the morphology of a GC's HB using the normalized expression $(B - R)/(B + V + R)$, where B is the number of HB stars bluer than the cluster's RR Lyrae region, R is the number of HB stars redder than the RR Lyrae region, and V is the number of HB stars within the RR Lyrae region (Lee 1990; Harris 1996).

Cluster	RA	Dec	μ_V	V_{tot}	M_{Vtot}	HBR	HBT[a]	$d_\odot$	r_{core}	σ_v	[Fe/H]
	$(J2000)$	$(J2000)$	$(mag/\Box'')$	(mag)	(mag)			(kpc)	$('')$	$(km\ s^{-1})$	(dex)
NGC 104	00 24 05.2	-72 04 51	14.43	3.95	-9.42	-0.99	7	4.5	24	9.8	-0.76
NGC 362	01 03 14.3	-70 50 54	14.88	6.40	-8.41	-0.87	6	8.5	11.4c	6.3	-1.16
NGC 2808	09 12 02.6	-64 51 47	15.17	6.20	-9.39	-0.49	0/7	9.6	15.6	14.2	-1.15
NGC 6093	16 17 02.5	-22 58 30	15.19	7.33	-8.23	0.93	0	10.0	9.0	12.5	-1.75
NGC 6388	17 36 17.0	-44 44 06	14.55	6.72	-9.42	-0.70	5	10.0	7.2	18.9	-0.60
NGC 6397	17 40 41.3	-53 40 25	15.65	5.73	-6.63	0.98	1	2.3	3c	3.3	-1.95
NGC 6752	19 10 52.0	-59 59 05	15.20	5.40	-7.73	1.00	0	4.0	10.2c	4.5	-1.56

Table 2.1. Properties of the Milky Way GC training set. From left-to-right, the table lists each cluster's: name, right ascension, declination, central V-band surface brightness, total apparent V-band magnitude, total absolute V-band magnitude, horizontal branch ratio, horizontal branch type, heliocentric distance, core radius, central velocity dispersion, and metallicity. Note that a "c" next to a cluster's core radius indicates that the cluster is core-collapsed. All data comes from the Milky Way GC catalog of Harris (1996), except for the central velocity dispersion data, which come from Pryor & Meylan (1993), and NGC 6388's HBR value, which comes from Puzia et al. (2002). [a]Horizontal branch types (HBT) classify the morphology of a GC's HB using an integer scale, where 1 corresponds to a HB with all of its stars on the blue side of the cluster's RR Lyrae region, and 7 corresponds to a HB with all of its stars on the red side of the RR Lyrae region (Dickens 1972). Modifications to the system include using an HBT of 0 for blue HBs that are extremely extended, and using two HBTs for HBs that are bimodal (Harris 1996).

more saturated lines and more line blends, which are particularly difficult to identify in integrated-light. Very low abundance clusters (NGC 6093 and NGC 6397) have IL spectra with much weaker lines, which results in fewer accessible lines for all elemental species. While the higher mass clusters (NGC 104, NGC 2808, NGC 6093, and NGC 6388) are generally brighter, and therefore yield higher signal-to-noise ratio spectra, their higher velocity-dispersions result in greater line broadening in their spectra. In addition to increasing the prevalence of line-blending, this increases the signal-to-noise ratio required to detect a line of a given strength because it reduces the central line decrement (see Figure 2.2). While extremes in these characteristics do provide challenges, the analysis is found to yield very accurate results over the full range of cluster properties.

While the seven GCs in the MW training set were chosen to represent "typical" GCs, it should also be noted that there is no such thing as a "typical" GC in at least two senses. First, while models of simple (single-age, single-abundance) stellar populations (SSPs) are very good at reproducing most characteristics of GCs, they do not accurately reproduce the full range of HB morphologies seen at all abundances and ages. In this sense, every GC is unique in its combination of abundance, age, and HB morphology, and the training set sample includes several clusters with the most

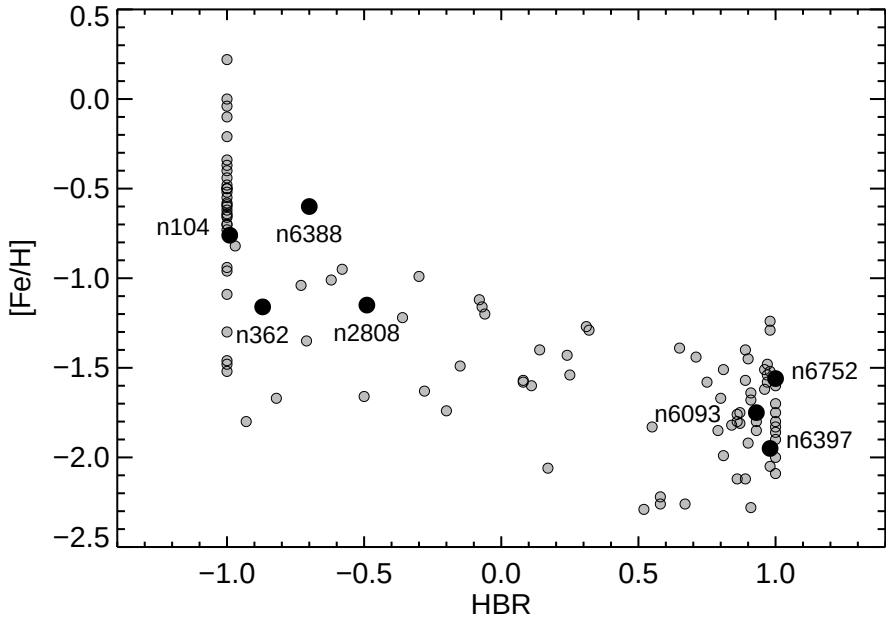

Figure 2.1. The Milky Way GC system's spread in metallicity and horizontal branch morphology demonstrated using the [Fe/H]–HBR relation. The training set clusters are plotted as large black dots, while the rest of the Milky Way clusters are plotted as small gray dots. Based on the definition of HBR, a value of −1.0 represents a GC with a purely red HB, while a value of +1.0 represents a GC with a purely blue HB. Therefore, the training set clusters probe both red and blue HB morphologies, which represent the two main peaks in the Milky Way's essentially bimodal HB distribution. All data comes from the Milky Way GC catalog of Harris (1996), except for NGC 6388's HBR value, which comes from Puzia et al. (2002).

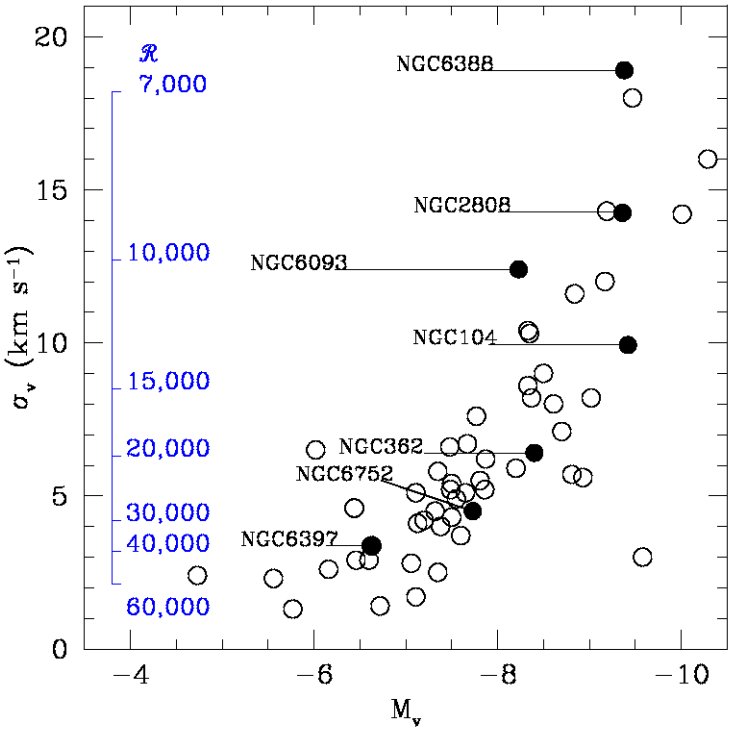

Figure 2.2. The M_V–σ_v relation for a subset of the Milky Way's GCs. Here, σ_v represents the GCs' central velocity dispersions and M_V represents their total absolute V-band magnitudes. The training set GCs are plotted as filled black dots, while the rest of the Milky Way GCs are plotted as open circles. The overplotted axis on the left indicates the limiting spectral resolution (i.e. $R \equiv \lambda / FWHM_\lambda$) that can be obtained for each cluster's absorption lines due to the Doppler broadening induced by each cluster's velocity dispersion. Therefore, the most massive (i.e. brightest) clusters are limited to line resolutions of ∼7000, while the least massive (i.e. dimmest) clusters are limited to line resolutions of ∼40,000.

extreme blue and red HB morphologies in the MW GC system. Second, while GCs are generally thought to be SSP systems, high spatial resolution photometry has recently shown that at least ∼10 clusters out the MW's ∼ 150 GCs contain complex stellar populations with multiple main sequences or split sub-giant branches (SGB). Two clusters in the training set sample (NGC 2808 and NGC 6388) are examples of GCs that exhibit complex populations. In this sense, the sample is indeed representative of the full-range of clusters that might be encountered when targeting extragalactic systems in the future. Peculiarities of the various clusters in the sample are discussed individually below.

Five of the clusters (NGC 104, NGC 362, NGC 6093, NGC 6397 and NGC 6752) are fairly typical MW GCs in that they appear to contain classical SSPs with well behaved HBs. Within the general context of the "second parameter problem" concerning HB morphology, a well behaved HB is one that is unimodal and red for metal-rich GCs, and unimodal and blue for metal-poor GCs. Of these five clusters, NGC 104, NGC 362, and NGC 6397 have normal HBs. NGC 104 is a metal-rich GC with a unimodal and red HB, and is frequently used as a standard example of the MW's metal-rich GC population. NGC 362 is an intermediate metallicity, core collapsed GC with a unimodal and red HB. NGC 6397 is a metal-poor, core collapsed GC with a unimodal and blue HB. The other two typical MW GCs, NGC 6093 and NGC 6752, also have relatively normal HBs. NGC 6093 is a metal-poor GC that has a blue HB that extends vertically down in magnitude, which forms an extremely blue tail. NGC 6752 is a metal-poor, core-collapsed GC that also has a blue HB with an extremely blue tail. The origin of these extremely blue tails currently remains an unexplained feature of HBs, and is not well reproduced in models of SSPs.

Clusters NGC 2808 and NGC 6388 possess peculiar, multiple stellar populations and HBs (Piotto 2009). NGC 2808 is an intermediate metallicity GC with a multimodal HB, consisting of a prominent red HB and a prominent blue HB that has a multiply subdivided, extremely blue tail. Furthermore, due to improvements in photometric accuracy, the main sequence of NGC 2808 was recently shown to divide into three distinct main sequence populations, which are currently thought to have

similar ages but different levels of He enrichment (Piotto et al. 2007). NGC 6388 is similarly complex. It has a bimodal HB that consists of a dominate red HB, a blue HB with an extremely blue tail, and two distinct stellar populations in the cluster's sub-giant branch (SGB) (Piotto 2009; Moretti et al. 2009; Busso et al. 2007). Again, it is thought that the different stellar populations have similar ages but different levels of He enrichment. At this point, better photometry is needed to determine if the main sequence of NGC 6388 also demonstrates the two distinct populations seen in its SBG (Piotto 2009; Busso et al. 2007). These two clusters are exemplary of the potentially complex stellar populations that are now understood to be present in a minority of GCs.

2.2 Observations

All data presented here were obtained using the the echelle spectrograph on the 2.5 m du Pont telescope at Las Campanas. The spectra cover the range 3700–7800 Å, with declining sensitivity and spectral resolution toward the blue end. Telluric absorption features limit the ability to analyze the spectra at the reddest end of this range, so the analysis focuses primarily on the high-quality spectra that were obtained from 5000–7500 Å.

The MW GCs in the training set are obviously spatially resolved and extended. As the goal of this work is to develop a method that enables abundance measurement of spatially unresolved, extragalactic GCs, the core region of each training set cluster was uniformly scanned to simulate the IL spectrum from an extragalactic GC. To both maximize the signal-to-noise ratio of the spectra and minimize the relative contribution from sky, the central 32×32 $arcsec^2$ region of each cluster was scanned. As the slit of the echelle spectrograph is 1×4 $arcsec^2$, this geometry allowed convenient and uniform sampling of the core. The observations were facilitated by a modification to the telescope guider program, kindly performed by Stephen Shectman, which enabled the echelle slit to uniformly scan from 16″ South-West to 16″ North-East of the field center. The cluster regions were scanned once per exposure, so clear conditions were necessary to ensure an unbiased weighting of the cluster light. As the entire slit

Cluster	Tot. Int. Time	SNR per pixel			
	(s)	7100 Å	5500 Å	4440 Å	3710 Å
NGC 104	11,030	145	100	61	19
NGC 362	11,021	111	89	53	16
NGC 2808	10,730	108	81	45	12
NGC 6093	7,350	68	52	29	8
NGC 6388	11,023	126	90	45	12
NGC 6397	18,374	69	57	38	19
NGC 6752	11,021	159	130	80	32

Table 2.2. The total integration times and signal-to-noise ratios for the training set clusters. The "SNR per pixel" column lists the signal-to-noise ratio at four locations within each cluster's IL spectrum. The four wavelength locations were chosen to representatively sample the entire range of the spectra, with the added condition that they were located within continuum regions.

was filled with cluster light during these scans, significant sky flux outside the telluric emission lines was only detected near twilight. To be conservative, exposures were also obtained off the cluster (i.e. on "pure sky") to allow measurement and subtraction of the sky signal from the science exposures. These sky exposures were taken throughout the night, temporally mixed with the cluster observations. All clusters, excluding NGC 2808, were observed during lunar dark time in 2000 July. NGC 2808 was observed during lunar dark time in 2001 January. The total integration time for each cluster is summarized in Table 2.2.

During each night, bias images (0 sec exposures) and dark images (900 sec exposures, shutter closed) were taken. Flat field images taken of the twilight sky with a broad-angle, diffusing slide in the optical path to blur-out spectral features and fill the inter-order regions of the CCD with light. These "milky flats" were median combined and then normalized with a smoothed version of the combined frame to produce a high fidelity flat field image that can be used to remove pixel-to-pixel sensitivity variations, even between orders. The smoothed version was made using a floating median with 1×31 pixel boxcar kernel. Before and after each cluster observation, wavelength calibration frames were taken using a Th-Ar lamp. Spectra of hot, rapidly rotating ($v \sin i > 300\ km\ s^{-1}$) B stars were also taken to serve as telluric reference spectra.

2.3 Data Reduction

The basic data reduction steps were implemented using the echelle package in IRAF[2], including the routines for overscan, bias subtraction, and flat-field division. Echelle orders were identified, traced, and extracted using IRAF's APALL routine. This routine also allows for the subtraction of inter-order, scattered-light, which is easy to measure in this spectrograph for orders bluer than 6000 Å, but difficult to measure at redder wavelengths because the wings of adjacent orders begin to overlap at those wavelengths. In order to measure the scattered light despite this overlap, an empirical scattered-light model was produced. For a detailed discussion of the scattered-light subtraction see McWilliam & Bernstein (2008). The sky spectra were scaled and subtracted from the individual integrated-light exposures using simple arithmetic routines. The extracted spectra were wavelength calibrated using standard IRAF routines and the Th-Ar spectra taken before and after each science spectrum.

In the analysis of the clusters' fully reduced spectra, the equivalent widths (EW) of spectral absorption lines were measured while simultaneously fitting the continuum level in each order. To do so, it is only necessary to roughly flux calibrate the spectra by normalizing out the strong echelle blaze function from each order. An adequate approximation of the blaze function for each order was obtained using observations of a bright G-star, which is roughly the color of the IL spectra. The approximate blaze function was obtained by fitting a low order polynomial to the G-star's spectrum in each order. No attempt was made to remove telluric absorption lines from the spectra, however telluric template stars were compared to each order of the final IL spectra to assure that no absorption lines were measured near telluric lines. Representative signal-to-noise values for each cluster's final IL spectrum are listed in Table 2.2, and Figure 2.3 displays a representative spectral region for each cluster centered at $\lambda = 5167.5$ Å.

[2]IRAF is distributed by the National Optical Astronomy Observatories, which are operated by the Association of Universities for Research in Astronomy, Inc., under cooperative agreement with the National Science Foundation.

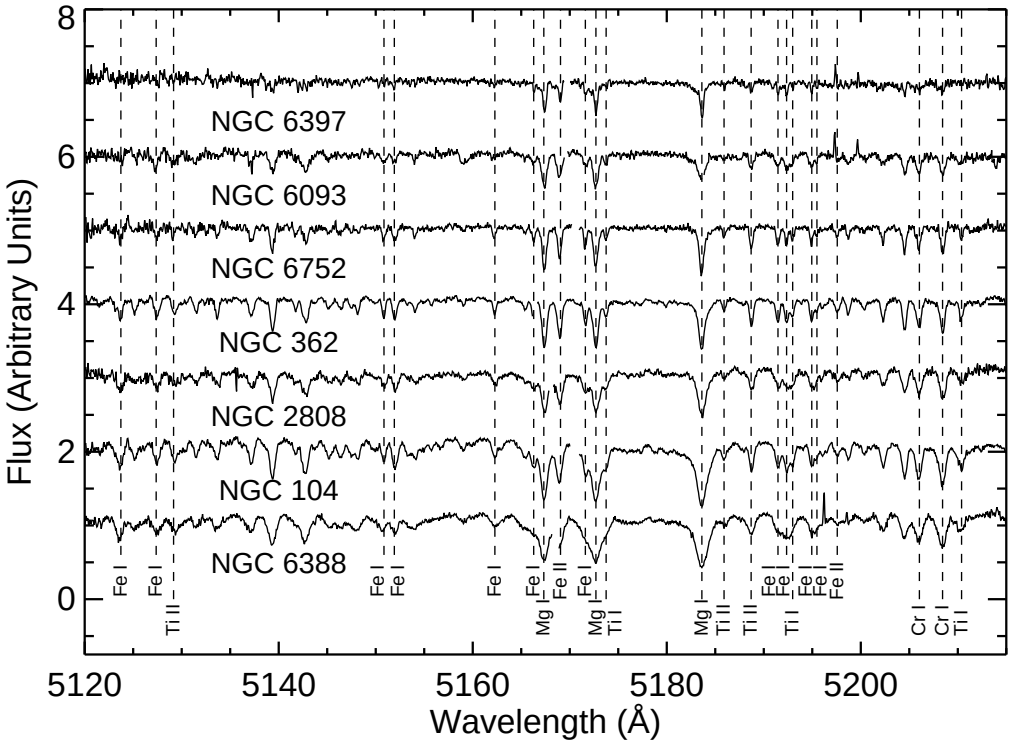

Figure 2.3. An example spectral region from the IL spectra of the training set clusters. The region shown here spans a range of 95 Å, and is centered on $\lambda = 5167.5$ Å. Note that the continuum levels of the spectra have been normalized to 1.0, and are plotted here with additive offsets to prevent overlap. The offsets were applied such that the metallicities of the clusters increase from top-to-bottom of the plot. The vertical dashed lines indicate various transition lines for several species, which are labeled near the bottom of the plot. Note that the line strengths clearly increase as the metallicities of the clusters increase.

2.4 EWs and Line Lists

The EWs of the absorption lines in the IL spectra were measured using GETJOB (McWilliam et al. 1995). This software includes semi-automated routines that allow the user to interactively fit a low-order polynomial to the continuum level of each spectral order using specified continuum regions, determine and apply a radial Doppler correction using a subset of suitable lines, and finally search for detectable absorption lines from a user-provided line list (see below). All lines can be visually inspected and line profile fits can be adjusted to use single, double, or triple Gaussian profiles to isolate desired lines and obtain their EWs. Particular care was taken in this process to confirm the accuracy of the continuum fit, and to check each line for blends and atmospheric absorption features. This degree of caution is particularly important in IL spectra analysis because blends and misidentifications are more common than in single RGB star spectra.

Because the final analysis method uses Fe I lines to identify the best-fitting stellar population for a cluster, it is particularly important that the analysis identify as many useful Fe I lines as possible. Therefore, a large line list of approximately 227 Fe lines and 274 non-Fe lines was compiled for the analysis of the IL spectra, based primarily on the line lists used for the analysis of RGB stars in McWilliam & Rich (1994) and McWilliam et al. (1995). Of these lines, 25 Fe lines and 32 non-Fe lines were added from the Vienna Atomic Line Database[3] (VALD) (Kupka et al. 2000). Any line excitation potentials not documented in the papers listed above were also obtained from VALD. The final list of Fe lines is given in Table 2.3, and the final list of lines for all other elements is given in Table 2.4. For any abundances given relative to solar, a solar Fe abundance of $log\,\epsilon(\mathrm{Fe}) = 7.50\ dex$ has been adopted, while solar abundances for all other elements come from Asplund et al. (2005).

The Fe line list is intended to include any lines that give consistent and reliable results in any of the training set clusters. Because each cluster has a unique combination of velocity dispersion, metallicity, and systemic velocity, each cluster has a

[3]http://vald.astro.univie.ac.at/

unique list of detectable and trustworthy Fe lines. The Fe line list is also intended to include Fe I lines that cover as wide a range as possible in wavelength, EP, and EW, all of which are powerful diagnostics for evaluating the quality of the abundance solutions (see Chapter 4).

The starting Fe I line list contains 227 lines. Of these, roughly 75-100 unblended lines were detected in any given cluster. In the Fe solution for each cluster, lines that deviated by more than 2-σ from the mean solution were rejected (see Chapters 3 and 4). An average of $\sim$14 Fe I lines in each cluster are rejected in this way. Of these, only a few lines were rejected in more than two clusters, suggesting that there were no lines in the starting list that should be universally rejected. In order to confirm that each cluster's final line list gave an unbiased solution compared to the RGB "clean" list of Fulbright et al. (2006), the results of these "clean" lines were explicitly compared with each cluster's final line list (see Chapters 3 and 4) and no statistical differences between the two lists were found. Previous work in extragalactic clusters has already demonstrated that using the more inclusive Fe line list is useful to guarantee a sufficient sample of Fe lines (see Colucci et al. 2009).

Because there are fewer (i.e. 10-15) detectable Fe II lines than Fe I lines, and because they tend to have a larger standard deviation in individual RGB spectra as well as in the IL spectra, a similar σ-clipping procedure is less effective at identifying high quality Fe II lines. Therefore, visual inspection of the Fe II lines in all seven GC IL spectra was used to select the best set of Fe II lines. In this case, "best" lines are those with minimal blends from other stellar and telluric lines, and are located in the most reliable continuum regions.

In the full analysis using theoretical SSPs, the non-Fe lines are analyzed only using the best-matching SSP once it has been identified from the Fe line analysis (see Chapter 4). Because many of the non-Fe elements have only a few potentially measurable transition lines (e.g. $\lesssim 10$) in the IL of a GC, line blending in any one line can significantly bias the mean abundance results for those elements and is therefore of particular concern. To identify line blending, the area around every non-Fe line was synthesized, including all nearby lines, based on an initial abundance analysis. All line

profiles were then visually compared with the synthesized profiles and line rankings of *A, B*, or *C* were assigned. Lines ranked as *A* indicate lines with very little or no blending, such that the lines can be accurately measured by fitting them with single or multiple Gaussian profiles simultaneously. Lines ranked as *B* either have sufficient blending such that a multiple Gaussian fit results in significantly overlapping lines or the continuum region near the line is difficult to establish. Finally, lines ranked as *C* suffer from severe blends or a very poorly constrained continuum. Only lines ranked as *A* or *B* quality are used in the analysis for any cluster. Table 2.4 indicates the line quality ranking for each non-Fe line as a superscript on the line's measured EW.

The EWs for all the Fe lines used in the analysis are listed in Table 2.3. The EWs for all other species are listed in Table 2.4. Based on curve-of-growth considerations, most lines with EWs $\gtrsim$ 150 mÅ begin to deviate from the linear portion of the curve-of-growth. An important exception to this saturation point are the Fe II lines, which begin to deviate from the linear portion of the curve-of-growth for EWs $\gtrsim$ 100 mÅ. Therefore, abundances are not reported for Fe I lines with EW $>$ 150 mÅ and Fe II lines with EW $>$ 100 mÅ, nor are they used in the dissertation's analysis. Meanwhile, all non-Fe line abundances are listed in Table 2.4, including those with EWs $>$ 150 mÅ both for the sake of completeness and because there are generally very few measurable non-Fe lines. However, these saturated lines with EWs $>$ 150 mÅ are also not used in the dissertation's analysis.

Table 2.3: The Fe line list, their measured EWs, and their calculated line abundances for the training set clusters. For each line transition, column 1 lists the elemental species, column 2 lists the wavelength in units of Å, column 3 lists the excitation potential (EP) in units of electron volts (eV), column 4 lists the oscillator strength in $log(gf)$ notation, and column 5 lists the references used for the EP and $log(gf)$ values. The cluster columns labeled "NGC 104" through "NGC 6752" are each composed of three sub-columns. For each cluster column, sub-column 1 lists the measured EW of each line in units of mÅ, sub-column 2 lists the calculated abundance ($log\epsilon_p$) of each line transition derived using the cluster's photometric CMD to define its stellar atmospheres (see Chapter 3), and sub-column 3 lists the calculated abundance ($log\epsilon_t$) of each line transition derived using the cluster's best 13 Gyr theoretical SSP to define its stellar atmospheres (see Chapter 4). Clean Fe I lines as determined by Fulbright et al. (2006) for the RGB star Arcturus are indicated with a superscript "a" on their wavelengths. Potentially clean Fe II lines as determined by visual inspection are indicated with a superscript "b" on their wavelengths. The line parameter references are listed in the order of (EP, $log(gf)$). The references are: [1]: McWilliam & Rich (1994); [2]: McWilliam et al. (1995); [3]: *The Vienna Atomic Line Database* (VALD); [4]: McWilliam & Bernstein (2008)

					NGC 104			NGC 362			NGC 2808			NGC 6093			NGC 6388			NGC 6397			NGC 6752		
Sp.	λ	EP	$log(gf)$	Ref.	EW	$log\epsilon_p$	$log\epsilon_t$	EW	$log\epsilon_p$	$log\epsilon_t$	EW	$log\epsilon_p$	$log\epsilon_t$	EW	$log\epsilon_p$	$log\epsilon_t$	EW	$log\epsilon_p$	$log\epsilon_t$	EW	$log\epsilon_p$	$log\epsilon_t$	EW	$log\epsilon_p$	$log\epsilon_t$
Fe I	4442.35	2.198	-1.228	3,2	···	···	···	···	···	···	···	···	···	···	···	···	···	···	···	38.1	5.49	5.32	···	···	···
Fe I	4443.20	3.071	-1.043	3,2	···	···	···	···	···	···	···	···	···	···	···	···	···	···	···	28.8	5.64	5.51	···	···	···
Fe I	4447.73	2.223	-1.339	3,2	···	···	···	···	···	···	···	···	···	···	···	···	···	···	···	···	···	···	···	···	···
Fe I	4459.10	2.176	-1.332	3,2	···	···	···	···	···	···	···	···	···	···	···	···	···	···	···	39.5	5.60	5.44	···	···	···
Fe I	4494.57	2.198	-1.143	3,2	···	···	···	···	···	···	···	···	···	···	···	···	···	···	···	24.7	4.93	4.82	···	···	···
Fe I	4528.63	2.176	-0.887	3,2	···	···	···	···	···	···	···	···	···	···	···	···	···	···	···	33.2	···	4.81	···	···	···
Fe I	4654.50	1.557	-2.721	3,2	···	···	···	···	···	···	···	···	···	···	···	···	···	···	···	26.8	5.88	5.79	···	···	···
Fe I	4691.42	2.990	-1.523	3,2	···	···	···	···	···	···	105	7.33	7.17	···	···	···	···	···	···	···	···	···	···	···	···
Fe I	4736.78	3.211	-0.752	3,2	···	···	···	97.9	6.71	6.48	128	7.19	7.01	···	···	···	138	7.23	7.06	22.1	5.40	5.32	···	···	···
Fe I	4871.32	2.865	-0.362	3,2	···	···	···	···	···	···	130	6.42	6.26	126	6.21	6.34	···	···	···	47.2	5.40	5.27	133	6.46	6.34
Fe I	4872.14	2.882	-0.567	3,2	···	···	···	134	6.78	6.53	···	···	···	108	6.15	6.26	···	···	···	···	···	···	132	6.67	6.53
Fe I	4890.76	2.875	-0.394	3,2	···	···	···	146	6.75	6.50	110	6.11	5.96	···	···	···	···	···	···	···	···	···	112	6.22	6.02
Fe I	4891.50	2.851	-0.111	3,2	···	···	···	···	···	···	···	···	···	115	5.77	5.90	···	···	···	46.7	5.12	5.00	136	6.23	6.10
Fe I	4903.32	2.882	-0.926	3,2	···	···	···	127	7.02	6.78	···	···	···	54.8	5.17	5.38	···	···	···	17.4	5.03	4.98	104	6.61	6.39
Fe I	4919.00	2.865	-0.342	3,2	···	···	···	···	···	···	147	6.61	6.43	104	5.78	5.91	···	···	···	46.6	5.36	5.24	136	6.46	6.33
Fe I	4920.51	2.832	0.068	3,2	···	···	···	···	···	···	···	···	···	145	5.95	6.12	···	···	···	···	···	···	149	6.16	6.04
Fe I	4938.82	2.875	-1.077	3,2	···	···	···	133	7.24	7.00	135	7.19	7.02	···	···	···	···	···	···	30.9	5.63	5.55	79.6	6.23	5.99
Fe I	4939.69	0.859	-3.252	3,2	···	···	···	128	6.94	6.68	149	7.11	6.94	···	···	···	···	···	···	13.9	5.06	5.04	80.0	6.17	5.84
Fe I	4966.10	3.332	-0.871	3,3	···	···	···	105	7.02	6.80	91.3	6.62	6.50	52.7	5.57	5.75	···	···	···	21.9	5.58	5.52	69.2	6.26	6.04
Fe I	4994.14	0.915	-2.969	3,2	···	···	···	108	6.40	6.13	106	6.21	6.06	96.6	5.83	6.09	137	6.62	6.47	···	···	···	111	6.58	6.23
Fe I	5001.87	3.881	0.050	3,2	···	···	···	87.9	6.32	6.12	71.4	5.83	5.74	59.4	5.46	5.59	123	6.85	6.70	···	···	···	93.6	6.42	6.26
Fe I	5006.12	2.832	-0.615	3,2	···	···	···	···	···	···	···	···	···	···	···	···	···	···	···	31.4	5.13	5.06	116	6.41	6.22
Fe I	5014.95	3.943	-0.303	3,3	···	···	···	76.6	6.46	6.29	···	···	···	36.5	5.30	5.45	···	···	···	···	···	···	64.3	6.21	6.03

Continued on next page

Table 2.3 – continued from previous page

					NGC 104			NGC 362			NGC 2808			NGC 6093			NGC 6388			NGC 6397			NGC 6752		
Sp.	λ	EP	$log(gf)$	Ref.	EW	$log\epsilon_p$	$log\epsilon_t$	EW	$log\epsilon_p$	$log\epsilon_t$	EW	$log\epsilon_p$	$log\epsilon_t$	EW	$log\epsilon_p$	$log\epsilon_t$	EW	$log\epsilon_p$	$log\epsilon_t$	EW	$log\epsilon_p$	$log\epsilon_t$	EW	$log\epsilon_p$	$log\epsilon_t$
Fe I	5041.08	0.958	-3.086	3,2	···	···	···	···	···	···	···	···	···	120	6.47	6.67	···	···	···	···	···	···	126	6.96	6.64
Fe I	5041.76	1.485	-2.203	3,2	···	···	···	···	···	···	···	···	···	113	6.10	6.29	···	···	···	37.1	5.53	5.48	135	6.79	6.52
Fe I	5049.83	2.279	-1.355	3,2	···	···	···	136	6.84	6.61	135	6.73	6.57	86.5	5.65	5.83	···	···	···	34.5	5.40	5.34	109	6.43	6.18
Fe I	5051.64	0.915	-2.764	3,2	···	···	···	146	6.70	6.46	···	···	···	70.3	4.92	5.28	···	···	···	43.9	5.71	5.66	114	6.40	6.06
Fe I	5068.77	2.940	-1.041	3,2	···	···	···	118	6.98	6.75	114	6.80	6.66	63.1	5.50	5.70	···	···	···	42.6	5.97	5.88	99.0	6.64	6.41
Fe I	5074.75	4.220	-0.160	3,2	71.2	6.21	6.26	74.2	6.54	6.38	64.0	6.22	6.14	110	7.11	7.21	111	7.16	7.03	19.9	5.68	5.62	···	···	···
Fe I	5083.34	0.958	-2.842	3,2	···	···	···	147	6.84	6.59	121	6.38	6.21	···	···	···	···	···	···	33.1	5.49	5.46	92.6	6.10	5.76
Fe I	5110.44	4.260	-3.758	3,2	···	···	···	···	···	···	140	11.2	6.14	112	10.6	5.97	···	···	···	35.6	5.49	5.47	···	···	···
Fe I	5123.73	1.011	-3.058	3,2	···	···	···	146	7.09	6.84	···	···	···	95.4	5.92	6.20	···	···	···	35.9	5.84	5.81	102	6.54	6.20
Fe I	5127.37	0.915	-3.249	3,2	···	···	···	132	6.98	6.73	···	···	···	61.4	5.14	5.49	···	···	···	···	···	···	···	···	···
Fe I	5150.85	0.990	-3.037	3,2	138	6.62	6.60	96.3	6.24	5.98	113	6.43	6.28	91.1	5.76	6.05	···	···	···	15.5	5.02	5.01	89.2	6.21	5.89
Fe I	5151.92	1.011	-3.321	3,2	130	6.79	6.78	134	7.18	6.93	···	···	···	72.8	5.61	5.94	···	···	···	35.7	6.09	6.06	···	···	···
Fe I	5162.28	4.178	0.020	3,2	136	7.21	7.17	80.6	6.44	6.28	111	6.99	6.85	···	···	···	142	7.42	7.24	24.1	5.58	5.52	64.9	6.12	5.94
Fe I	5166.28	0.000	-4.123	3,2	···	···	···	···	···	···	···	···	···	···	···	···	···	···	···	36.1	5.86	5.84	···	···	···
Fe I	5171.61	1.485	-1.721	3,2	···	···	···	···	···	···	···	···	···	98.6	5.25	5.49	···	···	···	···	···	···	110	5.90	5.58
Fe I	5191.46	3.038	-0.551	3,2	···	···	···	···	···	···	···	···	···	97.3	5.92	6.06	···	···	···	···	···	···	119	6.55	6.38
Fe I	5192.35	2.998	-0.421	3,2	···	···	···	···	···	···	···	···	···	116	6.12	6.26	···	···	···	59.4	5.82	5.72	95.5	5.99	5.75
Fe I	5194.95	1.557	-2.021	3,2	···	···	···	131	6.51	6.27	···	···	···	96.9	5.59	5.83	86.6	5.32	5.25	35.9	5.35	5.31	95.3	5.98	5.66
Fe I	5195.48	4.220	-0.002	3,3	···	···	···	···	···	···	···	···	···	26.0	5.01	5.15	···	···	···	18.1	5.44	5.39	49.6	5.81	5.66
Fe I	5216.28	1.608	-2.082	3,2	···	···	···	132	6.64	6.39	125	6.44	6.29	103	5.82	6.05	127	6.33	6.22	···	···	···	99.0	6.17	5.85
Fe I	5225.53	0.110	-4.755	3,2	···	···	···	82.6	6.56	6.26	···	···	···	63.1	5.60	5.99	···	···	···	···	···	···	63.1	6.19	5.84
Fe I	5232.95	2.940	-0.057	3,2	···	···	···	···	···	···	···	···	···	···	···	···	···	···	···	54.1	5.26	5.17	125	6.03	5.87
Fe I	5254.95	0.110	-4.764	3,2	···	···	···	113	7.12	6.85	···	···	···	···	···	···	···	···	···	···	···	···	55.2	5.96	5.60
Fe I	5266.56	2.998	-0.385	3,2	···	···	···	···	···	···	130	6.46	6.30	82.3	5.33	5.50	···	···	···	42.7	5.34	5.27	95.4	5.93	5.69
Fe I	5269.55	0.859	-1.333	3,2	···	···	···	···	···	···	···	···	···	···	···	···	···	···	···	···	···	···	···	···	···
Fe I	5281.80	3.038	-0.833	3,2	···	···	···	105	6.56	6.35	117	6.69	6.56	84.4	5.85	6.02	···	···	···	21.8	5.20	5.16	80.0	6.08	5.83
Fe I	5283.63	3.241	-0.524	3,2	···	···	···	130	6.93	6.70	149	7.11	6.96	···	···	···	···	···	···	28.2	5.30	5.26	98.4	6.36	6.14
Fe I	5302.31	3.283	-0.720	3,2	140	7.04	7.01	118	6.95	6.73	127	7.03	6.88	67.9	5.62	5.81	···	···	···	21.1	5.31	5.27	66.7	5.91	5.69
Fe I	5307.37	1.608	-2.912	3,2	95.6	6.36	6.40	80.8	6.44	6.20	83.3	6.34	6.23	75.2	5.92	6.23	···	···	···	···	···	···	75.3	6.40	6.10
Fe I	5324.19	3.211	-0.103	3,2	···	···	···	···	···	···	···	···	···	89.7	5.46	5.60	···	···	···	41.9	5.23	5.17	104	6.02	5.82
Fe I	5328.54	1.557	-1.850	3,2	···	···	···	···	···	···	···	···	···	···	···	···	···	···	···	54.3	5.66	5.61	···	···	···
Fe I	5339.94	3.266	-0.720	3,2	133	6.90	6.90	105	6.67	6.46	109	6.66	6.54	61.6	5.43	5.63	···	···	···	24.7	5.40	5.37	75.8	6.10	5.86
Fe I	5367.48	4.415	0.443	3,3	102	6.45	6.46	89.0	6.41	6.24	71.6	5.94	5.87	88.7	6.22	6.32	···	···	···	18.6	5.19	5.14	72.5	6.06	5.91
Fe I	5369.97	4.371	0.536	3,2	···	···	···	88.0	6.25	6.09	126	6.89	6.74	···	···	···	···	···	···	···	···	···	87.5	6.22	6.08
Fe I	5371.50	0.958	-1.644	3,2	···	···	···	···	···	···	···	···	···	···	···	···	···	···	···	73.9	5.32	5.31	···	···	···
Fe I	5383.38	4.312	0.645	3,2	105	6.18	6.19	108	6.49	6.29	101	6.27	6.16	77.9	5.68	5.79	···	···	···	38.2	5.44	5.38	82.3	5.96	5.81
Fe I	5389.49	4.415	-0.410	3,2	···	···	···	74.6	6.92	6.78	···	···	···	···	···	···	···	···	···	···	···	···	45.3	6.30	6.15

Continued on next page

Table 2.3 – continued from previous page

					NGC 104			NGC 362			NGC 2808			NGC 6093			NGC 6388			NGC 6397			NGC 6752		
Sp.	λ	EP	$log(gf)$	Ref.	EW	$log\epsilon_p$	$log\epsilon_t$	EW	$log\epsilon_p$	$log\epsilon_t$	EW	$log\epsilon_p$	$log\epsilon_t$	EW	$log\epsilon_p$	$log\epsilon_t$	EW	$log\epsilon_p$	$log\epsilon_t$	EW	$log\epsilon_p$	$log\epsilon_t$	EW	$log\epsilon_p$	$log\epsilon_t$
Fe I	5393.18	3.241	-0.715	3,2	126	6.75	6.75	105	6.60	6.40	103	6.49	6.37	107	6.43	6.58	···	···	···	24.7	5.36	5.33	79.7	6.14	5.90
Fe I	5397.14	0.915	-1.982	3,2	···	···	···	···	···	···	···	···	···	···	···	···	···	···	···	68.0	5.47	5.45	144	5.91	5.59
Fe I	5405.78	0.990	-1.852	3,2	···	···	···	···	···	···	···	···	···	···	···	···	···	···	···	69.5	5.45	5.44	131	5.70	5.36
Fe I	5424.08	4.320	0.520	3,2	···	···	···	93.6	6.32	6.15	129	6.88	6.73	82.4	5.90	6.00	···	···	···	48.4	5.81	5.74	87.6	6.18	6.03
Fe I	5429.71	0.958	-1.881	3,2	···	···	···	···	···	···	···	···	···	···	···	···	···	···	···	81.1	5.69	5.69	···	···	···
Fe I	5434.53	1.011	-2.126	3,2	···	···	···	···	···	···	···	···	···	110	5.16	5.43	···	···	···	69.0	5.72	5.70	123	5.87	5.52
Fe I	5446.92	0.990	-3.109	3,2	···	···	···	···	···	···	···	···	···	···	···	···	···	···	···	76.3	6.84	6.84	···	···	···
Fe I	5455.62	1.011	-2.091	3,2	···	···	···	···	···	···	···	···	···	···	···	···	···	···	···	71.5	5.74	5.72	···	···	···
Fe I	5460.87[a]	3.071	-3.580	3,3	···	···	···	···	···	···	···	···	···	···	···	···	57.9	7.98	7.96	···	···	···	···	···	···
Fe I	5462.96[a]	4.473	-0.234	3,	115	7.39	7.38	···	···	···	94.1	7.15	7.05	···	···	···	···	···	···	···	···	···	···	···	···
Fe I	5497.53	1.011	-2.825	3,2	···	···	···	140	6.61	6.38	141	6.55	6.40	97.0	5.52	5.83	···	···	···	32.3	5.41	5.41	119	6.47	6.11
Fe I	5501.48	0.958	-3.046	3,2	···	···	···	120	6.49	6.24	···	···	···	86.1	5.41	5.76	···	···	···	31.1	5.53	5.52	112	6.51	6.14
Fe I	5506.79	0.990	-2.789	3,2	···	···	···	···	···	···	146	6.55	6.40	108	5.70	5.96	···	···	···	36.6	5.48	5.48	101	6.10	5.73
Fe I	5522.45[a]	4.209	-1.450	4,4	34.0	6.62	6.66	···	···	···	···	···	···	···	···	···	···	···	···	···	···	···	···	···	···
Fe I	5543.94[a]	4.218	-1.040	4,4	46.1	6.49	6.54	32.7	6.34	6.24	···	···	···	···	···	···	···	···	···	···	···	···	···	···	···
Fe I	5560.21[a]	4.435	-1.090	4,4	···	···	···	22.5	6.35	6.26	···	···	···	···	···	···	66.2	7.26	7.26	···	···	···	···	···	···
Fe I	5569.63	3.417	-0.500	3,2	143	6.96	6.94	106	6.57	6.39	108	6.52	6.41	84.1	5.85	6.02	···	···	···	24.5	5.30	5.27	71.4	5.88	5.66
Fe I	5572.85	3.396	-0.275	3,2	···	···	···	134	6.82	6.61	136	6.78	6.64	77.3	5.46	5.63	···	···	···	42.2	5.55	5.50	84.2	5.92	5.70
Fe I	5576.10	3.430	-0.900	3,2	···	···	···	84.8	6.52	6.35	86.9	6.47	6.38	59.8	5.70	5.90	106	6.80	6.73	20.2	5.56	5.54	48.2	5.73	5.54
Fe I	5586.77	3.370	-0.096	3,2	141	6.51	6.49	125	6.48	6.27	130	6.48	6.34	87.6	5.49	5.65	···	···	···	43.2	5.37	5.33	100	6.94	6.81
Fe I	5587.57[a]	4.143	-1.750	3,	···	···	···	···	···	···	···	···	···	···	···	···	39.3	7.00	7.01	···	···	···	···	···	···
Fe I	5615.66	3.332	0.050	3,2	···	···	···	···	···	···	···	···	···	114	5.84	5.99	···	···	···	40.5	5.11	5.07	129	6.29	6.14
Fe I	5618.63[a]	4.209	-1.275	4,4	47.2	6.73	6.78	26.4	6.38	6.28	···	···	···	···	···	···	···	···	···	···	···	···	···	···	···
Fe I	5633.95[a]	4.991	-0.230	4,4	···	···	···	34.5	6.44	6.36	···	···	···	69.2	7.05	7.14	···	···	···	···	···	···	···	···	···
Fe I	5638.26[a]	4.220	-0.870	3,3	118	7.79	7.78	57.1	6.74	6.61	···	···	···	···	···	···	···	···	···	···	···	···	···	···	···
Fe I	5662.52[a]	4.178	-0.573	3,3	···	···	···	···	···	···	···	···	···	···	···	···	···	···	···	···	···	···	22.7	5.57	5.42
Fe I	5679.02[a]	4.652	-0.920	3,3	···	···	···	27.1	6.55	6.46	···	···	···	···	···	···	···	···	···	···	···	···	···	···	···
Fe I	5731.76[a]	4.256	-1.300	3,3	···	···	···	···	···	···	···	···	···	···	···	···	73.4	7.40	7.39	···	···	···	···	···	···
Fe I	5741.85	4.256	-1.672		26.2	6.69	6.73	···	···	···	···	···	···	···	···	···	···	···	···	···	···	···	···	···	···
Fe I	5752.03[a]	4.549	-0.864	4,4	51.5	6.80	6.84	21.2	6.19	6.11	···	···	···	···	···	···	···	···	···	···	···	···	···	···	···
Fe I	5763.00	4.209	-0.450	3,3	97.0	6.93	6.96	85.2	6.90	6.75	83.6	6.78	6.71	···	···	···	···	···	···	···	···	···	40.6	5.95	5.79
Fe I	5775.08[a]	4.220	-1.297	4,4	47.3	6.75	6.80	42.1	6.79	6.68	···	···	···	···	···	···	···	···	···	···	···	···	···	···	···
Fe I	5778.45[a]	2.588	-3.440	4,4	40.6	6.76	6.76	···	···	···	···	···	···	···	···	···	···	···	···	···	···	···	···	···	···
Fe I	5862.36[a]	4.549	-0.051	4,4	82.8	6.63	6.66	54.4	6.19	6.08	70.1	6.47	6.41	···	···	···	102	7.07	7.02	···	···	···	39.6	5.89	5.75
Fe I	5905.67[a]	4.652	-0.690	4,4	54.7	6.80	6.84	···	···	···	···	···	···	···	···	···	···	···	···	8.66	6.08	6.06	22.2	6.19	6.05
Fe I	5934.66[a]	3.929	-1.070	4,4	97.8	7.21	7.24	51.7	6.43	6.31	···	···	···	···	···	···	140	8.08	7.96	···	···	···	···	···	···
Fe I	5943.58[a]	2.198	-4.456	4,4	31.2	7.02	6.99	26.7	7.00	6.86	···	···	···	···	···	···	···	···	···	···	···	···	···	···	···

Continued on next page

Table 2.3 – continued from previous page

					NGC 104			NGC 362			NGC 2808			NGC 6093			NGC 6388			NGC 6397			NGC 6752		
Sp.	λ	EP	$log(gf)$	Ref.	EW	$log\epsilon_p$	$log\epsilon_t$	EW	$log\epsilon_p$	$log\epsilon_t$	EW	$log\epsilon_p$	$log\epsilon_t$	EW	$log\epsilon_p$	$log\epsilon_t$	EW	$log\epsilon_p$	$log\epsilon_t$	EW	$log\epsilon_p$	$log\epsilon_t$	EW	$log\epsilon_p$	$log\epsilon_t$
Fe I	5975.35[a]	4.076	-0.545	3,	35.3	5.55	5.59	19.6	5.22	5.13	···	···	···	···	···	···	···	···	···	···	···	···	···	···	···
Fe I	5976.78[a]	3.943	-1.503	4,4	56.8	6.81	6.85	37.9	6.54	6.44	42.9	6.59	6.54	···	···	···	88.1	7.52	7.49	···	···	···	28.3	6.35	6.17
Fe I	6003.01	3.882	-1.120	4,4	85.3	6.93	6.98	54.9	6.49	6.36	71.2	6.76	6.70	···	···	···	116	7.64	7.57	···	···	···	39.5	6.19	6.00
Fe I	6012.21[a]	2.223	-4.038	4,4	37.2	6.78	6.76	28.8	6.67	6.53	···	···	···	···	···	···	···	···	···	···	···	···	···	···	···
Fe I	6024.06[a]	4.549	-0.120	4,4	90.8	6.83	6.86	66.4	6.50	6.38	69.4	6.50	6.44	39.6	5.72	5.86	103	7.15	7.10	···	···	···	40.9	5.98	5.83
Fe I	6027.05[a]	4.076	-1.089	4,4	58.5	6.58	6.63	40.8	6.35	6.24	···	···	···	···	···	···	72.2	6.92	6.92	···	···	···	21.8	5.90	5.73
Fe I	6065.48	2.608	-1.530	3,3	139	6.84	6.83	105	6.49	6.30	134	6.94	6.81	63.5	5.27	5.52	···	···	···	22.1	5.36	5.36	71.4	5.89	5.60
Fe I	6078.49[a]	4.796	-0.481	4,4	97.3	7.59	7.61	42.3	6.60	6.52	···	···	···	···	···	···	···	···	···	···	···	···	···	···	···
Fe I	6096.66[a]	3.984	-1.830	4,4	34.3	6.69	6.72	26.0	6.58	6.48	···	···	···	···	···	···	83.3	7.76	7.75	···	···	···	···	···	···
Fe I	6098.24[a]	4.559	-1.880	,3	···	···	···	14.9	6.96	6.89	···	···	···	···	···	···	···	···	···	···	···	···	···	···	···
Fe I	6102.17[a]	4.835	-0.657	3,	···	···	···	31.7	6.57	6.50	···	···	···	···	···	···	···	···	···	···	···	···	···	···	···
Fe I	6136.62	2.453	-1.410	3,2	···	···	···	···	···	···	···	···	···	126	6.27	6.48	···	···	···	59.0	6.08	6.08	130	6.70	6.44
Fe I	6137.70	2.588	-1.346	3,2	···	···	···	126	6.64	6.450	148	6.92	6.78	78.8	5.39	5.64	···	···	···	42.6	5.74	5.74	94.9	6.23	5.94
Fe I	6151.62[a]	2.180	-3.330	1,1	55.3	6.38	6.37	52.7	6.57	6.39	···	···	···	···	···	···	57.1	6.52	6.44	···	···	···	33.0	6.16	5.85
Fe I	6173.34	2.220	-2.863	1,1	89.1	6.70	6.71	73.7	6.64	6.45	69.3	6.44	6.35	···	···	···	118	7.36	7.28	···	···	···	43.1	6.04	5.74
Fe I	6180.21	2.730	-2.628	1,1	80.8	6.90	6.92	55.0	6.59	6.43	46.6	6.30	6.23	···	···	···	103	7.43	7.38	···	···	···	···	···	···
Fe I	6188.00[a]	3.940	-1.673	1,1	30.4	6.38	6.41	18.2	6.11	6.02	25.2	6.28	6.24	···	···	···	···	···	···	···	···	···	31.7	6.58	6.40
Fe I	6191.57	2.433	-1.416	3,2	···	···	···	···	···	···	···	···	···	···	···	···	···	···	···	29.7	5.28	5.30	108	6.30	6.00
Fe I	6200.32	2.610	-2.386	1,1	79.0	6.49	6.51	67.6	6.50	6.32	71.3	6.48	6.39	38.7	5.54	5.74	132	7.63	7.55	···	···	···	42.2	6.00	5.73
Fe I	6213.44	2.220	-2.481	1,2	128	7.09	7.09	89.2	6.58	6.39	···	···	···	75.4	5.95	6.22	···	···	···	22.9	5.90	5.92	66.0	6.21	5.92
Fe I	6219.29	2.120	-2.448	1,2	102	6.41	6.42	85.5	6.46	6.26	81.1	6.25	6.15	48.9	5.30	5.54	118	6.93	6.85	19.2	5.72	5.74	68.7	6.22	5.92
Fe I	6226.73[a]	3.884	-2.120	4,4	23.0	6.56	6.58	···	···	···	···	···	···	···	···	···	45.5	7.14	7.14	···	···	···	···	···	···
Fe I	6229.23	2.830	-2.821	1,1	57.3	6.75	6.76	19.8	5.89	5.78	···	···	···	···	···	···	88.8	7.45	7.40	···	···	···	···	···	···
Fe I	6230.74	2.559	-1.276	3,2	···	···	···	147	6.86	6.65	148	6.78	6.65	109	5.90	6.12	···	···	···	36.1	5.46	5.46	101	6.18	5.88
Fe I	6240.65[a]	2.220	-3.212	1,1	···	···	···	44.4	6.26	6.10	···	···	···	···	···	···	···	···	···	···	···	···	···	···	···
Fe I	6246.33	3.600	-0.796	1,1	98.1	6.52	6.55	80.3	6.35	6.21	87.0	6.41	6.34	···	···	···	101	6.65	6.61	···	···	···	58.3	5.96	5.74
Fe I	6252.56	2.404	-1.767	3,2	···	···	···	98.3	6.28	6.09	···	···	···	113	6.27	6.50	···	···	···	41.2	5.92	5.94	93.7	6.32	6.01
Fe I	6254.25	2.280	-2.435	1,1	135	7.22	7.22	95.2	6.72	6.53	97.9	6.67	6.57	90.7	6.30	6.56	140	7.39	7.30	···	···	···	58.4	6.06	5.76
Fe I	6265.14	2.180	-2.532	1,1	135	7.19	7.18	85.8	6.51	6.31	99.2	6.66	6.56	52.9	5.45	5.70	···	···	···	24.6	5.96	5.98	71.3	6.33	6.02
Fe I	6270.23[a]	2.860	-2.543	1,1	58.1	6.52	6.53	34.1	6.11	5.98	56.0	6.58	6.50	···	···	···	···	···	···	···	···	···	57.7	6.82	6.56
Fe I	6297.80	2.220	-2.669	1,1	95.3	6.62	6.63	106.6	7.10	6.90	···	···	···	···	···	···	···	···	···	···	···	···	43.3	5.83	5.53
Fe I	6301.51	3.650	-0.718	1,2	131	7.09	7.09	71.9	6.14	6.00	84.1	6.32	6.25	···	···	···	···	···	···	···	···	···	68.9	6.17	5.94
Fe I	6302.49[a]	3.686	-1.131	3,	89.1	6.76	6.79	32.9	5.69	5.58	51.4	6.06	6.01	···	···	···	···	···	···	···	···	···	···	···	···
Fe I	6311.50	2.830	-3.153	1,1	64.6	7.21	7.22	···	···	···	···	···	···	···	···	···	53.5	7.04	7.00	···	···	···	21.1	6.42	6.14
Fe I	6322.69	2.590	-2.438	1,1	84.1	6.61	6.62	69.2	6.53	6.36	78.1	6.62	6.53	49.7	5.79	6.01	···	···	···	···	···	···	40.2	5.96	5.68
Fe I	6330.85[a]	4.730	-1.640	1,1	20.7	7.04	7.08	9.65	6.66	6.60	···	···	···	···	···	···	···	···	···	···	···	···	···	···	···
Fe I	6335.34	2.200	-2.175	1,1	125	6.68	6.68	100.6	6.46	6.27	104	6.43	6.32	70.0	5.48	5.74	149	7.16	7.06	24.1	5.60	5.63	66.3	5.88	5.56

Continued on next page

Table 2.3 – continued from previous page

					NGC 104			NGC 362			NGC 2808			NGC 6093			NGC 6388			NGC 6397			NGC 6752		
Sp.	λ	EP	$log(gf)$	Ref.	EW	$log\epsilon_p$	$log\epsilon_t$	EW	$log\epsilon_p$	$log\epsilon_t$	EW	$log\epsilon_p$	$log\epsilon_t$	EW	$log\epsilon_p$	$log\epsilon_t$	EW	$log\epsilon_p$	$log\epsilon_t$	EW	$log\epsilon_p$	$log\epsilon_t$	EW	$log\epsilon_p$	$log\epsilon_t$
Fe I	6336.83	3.690	-0.667	1,1	97.1	6.63	6.66	75.1	6.20	6.06	83.6	6.30	6.23	52.9	5.47	5.65	126	7.08	7.02	11.0	5.15	5.16	59.3	5.94	5.72
Fe I	6353.85	0.910	-6.360	1,1	...	...	...	11.0	6.37	6.22	...	...	...	...	...	...	...	...	...	...	...	...	...	...	...
Fe I	6355.04	2.840	-2.328	1,1	...	...	...	55.4	6.40	6.25	76.1	6.76	6.68	...	...	...	118	7.55	7.48	...	...	...	36.5	6.05	5.79
Fe I	6380.75	4.190	-1.366	1,1	59.2	6.97	7.02	24.5	6.29	6.21	...	...	...	...	...	...	88.9	7.63	7.62	...	...	...	...	...	...
Fe I	6392.54	2.280	-3.957	1,1	...	...	...	17.5	6.18	6.06	...	...	...	...	...	...	...	...	...	...	...	...	...	...	...
Fe I	6393.61	2.430	-1.576	1,2	...	...	...	125	6.58	6.39	133	6.64	6.52	92.2	5.64	5.90	...	...	...	...	...	...	102	6.30	5.98
Fe I	6400.01	3.602	-0.290	3,2	...	...	...	...	...	...	...	...	...	123	6.42	6.59	...	...	...	41.8	5.65	5.65	109	6.46	6.24
Fe I	6411.66	3.650	-0.646	1,1	121	6.83	6.84	93.9	6.52	6.37	104	6.64	6.55	65.4	5.66	5.85	139	7.22	7.14	...	...	...	59.3	5.86	5.64
Fe I	6419.96[a]	4.730	-0.183	1,1	...	...	...	58.3	6.54	6.45	59.4	6.51	6.46	...	...	...	...	...	...	...	...	...	24.9	5.81	5.67
Fe I	6421.36	2.280	-2.014	1,2	144	6.89	6.86	122	6.78	6.58	117	6.58	6.47	66.2	5.31	5.58	...	...	...	36.5	5.88	5.92	81.8	6.15	5.82
Fe I	6430.86	2.180	-1.946	1,2	...	...	...	120	6.56	6.37	120	6.48	6.36	83.1	5.48	5.76	...	...	...	26.9	5.43	5.46	87.8	6.09	5.75
Fe I	6475.63	2.560	-2.929		93.2	7.20	7.21	...	...	...	...	...	...	...	...	...	...	...	...	...	...	...	...	...	...
Fe I	6481.88	2.280	-2.985	1,1	...	...	...	...	...	...	...	...	...	...	...	...	...	...	...	...	...	...	32.3	5.90	5.58
Fe I	6494.99	2.400	-1.239	1,2	...	...	...	142	6.49	6.29	...	...	...	...	...	...	...	...	...	...	...	...	...	...	...
Fe I	6498.94	0.960	-4.675	1,1	...	...	...	63.8	6.53	6.33	...	...	...	...	...	...	81.4	6.76	6.63	...	...	...	47.3	6.34	5.93
Fe I	6518.37[a]	2.832	-2.397	1,1	86.0	6.86	6.87	52.5	6.36	6.21	98.5	7.25	7.16	...	...	...	...	...	...	...	...	...	...	...	...
Fe I	6533.94	4.540	-1.360	1,1	27.8	6.73	6.77	...	...	...	...	...	...	...	...	...	...	...	...	...	...	...	...	...	...
Fe I	6546.25	2.750	-1.536	1,1	...	...	...	107	6.57	6.39	85.4	6.03	5.94	...	...	...	...	...	...	23.6	5.50	5.52	83.2	6.21	5.92
Fe I	6569.22	4.730	-0.380	1,1	...	...	...	68.4	6.93	6.84	64.6	6.79	6.75	82.0	7.03	7.15	86.3	7.21	7.21	...	...	...	...	...	...
Fe I	6571.18	4.290	-2.950	1,1	...	...	...	...	...	...	...	...	...	...	...	...	...	...	...	...	...	...	45.4	8.56	8.38
Fe I	6574.23	0.990	-5.009	1,1	...	...	...	54.4	6.63	6.44	55.0	6.57	6.44	...	...	...	...	...	...	...	...	...	...	...	...
Fe I	6575.04	2.590	-2.714	1,1	...	...	...	52.7	6.37	6.21	17.2	5.29	5.20	41.0	5.82	6.01	...	...	...	...	...	...	...	...	...
Fe I	6593.87	2.430	-2.377	1,1	112	6.83	6.83	...	...	...	...	...	...	...	...	...	...	...	...	...	...	...	63.1	6.22	5.92
Fe I	6597.56[a]	4.770	-0.970	1,1	...	...	...	...	...	...	22.6	6.48	6.45	...	...	...	...	...	...	...	...	...	...	...	...
Fe I	6608.04	2.270	-3.939	1,1	51.6	6.99	6.96	...	...	...	25.0	6.36	6.26	...	...	...	...	...	...	...	...	...	31.7	6.80	6.48
Fe I	6625.04	1.010	-5.277	1,1	86.7	7.41	7.36	48.2	6.74	6.56	...	...	...	...	...	...	...	...	...	...	...	...	48.3	7.01	6.59
Fe I	6627.56	4.530	-1.559		24.6	6.81	6.84	...	...	...	...	...	...	...	...	...	...	...	...	...	...	...	...	...	...
Fe I	6646.97	2.600	-3.917		26.2	6.78	6.74	...	...	...	...	...	...	...	...	...	...	...	...	...	...	...	...	...	...
Fe I	6648.12	1.010	-5.730	1,1	37.4	6.78	6.67	...	...	...	28.9	6.56	6.42	...	...	...	...	...	...	...	...	...	...	...	...
Fe I	6678.00	2.690	-1.395	1,1	144	6.76	6.75	130	6.74	6.56	115	6.38	6.28	84.3	5.56	5.79	...	...	...	20.3	5.17	5.20	78.5	5.89	5.58
Fe I	6703.58	2.760	-3.059	1,1	48.8	6.66	6.65	34.0	6.41	6.29	...	...	...	...	...	...	44.4	6.63	6.57	...	...	...	24.2	6.29	6.00
Fe I	6705.10	4.610	-1.060	1,1	26.2	6.43	6.47	...	...	...	...	...	...	...	...	...	...	...	...	...	...	...	...	...	...
Fe I	6710.32	1.480	-4.807	1,1	44.1	6.65	6.57	30.6	6.36	6.21	33.1	6.41	6.28	...	...	...	48.2	6.82	6.69	...	...	...	16.3	6.16	5.74
Fe I	6715.39	4.590	-1.540		33.4	7.07	7.11	...	...	...	...	...	...	...	...	...	...	...	...	38.1	5.49	5.32	...	...	...
Fe I	6726.67[a]	4.607	-1.087	1,1	52.2	7.03	7.08	19.8	6.34	6.28	...	...	...	...	...	...	...	...	...	...	...	...	...	...	...
Fe I	6730.29[a]	4.913	-1.457		...	...	...	8.47	6.60	6.55	...	...	...	...	...	...	...	...	...	...	...	...	...	...	...
Fe I	6733.15[a]	4.620	-1.479	1,1	27.2	6.90	6.94	...	...	...	...	...	...	...	...	...	13.5	6.53	6.54	...	...	...	12.1	6.52	6.36

Continued on next page

Table 2.3 – continued from previous page

					NGC 104			NGC 362			NGC 2808			NGC 6093			NGC 6388			NGC 6397			NGC 6752		
Sp.	λ	EP	$log(gf)$	Ref.	EW	$log\epsilon_p$	$log\epsilon_t$	EW	$log\epsilon_p$	$log\epsilon_t$	EW	$log\epsilon_p$	$log\epsilon_t$	EW	$log\epsilon_p$	$log\epsilon_t$	EW	$log\epsilon_p$	$log\epsilon_t$	EW	$log\epsilon_p$	$log\epsilon_t$	EW	$log\epsilon_p$	$log\epsilon_t$
Fe I	6739.52[a]	1.560	-4.801	1,1	38.3	6.61	6.52	...	...	...	...	...	...	...	...	...	41.4	6.76	6.63	...	...	...	...	...	...
Fe I	6750.16	2.420	-2.592	1,1	119	7.14	7.13	75.8	6.52	6.35	67.3	6.25	6.16	35.7	5.33	5.50	97.3	6.80	6.74	...	...	...	50.0	6.10	5.79
Fe I	6752.72	4.640	-1.263	1,1	48.5	7.17	7.22	...	...	...	...	...	...	...	...	...	44.1	7.12	7.16	...	...	...	...	...	...
Fe I	6806.86	2.730	-2.633	1,1	35.3	5.88	5.86	37.6	6.03	5.90	42.4	6.10	6.02	...	...	...	63.2	6.54	6.49	...	...	...	...	...	...
Fe I	6810.27[a]	4.590	-0.992	1,1	39.9	6.68	6.73	20.6	6.24	6.18	...	...	...	...	...	...	56.2	7.05	7.08	...	...	...	...	...	...
Fe I	6820.37[a]	4.620	-1.214	1,1	37.0	6.87	6.92	...	...	...	...	...	...	...	...	...	...	...	...	...	...	...	...	...	...
Fe I	6828.60[a]	4.640	-0.843	1,1	51.0	6.79	6.84	...	...	...	...	...	...	...	...	...	50.2	6.82	6.85	...	...	...	18.6	6.15	5.99
Fe I	6837.01[a]	4.593	-1.810	3,	...	...	...	...	...	...	...	...	...	...	...	...	15.8	6.91	6.93	...	...	...	...	...	...
Fe I	6839.84	2.560	-3.378	1,1	37.3	6.45	6.42	40.2	6.61	6.48	...	...	...	...	...	...	...	...	...	...	...	...	14.9	6.03	5.70
Fe I	6841.34	4.610	-0.733	1,1	77.4	7.16	7.22	49.3	6.71	6.63	...	...	...	...	...	...	113	7.91	7.86	...	...	...	14.4	5.85	5.69
Fe I	6842.68[a]	4.640	-1.224	1,1	...	...	...	23.0	6.60	6.54	...	...	...	...	...	...	...	...	...	...	...	...	...	...	...
Fe I	6843.66[a]	3.650	-0.863	1,1	49.7	5.58	5.60	37.2	5.41	5.31	...	...	...	...	...	...	...	...	...	...	...	...	25.1	5.19	4.97
Fe I	6851.65	1.600	-5.247	1,1	27.9	6.81	6.71	...	...	...	...	...	...	...	...	...	...	...	...	...	...	...	12.1	6.56	6.14
Fe I	6855.16[a]	4.559	-0.741	4,4	74.1	7.04	7.10	...	...	...	51.8	6.66	6.63	...	...	...	...	...	...	...	...	...	...	...	...
Fe I	6857.25[a]	4.076	-2.050	4,4	35.8	6.99	7.03	...	...	...	...	...	...	...	...	...	...	...	...	...	...	...	...	...	...
Fe I	6858.16	4.590	-0.939	1,1	45.4	6.72	6.77	...	...	...	...	...	...	...	...	...	...	...	...	...	...	...	...	...	...
Fe I	6911.52[a]	2.420	-3.967	1,1	...	...	...	27.0	6.62	6.50	...	...	...	...	...	...	...	...	...	...	...	...	...	...	...
Fe I	6916.68[a]	4.154	-1.359	1,1	...	...	...	43.3	6.65	6.56	...	...	...	...	...	...	...	...	...	...	...	...	...	...	...
Fe I	6978.86	2.480	-2.465	1,1	...	...	...	94.8	6.79	6.62	106	6.93	6.84	45.2	5.46	5.66	...	...	...	...	...	...	...	...	...
Fe I	6988.52	2.404	-3.519		77.8	7.21	7.19	...	...	...	...	...	...	...	...	...	...	...	...	...	...	...	...	...	...
Fe I	7022.96	4.190	-1.148		72.8	6.96	7.01	...	...	...	...	...	...	...	...	...	...	...	...	...	...	...	...	...	...
Fe I	7068.42	4.070	-1.319	1,1	128	8.03	8.03	33.3	6.26	6.18	44.9	6.48	6.44	...	...	...	...	...	...	...	...	...	...	...	...
Fe I	7069.53[a]	2.559	-4.340	3,3	...	...	...	...	...	...	21.0	6.94	6.85	...	...	...	...	...	...	...	...	...	...	...	...
Fe I	7086.72[a]	3.603	-2.642	3,	...	...	...	14.6	6.40	6.32	...	...	...	...	...	...	...	...	...	...	...	...	...	...	...
Fe I	7090.39	4.230	-1.109	1,1	78.0	7.07	7.11	50.9	6.64	6.55	...	...	...	...	...	...	122	7.96	7.92	...	...	...	40.5	6.48	6.30
Fe I	7112.17	2.990	-3.001	1,1	...	...	...	23.0	6.26	6.16	29.9	6.44	6.36	...	...	...	...	...	...	...	...	...	...	...	...
Fe I	7114.55[a]	2.692	-3.937	4,4	...	...	...	...	...	...	...	...	...	...	...	...	...	...	...	...	...	...	...	...	...
Fe I	7130.92[a]	4.300	-0.708	1,1	...	...	...	67.9	6.67	6.57	98.3	7.23	7.16	...	...	...	...	...	...	...	...	...	24.8	5.78	5.59
Fe I	7132.98[a]	4.060	-1.635	1,1	58.9	7.03	7.07	...	...	...	...	...	...	...	...	...	62.5	7.15	7.16	...	...	...	...	...	...
Fe I	7142.52	4.930	-1.017	1,1	...	...	...	...	...	...	...	...	...	...	...	...	...	...	...	...	...	...	...	...	...
Fe I	7145.31	4.610	-1.240	1,1	77.8	7.65	7.70	...	...	...	...	...	...	...	...	...	...	...	...	...	...	...	...	...	...
Fe I	7151.46	2.480	-3.657	1,1	69.9	7.26	7.25	...	...	...	25.3	6.29	6.19	...	...	...	...	...	...	...	...	...	...	...	...
Fe I	7155.63	4.990	-1.017	1,1	...	...	...	...	...	...	...	...	...	...	...	...	87.4	8.12	8.13	...	...	...	...	...	...
Fe I	7219.68[a]	4.076	-1.617	1,1	81.1	7.44	7.47	17.6	6.09	6.02	...	...	...	...	...	...	...	...	...	...	...	...	...	...	...
Fe I	7228.70	2.750	-3.307	1,1	78.5	7.41	7.41	...	...	...	...	...	...	...	...	...	...	...	...	...	...	...	...	...	...
Fe I	7401.68[a]	4.186	-1.690	3,	72.4	7.46	6.83	44.8	7.00	6.92	...	...	...	...	...	...	...	...	...	...	...	...	...	...	...
Fe I	7411.16	4.280	-0.287	1,1	119	7.04	7.06	...	...	...	51.3	5.80	5.77	...	...	...	86.1	6.49	6.50	...	...	...	65.8	6.24	6.04

Continued on next page

Table 2.3 – continued from previous page

					NGC 104			NGC 362			NGC 2808			NGC 6093			NGC 6388			NGC 6397			NGC 6752		
Sp.	λ	EP	$log(gf)$	Ref.	EW	$log\epsilon_p$	$log\epsilon_t$	EW	$log\epsilon_p$	$log\epsilon_t$	EW	$log\epsilon_p$	$log\epsilon_t$	EW	$log\epsilon_p$	$log\epsilon_t$	EW	$log\epsilon_p$	$log\epsilon_t$	EW	$log\epsilon_p$	$log\epsilon_t$	EW	$log\epsilon_p$	$log\epsilon_t$
Fe I	7430.54[a]	2.588	-3.860	3,3	···	···	···	···	···	···	···	···	···	···	···	···	20.0	6.52	6.44	···	···	···	···	···	···
Fe I	7445.76	4.260	0.053	1,1	126	6.81	6.81	86.3	6.20	6.10	89.5	6.21	6.15	52.2	5.30	5.44	102	6.44	6.43	···	···	···	72.8	6.02	5.82
Fe I	7461.53[a]	2.560	-3.507	1,1	···	···	···	35.4	6.52	6.39	···	···	···	···	···	···	···	···	···	···	···	···	32.7	6.65	6.33
Fe I	7491.65[a]	4.301	-1.067	1,1	100	7.50	7.53	···	···	···	···	···	···	···	···	···	···	···	···	···	···	···	···	···	···
Fe I	7531.15	4.370	-0.557	1,1	···	···	···	···	···	···	···	···	···	···	···	···	···	···	···	38.0	6.49	6.52	···	···	···
Fe II	4178.86	2.583	-2.489	3,2	···	···	···	···	···	···	···	···	···	···	···	···	···	···	···	···	···	···	69.5	6.38	6.07
Fe II	4416.83	2.778	-2.580	3,2	···	···	···	80.0	6.48	6.53	···	···	···	···	···	···	···	···	···	···	···	···	···	···	···
Fe II	4508.29[b]	2.856	-2.318	3,2	···	···	···	101	6.97	7.02	61.4	6.00	6.04	···	···	···	99.3	7.08	7.35	20.9	5.33	5.15	67.7	6.33	6.03
Fe II	4515.34[b]	2.844	-2.422	3,2	···	···	···	63.9	6.11	6.18	129	7.67	7.67	63.8	6.05	6.01	···	···	···	···	···	···	···	···	···
Fe II	4520.23[b]	2.807	-2.590	3,2	···	···	···	···	···	···	76.7	6.60	6.64	···	···	···	93.5	7.15	7.44	···	···	···	83.1	6.94	6.65
Fe II	4522.64	2.844	-2.050	3,2	···	···	···	···	···	···	···	···	···	···	···	···	···	···	···	36.9	5.57	5.33	···	···	···
Fe II	4583.84[b]	2.807	-1.890	3,2	···	···	···	122	6.94	6.95	···	···	···	73.2	5.70	5.67	···	···	···	47.9	5.67	5.41	67.4	5.83	5.54
Fe II	4620.52	2.828	-3.287	3,2	···	···	···	49.8	6.59	6.65	···	···	···	···	···	···	···	···	···	···	···	···	···	···	···
Fe II	4923.93[b]	2.891	-1.307	3,2	126	6.54	6.70	146	6.76	6.75	150	6.80	6.80	91.1	5.54	5.55	···	···	···	50.6	5.17	4.93	128	6.54	6.34
Fe II	5018.45[b]	2.891	-1.292	3,2	···	···	···	···	···	···	···	···	···	118	6.06	6.11	···	···	···	···	···	···	···	···	···
Fe II	5197.58[b]	3.230	-2.167	3,2	77.0	6.73	6.96	104	7.14	7.22	121	7.51	7.56	···	···	···	···	···	···	···	···	···	63.4	6.31	6.04
Fe II	5234.63	3.221	-2.268	3,2	···	···	···	···	···	···	···	···	···	···	···	···	···	···	···	23.6	5.62	5.48	52.1	6.12	5.86
Fe II	5276.00[b]	3.199	-1.963	3,2	···	···	···	···	···	···	138	7.55	7.58	69.4	5.90	5.92	···	···	···	18.6	5.12	4.99	83.5	6.54	6.27
Fe II	5316.62[b]	3.153	-1.889	3,2	122	7.26	7.45	138	7.42	7.44	127	7.24	7.29	75.7	5.92	5.92	···	···	···	27.4	5.29	5.14	109	6.97	6.73
Fe II	5534.85	3.245	-2.790	3,2	72.7	7.16	7.42	61.8	6.72	6.82	···	···	···	···	···	···	···	···	···	···	···	···	43.2	6.42	6.17
Fe II	6238.39	3.889	-2.630	3,3	42.8	7.11	7.34	35.3	6.58	6.69	···	···	···	···	···	···	45.6	7.12	7.49	···	···	···	···	···	···
Fe II	6247.56[b]	3.892	-2.380	4,4	33.4	6.57	6.79	34.5	6.27	6.38	27.0	6.10	6.20	···	···	···	57.0	7.09	7.47	···	···	···	···	···	···
Fe II	6416.93	3.890	-2.740	1,1	32.9	6.91	7.14	25.0	6.47	6.57	16.3	6.22	6.31	···	···	···	···	···	···	···	···	···	17.3	6.30	6.10
Fe II	6432.68[b]	2.890	-3.550	1,1	20.0	6.31	6.518	21.6	6.08	6.15	19.4	6.03	6.10	···	···	···	39.1	6.82	7.15	···	···	···	15.1	5.92	5.68
Fe II	6456.39[b]	3.903	-2.075	3,2	52.7	6.80	7.06	44.1	6.30	6.42	···	···	···	···	···	···	···	···	···	9.92	5.46	5.39	54.9	6.64	6.40
Fe II	6516.08	2.891	-3.410	3,	···	···	···	35.5	6.31	6.39	···	···	···	···	···	···	···	···	···	···	···	···	···	···	···

Table 2.4: The non-Fe line list, their measured EWs, and their calculated line abundances for the training set clusters. For a description of the table's organization, see Table 2.3. Lines that have wavelengths marked with a superscript "h" were synthesized using hyperfine structure considerations. Each EW is annotated with an *A*, *B*, or *C* line quality rank, which corresponds to the relative quality of the line profile from which the EW was measured. This ranking system is described in § 2.4. In order to avoid the worst effects of line blending, only lines ranked *A* or *B* are adopted as the final line abundances for any given cluster. Meanwhile, in order to avoid the effects of line saturation, only lines with EW $\leq$ 150 mÅ are adopted as the final line abundances of any given cluster.

					NGC 104			NGC 362			NGC 2808			NGC 6093			NGC 6388			NGC 6397			NGC 6752		
Sp.	λ	EP	$log(gf)$	Ref.	EW	$log\epsilon_p$	$log\epsilon_t$	EW	$log\epsilon_p$	$log\epsilon_t$	EW	$log\epsilon_p$	$log\epsilon_t$	EW	$log\epsilon_p$	$log\epsilon_t$	EW	$log\epsilon_p$	$log\epsilon_t$	EW	$log\epsilon_p$	$log\epsilon_t$	EW	$log\epsilon_p$	$log\epsilon_t$
Al I	3944.02^h	0.000	-0.638	3,2	... ^{C}	...	...	... ^{C}	...	...	... ^{C}	...	...	... ^{C}	...	...	... ^{C}	...	...	... ^{C}	...	...	... ^{C}	...	...
Al I	3961.54^h	0.014	-0.336	3,2	... ^{C}	...	...	... ^{C}	...	...	... ^{C}	...	...	... ^{C}	...	...	... ^{C}	...	...	... ^{C}	...	...	... ^{C}	...	...
Al I	6696.02	3.140	-1.481	1,1	59.1^A	6.20	6.13	23.6^A	5.59	5.49	46.7^B	6.07	5.99	... ^{C}	...	...	87.4^A	6.69	6.56	... ^{C}	...	...	23.0^B	5.71	5.56
Al I	6698.67	3.140	-1.782	1,1	38.9^A	6.13	6.05	... ^{C}	...	...	... ^{C}	...	...	... ^{C}	...	...	... ^{C}	...	...	... ^{C}	...	...	... ^{C}	...	...
Ba II	4130.66^h	2.722	0.440	3,2	... ^{C}	...	...	... ^{C}	...	...	... ^{C}	...	...	... ^{C}	...	...	... ^{C}	...	...	... ^{C}	...	...	... ^{C}	...	...
Ba II	4554.04^h	0.000	0.163	3,2	230^A	1.66	1.72	180^A	1.42	1.26	179^A	1.38	1.26	158^A	0.91	0.98	... ^{C}	...	...	54.4^A	0.06	-0.26	149^A	1.19	0.84
Ba II	4934.10^h	0.000	-0.157	3,2	237^B	1.87	1.91	193^A	1.62	1.47	204^B	1.70	1.58	149^A	0.80	0.88	... ^{C}	...	...	53.2^A	0.09	-0.12	157^A	1.35	0.96
Ba II	5853.69^h	0.604	-1.010	3,2	82.2^A	1.34	1.42	83.5^A	1.37	1.30	85.1^A	1.38	1.14	79.6^A	0.92	1.10	144^B	2.80	2.78	19.2^B	0.44	0.34	72.9^B	1.38	0.95
Ba II	6141.71^h	0.704	-0.077	1,1	148^A	1.86	1.90	144^A	1.72	1.63	131^A	1.48	1.41	109^A	0.70	0.86	139^A	1.82	1.81	47.7^B	0.54	0.42	103^A	1.19	0.75
Ba II	6496.91^h	0.604	-0.377	1,1	159^B	1.99	2.03	131^A	1.55	1.47	112^A	1.17	1.11	169^B	1.71	1.89	... ^{C}	...	...	38.9^B	0.40	0.11	153^B	2.02	1.66
Ca I	4226.74	0.000	0.243	3,2	... ^{C}	...	...	... ^{C}	...	...	... ^{C}	...	...	319^B	4.47	4.68	... ^{C}	...	...	... ^{C}	...	...	... ^{C}	...	...
Ca I	4283.01	1.886	-0.220	3,2	... ^{C}	...	...	100^B	5.46	5.19	... ^{C}	...	...	... ^{C}	...	...	... ^{C}	...	...	... ^{C}	...	...	99.4^A	5.42	5.24
Ca I	4318.66	1.899	-0.210	3,2	166^A	5.97	5.90	119^A	5.78	5.49	... ^{C}	...	...	43.4^B	4.01	4.10	169^B	6.15	5.82	... ^{C}	...	...	111^A	5.59	5.44
Ca I	4425.44	1.879	-0.358	3,2	... ^{C}	...	...	109^A	5.68	5.41	... ^{C}	...	...	... ^{C}	...	...	... ^{C}	...	...	... ^{C}	...	...	105^A	5.59	5.43
Ca I	4435.68	1.886	-0.010	3,2	... ^{C}	...	...	... ^{C}	...	...	... ^{C}	...	...	... ^{C}	...	...	... ^{C}	...	...	... ^{C}	...	...	104^A	5.23	5.06
Ca I	4454.79	1.899	0.260	3,2	... ^{C}	...	...	... ^{C}	...	...	295^B	6.45	6.22	... ^{C}	...	...	... ^{C}	...	...	... ^{C}	...	...	140^B	5.42	5.36
Ca I	5260.39	2.521	-1.720	3,3	... ^{C}	...	...	... ^{C}	...	...	... ^{C}	...	...	... ^{C}	...	...	... ^{C}	...	...	... ^{C}	...	...	... ^{C}	...	...
Ca I	5265.56	2.523	-0.260	3,2	... ^{C}	...	...	... ^{C}	...	...	... ^{C}	...	...	... ^{C}	...	...	... ^{C}	...	...	... ^{C}	...	...	95.0^A	5.70	5.54
Ca I	5349.47	2.709	-0.310	3,2	110^A	5.89	5.82	88.0^A	5.74	5.56	112^B	6.14	5.99	39.4^B	4.60	4.73	175^B	6.90	6.60	... ^{C}	...	...	48.3^A	4.99	4.84
Ca I	5581.96	2.523	-0.555	3,2	106^A	5.79	5.73	74.0^A	5.44	5.27	64.1^A	5.16	5.06	53.1^B	4.87	5.02	97.9^A	5.70	5.53	... ^{C}	...	...	41.5^B	4.84	4.67
Ca I	5588.76	2.526	0.358	3,2	149^A	5.68	5.56	126^A	5.53	5.32	124^A	5.44	5.28	75.0^A	4.44	4.56	... ^{C}	...	...	33.7^B	4.25	4.22	101^A	5.13	4.98
Ca I	5590.11	2.521	-0.571	3,2	100^A	5.70	5.66	... ^{C}	...	...	81.9^A	5.53	5.42	50.9^A	4.84	4.98	... ^{C}	...	...	... ^{C}	...	...	53.8^A	5.12	4.95
Ca I	5601.28	2.526	-0.690	3,2	98.8^A	5.79	5.73	81.1^A	5.72	5.54	97.3^A	5.97	5.84	... ^{C}	...	...	156^B	6.84	6.56	... ^{C}	...	...	56.5^A	5.30	5.13
Ca I	5857.46	2.933	0.240	3,2	186^A	6.48	6.38	121^A	5.94	5.74	151^A	6.31	6.13	108^B	5.57	5.68	204^A	6.75	6.45	... ^{C}	...	...	101^A	5.60	5.48
Ca I	5867.57	2.933	-0.801	3,3	53.7^A	6.31	6.25	... ^{C}	...	...	... ^{C}	...	...	... ^{C}	...	...	... ^{C}	...	...	... ^{C}	...	...	... ^{C}	...	...
Ca I	6102.73	1.879	-0.790	3,2	... ^{C}	...	...	141^B	6.06	5.84	198^A	6.67	6.46	96.7^A	5.10	5.27	300^A	7.18	6.83	43.6^A	4.93	4.93	101^A	5.50	5.25
Ca I	6122.23	1.886	-0.320	3,2	237^A	6.28	6.14	168^A	5.96	5.73	162^A	5.83	5.64	109^A	4.88	5.04	251^A	6.48	6.14	46.0^A	4.52	4.53	120^A	5.35	5.14
Ca I	6156.02	2.521	-2.497	3,3	... ^{C}	...	...	... ^{C}	...	...	... ^{C}	...	...	... ^{C}	...	...	... ^{C}	...	...	... ^{C}	...	...	... ^{C}	...	...
Ca I	6161.30	2.523	-1.293	3,3	... ^{C}	...	...	... ^{C}	...	...	... ^{C}	...	...	... ^{C}	...	...	... ^{C}	...	...	... ^{C}	...	...	52.8^A	5.75	5.56

Continued on next page

Table 2.4 – continued from previous page

					NGC 104			NGC 362			NGC 2808			NGC 6093			NGC 6388			NGC 6397			NGC 6752		
Sp.	λ	EP	$log(gf)$	Ref.	EW	$log\epsilon_p$	$log\epsilon_t$	EW	$log\epsilon_p$	$log\epsilon_t$	EW	$log\epsilon_p$	$log\epsilon_t$	EW	$log\epsilon_p$	$log\epsilon_t$	EW	$log\epsilon_p$	$log\epsilon_t$	EW	$log\epsilon_p$	$log\epsilon_t$	EW	$log\epsilon_p$	$log\epsilon_t$
Ca I	6162.18	1.899	-0.090	3,2	... [C]	...	...	178[A]	5.85	5.61	170[B]	5.70	5.51	108[B]	4.64	4.80	... [C]	...	...	60.1[A]	4.61	4.61	145[A]	5.47	5.32
Ca I	6166.44	2.52	-1.142	1,1	86.3[A]	5.90	5.82	46.6[A]	5.33	5.18	70.8[B]	5.77	5.66	... [C]	...	...	... [C]	...	...	... [C]	...	...	... [C]	...	...
Ca I	6169.04	2.520	-0.797	1,1	... [C]	...	...	... [C]	...	...	... [C]	...	...	... [C]	...	...	... [C]	...	...	... [C]	...	...	... [C]	...	...
Ca I	6169.56	2.526	-0.478	1,1	... [C]	...	...	... [C]	...	...	... [C]	...	...	... [C]	...	...	... [C]	...	...	... [C]	...	...	... [C]	...	...
Ca I	6417.68	4.441	-2.304	3,3	... [C]	...	...	... [C]	...	...	... [C]	...	...	... [C]	...	...	... [C]	...	...	... [C]	...	...	... [C]	...	...
Ca I	6439.08	2.526	0.390	3,2	... [C]	...	...	156[A]	5.76	5.54	145[A]	5.54	5.38	106[A]	4.82	4.96	214[A]	6.20	5.89	54.3[A]	4.58	4.60	112[A]	5.15	4.97
Ca I	6449.82	2.521	-0.502	3,	... [C]	...	...	... [C]	...	...	... [C]	...	...	99.0[B]	5.56	5.70	312[B]	7.61	7.28	... [C]	...	...	74.6[B]	5.36	5.15
Ca I	6455.60	2.523	-1.290	3,2	88.5[A]	6.04	5.95	65.6[B]	5.82	5.67	... [C]	...	...	... [C]	...	...	... [C]	...	...	... [C]	...	...	29.3[A]	5.18	4.98
Ca I	6462.68	2.523	0.262	3,2	242[A]	6.39	6.26	192[A]	6.27	6.03	195[A]	6.23	6.04	... [C]	...	...	260[A]	6.61	6.29	52.4[A]	4.67	4.68	140[A]	5.64	5.54
Ca I	6464.68	2.526	-4.274	3,3	... [C]	...	...	... [C]	...	...	... [C]	...	...	... [C]	...	...	... [C]	...	...	... [C]	...	...	... [C]	...	...
Ca I	6471.66	2.526	-0.686	4,4	120[A]	6.02	5.91	90.1[A]	5.70	5.54	77.6[B]	5.40	5.28	50.0[B]	4.79	4.93	... [C]	...	...	... [C]	...	...	36.8[B]	4.76	4.57
Ca I	6493.78	2.521	-0.109	3,	144[C]	5.81	5.72	65.0[A]	4.63	4.48	... [C]	...	...	... [C]	...	...	... [C]	...	...	... [C]	...	...	... [C]	...	...
Ca I	6508.85	2.52	-2.500	1,1	... [C]	...	...	... [C]	...	...	... [C]	...	...	... [C]	...	...	... [C]	...	...	... [C]	...	...	... [C]	...	...
Ca I	6572.80	0.000	-4.310	1,1	... [C]	...	...	48.9[A]	5.22	4.99	89.0[A]	6.07	5.88	... [C]	...	...	... [C]	...	...	... [C]	...	...	... [C]	...	...
Ca I	6719.69	2.71	-2.550	1,1	... [C]	...	...	... [C]	...	...	... [C]	...	...	... [C]	...	...	... [C]	...	...	... [C]	...	...	... [C]	...	...
Ca I	7148.15	2.709	0.137	1,1	180[A]	6.14	6.03	143[A]	5.88	5.69	168[A]	6.17	6.00	88.2[A]	4.82	4.96	233[A]	6.70	6.39	... [C]	...	...	110[A]	5.47	5.28
Ca I	7326.16	2.93	-0.230	1,1	137[A]	6.19	6.06	... [C]	...	...	... [C]	...	...	107[A]	5.77	5.90	... [C]	...	...	... [C]	...	...	56.6[A]	5.11	4.93
Ce II	3999.24	0.295	0.390	3,2	... [C]	...	...	... [C]	...	...	... [C]	...	...	... [C]	...	...	... [C]	...	...	... [C]	...	...	... [C]	...	...
Ce II	4031.33	0.320	0.080	3,3	... [C]	...	...	... [C]	...	...	... [C]	...	...	... [C]	...	...	... [C]	...	...	... [C]	...	...	... [C]	...	...
Ce II	4083.23	0.701	0.940	3,2	... [C]	...	...	... [C]	...	...	... [C]	...	...	... [C]	...	...	... [C]	...	...	79.8[A]	2.76	2.36	... [C]	...	...
Ce II	4120.84	0.320	0.040	3,2	... [C]	...	...	... [C]	...	...	... [C]	...	...	... [C]	...	...	... [C]	...	...	... [C]	...	...	... [C]	...	...
Ce II	4127.38	0.684	0.760	3,2	... [C]	...	...	... [C]	...	...	... [C]	...	...	... [C]	...	...	... [C]	...	...	... [C]	...	...	... [C]	...	...
Ce II	4222.60	0.122	0.480	3,2	... [C]	...	...	... [C]	...	...	... [C]	...	...	... [C]	...	...	... [C]	...	...	... [C]	...	...	... [C]	...	...
Ce II	4562.37	0.478	0.500	3,2	... [C]	...	...	... [C]	...	...	... [C]	...	...	... [C]	...	...	... [C]	...	...	... [C]	...	...	... [C]	...	...
Ce II	4628.16	0.516	0.390	3,2	... [C]	...	...	27.0[B]	0.34	0.26	... [C]	...	...	... [C]	...	...	... [C]	...	...	... [C]	...	...	21.0[B]	0.26	-0.07
Co I	3845.47	0.923	0.010	3,2	... [C]	...	...	... [C]	...	...	... [C]	...	...	... [C]	...	...	... [C]	...	...	... [C]	...	...	... [C]	...	...
Co I	3995.32	0.923	-0.220	3,2	... [C]	...	...	... [C]	...	...	... [C]	...	...	... [C]	...	...	... [C]	...	...	... [C]	...	...	... [C]	...	...
Co I	4118.78[h]	1.049	-0.490	3,2	326[B]	5.68	5.69	... [C]	...	...	175[B]	5.12	4.95	... [C]	...	...	... [C]	...	...	... [C]	...	...	... [C]	...	...
Co I	4121.32[h]	0.923	-0.320	3,2	... [C]	...	...	88.8[A]	3.57	3.24	... [C]	...	...	... [C]	...	...	... [C]	...	...	47.3[B]	3.46	3.22	115[A]	4.22	3.84
Co I	6189.00[h]	1.710	-2.450	1,1	77.5[B]	4.84	4.82	34.7[A]	4.20	4.08	... [C]	...	...	... [C]	...	...	... [C]	...	...	... [C]	...	...	... [C]	...	...
Co I	6678.85	1.96	-2.680	1,1	... [C]	...	...	... [C]	...	...	... [C]	...	...	... [C]	...	...	... [C]	...	...	... [C]	...	...	... [C]	...	...
Co I	6814.94[h]	1.956	-1.900	1,1	46.0[A]	4.16	4.12	33.9[A]	3.93	3.82	41.5[A]	4.08	3.98	... [C]	...	...	71.5[A]	4.65	4.57	... [C]	...	...	... [C]	...	...
Co I	7052.87[h]	1.956	-1.620	1,1	108[A]	5.20	5.19	64.9[A]	4.63	4.48	64.9[B]	4.57	4.48	... [C]	...	...	... [C]	...	...	... [C]	...	...	... [C]	...	...
Co I	7417.39	2.040	-2.070	1,1	... [C]	...	...	... [C]	...	...	... [C]	...	...	... [C]	...	...	... [C]	...	...	... [C]	...	...	... [C]	...	...
Cr I	4254.35	0.000	-0.114	3,2	342[B]	4.36	4.22	153[A]	3.80	3.49	... [C]	...	...	... [C]	...	...	304[B]	4.33	3.97	... [C]	...	...	165[A]	4.063	3.80
Cr I	4274.81	0.000	-0.231	3,2	308[B]	4.36	4.21	205[B]	4.28	3.98	202[B]	4.18	3.93	141[B]	3.78	3.86	... [C]	...	...	... [C]	...	...	158[B]	4.12	3.85
Cr I	4289.73	0.000	-0.361	3,2	842[B]	5.44	5.29	... [C]	...	...	... [C]	...	...	... [C]	...	...	... [C]	...	...	... [C]	...	...	... [C]	...	...

Continued on next page

Table 2.4 – continued from previous page

					NGC 104			NGC 362			NGC 2808			NGC 6093			NGC 6388			NGC 6397			NGC 6752		
Sp.	λ	EP	$log(gf)$	Ref.	EW	$log\epsilon_p$	$log\epsilon_t$	EW	$log\epsilon_p$	$log\epsilon_t$	EW	$log\epsilon_p$	$log\epsilon_t$	EW	$log\epsilon_p$	$log\epsilon_t$	EW	$log\epsilon_p$	$log\epsilon_t$	EW	$log\epsilon_p$	$log\epsilon_t$	EW	$log\epsilon_p$	$log\epsilon_t$
Cr I	5206.04	0.941	0.019	3,2	378^A	5.26	5.06	223^A	4.90	4.63	226^A	4.88	4.63	148^A	4.16	4.33	349^A	5.29	4.92	19.0^B	2.48	2.47	147^A	4.45	4.21
Cr I	5208.43	0.941	0.158	3,2	457^A	5.31	5.11	260^A	4.95	4.68	272^A	4.97	4.71	194^A	4.43	4.61	419^A	5.34	4.97	65.4^B	3.69	3.64	184^A	4.63	4.43
Cr I	5345.81	1.004	-0.980	3,2	156^A	5.09	4.95	95.9^A	4.50	4.23	99.1^A	4.44	4.27	55.1^A	3.26	3.56	176^A	5.41	5.09	12.9^B	3.24	3.26	71.8^A	4.14	3.80
Cr I	5409.80	1.030	-0.720	3,2	180^B	5.10	4.94	120^A	4.68	4.41	145^B	4.96	4.73	103^A	4.14	4.36	205^B	5.42	5.08	23.9^B	3.46	3.46	86.4^A	4.22	3.88
Cr I	6330.09	0.941	-2.920	1,1	61.5^A	4.91	4.75	40.8^A	4.59	4.38	53.4^B	4.89	4.71	... ^{C}	...	...	87.6^A	5.50	5.26	... ^{C}	...	...	... ^{C}	...	...
Cr I	6881.72	3.44	-0.450	1,1	... ^{C}	...	...	... ^{C}	...	...	... ^{C}	...	...	... ^{C}	...	...	... ^{C}	...	...	... ^{C}	...	...	... ^{C}	...	...
Cr I	7400.23	2.900	-0.111	1,1	104^A	5.23	5.12	87.8^B	5.13	4.96	52.0^B	4.38	4.25	... ^{C}	...	...	108^B	5.36	5.18	... ^{C}	...	...	47.2^A	4.54	4.28
Cr I	7462.34	2.914	-0.010	1,1	... ^{C}	...	...	75.9^B	4.80	4.64	... ^{C}	...	...	... ^{C}	...	...	... ^{C}	...	...	... ^{C}	...	...	70.5^B	4.93	4.66
Cu I	5782.14^h	1.642	-1.720	3,3	108^A	3.41	3.45	45.0^A	2.61	2.48	58.5^A	2.80	2.72	... ^{C}	...	...	... ^{C}	...	...	... ^{C}	...	...	19.8^B	2.186	1.879
Dy II	4073.12	0.538	-0.27	3,2	... ^{C}	...	...	... ^{C}	...	...	... ^{C}	...	...	... ^{C}	...	...	... ^{C}	...	...	... ^{C}	...	...	... ^{C}	...	...
Dy II	4103.32	0.103	-0.42	3,2	... ^{C}	...	...	... ^{C}	...	...	... ^{C}	...	...	... ^{C}	...	...	... ^{C}	...	...	... ^{C}	...	...	... ^{C}	...	...
Eu II	3819.67	0.000	0.491	3,2	... ^{C}	...	...	... ^{C}	...	...	... ^{C}	...	...	... ^{C}	...	...	... ^{C}	...	...	... ^{C}	...	...	... ^{C}	...	...
Eu II	3907.10	0.207	0.196	3,2	... ^{C}	...	...	... ^{C}	...	...	... ^{C}	...	...	... ^{C}	...	...	... ^{C}	...	...	... ^{C}	...	...	... ^{C}	...	...
Eu II	4129.73^h	0.000	0.204	3,2	... ^{C}	...	...	... ^{C}	...	...	... ^{C}	...	...	... ^{C}	...	...	... ^{C}	...	...	... ^{C}	...	...	... ^{C}	...	...
Eu II	4205.05	0.000	0.117	3,2	... ^{C}	...	...	... ^{C}	...	...	... ^{C}	...	...	... ^{C}	...	...	... ^{C}	...	...	... ^{C}	...	...	... ^{C}	...	...
Eu II	4435.58	0.207	-0.085	3,3	... ^{C}	...	...	... ^{C}	...	...	... ^{C}	...	...	... ^{C}	...	...	... ^{C}	...	...	... ^{C}	...	...	97.3^B	1.79	1.39
Eu II	4522.57	0.207	-0.678	3,2	... ^{C}	...	...	... ^{C}	...	...	... ^{C}	...	...	... ^{C}	...	...	... ^{C}	...	...	... ^{C}	...	...	62.4^B	1.41	0.99
Eu II	6437.70	1.320	-0.273	3,3	... ^{C}	...	...	... ^{C}	...	...	... ^{C}	...	...	... ^{C}	...	...	... ^{C}	...	...	... ^{C}	...	...	... ^{C}	...	...
Eu II	6645.13^h	1.380	0.204	1,1	19.5^A	0.06	0.10	... ^{C}	...	...	... ^{C}	...	...	... ^{C}	...	...	... ^{C}	...	...	... ^{C}	...	...	14.6^B	-0.143	-0.418
La II	3995.75	0.173	0.190	3,2	... ^{C}	...	...	... ^{C}	...	...	... ^{C}	...	...	... ^{C}	...	...	... ^{C}	...	...	... ^{C}	...	...	... ^{C}	...	...
La II	4086.71	0.000	0.060	3,2	... ^{C}	...	...	... ^{C}	...	...	... ^{C}	...	...	... ^{C}	...	...	... ^{C}	...	...	... ^{C}	...	...	... ^{C}	...	...
La II	4123.23	0.321	0.500	3,2	... ^{C}	...	...	72.4^B	0.76	0.64	... ^{C}	...	...	... ^{C}	...	...	... ^{C}	...	...	... ^{C}	...	...	... ^{C}	...	...
La II	4322.50	0.173	-0.500	3,2	... ^{C}	...	...	... ^{C}	...	...	... ^{C}	...	...	... ^{C}	...	...	... ^{C}	...	...	... ^{C}	...	...	... ^{C}	...	...
La II	4333.76	0.173	0.190	3,2	66.1^B	0.37	0.56	... ^{C}	...	...	... ^{C}	...	...	... ^{C}	...	...	... ^{C}	...	...	... ^{C}	...	...	... ^{C}	...	...
La II	4429.90	0.235	-0.366	3,3	... ^{C}	...	...	... ^{C}	...	...	... ^{C}	...	...	... ^{C}	...	...	... ^{C}	...	...	... ^{C}	...	...	... ^{C}	...	...
La II	6390.48^h	0.321	-1.520	1,1	25.1^A	0.74	0.70	20.4^A	0.45	0.39	... ^{C}	...	...	... ^{C}	...	...	... ^{C}	...	...	... ^{C}	...	...	... ^{C}	...	...
La II	6774.26	0.126	-1.810	1,1	24.6^B	0.68	0.62	24.1^A	0.55	0.48	... ^{C}	...	...	... ^{C}	...	...	... ^{C}	...	...	... ^{C}	...	...	... ^{C}	...	...
Mg I	3829.36	2.709	-0.208	3,2	... ^{C}	...	...	... ^{C}	...	...	... ^{C}	...	...	... ^{C}	...	...	... ^{C}	...	...	129^B	5.66	5.39	... ^{C}	...	...
Mg I	3832.31	2.712	0.145	3,2	... ^{C}	...	...	... ^{C}	...	...	... ^{C}	...	...	... ^{C}	...	...	... ^{C}	...	...	... ^{C}	...	...	... ^{C}	...	...
Mg I	3838.30	2.717	0.414	3,2	... ^{C}	...	...	... ^{C}	...	...	... ^{C}	...	...	... ^{C}	...	...	... ^{C}	...	...	... ^{C}	...	...	... ^{C}	...	...
Mg I	4167.28	4.346	-0.995	3,2	... ^{C}	...	...	138^B	7.29	7.04	... ^{C}	...	...	96.4^B	6.76	6.64	... ^{C}	...	...	... ^{C}	...	...	130^B	7.08	7.01
Mg I	4351.92	4.346	-0.520	3,2	... ^{C}	...	...	240^B	7.64	7.36	... ^{C}	...	...	... ^{C}	...	...	... ^{C}	...	...	... ^{C}	...	...	... ^{C}	...	...
Mg I	4571.10	0.000	-5.569	3,2	... ^{C}	...	...	117^B	6.91	6.61	... ^{C}	...	...	... ^{C}	...	...	... ^{C}	...	...	... ^{C}	...	...	107^A	6.94	6.57
Mg I	4703.00	4.346	-0.377	3,2	230^B	7.25	7.16	143^A	6.78	6.55	133^A	6.61	6.43	138^A	6.57	6.62	177^A	7.05	6.77	31.4^B	5.22	5.12	118^A	6.34	6.26
Mg I	5167.33	2.709	-0.856	3,2	... ^{C}	...	...	400^A	7.08	6.82	... ^{C}	...	...	293^B	6.41	6.63	... ^{C}	...	...	... ^{C}	...	...	318^A	6.63	6.63
Mg I	5172.70	2.712	-0.381	3,2	... ^{C}	...	...	441^B	6.71	6.45	... ^{C}	...	...	302^B	5.97	6.19	... ^{C}	...	...	... ^{C}	...	...	... ^{C}	...	...
Mg I	5183.62	2.717	-0.158	3,2	1057^A	7.05	6.98	556^A	6.72	6.46	576^A	6.66	6.48	353^A	5.92	6.15	942^A	7.11	6.85	... ^{C}	...	...	357^A	6.06	6.07

Continued on next page

Table 2.4 – continued from previous page

					NGC 104			NGC 362			NGC 2808			NGC 6093			NGC 6388			NGC 6397			NGC 6752		
Sp.	λ	EP	$log(gf)$	Ref.	EW	$log\epsilon_p$	$log\epsilon_t$	EW	$log\epsilon_p$	$log\epsilon_t$	EW	$log\epsilon_p$	$log\epsilon_t$	EW	$log\epsilon_p$	$log\epsilon_t$	EW	$log\epsilon_p$	$log\epsilon_t$	EW	$log\epsilon_p$	$log\epsilon_t$	EW	$log\epsilon_p$	$log\epsilon_t$
Mg I	5528.42	4.346	-0.341	3,2	254^{A}	7.36	7.29	151^{A}	6.74	6.54	157^{A}	6.76	6.60	114^{A}	6.04	6.12	247^{A}	7.48	7.22	47.7^{A}	5.43	5.37	132^{A}	6.39	6.32
Mg I	6319.24	5.11	-2.215	1,1	... ^{C}	...	...	16.4^{B}	6.89	6.83	... ^{C}	...	...	... ^{C}	...	...	... ^{C}	...	...	... ^{C}	...	...	... ^{C}	...	...
Mg I	6894.89	5.75	-2.390	1,1	... ^{C}	...	...	... ^{C}	...	...	... ^{C}	...	...	... ^{C}	...	...	... ^{C}	...	...	... ^{C}	...	...	... ^{C}	...	...
Mg I	6965.41	5.75	-1.720	1,1	... ^{C}	...	...	... ^{C}	...	...	... ^{C}	...	...	... ^{C}	...	...	... ^{C}	...	...	... ^{C}	...	...	... ^{C}	...	...
Mg I	7387.70	5.75	-0.870	1,1	61.7^{A}	7.06	7.08	... ^{C}	...	...	... ^{C}	...	...	... ^{C}	...	...	... ^{C}	...	...	... ^{C}	...	...	... ^{C}	...	...
Mn I	4030.76^{h}	0.000	-0.470	3,2	... ^{C}	...	...	... ^{C}	...	...	... ^{C}	...	...	... ^{C}	...	...	... ^{C}	...	...	61.2^{B}	2.72	2.46	... ^{C}	...	...
Mn I	4033.07^{h}	0.000	-0.618	3,2	... ^{C}	...	...	118^{B}	3.10	2.73	... ^{C}	...	...	... ^{C}	...	...	... ^{C}	...	...	48.0^{B}	2.62	2.40	142^{B}	3.65	3.24
Mn I	4034.49^{h}	0.000	-0.811	3,2	255^{B}	4.21	4.20	106^{B}	3.18	2.82	215^{B}	4.33	4.11	... ^{C}	...	...	... ^{C}	...	...	... ^{C}	...	...	141^{B}	3.90	3.52
Mn I	4041.37	2.114	0.285	3,2	... ^{C}	...	...	... ^{C}	...	...	... ^{C}	...	...	... ^{C}	...	...	... ^{C}	...	...	... ^{C}	...	...	... ^{C}	...	...
Mn I	4754.04^{h}	2.282	-0.086	3,2	116^{A}	4.10	4.14	72.2^{A}	3.77	3.54	... ^{C}	...	...	... ^{C}	...	...	144^{B}	4.73	4.57	... ^{C}	...	...	59.9^{A}	3.55	3.36
Mn I	4823.51^{h}	2.319	0.144	3,2	171^{B}	5.03	5.02	109^{A}	4.44	4.18	130^{B}	4.69	4.53	64.5^{B}	3.30	3.52	190^{B}	5.39	5.17	... ^{C}	...	...	92.1^{B}	4.18	3.93
Mn I	5399.50^{h}	3.853	-0.287	3,3	11.4^{B}	4.02	4.00	5.1^{B}	3.73	3.64	... ^{C}	...	...	... ^{C}	...	...	... ^{C}	...	...	... ^{C}	...	...	... ^{C}	...	...
Mn I	5537.75^{h}	2.187	-2.017	3,3	68.5^{A}	4.79	4.76	30.2^{B}	4.26	4.12	35.4^{A}	4.33	4.22	... ^{C}	...	...	... ^{C}	...	...	... ^{C}	...	...	33.9^{B}	4.55	4.27
Mn I	6013.50^{h}	3.072	-0.251	3,3	79.8^{A}	4.35	4.34	39.3^{B}	3.84	3.70	50.3^{A}	3.90	3.82	... ^{C}	...	...	112^{B}	4.89	4.80	... ^{C}	...	...	9.4^{B}	3.12	2.87
Mn I	6016.65^{h}	3.073	-0.216	3,3	87.4^{A}	4.46	4.46	60.0^{A}	4.24	4.09	58.9^{A}	4.14	4.06	30.0^{B}	3.48	3.62	120^{A}	5.03	4.93	... ^{C}	...	...	20.3^{B}	3.50	3.26
Na I	5889.97^{h}	0.000	0.112	3,2	825^{A}	6.35	6.25	348^{A}	5.31	5.03	414^{A}	5.49	5.25	... ^{C}	...	...	872^{B}	6.60	6.24	... ^{C}	...	...	274^{A}	4.93	4.83
Na I	5895.94^{h}	0.000	-0.191	3,2	628^{A}	6.18	6.04	311^{A}	5.42	5.16	344^{A}	5.52	5.28	... ^{C}	...	...	664^{A}	6.39	6.03	... ^{C}	...	...	241^{A}	5.03	4.91
Na I	6154.23	2.10	-1.570	1,1	53.6^{A}	5.98	5.91	24.4^{B}	5.51	5.40	... ^{C}	...	...	... ^{C}	...	...	... ^{C}	...	...	... ^{C}	...	...	... ^{C}	...	...
Na I	6160.75	2.100	-1.270	1,1	... ^{C}	...	...	... ^{C}	...	...	... ^{C}	...	...	... ^{C}	...	...	... ^{C}	...	...	... ^{C}	...	...	16.9^{B}	5.12	4.96
Nd II	3990.10	0.471	0.160	3,2	... ^{C}	...	...	... ^{C}	...	...	... ^{C}	...	...	... ^{C}	...	...	... ^{C}	...	...	... ^{C}	...	...	... ^{C}	...	...
Nd II	4061.08	0.471	0.500	3,2	... ^{C}	...	...	42.5^{B}	0.58	0.48	... ^{C}	...	...	... ^{C}	...	...	... ^{C}	...	...	... ^{C}	...	...	... ^{C}	...	...
Nd II	4358.17	0.321	-0.130	3,2	... ^{C}	...	...	... ^{C}	...	...	... ^{C}	...	...	... ^{C}	...	...	... ^{C}	...	...	... ^{C}	...	...	... ^{C}	...	...
Nd II	4462.99	0.559	0.076	3,2	... ^{C}	...	...	... ^{C}	...	...	... ^{C}	...	...	... ^{C}	...	...	... ^{C}	...	...	... ^{C}	...	...	... ^{C}	...	...
Nd II	5249.59	0.976	0.217	3,2	... ^{C}	...	...	... ^{C}	...	...	... ^{C}	...	...	... ^{C}	...	...	... ^{C}	...	...	... ^{C}	...	...	... ^{C}	...	...
Nd II	5319.82^{h}	0.550	-0.194	3,2	32.2^{A}	0.61	0.66	48.1^{A}	0.98	0.90	61.3^{A}	1.24	1.21	... ^{C}	...	...	... ^{C}	...	...	... ^{C}	...	...	13.4^{B}	0.07	-0.24
Ni I	3807.15	0.064	-1.180	3,2	... ^{C}	...	...	... ^{C}	...	...	... ^{C}	...	...	... ^{C}	...	...	... ^{C}	...	...	... ^{C}	...	...	... ^{C}	...	...
Ni I	3858.30	0.423	-0.970	3,2	... ^{C}	...	...	76.6^{B}	3.72	3.37	... ^{C}	...	...	... ^{C}	...	...	... ^{C}	...	...	... ^{C}	...	...	... ^{C}	...	...
Ni I	4231.03	3.542	0.160	3,2	... ^{C}	...	...	20.4^{B}	4.06	3.93	... ^{C}	...	...	... ^{C}	...	...	... ^{C}	...	...	... ^{C}	...	...	53.6^{A}	5.05	4.84
Ni I	4752.43	3.658	-0.700	3,2	... ^{C}	...	...	41.0^{B}	5.50	5.36	... ^{C}	...	...	... ^{C}	...	...	... ^{C}	...	...	... ^{C}	...	...	... ^{C}	...	...
Ni I	5476.92	1.826	-0.890	3,2	... ^{C}	...	...	... ^{C}	...	...	... ^{C}	...	...	... ^{C}	...	...	... ^{C}	...	...	45.8^{A}	4.42	4.37	... ^{C}	...	...
Ni I	6327.60	1.676	-3.150	1,1	52.5^{B}	5.36	5.36	42.4^{A}	5.25	5.11	... ^{C}	...	...	43.1^{B}	4.97	5.19	... ^{C}	...	...	... ^{C}	...	...	... ^{C}	...	...
Ni I	6339.12	4.150	-0.550	1,1	83.0^{A}	6.42	6.48	... ^{C}	...	...	31.4^{B}	5.36	5.34	... ^{C}	...	...	53.1^{B}	5.88	5.93	... ^{C}	...	...	... ^{C}	...	...
Ni I	6350.50	4.16	-1.810	1,1	... ^{C}	...	...	... ^{C}	...	...	... ^{C}	...	...	... ^{C}	...	...	... ^{C}	...	...	... ^{C}	...	...	... ^{C}	...	...
Ni I	6366.49	4.170	-0.950	1,1	... ^{B}	...	...	... ^{C}	...	...	25.4^{B}	5.62	5.61	... ^{C}	...	...	... ^{C}	...	...	... ^{C}	...	...	... ^{C}	...	...
Ni I	6482.81	1.935	-2.630	1,1	64.3^{A}	5.38	5.40	48.0^{B}	5.18	5.03	... ^{C}	...	...	... ^{C}	...	...	... ^{C}	...	...	... ^{C}	...	...	20.1^{B}	4.52	4.22
Ni I	6586.32	1.951	-2.810	1,1	61.9^{B}	5.52	5.53	41.6^{B}	5.19	5.06	53.9^{A}	5.42	5.34	... ^{C}	...	...	52.7^{A}	5.43	5.38	15.2^{B}	5.32	5.34	... ^{C}	...	...
Ni I	6643.64	1.676	-2.300	1,1	120^{A}	5.81	5.82	82.8^{A}	5.29	5.12	81.5^{A}	5.17	5.08	74.6^{A}	4.74	5.02	120^{B}	5.90	5.84	16.8^{B}	4.58	4.60	50.1^{A}	4.70	4.38

Continued on next page

Table 2.4 – continued from previous page

					NGC 104			NGC 362			NGC 2808			NGC 6093			NGC 6388			NGC 6397			NGC 6752		
Sp.	λ	EP	$log(gf)$	Ref.	EW	$log\epsilon_p$	$log\epsilon_t$	EW	$log\epsilon_p$	$log\epsilon_t$	EW	$log\epsilon_p$	$log\epsilon_t$	EW	$log\epsilon_p$	$log\epsilon_t$	EW	$log\epsilon_p$	$log\epsilon_t$	EW	$log\epsilon_p$	$log\epsilon_t$	EW	$log\epsilon_p$	$log\epsilon_t$
Ni I	6767.78	1.826	-2.170	1,1	100^{A}	5.47	5.48	78.0^{A}	5.21	5.04	72.8^{A}	5.02	4.92	48.8^{B}	4.24	4.45	131^{A}	6.14	6.07	... ^{C}	...	...	... ^{C}	...	...
Ni I	6772.32	3.660	-0.980	1,1	44.4^{B}	5.44	5.50	26.0^{A}	5.06	4.99	... ^{C}	...	...	... ^{C}	...	...	... ^{C}	...	...	... ^{C}	...	...	... ^{C}	...	...
Ni I	7110.90	1.935	-2.980	1,1	67.1^{A}	5.70	5.69	33.4^{B}	5.02	4.91	25.6^{B}	4.77	4.68	... ^{C}	...	...	... ^{C}	...	...	... ^{C}	...	...	41.2^{B}	5.40	5.09
Ni I	7122.21	3.542	0.040	1,1	... ^{B}	...	...	73.3^{A}	4.93	4.83	84.3^{A}	5.10	5.05	46.4^{B}	4.11	4.27	123^{B}	5.87	5.84	... ^{C}	...	...	53.6^{A}	4.60	4.39
Ni I	7291.50	1.93	-2.780	1,1	... ^{C}	...	...	... ^{C}	...	...	... ^{C}	...	...	... ^{C}	...	...	... ^{C}	...	...	... ^{C}	...	...	... ^{C}	...	...
Ni I	7393.61	3.606	-0.270	1,1	107^{A}	5.84	5.88	75.0^{A}	5.30	5.21	... ^{C}	...	...	... ^{C}	...	...	79.8^{B}	5.39	5.41	... ^{C}	...	...	41.8^{B}	4.69	4.49
Ni I	7414.51	1.986	-2.570	1,1	133^{A}	6.53	6.53	59.0^{A}	5.26	5.12	... ^{C}	...	...	36.1^{A}	4.45	4.61	... ^{C}	...	...	12.7^{B}	4.93	4.97	38.3^{A}	4.94	4.63
Ni I	7422.29	3.635	-0.140	1,1	95.3^{A}	5.52	5.56	55.6^{A}	4.81	4.73	80.8^{A}	5.28	5.23	... ^{C}	...	...	... ^{C}	...	...	14.4^{B}	4.34	4.35	27.8^{A}	4.24	4.05
Ni I	7522.78	3.660	-0.400	1,1	103^{A}	5.93	5.98	... ^{C}	...	...	... ^{C}	...	...	... ^{C}	...	...	97.3^{A}	5.91	5.92	8.7^{B}	4.35	4.36	36.3^{B}	4.74	4.55
Ni I	7525.12	3.635	-0.520	1,1	80.0^{A}	5.58	5.63	... ^{C}	...	...	46.4^{B}	4.95	4.92	... ^{C}	...	...	... ^{C}	...	...	... ^{C}	...	...	36.7^{B}	4.84	4.65
Ni I	7555.61	3.850	0.110	1,1	117^{A}	5.91	5.95	... ^{C}	...	...	56.2^{B}	4.78	4.75	... ^{C}	...	...	69.1^{B}	5.09	5.12	... ^{C}	...	...	59.7^{A}	4.97	4.77
O I	6300.31	0.000	-9.750	3,	... ^{C}	...	...	... ^{C}	...	...	... ^{C}	...	...	... ^{C}	...	...	... ^{C}	...	...	... ^{C}	...	...	... ^{C}	...	...
O I	6363.79	0.020	-10.30	3,3	... ^{C}	...	...	... ^{C}	...	...	... ^{C}	...	...	... ^{C}	...	...	... ^{C}	...	...	... ^{C}	...	...	... ^{C}	...	...
Sc I	6210.67^{h}	0.000	-1.570	1,1	... ^{C}	...	...	22.8^{A}	2.00	1.75	... ^{C}	...	...	... ^{C}	...	...	26.6^{B}	2.14	1.60	... ^{C}	...	...	... ^{C}	...	...
Sc II	4246.84^{h}	0.315	0.240	3,2	... ^{C}	...	...	146^{A}	2.23	2.12	... ^{C}	...	...	... ^{C}	...	...	... ^{C}	...	...	79.2^{B}	1.86	1.33	124^{B}	2.07	1.70
Sc II	4314.09^{h}	0.618	-0.100	3,2	... ^{C}	...	...	... ^{C}	...	...	... ^{C}	...	...	121^{B}	2.32	2.32	... ^{C}	...	...	... ^{C}	...	...	... ^{C}	...	...
Sc II	4400.40^{h}	0.605	-0.540	3,2	... ^{C}	...	...	... ^{C}	...	...	... ^{C}	...	...	... ^{C}	...	...	... ^{C}	...	...	... ^{C}	...	...	116^{B}	2.92	2.52
Sc II	4415.56^{h}	0.595	-0.670	3,2	... ^{C}	...	...	... ^{C}	...	...	... ^{C}	...	...	... ^{C}	...	...	... ^{C}	...	...	... ^{C}	...	...	... ^{C}	...	...
Sc II	4670.41	1.357	-0.580	3,2	... ^{C}	...	...	102^{A}	3.14	3.10	97.7^{A}	3.04	3.00	48.6^{A}	1.69	1.76	117^{B}	3.48	3.58	... ^{C}	...	...	63.7^{B}	2.46	2.10
Sc II	5031.02	1.357	-0.400	3,2	108^{A}	2.92	3.07	77.3^{A}	2.25	2.22	78.3^{A}	2.26	2.25	73.5^{B}	1.98	2.05	126^{B}	3.36	3.45	30.0^{B}	1.79	1.62	68.6^{A}	2.27	1.92
Sc II	5526.82^{h}	1.768	0.020	3,2	77.8^{A}	2.24	2.38	65.8^{A}	1.94	1.94	81.6^{A}	2.26	2.27	54.6^{A}	1.44	1.54	94.1^{B}	2.68	2.81	17.6^{A}	1.29	1.18	65.3^{A}	2.12	1.80
Sc II	5657.88	1.507	-0.600	3,2	... ^{C}	...	...	... ^{C}	...	...	... ^{C}	...	...	... ^{C}	...	...	... ^{C}	...	...	... ^{C}	...	...	66.3^{B}	2.43	2.09
Sc II	6604.60^{h}	1.357	-1.480	1,1	55.6^{A}	2.67	2.75	44.8^{B}	2.34	2.32	54.4^{A}	2.53	2.52	33.0^{B}	1.76	1.86	36.0^{A}	2.25	2.30	... ^{C}	...	...	... ^{C}	...	...
Si I	3905.53	1.909	-1.041	3,2	... ^{C}	...	...	280^{B}	6.56	6.26	... ^{C}	...	...	... ^{C}	...	...	... ^{C}	...	...	... ^{C}	...	...	323^{B}	6.49	6.44
Si I	4102.94	1.909	-3.100	3,2	... ^{C}	...	...	... ^{C}	...	...	... ^{C}	...	...	... ^{C}	...	...	... ^{C}	...	...	... ^{C}	...	...	... ^{C}	...	...
Si I	5690.43	4.930	-1.870	3,3	40.1^{A}	6.93	7.02	33.9^{B}	6.97	6.92	... ^{C}	...	...	... ^{C}	...	...	... ^{C}	...	...	... ^{C}	...	...	... ^{C}	...	...
Si I	6237.33	5.610	-1.010	1,1	50.5^{A}	7.14	7.23	18.4^{A}	6.44	6.42	... ^{C}	...	...	... ^{C}	...	...	... ^{C}	...	...	... ^{C}	...	...	... ^{C}	...	...
Si I	6721.84	5.86	-1.169	1,1	... ^{C}	...	...	... ^{C}	...	...	... ^{C}	...	...	... ^{C}	...	...	51.3^{B}	7.64	7.75	... ^{C}	...	...	... ^{C}	...	...
Si I	6976.50	5.95	-1.044	1,1	33.2^{A}	7.21	7.31	... ^{C}	...	...	... ^{C}	...	...	... ^{C}	...	...	... ^{C}	...	...	... ^{C}	...	...	17.4^{B}	6.78	6.71
Si I	7226.21	5.610	-1.440	1,1	31.8^{A}	7.19	7.30	9.6^{B}	6.49	6.48	... ^{C}	...	...	... ^{C}	...	...	... ^{C}	...	...	... ^{C}	...	...	32.3^{B}	7.17	7.09
Si I	7235.33	5.61	-1.460	1,1	... ^{C}	...	...	... ^{C}	...	...	... ^{C}	...	...	... ^{C}	...	...	... ^{C}	...	...	... ^{C}	...	...	... ^{C}	...	...
Si I	7405.79	5.610	-0.660	1,1	101^{A}	7.61	7.70	67.9^{B}	7.06	7.05	63.0^{A}	6.95	6.97	34.0^{A}	6.27	6.33	78.0^{B}	7.32	7.43	... ^{C}	...	...	58.5^{A}	6.87	6.79
Si I	7415.96	5.610	-0.730	1,1	... ^{C}	...	...	29.8^{B}	6.42	6.41	47.6^{B}	6.75	6.77	... ^{C}	...	...	... ^{C}	...	...	... ^{C}	...	...	60.7^{B}	6.98	6.90
Si I	7423.51	5.620	-0.580	1,1	... ^{C}	...	...	62.6^{A}	6.90	6.89	56.3^{A}	6.77	6.79	27.2^{A}	6.05	6.11	... ^{C}	...	...	... ^{C}	...	...	27.6^{A}	6.20	6.13
Sm II	4318.94	0.277	-0.27	3,2	... ^{C}	...	...	... ^{C}	...	...	... ^{C}	...	...	... ^{C}	...	...	... ^{C}	...	...	... ^{C}	...	...	... ^{C}	...	...
Sm II	4537.95	0.485	-0.23	3,2	... ^{C}	...	...	... ^{C}	...	...	... ^{C}	...	...	... ^{C}	...	...	... ^{C}	...	...	... ^{C}	...	...	... ^{C}	...	...
Sm II	4642.23	0.378	-0.520	3,2	... ^{C}	...	...	29.0^{A}	0.67	0.58	... ^{C}	...	...	... ^{C}	...	...	... ^{C}	...	...	... ^{C}	...	...	... ^{C}	...	...

Continued on next page

Table 2.4 – continued from previous page

					NGC 104			NGC 362			NGC 2808			NGC 6093			NGC 6388			NGC 6397			NGC 6752		
Sp.	λ	EP	$log(gf)$	Ref.	EW	$log\epsilon_p$	$log\epsilon_t$	EW	$log\epsilon_p$	$log\epsilon_t$	EW	$log\epsilon_p$	$log\epsilon_t$	EW	$log\epsilon_p$	$log\epsilon_t$	EW	$log\epsilon_p$	$log\epsilon_t$	EW	$log\epsilon_p$	$log\epsilon_t$	EW	$log\epsilon_p$	$log\epsilon_t$
Sr II	4077.72	0.000	0.150	3,2	... [C]	...	...	237[B]	1.85	1.68	... [C]	...	...	177[B]	1.15	1.24	... [C]	...	...	... [C]	...	...	255[A]	1.81	1.62
Sr II	4215.54[h]	0.000	-0.170	3,2	... [C]	...	...	227[B]	2.06	1.90	... [C]	...	...	... [C]	...	...	... [C]	...	...	... [C]	...	...	200[A]	1.83	1.62
Ti I	3998.64	0.048	-0.056	3,2	... [C]	...	...	... [C]	...	...	... [C]	...	...	... [C]	...	...	... [C]	...	...	... [C]	...	...	... [C]	...	...
Ti I	4527.31	0.813	-0.470	3,2	... [C]	...	...	... [C]	...	...	... [C]	...	...	... [C]	...	...	... [C]	...	...	... [C]	...	...	... [C]	...	...
Ti I	4533.25	0.848	0.476	3,2	... [C]	...	...	116[B]	4.40	4.10	... [C]	...	...	... [C]	...	...	... [C]	...	...	... [C]	...	...	76.0[B]	3.73	3.43
Ti I	4534.78	0.836	0.280	3,2	... [C]	...	...	86.4[B]	4.02	3.74	... [C]	...	...	82.9[B]	3.80	3.93	... [C]	...	...	... [C]	...	...	90.0[A]	4.24	3.92
Ti I	4535.58	0.826	0.130	3,2	... [C]	...	...	... [C]	...	...	... [C]	...	...	... [C]	...	...	... [C]	...	...	... [C]	...	...	... [C]	...	...
Ti I	4535.99	0.818	-0.035	3,3	... [C]	...	...	... [C]	...	...	... [C]	...	...	... [C]	...	...	... [C]	...	...	... [C]	...	...	... [C]	...	...
Ti I	4981.74	0.848	0.504	3,2	133[A]	4.01	3.86	131[A]	4.34	4.06	... [C]	...	...	... [C]	...	...	... [C]	...	...	... [C]	...	...	87.6[B]	3.74	3.43
Ti I	4991.07	0.836	0.380	3,2	215[B]	4.92	4.73	189[A]	5.04	4.76	140[B]	4.50	4.26	101[B]	3.80	3.97	174[B]	4.70	4.35	... [C]	...	...	122[B]	4.50	4.20
Ti I	4999.51	0.826	0.250	3,2	179[B]	4.76	4.58	119[A]	4.38	4.09	113[B]	4.18	3.97	110[A]	4.10	4.26	... [C]	...	...	21.6[B]	3.04	3.01	110[A]	4.42	4.10
Ti I	5014.24	0.813	0.110	3,2	... [C]	...	...	... [C]	...	...	... [C]	...	...	... [C]	...	...	... [C]	...	...	... [C]	...	...	107[B]	4.48	4.16
Ti I	5039.96	0.021	-1.130	3,2	... [C]	...	...	86.2[B]	4.16	3.85	... [C]	...	...	58.9[B]	3.19	3.53	... [C]	...	...	21.0[B]	3.54	3.52	71.9[A]	4.02	3.66
Ti I	5064.66	0.048	-0.991	3,2	... [C]	...	...	... [C]	...	...	... [C]	...	...	... [C]	...	...	... [C]	...	...	... [C]	...	...	... [C]	...	...
Ti I	5173.75	0.000	-1.118	3,2	... [C]	...	...	126[B]	4.70	4.40	... [C]	...	...	67.9[A]	3.30	3.64	... [C]	...	...	... [C]	...	...	88.6[A]	4.32	3.94
Ti I	5192.98	0.021	-1.006	3,2	... [C]	...	...	... [C]	...	...	... [C]	...	...	... [C]	...	...	... [C]	...	...	19.8[A]	3.33	3.33	61.4[B]	3.56	3.19
Ti I	5210.39	0.048	-0.884	3,2	167[B]	4.67	4.43	145[A]	4.75	4.45	167[B]	4.94	4.64	87.1[B]	3.56	3.88	228[B]	5.25	4.78	... [C]	...	...	89.2[A]	4.14	3.75
Ti I	5223.63	2.092	-0.558	1,1	... [C]	...	...	... [C]	...	...	... [C]	...	...	... [C]	...	...	... [C]	...	...	... [C]	...	...	... [C]	...	...
Ti I	5282.40	1.053	-1.300	3,3	44.4[A]	4.07	3.98	... [C]	...	...	... [C]	...	...	... [C]	...	...	... [C]	...	...	... [C]	...	...	15.7[B]	3.66	3.29
Ti I	5295.78	1.067	-1.633	1,1	34.9[A]	4.16	4.02	... [C]	...	...	... [C]	...	...	... [C]	...	...	... [C]	...	...	... [C]	...	...	... [C]	...	...
Ti I	5338.33	0.826	-1.870	3,3	... [C]	...	...	... [C]	...	...	... [C]	...	...	... [C]	...	...	... [C]	...	...	... [C]	...	...	13.6[B]	3.84	3.43
Ti I	5384.63	0.826	-2.910	3,3	... [C]	...	...	... [C]	...	...	... [C]	...	...	... [C]	...	...	28.4[B]	4.93	4.62	... [C]	...	...	... [C]	...	...
Ti I	5401.32	0.818	-2.890	3,3	23.0[B]	4.65	4.42	15.1[B]	4.46	4.25	... [C]	...	...	... [C]	...	...	... [C]	...	...	... [C]	...	...	... [C]	...	...
Ti I	5436.70	0.900	-2.500	3,3	... [C]	...	...	... [C]	...	...	... [C]	...	...	24.7[B]	4.58	4.76	... [C]	...	...	... [C]	...	...	29.2[B]	5.12	4.76
Ti I	5453.65	1.443	-1.610	3,3	48.0[A]	4.92	4.82	... [C]	...	...	... [C]	...	...	... [C]	...	...	... [C]	...	...	... [C]	...	...	... [C]	...	...
Ti I	5471.21	1.443	-1.400	1,1	... [C]	...	...	... [C]	...	...	... [C]	...	...	... [C]	...	...	... [C]	...	...	... [C]	...	...	... [C]	...	...
Ti I	5474.23	1.460	-1.230	1,1	... [C]	...	...	... [C]	...	...	... [C]	...	...	... [C]	...	...	... [C]	...	...	... [C]	...	...	... [C]	...	...
Ti I	5503.90	2.578	0.020	3,3	... [C]	...	...	... [C]	...	...	... [C]	...	...	... [C]	...	...	... [C]	...	...	... [C]	...	...	... [C]	...	...
Ti I	5648.57	2.495	-0.260	1,1	25.4[A]	4.27	4.14	... [C]	...	...	... [C]	...	...	... [C]	...	...	... [C]	...	...	... [C]	...	...	... [C]	...	...
Ti I	5866.46	1.067	-0.840	3,2	110[A]	4.86	4.75	62.1[A]	4.21	3.98	67.8[B]	4.23	4.08	... [C]	...	...	114[B]	4.98	4.74	... [C]	...	...	61.2[B]	4.42	4.06
Ti I	6303.77	1.440	-1.566	1,1	46.7[A]	4.65	4.46	16.7[B]	3.83	3.63	... [C]	...	...	... [C]	...	...	... [C]	...	...	... [C]	...	...	... [C]	...	...
Ti I	6554.24	1.443	-1.218	1,1	... [C]	...	...	54.0[A]	4.64	4.43	27.0[B]	3.85	3.63	... [C]	...	...	63.7[B]	4.68	4.42	... [C]	...	...	... [C]	...	...
Ti I	6556.08	1.460	-1.074	1,1	... [C]	...	...	... [C]	...	...	45.8[A]	4.26	4.08	... [C]	...	...	... [C]	...	...	25.8[B]	4.93	4.98	... [C]	...	...
Ti I	6743.13	0.900	-1.630	1,1	76.7[A]	4.55	4.36	56.8[A]	4.34	4.12	39.5[A]	3.85	3.62	58.0[B]	4.20	4.43	46.8[A]	3.98	3.60	... [C]	...	...	20.1[B]	3.73	3.26
Ti I	6861.50	2.27	-0.740	1,1	... [C]	...	...	... [C]	...	...	... [C]	...	...	... [C]	...	...	... [C]	...	...	... [C]	...	...	... [C]	...	...
Ti I	7209.47	1.460	-0.500	1,1	118[A]	4.80	4.63	74.4[A]	4.23	4.02	... [C]	...	...	24.2[B]	2.93	3.02	... [C]	...	...	... [C]	...	...	27.9[B]	3.50	3.09
Ti I	7216.19	1.443	-1.150	1,1	92.7[A]	4.98	4.80	34.1[A]	3.86	3.66	62.3[B]	4.55	4.36	... [C]	...	...	... [C]	...	...	... [C]	...	...	... [C]	...	...

Continued on next page

Table 2.4 – continued from previous page

					NGC 104			NGC 362			NGC 2808			NGC 6093			NGC 6388			NGC 6397			NGC 6752		
Sp.	λ	EP	$log(gf)$	Ref.	EW	$log\epsilon_p$	$log\epsilon_t$	EW	$log\epsilon_p$	$log\epsilon_t$	EW	$log\epsilon_p$	$log\epsilon_t$	EW	$log\epsilon_p$	$log\epsilon_t$	EW	$log\epsilon_p$	$log\epsilon_t$	EW	$log\epsilon_p$	$log\epsilon_t$	EW	$log\epsilon_p$	$log\epsilon_t$
Ti I	7251.72	1.430	-0.770	1,1	94.3[A]	4.60	4.43	... [C]	...	...	... [C]	...	...	... [C]	...	...	... [C]	...	...	... [C]	...	...	29.3[B]	3.77	3.35
Ti II	3913.47	1.116	-0.530	3,2	... [C]	...	...	203[B]	4.93	4.80	... [C]	...	...	... [C]	...	...	... [C]	...	...	... [C]	...	...	137[B]	4.38	4.17
Ti II	4012.39	0.574	-1.610	3,2	... [C]	...	...	193[B]	5.32	5.19	... [C]	...	...	... [C]	...	...	... [C]	...	...	... [C]	...	...	120[B]	4.66	4.34
Ti II	4028.35	1.892	-1.000	3,2	... [C]	...	...	90.8[A]	4.57	4.56	... [C]	...	...	... [C]	...	...	... [C]	...	...	... [C]	...	...	40.5[A]	3.98	3.60	53.0[A]	3.85	3.51
Ti II	4290.23	1.165	-1.120	3,2	... [C]	...	...	... [C]	...	...	... [C]	...	...	... [C]	...	...	... [C]	...	...	... [C]	...	...	... [C]	...	...	... [C]	...	...
Ti II	4300.05	1.180	-0.770	3,2	... [C]	...	...	... [C]	...	...	... [C]	...	...	... [C]	...	...	... [C]	...	...	... [C]	...	...	... [C]	...	...	... [C]	...	...
Ti II	4337.92	1.080	-1.130	3,2	... [C]	...	...	... [C]	...	...	... [C]	...	...	... [C]	...	...	... [C]	...	...	... [C]	...	...	... [C]	...	...	... [C]	...	...
Ti II	4394.07	1.221	-1.590	3,2	... [C]	...	...	66.0[A]	3.66	3.63	122[B]	5.00	4.94	... [C]	...	...	... [C]	...	...	... [C]	...	...	80.1[A]	4.28	3.88
Ti II	4395.04	1.084	-0.660	3,2	324[A]	5.32	5.38	234[A]	5.04	4.92	200[B]	4.80	4.73	197[A]	4.50	4.62	... [C]	...	...	83.6[B]	3.88	3.50	155[A]	4.46	4.24
Ti II	4395.85	1.243	-2.170	3,2	... [C]	...	...	26.4[A]	3.25	3.21	... [C]	...	...	... [C]	...	...	... [C]	...	...	25.5[B]	3.85	3.63	71.1[B]	4.65	4.27
Ti II	4399.78	1.237	-1.270	3,2	... [C]	...	...	122[A]	4.69	4.64	93.9[B]	4.07	4.00	78.3[B]	3.61	3.55	... [C]	...	...	50.1[B]	3.76	3.40	104[A]	4.53	4.17
Ti II	4417.72	1.165	-1.430	3,2	... [C]	...	...	114[A]	4.60	4.55	... [C]	...	...	81.6[B]	3.76	3.70	... [C]	...	...	... [C]	...	...	97.0[B]	4.45	4.07
Ti II	4418.34	1.237	-2.460	3,2	... [C]	...	...	72.1[B]	4.68	4.64	... [C]	...	...	... [C]	...	...	... [C]	...	...	... [C]	...	...	... [C]	...	...
Ti II	4443.81	1.080	-0.700	3,2	... [C]	...	...	144[B]	4.30	4.22	... [C]	...	...	... [C]	...	...	... [C]	...	...	... [C]	...	...	46.1[A]	2.90	2.57	141[A]	4.33	4.09
Ti II	4444.56	1.116	0.140	3,2	... [C]	...	...	... [C]	...	...	... [C]	...	...	... [C]	...	...	... [C]	...	...	... [C]	...	...	... [C]	...	...	... [C]	...	...
Ti II	4450.49	1.084	-1.450	3,2	... [C]	...	...	... [C]	...	...	145[B]	5.05	4.99	... [C]	...	...	168[B]	5.45	5.47	56.4[B]	3.96	3.58	134[B]	4.99	4.74
Ti II	4464.46	1.161	-2.080	3,2	175[B]	6.03	6.13	... [C]	...	...	... [C]	...	...	... [C]	...	...	... [C]	...	...	... [C]	...	...	82.7[B]	4.74	4.34
Ti II	4468.50	1.131	-0.600	3,2	151[B]	4.25	4.36	157[A]	4.41	4.32	173[B]	4.55	4.49	125[A]	3.75	3.79	... [C]	...	...	43.2[B]	2.74	2.44	107[A]	3.76	3.42
Ti II	4470.86	1.165	-2.280	3,2	... [C]	...	...	... [C]	...	...	... [C]	...	...	... [C]	...	...	... [C]	...	...	... [C]	...	...	... [C]	...	...
Ti II	4501.28	1.116	-0.750	3,2	215[B]	4.95	5.03	139[A]	4.28	4.21	152[A]	4.46	4.39	112[A]	3.64	3.64	... [C]	...	...	61.6[A]	3.42	3.02	132[A]	4.28	4.01
Ti II	4533.97	1.237	-0.770	3,2	... [C]	...	...	167[A]	4.78	4.69	... [C]	...	...	152[A]	4.34	4.44	... [C]	...	...	64.3[B]	3.62	3.22	158[A]	4.71	4.51
Ti II	4563.77	1.221	-0.960	3,2	192[A]	5.10	5.19	131[A]	4.44	4.38	153[A]	4.77	4.71	120[A]	4.06	4.10	... [C]	...	...	47.6[A]	3.28	2.98	124[A]	4.47	4.18
Ti II	4571.98	1.572	-0.530	3,2	... [C]	...	...	185[A]	5.06	4.97	188[B]	5.06	5.00	131[A]	4.19	4.26	... [C]	...	...	47.8[A]	3.20	2.90	143[A]	4.65	4.44
Ti II	4589.95	1.237	-1.790	3,2	108[A]	4.74	4.91	100[A]	4.62	4.59	77.7[B]	4.07	4.05	52.6[B]	3.30	3.35	... [C]	...	...	... [C]	...	...	92.3[A]	4.53	4.14
Ti II	4865.62	1.116	-2.610	3,2	... [C]	...	...	60.3[A]	4.26	4.23	... [C]	...	...	... [C]	...	...	... [C]	...	...	... [C]	...	...	46.6[B]	4.12	3.80
Ti II	5129.16	1.892	-1.390	3,2	... [C]	...	...	98.8[B]	4.70	4.70	... [C]	...	...	65.9[B]	3.77	3.83	... [C]	...	...	16.7[B]	3.22	3.10	94.9[A]	4.85	4.51
Ti II	5185.91	1.893	-1.350	3,2	... [C]	...	...	69.5[A]	3.98	3.99	36.7[B]	3.25	3.27	38.8[A]	3.07	3.15	... [C]	...	...	20.3[B]	3.32	3.19	56.4[A]	3.88	3.58
Ti II	5188.70	1.582	-1.210	3,2	195[A]	5.66	5.73	170[A]	5.43	5.37	161[A]	5.32	5.27	92.1[A]	3.83	3.88	223[A]	6.06	6.07	45.4[A]	3.64	3.44	127[A]	4.93	4.64
Ti II	5226.54	1.566	-1.300	3,2	... [C]	...	...	... [C]	...	...	... [C]	...	...	... [C]	...	...	... [C]	...	...	... [C]	...	...	... [C]	...	...
Ti II	5336.79	1.582	-1.700	3,2	95.0[A]	4.54	4.70	89.6[A]	4.39	4.39	80.1[A]	4.18	4.18	62.3[A]	3.56	3.65	128[A]	5.38	5.50	14.2[B]	3.07	2.96	68.6[A]	4.15	3.82
Ti II	5381.01	1.566	-2.080	3,2	84.3[A]	4.66	4.81	52.2[A]	3.93	3.92	85.1[B]	4.65	4.65	53.7[B]	3.70	3.80	98.2[B]	5.08	5.22	... [C]	...	...	46.0[A]	3.96	3.66
Ti II	6559.58	2.05	-2.480	1,1	... [C]	...	...	51.1[B]	4.71	4.73	... [C]	...	...	... [C]	...	...	... [C]	...	...	... [C]	...	...	... [C]	...	...
Ti II	7214.74	2.59	-1.740	1,1	... [C]	...	...	16.4[B]	3.72	3.76	... [C]	...	...	... [C]	...	...	... [C]	...	...	... [C]	...	...	... [C]	...	...
V I	4379.24	0.301	0.565	3,2	... [C]	...	...	66.6[B]	2.74	2.41	74.9[B]	2.63	2.47	... [C]	...	...	... [C]	...	...	... [C]	...	...	51.8[B]	2.47	2.19
V I	4389.99	0.275	0.235	3,2	... [C]	...	...	64.4[B]	2.98	2.65	... [C]	...	...	... [C]	...	...	... [C]	...	...	... [C]	...	...	... [C]	...	...
V I	6274.66[h]	0.267	-1.670	1,1	61.4[A]	3.43	3.22	... [C]	...	...	155[B]	5.30	5.08	... [C]	...	...	... [C]	...	...	... [C]	...	...	... [C]	...	...
V I	6285.16[h]	0.280	-1.510	1,1	79.3[A]	3.68	3.50	... [C]	...	...	37.8[B]	2.76	2.53	... [C]	...	...	... [C]	...	...	16.5[B]	3.78	3.83	... [C]	...	...

Continued on next page

Table 2.4 – continued from previous page

					NGC 104			NGC 362			NGC 2808			NGC 6093			NGC 6388			NGC 6397			NGC 6752		
Sp.	λ	EP	$log(gf)$	Ref.	EW	$log\epsilon_p$	$log\epsilon_t$	EW	$log\epsilon_p$	$log\epsilon_t$	EW	$log\epsilon_p$	$log\epsilon_t$	EW	$log\epsilon_p$	$log\epsilon_t$	EW	$log\epsilon_p$	$log\epsilon_t$	EW	$log\epsilon_p$	$log\epsilon_t$	EW	$log\epsilon_p$	$log\epsilon_t$
V I	6504.19	1.180	-1.230	1,1	23.1[B]	3.27	2.96	40.6[B]	3.89	3.68	30.2[B]	3.42	3.22	... [C]	...	...	... [C]	...	...	... [C]	...	...	... [C]	...	...
V I	6531.43[h]	1.220	-0.840	1,1	42.2[A]	3.40	3.16	25.6[B]	3.05	2.84	... [C]	...	...	... [C]	...	...	... [C]	...	...	... [C]	...	...	... [C]	...	...
V I	6543.51	1.190	-1.660	1,1	... [C]	...	...	... [C]	...	...	... [C]	...	...	... [C]	...	...	... [C]	...	...	... [C]	...	...	... [C]	...	...
V I	6812.36[h]	1.040	-2.110	1,1	11.9[A]	2.78	2.36	... [C]	...	...	... [C]	...	...	... [C]	...	...	... [C]	...	...	... [C]	...	...	... [C]	...	...
V II	3997.11	1.476	-1.230	3,2	... [C]	...	...	... [C]	...	...	... [C]	...	...	... [C]	...	...	... [C]	...	...	... [C]	...	...	... [C]	...	...
Y I	6401.95	0.066	-2.180	3,3	... [C]	...	...	... [C]	...	...	... [C]	...	...	... [C]	...	...	... [C]	...	...	... [C]	...	...	15.5[B]	3.32	2.79
Y I	6435.05	0.066	-0.820	1,1	... [C]	...	...	... [C]	...	...	... [C]	...	...	... [C]	...	...	... [C]	...	...	... [C]	...	...	... [C]	...	...
Y II	3950.36	0.104	-0.490	3,2	... [C]	...	...	... [C]	...	...	... [C]	...	...	... [C]	...	...	... [C]	...	...	... [C]	...	...	... [C]	...	...
Y II	4204.70	0.000	-0.720	3,2	... [C]	...	...	... [C]	...	...	... [C]	...	...	... [C]	...	...	... [C]	...	...	... [C]	...	...	... [C]	...	...
Y II	4374.94	0.409	0.160	3,2	... [C]	...	...	... [C]	...	...	... [C]	...	...	... [C]	...	...	... [C]	...	...	... [C]	...	...	85.5[B]	1.46	1.00
Y II	4398.01	0.130	-1.000	3,2	95.4[A]	2.10	2.27	... [C]	...	...	... [C]	...	...	... [C]	...	...	... [C]	...	...	... [C]	...	...	... [C]	...	...
Y II	4883.68	1.084	0.070	3,2	78.0[A]	1.51	1.65	61.0[A]	1.12	1.08	37.8[A]	0.47	0.47	... [C]	...	...	102[B]	2.25	2.34	... [C]	...	...	69.0[A]	1.57	1.18
Y II	5087.42	1.084	-0.17	3,2	... [C]	...	...	... [C]	...	...	... [C]	...	...	... [C]	...	...	... [C]	...	...	... [C]	...	...	... [C]	...	...
Y II	5205.73	1.033	-0.34	3,2	... [C]	...	...	... [C]	...	...	... [C]	...	...	... [C]	...	...	... [C]	...	...	... [C]	...	...	... [C]	...	...
Y II	5402.78	1.839	-0.510	3,3	21.8[A]	1.50	1.60	13.6[B]	1.09	1.08	... [C]	...	...	... [C]	...	...	... [C]	...	...	... [C]	...	...	... [C]	...	...
Y II	6795.41	1.73	-1.250	1,1	... [C]	...	...	... [C]	...	...	... [C]	...	...	... [C]	...	...	... [C]	...	...	... [C]	...	...	44.3[B]	3.11	2.99
Y II	7450.32	1.75	-0.780	1,1	... [C]	...	...	... [C]	...	...	... [C]	...	...	... [C]	...	...	... [C]	...	...	... [C]	...	...	... [C]	...	...
Zr I	6143.18[h]	0.071	-1.100	4,4	30.3[C]	2.07	1.73	34.7[B]	2.40	2.16	... [C]	...	...	... [C]	...	...	... [C]	...	...	15.4[B]	3.30	3.36	... [C]	...	...
Zr I	6762.40	0.000	-2.660	3,3	... [C]	...	...	18.1[B]	2.92	2.66	... [C]	...	...	... [C]	...	...	... [C]	...	...	... [C]	...	...	... [C]	...	...
Zr I	7439.89	0.543	-1.810	3,3	... [C]	...	...	... [C]	...	...	... [C]	...	...	... [C]	...	...	... [C]	...	...	... [C]	...	...	... [C]	...	...
Zr II	4161.21	0.713	-0.720	3,2	... [C]	...	...	... [C]	...	...	... [C]	...	...	... [C]	...	...	... [C]	...	...	... [C]	...	...	... [C]	...	...
Zr II	4208.98	0.713	-0.460	3,2	... [C]	...	...	... [C]	...	...	... [C]	...	...	... [C]	...	...	... [C]	...	...	17.7[B]	1.34	1.10	53.0[B]	2.03	1.63
Zr II	4496.97	0.713	-0.810	3,2	... [C]	...	...	100[B]	3.26	3.18	... [C]	...	...	70.8[B]	2.35	2.35	... [C]	...	...	... [C]	...	...	... [C]	...	...

CHAPTER 3

Photometric CMD Analysis

As a preliminary proof-of-concept for this dissertation's abundance analysis method, resolved stellar photometry from the training set clusters are used to define the clusters' model atmospheres, instead of using theoretical SSPs as the full analysis method requires. The rationale behind approaching the method using this *a priori* stellar population information is to decouple the method's light-weighted EW synthesis techniques from its theoretical SSP techniques. This preliminary analysis also critically allows the stellar populations observed inside the scanned regions to be investigated in order to verify that they are indeed fully populated SSPs, which is a key assumption behind the abundance analysis method.

The outline for this chapter is as follows. In § 3.1, photometry published in the literature is used to define the stellar populations located inside the scanned regions of the training set clusters. In § 3.1, the strategy used to sample this photometry, so that representative stellar types inside each cluster are identified, is discussed. The methods used to determine the atmospheric parameters of T_{eff}, $log(g_{\star})$, and ξ_v for these stellar types is also discussed. In § 3.2, the analysis method's light-weighted EW synthesis techniques are discussed. In § 3.3, the abundance analysis method is applied to all the observed Fe line EWs in each cluster's IL spectrum in order to simultaneously determine the mean metallicity for each cluster and also its model atmospheres' [M/H] value. In § 3.4, light-weighted EWs are synthesized to obtain the abundances for all non-Fe lines in the clusters' IL spectra. Finally, in § 3.5, the abundance results from this photometry-based analysis are compared against standard abundance results in the literature.

3.1 Stellar Populations within the Scanned Regions

The scanned regions used to obtain the IL spectra were chosen to include as much of the training set clusters as possible, without unnecessarily sacrificing the quality of the spectra by sampling the low-surface brightness regions found at large radii. This consideration naturally limited the observations to the high surface brightness regions inside the cores of the clusters. The first critical issue to establish regarding the effects of this observation method is how much of each cluster's overall stellar population is well sampled by its IL spectrum. A second critical issue to consider is whether those stellar populations can be accurately modeled using theoretical SSPs. To understand the stellar populations captured in the clusters' spectra, it is important to use HST photometry in order to resolve the stars in the inner regions of the clusters, while simultaneously extending to several core radii to adequately sample the full population. Conveniently, six of the seven clusters (NGC 104, NGC 362, NGC 2808, NGC 6093, NGC 6388, and NGC 6397) have HST WFPC2 photometry published by Piotto et al. (2002) in a fully reduced format. The seventh cluster (NGC 6752) has fully reduced HST ACS photometry from the ACS Survey of Galactic Globular Clusters (Sarajedini et al. 2007), which is currently unpublished, but was appreciatively obtained by private communication (Sarajedini 2008).

The six clusters observed by Piotto et al. were imaged in the HST's F439W and F555W bands. Piotto et al. transformed these F439W and F555W magnitudes into Johnson B and V magnitudes, respectively, which are adopted here. Not surprisingly, all of the Piotto et al. observations were made with the cores of the clusters centered on the PC chip (36×36 $arcsec^2$ field-of-view; 0.0455" per pixel) to obtain maximum spatial resolution in these dense regions. High-spatial resolution photometry is therefore available for the regions of the clusters that were included in the spectral scans. Because GC stellar populations should be well mixed azimuthally, and because mass segregation is a radial process, small rotational differences between the orientations of the spectroscopic scans and the PC chip are not a concern.

Figure 3.1 shows the pixel locations of the stars in the Piotto et al. WFPC2

Cluster	N_{Image}	N_{Scan}
NGC 104	28,925	5,837
NGC 362	20,359	6,622
NGC 2808	46,328	11,879
NGC 6093	11,390	3,088
NGC 6388	46,933	14,328
NGC 6397	16,507	3,189
NGC 6752	52,817	3,641

Table 3.1. The number of stars located in and around the scanned regions. Column "N_{Image}" lists the total number of stars located within each cluster's WFPC2 or ACS image, while column "N_{Scan}" lists the total number of stars located within each cluster's 32×32 $arcsec^2$ scanned region.

frames. The PC chip and the three WF chips arrayed around the PC chip cover an effective field-of-view equal to 143×143 $arcsec^2$, which well samples each cluster's stellar population beyond the cluster's core region. In this figure, stars inside and outside of the 32×32 $arcsec^2$ cores are marked by red and black dots, respectively. Note that all of the clusters are visibly quite dense in the cluster cores, while NGC 6397 is noticeably less so. This is consistent with the comparatively low mass of NGC 6397, as discussed further below. The total number of stars for which photometry is available in each cluster, both inside and outside of the scanned regions, are listed in Table 3.1.

The ACS observations of NGC 6752 are in bandpasses F606W and F814W and are again centered on the core of the cluster. Sarajedini et al. (2007) have converted the resulting photometry to Johnson-Cousins V and I magnitudes, respectively, which are adopted here. Note that the F606W and F814W filters are actually much broader than the Johnson-Cousins filters that they approximate, which complicates the transformations to the Johnson-Cousins system. As with the Piotto et al. data, the spectroscopic scanned region coincides with the 32×32 $arcsec^2$ center of the ACS data. Figure 3.2 again shows the pixel positions of the stars located inside and outside the scanned regions.

One critical issue to address regarding the scanned regions is whether they contain representative samples of the clusters' stellar populations. This is a concern because the 32×32 $arcsec^2$ scanned regions diagonally extend to only $R = 0.94 - 7.5 \times R_{core}$, with an average extension of $R = 2.8 \times R_{core}$ (see Table 2.1). This is in contrast to

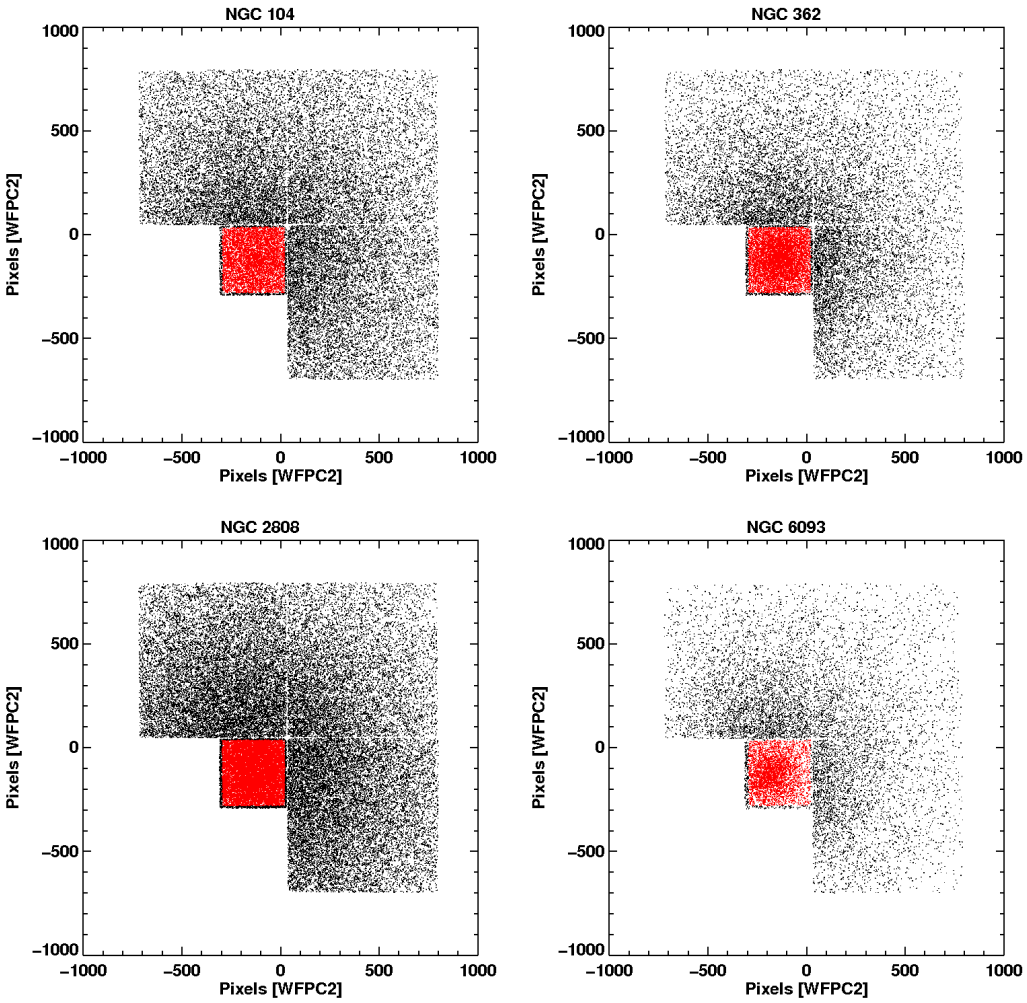

Figure 3.1. HST pixel positions for the stars located within the central regions of NGC 104, NGC 362, NGC 2808, and NGC 6093. Red dots correspond to stars located inside the 32×32 $arcsec^2$ scanned regions, while black dots correspond to stars located outside the scanned regions. The geometric center of each red scanned region corresponds to the center of its cluster. The stellar identifications and pixel astrometry were obtained from the published HST WFPC2 data of Piotto et al. (2002).

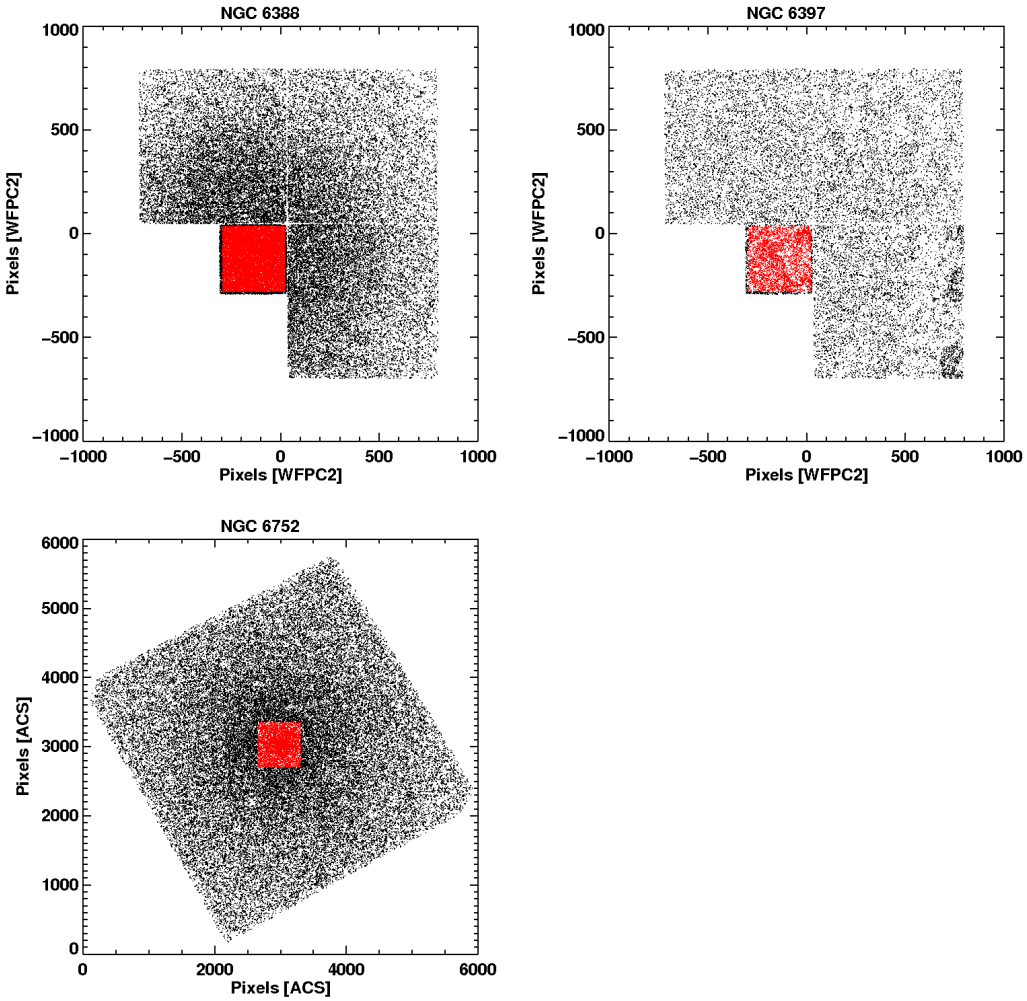

Figure 3.2. HST pixel positions for the stars located within the central regions of NGC 6388, NGC 6397, and NGC 6752. Red dots correspond to stars located inside the 32×32 $arcsec^2$ scanned regions, while black dots correspond to stars located outside the scanned regions. The geometric center of each red scanned region corresponds to the center of its cluster. The stellar identifications and pixel astrometry for NGC 6388 and NGC 6397 were obtained from Piotto et al. (2002). The stellar identifications and pixel astrometry for NGC 6752 were obtained from the HST ACS Survey of Galactic Globular Clusters (Sarajedini et al. 2007, obtained by private communication).

the near complete radial coverage that can be achieved in real extragalactic GCs.

To confirm that the scans contain a sufficient sample of the clusters' stellar populations, CMDs of the stars inside and outside the scanned regions are compared for each cluster in Figures 3.3 and 3.4. Again, red and black dots indicate stars in the HST data sets which lie inside and outside of the scanned regions, respectively. In Figures 3.5 and 3.6 histograms of these stellar samples are shown in terms of fractional V-band flux as a function of M_V. It is clear from these figures that the scanned regions do sufficiently sample the clusters' total stellar populations at the faint ends; any differences due to mass segregation are not significant. Also, note that while each cluster has photometry with different limiting magnitudes, these observational cut-offs are all sufficiently deep that the clusters are essentially complete in terms of total flux at the faint ends. Along the red giant branch (RGB), however, some differences are evident between the fractional flux contained within the core and in the full cluster CMD. Because the RGB represents only a small number of rapidly-evolving stars that contribute significantly to the total cluster flux, the fraction of light from RGB stars in any sampled region is likely to show stochastic variations from other regions of the cluster. These RGB variations are particularly noticeable in NGC 6397 and NGC 6752.

In NGC 6397, the scanned region does not contain stars within $\sim 1.5\ mag$ of the tip of the RGB, which contains almost 20% of the total cluster light. This kind of statistical fluctuation is not unexpected in a low-mass cluster. It can be accommodated in the theoretical SSP analysis by simply scaling the total number of stars in the SSP to match the total flux in the scanned region, which is an observable quantity in the training set and any future GC target. This issue is further discussed in Chapter 4. Note that it is unlikely that similar low mass clusters will be sampled in real extragalactic GC systems due to their unfavorably low flux levels. In NGC 6752, the scanned region contains significant deviations in the fractional flux at various points all along the RGB. This is either due to real, stochastic variations between the scanned region and the rest of the cluster, or it is due to some other uncontrollable issue, such as interlopers along the line of sight, photometric errors, or binary stars.

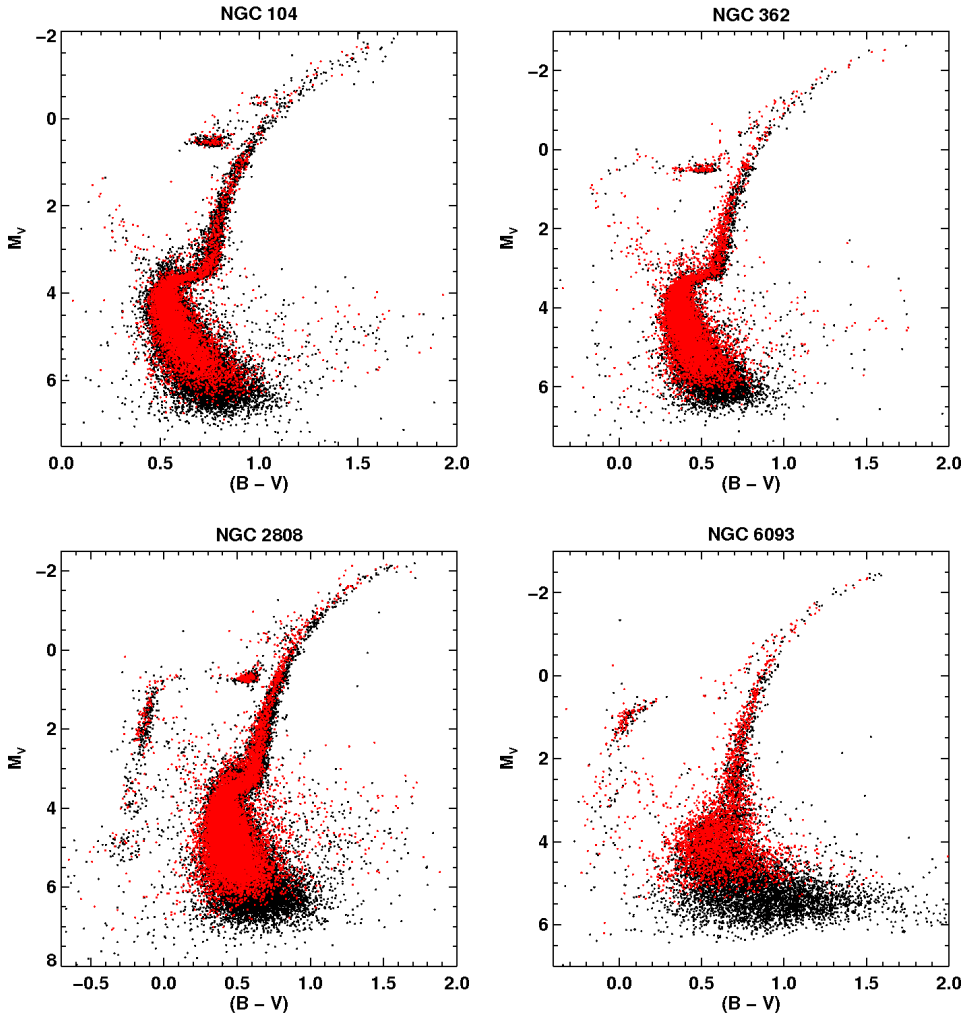

Figure 3.3. CMDs of stars located within the central regions of NGC 104, NGC 362, NGC 2808 and NGC 6093. Red dots correspond to stars located inside each cluster's 32×32 $arcsec^2$ scanned region. Black dots correspond to stars located outside the scanned regions. The stellar identifications and HST photometry were obtained from Piotto et al. (2002). Note that the Piotto et al. photometry were originally observed in WFPC2 F439W and F555W magnitudes and were then transformed to Johnson B and V magnitudes, respectively. The plotted colors have been corrected for reddening, and the V magnitudes have been converted to absolute V magnitudes.

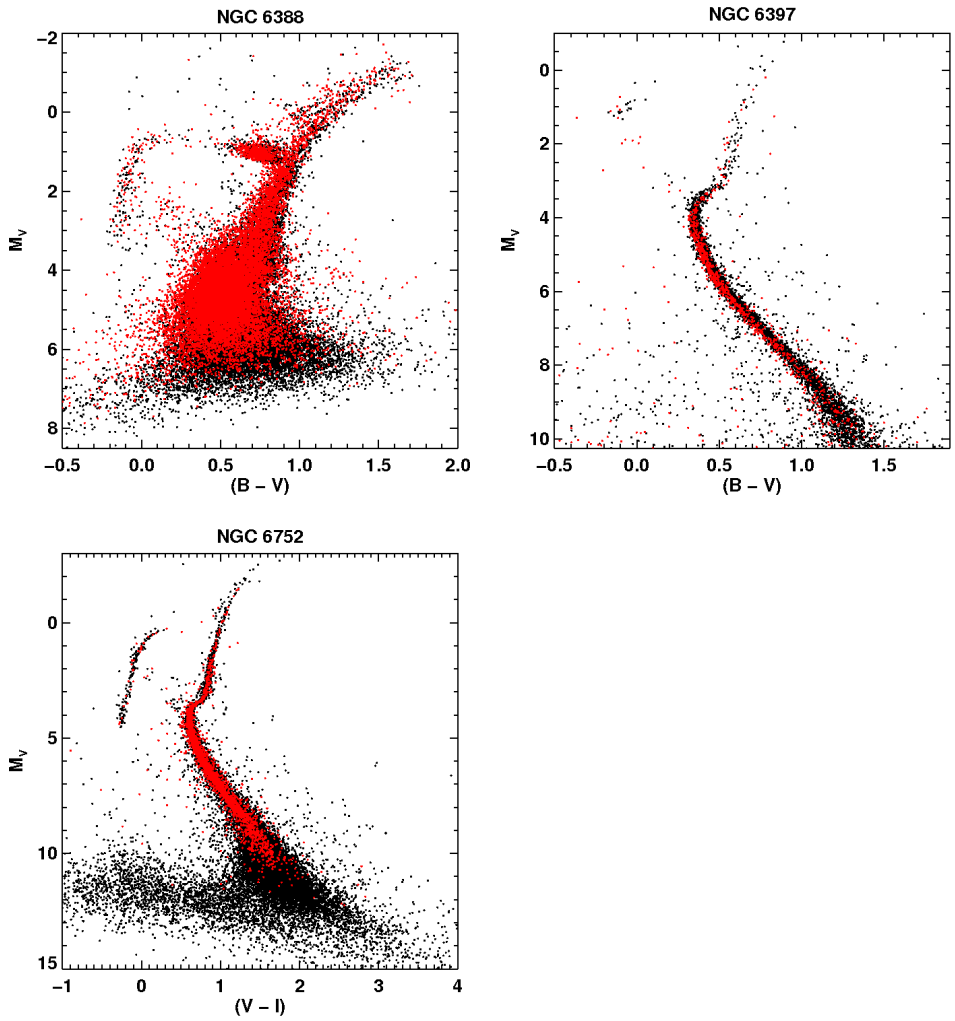

Figure 3.4. CMDs of stars located within the central regions of NGC 6388, NGC 6397, and NGC 6752. Red dots correspond to stars located inside each cluster's 32×32 $arcsec^2$ scanned region. Black dots correspond to stars located outside the scanned regions. The stellar identifications and HST photometry used for NGC 6388 and NGC 6397 were obtained from Piotto et al. (2002). The stellar identifications and HST photometry used for NGC 6752 were obtained from the HST ACS Survey of Galactic Globular Clusters (Sarajedini et al. 2007, obtained by private communication). Note that the ACS Survey photometry were originally observed in ACS F606W and F814W magnitudes and were then transformed to Johnson-Cousins V and I magnitudes, respectively. The large "cloud" of stars dimmer than ~ 10 *mag* for NGC 6752 are the result of decreased photometric and astrometric accuracy for dim objects, and possibly background contamination. The plotted colors have been corrected for reddening, and the V magnitudes have been converted to absolute V magnitudes.

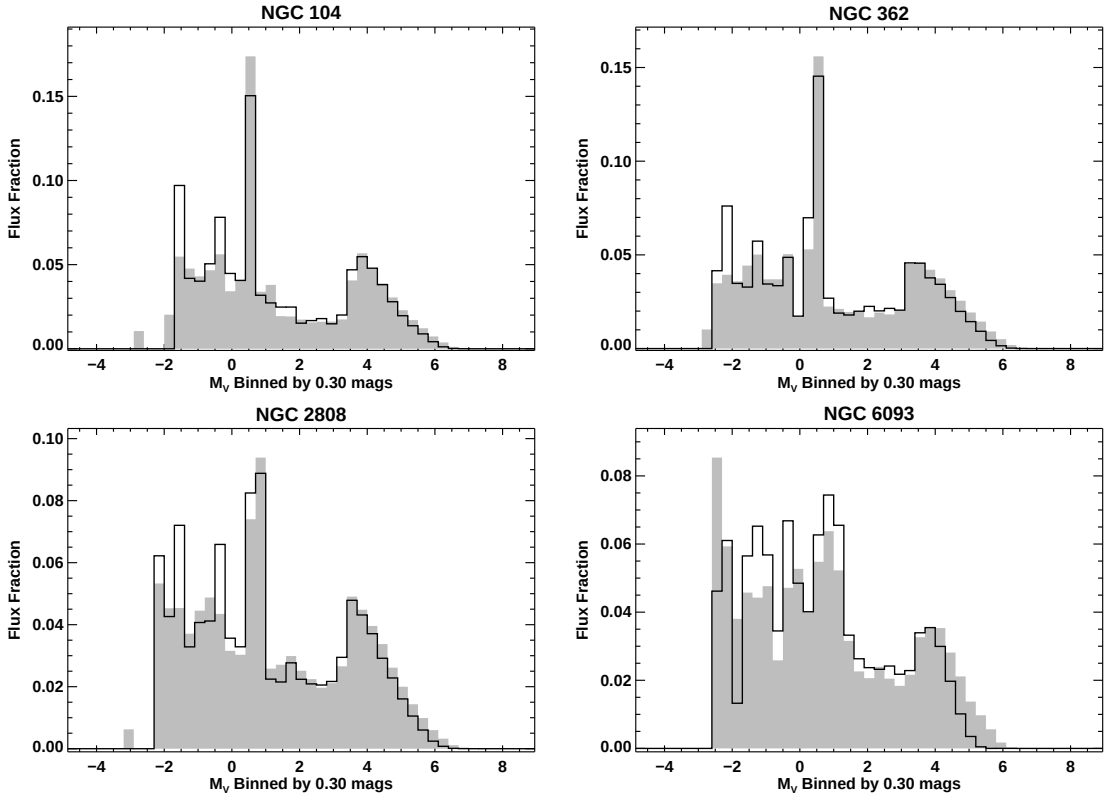

Figure 3.5. Histograms comparing the amount of V-band flux observed inside the full HST field-of-views versus the scanned regions of NGC 104, NGC 362, NGC 2808, and NGC 6093. The grey filled histograms correspond to the clusters' entire HST field-of-views, while the empty histograms outlined in black correspond to the clusters' scanned regions. Both histograms are binned by 0.3 *mag* in M_V and are normalized with respect to the total amount of M_V flux observed within their respective regions.

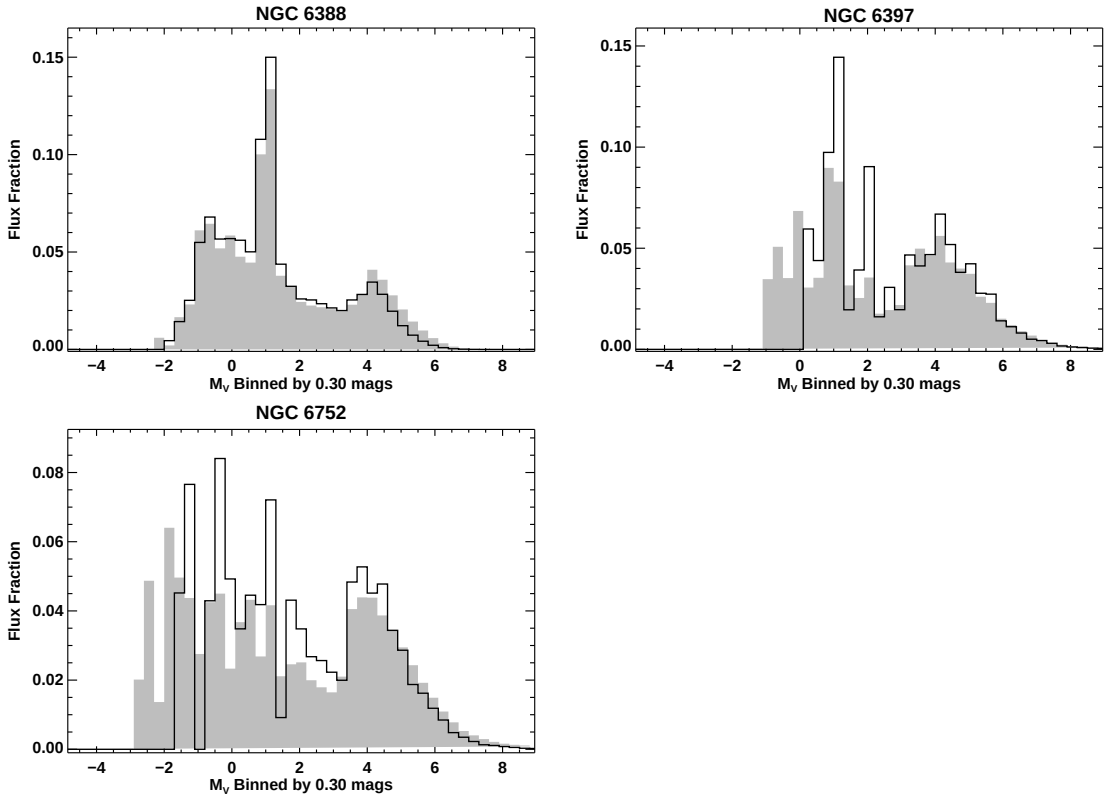

Figure 3.6. Histograms comparing the amount of V-band flux observed inside the full HST field-of-views versus the scanned regions of NGC 6388, NGC 6397, and NGC 6752 The grey filled histograms correspond to the clusters' entire HST field-of-views, while the empty histograms outlined in black correspond to the clusters' scanned regions. Both histograms are binned by 0.3 *mag* in M_V and are normalized with respect to the total amount of M_V flux observed within their respective regions.

Cluster	$(m - M)_V$	E(B - V)	Ref.
NGC 104	13.50	0.024	4
NGC 362	14.98	0.056	2
NGC 2808	15.56	0.20	3
NGC 6093	15.56	0.18	1
NGC 6388	16.14	0.37	1
NGC 6397	12.58	0.183	4
NGC 6752	13.24	0.040	4

Table 3.2. The adopted distance moduli and color excesses for the clusters. The references are: [1]: Harris (1996); [2]: Carretta et al. (2000); [3]: Saad & Lee (2001); [4]: Gratton et al. (2003)

Either way it presents an interesting empirical test of the accuracy of an IL spectra abundance measurement.

Atmospheric Parameters from Photometry

The training set clusters' observed photometry is used to directly calculate T_{eff}, $log(g_\star)$, and ξ_v parameters for the model atmospheres that represent the stars located inside their scanned regions. As a first step in the calculation of these parameters, the photometry was dereddened and converted from apparent V-band magnitudes to absolute magnitudes, M_V. M_V magnitudes were produced using distance moduli derived from Hipparcos data for NGC 104, NGC 362, NGC 2808, NGC 6397, and NGC 6752 and from Harris (1996) for NGC 6093 and NGC 6388. The applied reddening corrections used the average total-to-selective extinction ratio, $R = 3.136$, for the Galaxy as determined by Winkler (1997). Color excesses were adopted from the same sources as the distance moduli. All distance moduli, color excesses, and their references are listed in Table 3.2.

To reduce the number of computations needed to analyze each cluster, the stars inside each cluster's scanned region were binned in M_V along their CMD in order to obtain ∼28 representative stellar types (see Figures 3.7 and 3.8). Each bin contains roughly 3.5% of each scanned region's V-band flux and is quantified by the flux-weighted average M_V and color of the stars in that corresponding portion of the CMD. These ∼28 representative stellar types will be referred to as the "average stellar types" that represent a cluster.

Stellar atmospheres for each cluster's average stellar types are based on Kurucz

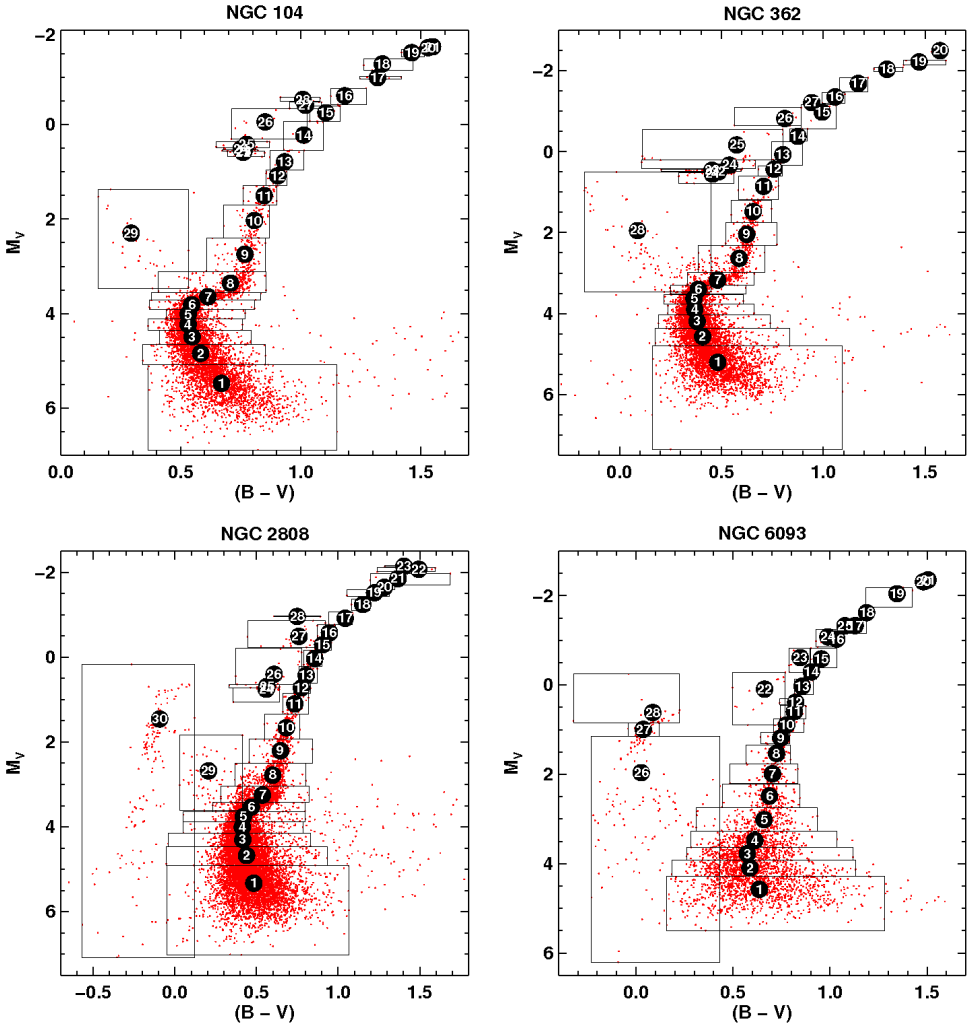

Figure 3.7. The scanned region CMDs of NGC 104, NGC 362, NGC 2808, and NGC 6093 binned into ∼28 representative stellar types. The small red dots correspond to the stars resolved within each cluster's scanned region (see Figure 3.1). Each black rectangle bins approximately 3.5% of its scanned region's V-band flux. Each numbered black dot represents the flux-weighted average color and magnitude location of all the stars enclosed within its black rectangle. Besides these flux-weighted CMD locations, the enclosed stars also have flux-weighted average effective temperatures, surface gravities, radii, and microturbulent velocities assigned to them. These stellar parameters are listed in Tables 3.3 through 3.6. Note that the number assigned to each black dot corresponds to the "Bin" number referenced in the first column of these tables.

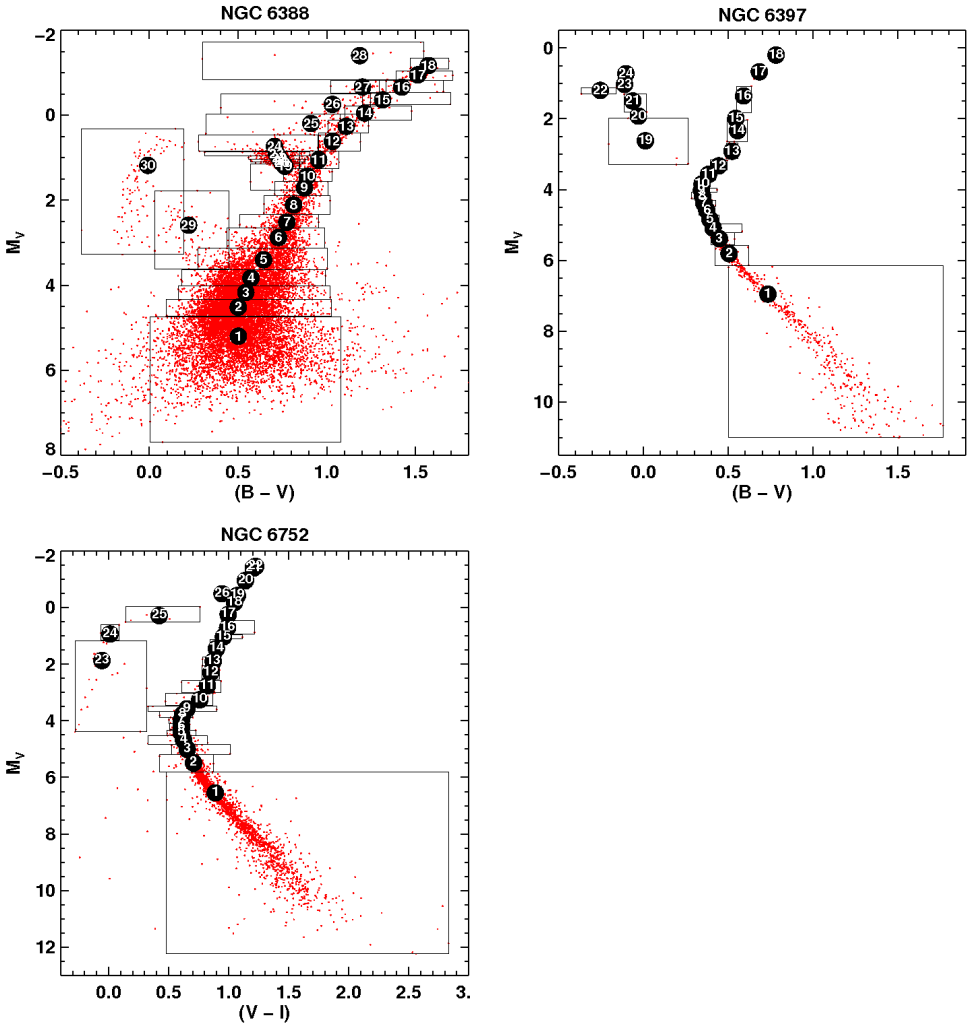

Figure 3.8. The scanned region CMDs of NGC 6388, NGC 6397 and NGC 6752 binned into ∼28 representative stellar types. All plotting conventions and analysis match those described in Figure 3.7, except each stellar types' flux-weighted parameters are listed in Tables 3.7 through 3.9.

model atmosphere grids[1]. The stellar parameters used to produce these atmospheres are calculated as described below.

Specific gravity, $log(g_\star)$, is calculated with respect to the Sun as

$$log(g/g_\odot) = log(\mathcal{M}/\mathcal{M}_\odot) - log(L/L_\odot) + 4\,log(T_{eff}/T_{eff,\odot}), \tag{3.1}$$

in which $\mathcal{M}$ is the stellar mass, L is the bolometric luminosity, and T_{eff} is the effective temperature. The parameters, L, $\mathcal{M}$, and T_{eff}, are obtained as follows. $\mathcal{M}$ is assumed to be equal to 0.8 $\mathcal{M}_\odot$, which is the characteristic mass of the clusters' TO stars. L is computed using

$$log(L/L_\odot) = -0.4\,(M_{bol} - M_{bol,\odot}), \tag{3.2}$$

in which M_{bol} is the star's bolometric magnitude and $M_{bol,\odot}$ is the bolometric magnitude of the Sun. Bolometric corrections (BC) are used to compute M_{bol} using

$$M_{bol} = M_V + BC. \tag{3.3}$$

The required BC values are interpolated from a Kurucz grid (2002 unpublished). Finally, T_{eff} is determined using the color-temperature relations of Alonso et al. (1999).

Microturbulent velocities, ξ_v, were obtained using the $log(g_\star)$–ξ_v relation discussed in Fulbright et al. (2006)

$$\xi_v = \xi_{v,\odot} + \frac{log(g_\odot) - log(g_\star)}{log(g_\odot) - log(g_{Arct})}(\xi_{v,Arct} - \xi_{v,\odot}). \tag{3.4}$$

This relation is a simple linear regression through the solar value $\xi_\odot = 1.00\ km\ s^{-1}$ at $\log(g_\odot) = 4.44$, and the value for Arcturus, $\xi_{\rm Arct} = 1.60\ km\ s^{-1}$ at $\log(g_{\rm Arct}) = 1.60$. In the analysis of individual stars, microturbulence is an empirically adjusted parameter. However, empirical values from the literature over a broad range of stellar

[1]Kurucz 2002, unpublished, but available at http://kurucz.harvard.edu/grids.html

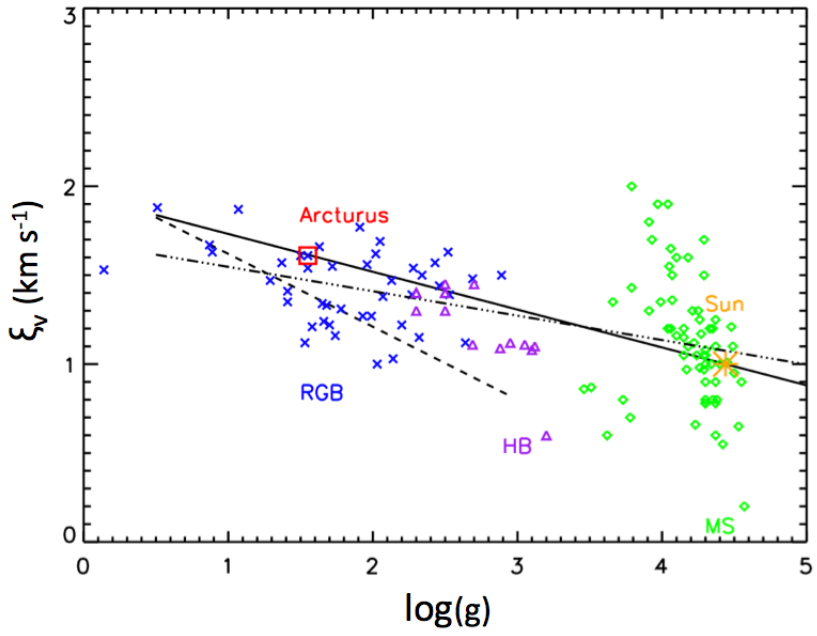

Figure 3.9. The relationship between specific gravity and microtubulence. This relationship is plotted for a sample of nearby dwarf stars (Bensby et al. 2005) in green diamonds, horizontal branch stars (Feltzing et al. 2009) in purple triangles, and red giants (Fulbright et al. 2006) plotted in blue crosses. The dot-dashed line shows a linear fit to the full sample. The solid line shows the law adopted for microturbulence in this work. The difference between the two fits is not statistically significant, particularly because the points represent microturbulence which are poorly-constrained, adjusted-parameters in the abundance solutions for the stars shown. The dashed line shows the relationship used in (Kirby et al. 2008). Points indicating the Sun and Arcturus are labeled.

types are consistent with this simple function, as can be seen in Figure 3.9. An iterative adjustment of ξ_v is not possible in this analysis and, as discussed below, nothing more complicated is found to be necessary in order to obtain accurate results in the IL analysis.

Finally, to combine the EWs synthesized for each cluster's ∼28 average stellar types into a single light-weighted EW, their radii (R) must be known in order to compute their surface fluxes. Stellar radii are calculated using

$$R/R_{\odot} = (T_{eff,\odot}/T_{eff})^2\sqrt{L/L_{\odot}}. \tag{3.5}$$

All atmospheric parameters for the average stellar types, and the number of stars that each stellar type represents, are listed in Tables 3.3 through 3.9.

The only remaining parameter needed to fully-define the model atmospheres are

their overall metal abundances, [M/H], which are parametrized with respect to the clusters' [Fe/H] and their adopted abundance ratio distribution. The determination of the clusters' [Fe/H] is discussed in the next section.

3.2 Light-weighted EW Synthesis

The most detailed and important step in the abundance analysis method is the synthesis of light-weighted EWs. The method's light-weighted line synthesis routine physically consists of a largely automated program called ILABUNDS. At its heart, ILABUNDS consists of four primary components: the stellar spectrum synthesis code MOOG (Sneden 1973), a model atmosphere interpolation routine, a routine that computes flux-weighted EWs, and an overarching algorithm that properly controls all of the iterations through the code. Line synthesis conducted by ILABUNDS is handled using MOOG as a subroutine. Model atmosphere interpolation is done using a grid of α-enhanced Kurucz model atmospheres (Castelli & Kurucz 2004) that were produced using the latest opacity distribution function (AODFNEW). Interpolations within this Kurucz atmosphere grid are conducted by linearly interpolating to the desired model atmosphere's combination of T_{eff}, $log(g_{\star})$, and [M/H]. All instances of light-weighted EW computation involves selecting an observed absorption line, synthesizing that line's EW individually for all of the cluster's average stellar types, and then merging all those EWs together through the computation of a flux-weighted EW for all the stars represented by those stellar types.

The equation used by ILABUNDS to calculate each line's flux-weighted EW is

$$\overline{EW} = \frac{\sum_{i=1}^{N_{bin}} EW_i w_i}{\sum_{i=1}^{N_{bin}} w_i} \tag{3.6}$$

where $\overline{EW}$ is the final flux-weighted EW for the synthesized line, N_{bin} is the total number of average stellar types used to represent the cluster's stellar population, EW_i is the EW synthesized by MOOG for the i^{th} stellar type, and w_i is the flux weighting

Box	$\langle M_v \rangle$ (mag)	$\langle (B-V) \rangle$ (mag)	T_{eff} (K)	$log(g_\star)$ $(log(cgs))$	ξ_v $(km\ s^{-1})$	R $(R_\odot)$	N_{stars}	Flux Frac.
1	5.478	0.670	5388	4.395	1.01	0.94	1760	0.035
2	4.845	0.583	5681	4.255	1.04	1.10	949	0.035
3	4.494	0.548	5807	4.160	1.06	1.23	684	0.035
4	4.229	0.531	5871	4.076	1.08	1.36	536	0.035
5	4.013	0.531	5871	3.990	1.10	1.50	439	0.035
6	3.812	0.546	5815	3.891	1.12	1.68	365	0.035
7	3.644	0.613	5573	3.736	1.15	2.01	313	0.035
8	3.358	0.707	5277	3.503	1.20	2.62	242	0.035
9	2.744	0.768	5099	3.178	1.27	3.81	139	0.035
10	2.030	0.807	5007	2.851	1.34	5.56	72	0.035
11	1.502	0.848	4928	2.601	1.39	7.42	44	0.035
12	1.083	0.904	4824	2.379	1.44	9.57	30	0.036
13	0.786	0.933	4772	2.234	1.47	11.31	23	0.036
14	0.220	1.013	4633	1.928	1.53	16.09	14	0.036
15	-0.255	1.105	4484	1.647	1.59	22.22	9	0.036
16	-0.613	1.184	4364	1.422	1.64	28.81	7	0.039
17	-0.997	1.320	4172	1.123	1.71	40.64	5	0.040
18	-1.287	1.340	4145	0.985	1.74	47.65	4	0.042
19	-1.525	1.463	3987	0.752	1.78	62.31	3	0.039
20	-1.632	1.531	3906	0.621	1.81	72.42	3	0.043
21	-1.651	1.549	3884	0.591	1.82	74.99	1	0.015
22	0.587	0.760	5120	2.330	1.45	10.13	19	0.036
23	0.549	0.764	5109	2.310	1.45	10.36	19	0.037
24	0.511	0.752	5142	2.310	1.45	10.37	18	0.036
25	0.417	0.775	5081	2.244	1.47	11.18	17	0.037
26	-0.058	0.852	4920	1.976	1.52	15.22	11	0.036
27	-0.410	1.020	4622	1.670	1.59	21.65	8	0.038
28	-0.535	1.009	4640	1.631	1.60	22.63	4	0.021
29	2.297	0.294	7034	3.657	1.17	2.20	30	0.010

Table 3.3. NGC 104's representative average stellar types as derived from its scanned region's CMD. The "Box" column lists the labels assigned to the rectangular regions used to convert the photometric CMD into its ∼28 average stellar types. These rectangular regions are shown in Figure 3.7. For each average stellar type: the "$\langle M_V \rangle$" column lists the flux-weighted average M_V magnitude; the "$\langle (B-V) \rangle$" column lists the flux-weighted average $(B-V)$ color; the "T_{eff}" column lists the effective temperature; the "$log(g_\star)$" column lists the surface gravity; the "ξ_v" column lists the microturbulent velocity; the "R" column lists the radius; the "N_{stars}" column lists the number of stars represented by each average stellar type; and the "Flux Frac." column lists the amount of flux that each average stellar type's N_{stars} stars emit, normalized to the total flux of the scanned region.

Box	$\langle M_v \rangle$ (mag)	$\langle (B-V) \rangle$ (mag)	T_{eff} (K)	$log(g_\star)$ $(log(cgs))$	ξ_v $(km\ s^{-1})$	R $(R_\odot)$	N_{stars}	Flux Frac.
1	5.205	0.482	5908	4.462	1.00	0.87	2110	0.035
2	4.568	0.408	6211	4.302	1.03	1.05	1131	0.035
3	4.195	0.381	6330	4.189	1.05	1.19	800	0.035
4	3.899	0.369	6384	4.088	1.07	1.34	609	0.035
5	3.634	0.366	6389	3.984	1.10	1.51	477	0.035
6	3.402	0.387	6279	3.860	1.12	1.74	385	0.035
7	3.174	0.481	5885	3.645	1.17	2.23	313	0.035
8	2.636	0.587	5516	3.302	1.24	3.31	194	0.035
9	2.043	0.624	5401	3.020	1.30	4.57	112	0.035
10	1.481	0.656	5305	2.759	1.36	6.18	67	0.035
11	0.857	0.707	5154	2.445	1.42	8.87	38	0.036
12	0.433	0.759	4986	2.199	1.48	11.77	25	0.035
13	0.074	0.802	4883	2.004	1.52	14.73	19	0.037
14	-0.378	0.876	4760	1.760	1.57	19.51	12	0.035
15	-0.977	0.995	4574	1.412	1.64	29.12	8	0.041
16	-1.354	1.058	4481	1.204	1.69	37.01	5	0.036
17	-1.684	1.172	4323	0.964	1.74	48.80	4	0.039
18	-2.036	1.312	4144	0.683	1.80	67.44	3	0.041
19	-2.217	1.471	3959	0.445	1.85	88.74	3	0.048
20	-2.496	1.573	3849	0.214	1.90	115.73	2	0.042
21	0.552	0.456	5978	2.640	1.38	7.09	28	0.035
22	0.501	0.485	5868	2.582	1.40	7.58	27	0.036
23	0.460	0.454	5985	2.606	1.39	7.37	26	0.036
24	0.333	0.539	5675	2.447	1.42	8.85	23	0.035
25	-0.167	0.575	5555	2.204	1.48	11.71	16	0.038
26	-0.818	0.811	4868	1.641	1.60	22.39	8	0.035
27	-1.212	0.944	4651	1.364	1.65	30.78	3	0.019
28	1.949	0.088	8427	3.815	1.13	1.83	97	0.026

Table 3.4. NGC 362's representative average stellar types as derived from its scanned region's CMD. See Table 3.3 for available explanations.

Box	$\langle M_v \rangle$ (mag)	$\langle (B-V) \rangle$ (mag)	T_{eff} (K)	$log(g_\star)$ $(log(cgs))$	ξ_v $(km\ s^{-1})$	R $(R_\odot)$	N_{stars}	Flux Frac.
1	5.328	0.483	5931	4.522	0.98	0.81	3821	0.035
2	4.674	0.439	6108	4.316	1.03	1.03	2006	0.035
3	4.302	0.416	6205	4.198	1.05	1.18	1420	0.035
4	4.011	0.413	6218	4.086	1.08	1.34	1085	0.035
5	3.760	0.419	6192	3.979	1.10	1.52	861	0.035
6	3.536	0.468	5977	3.823	1.13	1.82	700	0.035
7	3.252	0.536	5711	3.620	1.17	2.29	541	0.035
8	2.780	0.599	5500	3.355	1.23	3.11	352	0.035
9	2.207	0.647	5354	3.069	1.29	4.32	208	0.035
10	1.663	0.683	5251	2.811	1.35	5.82	126	0.035
11	1.102	0.734	5084	2.513	1.41	8.20	75	0.035
12	0.724	0.775	4968	2.308	1.45	10.39	53	0.035
13	0.429	0.804	4903	2.157	1.49	12.36	41	0.036
14	0.036	0.856	4813	1.954	1.53	15.60	28	0.035
15	-0.294	0.905	4731	1.779	1.57	19.09	21	0.036
16	-0.574	0.947	4664	1.628	1.60	22.73	16	0.035
17	-0.916	1.043	4516	1.403	1.65	29.43	12	0.036
18	-1.239	1.151	4361	1.170	1.70	38.49	9	0.037
19	-1.517	1.223	4264	0.992	1.73	47.24	7	0.037
20	-1.646	1.284	4185	0.877	1.76	53.95	6	0.036
21	-1.850	1.367	4082	0.708	1.79	65.56	6	0.043
22	-2.069	1.494	3934	0.482	1.84	84.97	5	0.044
23	-2.142	1.403	4039	0.552	1.83	78.40	2	0.019
24	0.756	0.560	5625	2.598	1.39	7.43	55	0.036
25	0.692	0.563	5615	2.569	1.40	7.69	51	0.035
26	0.403	0.607	5475	2.401	1.43	9.33	42	0.036
27	-0.489	0.760	5007	1.844	1.55	17.72	18	0.036
28	-0.959	0.749	5038	1.671	1.59	21.61	2	0.006
29	2.680	0.206	7663	3.950	1.10	1.57	50	0.005
30	1.458	-0.093	10000	3.988	1.10	1.50	147	0.033

Table 3.5. NGC 2808's representative average stellar types as derived from its scanned region's CMD. See Table 3.3 for available explanations.

Box	$\langle M_v \rangle$ (mag)	$\langle (B-V) \rangle$ (mag)	T_{eff} (K)	$log(g_\star)$ $(log(cgs))$	ξ_v $(km\ s^{-1})$	R $(R_\odot)$	N_{stars}	Flux Frac.
1	4.573	0.636	5293	3.982	1.10	1.51	904	0.035
2	4.094	0.587	5455	3.852	1.13	1.76	570	0.035
3	3.777	0.574	5499	3.742	1.15	1.99	425	0.035
4	3.478	0.612	5373	3.574	1.18	2.42	323	0.035
5	3.014	0.660	5228	3.331	1.24	3.20	212	0.035
6	2.484	0.688	5147	3.085	1.29	4.25	131	0.035
7	1.987	0.703	5101	2.866	1.33	5.46	82	0.035
8	1.531	0.724	5023	2.650	1.38	7.01	55	0.036
9	1.185	0.746	4952	2.478	1.42	8.54	39	0.035
10	0.891	0.776	4873	2.321	1.45	10.23	30	0.035
11	0.594	0.816	4798	2.165	1.48	12.25	23	0.036
12	0.385	0.823	4788	2.076	1.50	13.57	19	0.036
13	0.025	0.856	4737	1.905	1.54	16.51	14	0.036
14	-0.295	0.904	4666	1.736	1.58	20.05	11	0.039
15	-0.586	0.955	4593	1.577	1.61	24.09	8	0.036
16	-1.030	1.034	4484	1.332	1.66	31.94	6	0.041
17	-1.330	1.129	4360	1.126	1.71	40.51	5	0.045
18	-1.619	1.189	4285	0.956	1.74	49.25	3	0.036
19	-2.046	1.345	4103	0.634	1.81	71.37	3	0.052
20	-2.312	1.482	3955	0.390	1.86	94.44	2	0.045
21	-2.353	1.505	3932	0.349	1.87	99.07	1	0.023
22	0.091	0.663	5219	2.163	1.48	12.27	16	0.038
23	-0.614	0.846	4752	1.658	1.59	21.94	8	0.037
24	-1.079	0.989	4545	1.351	1.66	31.27	5	0.036
25	-1.327	1.077	4427	1.173	1.70	38.35	1	0.009
26	1.961	0.026	9182	3.923	1.11	1.62	112	0.035
27	0.993	0.037	8684	3.471	1.21	2.72	33	0.035
28	0.616	0.086	8080	3.221	1.26	3.63	22	0.032

Table 3.6. NGC 6093's representative average stellar types as derived from its scanned region's CMD. See Table 3.3 for available explanations.

Box	$\langle M_v \rangle$ (mag)	$\langle (B-V) \rangle$ (mag)	T_{eff} (K)	$log(g_\star)$ $(log(cgs))$	ξ_v $(km\ s^{-1})$	R $(R_\odot)$	N_{stars}	Flux Frac.
1	5.200	0.502	6030	4.519	0.98	0.81	4962	0.035
2	4.517	0.501	6034	4.249	1.04	1.11	2467	0.035
3	4.169	0.544	5868	4.055	1.08	1.39	1787	0.035
4	3.830	0.573	5761	3.883	1.12	1.69	1310	0.035
5	3.401	0.644	5505	3.617	1.18	2.30	886	0.035
6	2.878	0.728	5251	3.303	1.24	3.30	548	0.035
7	2.518	0.775	5122	3.101	1.28	4.17	391	0.035
8	2.109	0.813	5036	2.898	1.33	5.27	270	0.035
9	1.708	0.874	4916	2.677	1.38	6.79	186	0.035
10	1.432	0.890	4885	2.551	1.40	7.85	144	0.035
11	1.050	0.954	4766	2.336	1.45	10.05	102	0.035
12	0.616	1.032	4629	2.083	1.50	13.46	69	0.036
13	0.261	1.110	4500	1.863	1.55	17.34	49	0.035
14	-0.052	1.214	4339	1.626	1.60	22.77	37	0.035
15	-0.364	1.315	4193	1.391	1.65	29.85	28	0.036
16	-0.661	1.422	4050	1.150	1.70	39.38	21	0.035
17	-0.951	1.513	3935	0.920	1.75	51.31	17	0.037
18	-1.170	1.572	3864	0.755	1.78	62.07	10	0.027
19	1.199	0.764	5151	2.589	1.39	7.51	116	0.035
20	1.114	0.747	5196	2.576	1.40	7.62	107	0.035
21	1.064	0.742	5211	2.563	1.40	7.74	102	0.035
22	0.999	0.731	5242	2.552	1.40	7.84	97	0.035
23	0.909	0.717	5285	2.535	1.41	8.00	89	0.035
24	0.735	0.705	5324	2.481	1.42	8.51	76	0.035
25	0.194	0.911	4845	2.038	1.51	14.17	47	0.036
26	-0.254	1.032	4629	1.737	1.58	20.05	31	0.036
27	-0.664	1.201	4358	1.396	1.65	29.67	21	0.035
28	-1.402	1.185	4382	1.119	1.71	40.80	8	0.026
29	2.588	0.221	7629	3.920	1.11	1.62	75	0.006
30	1.179	-0.009	9409	3.653	1.17	2.21	95	0.024

Table 3.7. NGC 6388's representative average stellar types as derived from its scanned region's CMD. See Table 3.3 for available explanations.

Box	$\langle M_v \rangle$ (mag)	$\langle (B-V) \rangle$ (mag)	T_{eff} (K)	$log(g_\star)$ $(log(cgs))$	ξ_v $(km\ s^{-1})$	R $(R_\odot)$	N_{stars}	Flux Frac.
1	6.951	0.734	4971	4.793	0.92	0.59	439	0.035
2	5.810	0.505	5720	4.629	0.96	0.72	101	0.035
3	5.388	0.449	5938	4.530	0.98	0.80	68	0.035
4	5.084	0.411	6095	4.457	1.00	0.88	52	0.036
5	4.843	0.392	6177	4.385	1.01	0.95	41	0.035
6	4.589	0.374	6257	4.308	1.03	1.04	33	0.036
7	4.390	0.357	6334	4.252	1.04	1.11	28	0.036
8	4.188	0.349	6371	4.183	1.05	1.20	23	0.036
9	4.014	0.343	6399	4.123	1.07	1.29	20	0.037
10	3.838	0.346	6385	4.049	1.08	1.40	17	0.037
11	3.572	0.384	6213	3.892	1.12	1.68	13	0.036
12	3.328	0.445	5952	3.714	1.15	2.06	11	0.038
13	2.917	0.522	5654	3.450	1.21	2.79	7	0.035
14	2.334	0.555	5537	3.176	1.27	3.82	5	0.042
15	1.989	0.545	5572	3.052	1.30	4.41	3	0.036
16	1.355	0.591	5415	2.741	1.36	6.31	3	0.061
17	0.674	0.683	5131	2.353	1.44	9.86	2	0.079
18	0.199	0.782	4833	2.023	1.51	14.42	1	0.062
19	2.622	0.012	9694	4.242	1.04	1.12	6	0.036
20	1.924	-0.029	10000	4.012	1.09	1.46	3	0.038
21	1.496	-0.062	10000	3.905	1.11	1.65	2	0.036
22	1.199	-0.170	10000	4.123	1.07	1.28	2	0.049
23	1.028	-0.111	10000	3.821	1.13	1.82	2	0.057
24	0.725	-0.103	10000	3.707	1.16	2.07	1	0.038

Table 3.8. NGC 6397's representative average stellar types as derived from its scanned region's CMD. See Table 3.3 for available explanations.

Box	$\langle M_v \rangle$ (mag)	$\langle (B-V) \rangle$ (mag)	T_{eff} (K)	$log(g_\star)$ $(log(cgs))$	ξ_v $(km\ s^{-1})$	R $(R_\odot)$	N_{stars}	Flux Frac.
1	6.549	0.888	5064	4.677	0.95	0.68	1790	0.035
2	5.489	0.708	5602	4.468	0.99	0.86	473	0.035
3	5.010	0.655	5796	4.343	1.02	1.00	302	0.035
4	4.683	0.625	5915	4.250	1.04	1.11	223	0.035
5	4.423	0.605	5998	4.173	1.06	1.21	175	0.035
6	4.223	0.605	5998	4.093	1.07	1.33	146	0.035
7	3.986	0.606	5994	3.997	1.09	1.49	118	0.035
8	3.775	0.618	5944	3.897	1.12	1.67	97	0.035
9	3.578	0.653	5770	3.762	1.14	1.95	81	0.035
10	3.258	0.758	5364	3.486	1.20	2.68	61	0.035
11	2.763	0.822	5163	3.205	1.26	3.70	39	0.036
12	2.298	0.852	5082	2.984	1.31	4.77	25	0.035
13	1.896	0.871	5033	2.802	1.35	5.88	18	0.037
14	1.451	0.898	4965	2.592	1.39	7.49	12	0.037
15	1.032	0.956	4827	2.356	1.44	9.83	8	0.036
16	0.709	0.991	4749	2.187	1.48	11.94	6	0.036
17	0.241	0.996	4738	1.994	1.52	14.91	4	0.037
18	-0.183	1.048	4629	1.761	1.57	19.49	3	0.042
19	-0.428	1.072	4581	1.635	1.60	22.54	3	0.052
20	-0.961	1.140	4454	1.341	1.66	31.60	2	0.056
21	-1.396	1.205	4342	1.090	1.71	42.23	1	0.043
22	-1.460	1.225	4310	1.041	1.72	44.64	1	0.045
23	1.869	-0.056	9942	3.968	1.10	1.54	22	0.036
24	0.930	0.011	9273	3.523	1.20	2.56	8	0.040
25	0.282	0.420	6619	2.732	1.36	6.38	5	0.045
26	-0.491	0.945	4853	1.761	1.57	19.49	2	0.037

Table 3.9. NGC 6752's representative average stellar types as derived from its scanned region's CMD. See Table 3.3 for available explanations.

that corresponds to EW_i. These weights are calculated using

$$w_i = R_i^2 N_{\star_i} F_{c_i} \tag{3.7}$$

where R_i is the radius of the i^{th} average stellar type, $N_{\star_i}$ is the number of stars represented by the i^{th} average stellar type, and F_{c_i} is the continuum flux at the surface of the i^{th} average stellar type. Each stellar type's F_c is calculated by MOOG as a by-product of the line synthesis calculations, while R is calculated during the calculation of the model atmosphere parameters (see § 3.1). These weights are proportional to the total continuum flux contributed by all the stars that the i^{th} average stellar type represents. Finally, the iteration algorithm behind ILABUNDS can be found in Appendix A.

3.3 Fe Abundances

Following the standard abundance analysis used for individual stars, the abundance analysis of Fe lines proceeds iteratively, until the mean metallicity obtained from a cluster's Fe lines and the metallicity used in the cluster's model atmospheres converge. In this way, the model atmosphere and Fe abundance solutions are jointly determined. The mean Fe abundance from all measured Fe lines in an IL spectrum is calculated using a robust σ-clipping routine. To do this, the individual Fe abundances synthesized for the Fe lines are all fit as a linear function of their EP, EW, and wavelength, respectively. Lines for which the Fe abundances have more than a ± 2 RMS deviation from the linear fit for any of these relationships are rejected. The mean Fe abundance converges in 2 or 3 rejection cycles. The final mean Fe abundances for the clusters are listed in the left-hand columns of Tables 3.10 through 3.16. The individual Fe line results for each cluster as a function of EP, EW, and wavelength are shown in Figures 3.10 and 3.11.

The relationships shown in these plots are typically used to diagnose errors in stellar atmosphere parameters. The relatively weak slopes seen here are a strong indication that the method is able to identify accurate [Fe/H] solutions using IL-

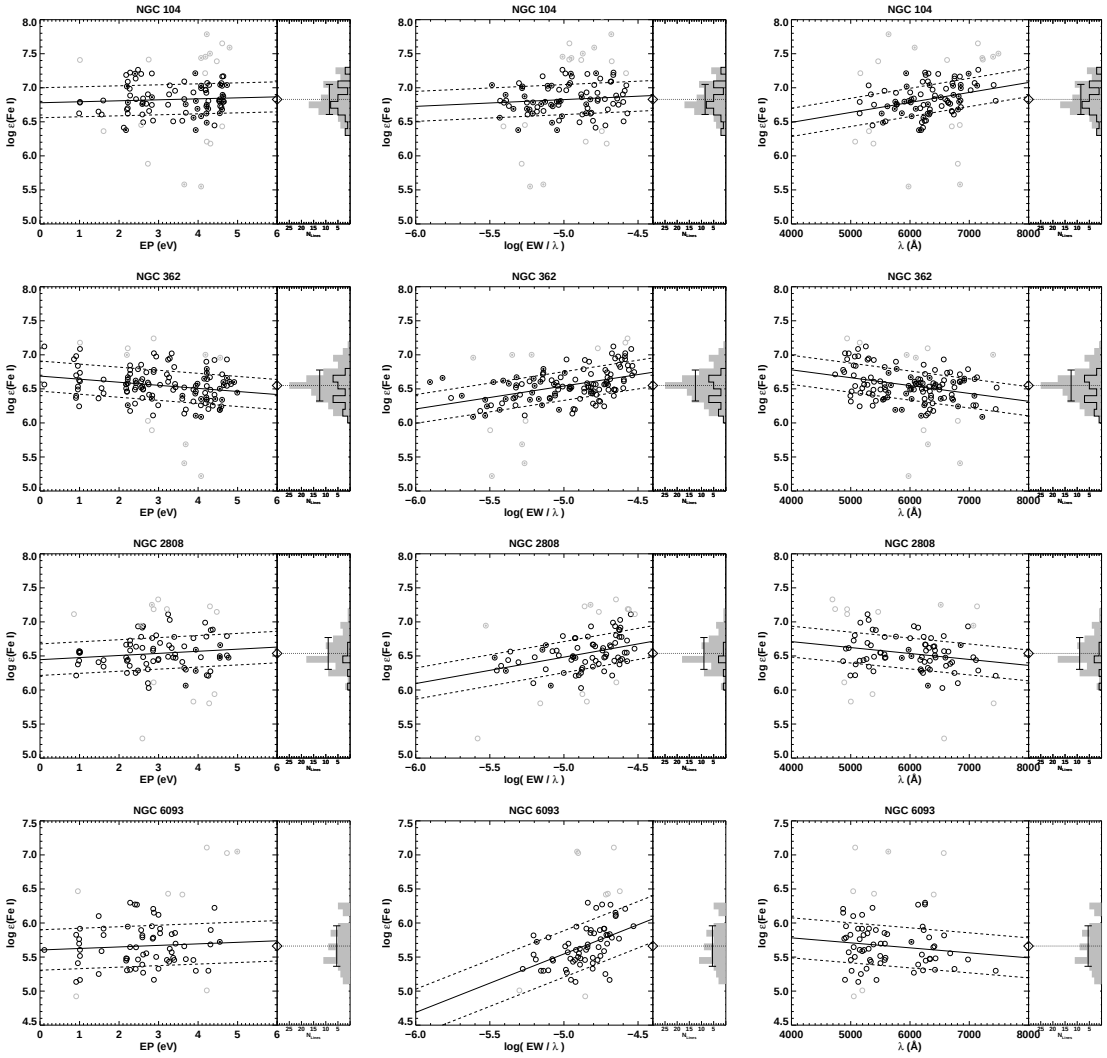

Figure 3.10. Fe line abundances synthesized from the IL spectra of NGC 104, NGC 362, NGC 2808, and NGC 6093, when using each cluster's photometric CMD to define its set of model atmospheres. From top-to-bottom, rows 1, 2, 3, and 4 pertain to NGC 104, NGC 362, NGC 2808, and NGC 6093, respectively. From left-to-right, columns 1, 2, and 3 show the Fe line abundances versus their EPs, reduced EWs (i.e. $log(EW/\lambda)$), and λ, respectively. Within the left panel of each plot, black circles, grey circles, and filled circles respectively correspond to Fe I abundances that survived the σ-clipping routine, Fe I abundances that failed the σ-clipping routine, and "clean" Fe I lines in Arcturus, as defined by Fulbright et al. (2006). The solid black lines depict the linear best-fit lines for the Fe I abundance data. The black dotted lines denote a distance of ± 1 RMS deviation around the best-fit lines for the Fe I abundance data. The right panel of each plot displays an Fe I line abundance histogram, which is a projection of the left panel's abundance plot. The light grey histograms correspond to all the Fe I line abundances, while the histograms outlined in black correspond to the "clean" Fe I lines in Arcturus. The black diamonds located between the left and right panels correspond to the mean Fe I abundances for the clusters. Finally, the solid black error bars, overlaid on each histogram, correspond to the ± 1 standard deviations of the Fe I abundance sample.

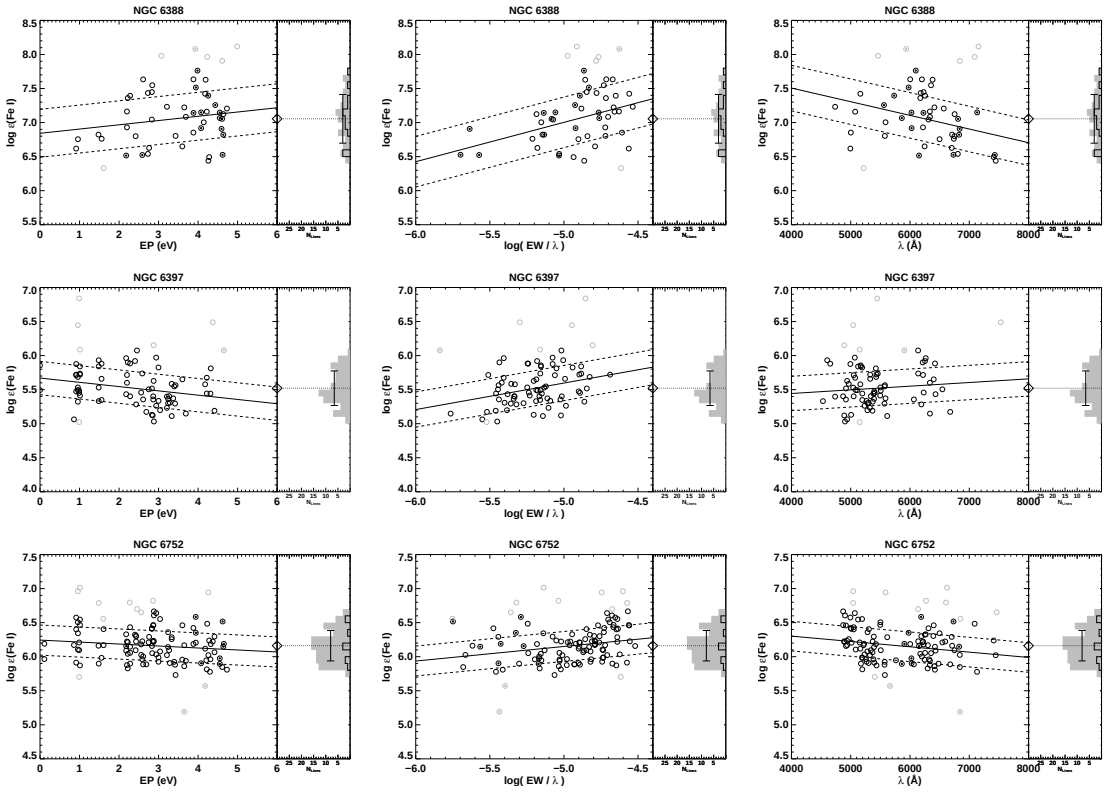

Figure 3.11. Fe line abundances synthesized from the IL spectra of NGC 6388, NGC 6397, and NGC 6752, when using each cluster's photometric CMD to define its set of model atmospheres. See Figure 3.10 for a description of the plotting conventions and notations.

ABUNDS and that the stellar parameter calculations are sufficiently accurate to do so with uncertainties comparable to those typically obtained from the analysis of individual stars. With the Fe abundances measured, the model atmospheres can be finalized using either solar or α-enriched abundances. Anticipating the results below, α-enriched abundances are adopted here. As shown in Sections 3.4 and 4.5, the analysis of Ca, Si, and Ti can be used to confirm the appropriateness of this choice, even without prior knowledge of the overall GC abundances. In the analysis of extragalactic GC systems (see Colucci et al. 2009), these α-abundances are checked and then one final iteration on the Fe solution is conducted to assure that the correct atmospheric models are used in all analyses.

	Photometric CMD Analysis					Theoretical SSP Analysis					Standard Stellar Analysis			
Species	$log\,\epsilon(X)$	σ_{mean}	σ	N_{lines}	[X/Fe]	$log\,\epsilon(X)$	σ_{mean}	σ	N_{lines}	[X/Fe]	$log\,\epsilon(X)$	σ	N_{stars}	[X/Fe]
Fe I	6.83	0.02	0.22	83	-0.67	6.83	0.02	0.22	85	-0.67	6.89	0.04	24	-0.61
Fe II	6.80	0.11	0.30	7	-0.70	7.03	0.12	0.31	7	-0.47	6.89	0.08	24	-0.61
Al I	6.16	0.03	0.04	2	0.46	6.09	0.04	0.06	2	0.39	5.97	0.16	16	0.21
Ba II	1.60	0.26	0.37	2	0.13	1.66	0.24	0.34	2	-0.04	1.78	0.07	6	0.22
Ca I	5.93	0.06	0.21	10	0.29	5.85	0.06	0.20	10	0.21	5.78	0.06	16	0.08
Co I	4.73	0.30	0.53	3	0.48	4.71	0.32	0.55	3	0.46	...	...	...	...
Cr I	5.07	0.16	0.23	2	0.10	4.94	0.19	0.26	2	-0.03	5.11	0.07	11	0.08
Cu I	3.41	...	...	1	-0.13	3.45	...	...	1	-0.08	...	...	...	...
Eu II	0.06	...	...	1	0.24	0.10	...	...	1	0.05	0.11	0.14	13	0.20
La II	0.74	...	...	1	0.31	0.70	...	...	1	0.04	0.82	0.16	11	0.31
Mg I	7.06	...	...	1	0.20	7.08	...	...	1	0.23	7.18	0.10	14	0.26
Mn I	4.34	0.14	0.31	5	-0.37	4.34	0.13	0.30	5	-0.38	4.36	0.12	12	-0.42
Na I	5.98	...	...	1	0.48	5.91	...	...	1	0.41	5.92	0.37	23	0.36
Nd II	0.61	...	...	1	-0.14	0.66	...	...	1	-0.32	1.32	0.09	7	0.48
Ni I	5.62	0.06	0.21	12	0.06	5.65	0.06	0.21	12	0.09	5.62	0.14	12	0.00
Sc II	2.46	0.21	0.30	2	0.11	2.57	0.18	0.26	2	-0.01	2.58	0.15	12	0.14
Si I	7.21	0.11	0.25	5	0.38	7.31	0.11	0.25	5	0.48	7.11	0.14	16	0.21
Ti I	4.54	0.10	0.34	12	0.32	4.39	0.10	0.33	12	0.16	4.58	0.10	16	0.29
Ti II	4.64	0.06	0.10	3	0.45	4.80	0.06	0.10	3	0.37	4.76	0.15	15	0.47
V I	3.32	0.19	0.38	4	0.00	3.06	0.24	0.49	4	-0.27	3.36	0.08	10	-0.02
Y II	1.70	0.20	0.34	3	0.19	1.84	0.22	0.37	3	0.10	2.12	0.36	9	0.52

Table 3.10. NGC 104's abundances. The "Photometric CMD Analysis" column contains abundance data derived using the IL spectra analysis method, when using the cluster's photometric CMD to define its stellar atmospheres. The "Theoretical SSP Analysis" column contains abundance data derived using the IL spectra analysis method, when using the cluster's best matching 13 *Gyr* theoretical SSP to define its stellar atmospheres (see Chapter 4). The "Standard Stellar Analysis" column contains abundance data derived from conventional stellar abundance analyses published throughout the literature (see Appendix B). The σ_{mean} and σ sub-columns equal the standard deviation of each species' mean line abundance and its entire sample of line abundances, respectively (i.e. $\sigma_{mean} = \frac{\sigma}{\sqrt{N_{lines}}}$). Note that for Fe I and Fe II, the values in the [X/Fe] column represent [Fe/H] values. The accuracy of the method's abundance results can be ascertained by directly comparing their values to the standard stellar abundances.

	Photometric CMD Analysis					Theoretical SSP Analysis					Standard Stellar Analysis			
Species	$log\,\epsilon(X)$	σ_{mean}	σ	N_{lines}	[X/Fe]	$log\,\epsilon(X)$	σ_{mean}	σ	N_{lines}	[X/Fe]	$log\,\epsilon(X)$	σ	N_{stars}	[X/Fe]
Fe I	6.54	0.02	0.22	116	-0.96	6.38	0.02	0.19	112	-1.12	6.20	0.03	7	-1.29
Fe II	6.39	0.07	0.21	10	-1.11	6.48	0.07	0.22	10	-1.02	6.18	0.07	7	-1.32
Al I	5.59	···	···	1	0.18	5.49	···	···	1	0.25	5.45	0.24	12	0.38
Ba II	1.55	0.10	0.18	3	0.49	1.46	0.10	0.16	3	0.32	1.08	0.22	12	0.24
Ca I	5.66	0.06	0.24	14	0.31	5.46	0.06	0.24	14	0.27	5.21	0.07	12	0.19
Ce II	0.34	···	···	1	-0.13	0.26	···	···	1	-0.30	···	···	···	···
Co I	4.08	0.22	0.45	4	0.12	3.91	0.26	0.52	4	0.11	···	···	···	···
Cr I	4.74	0.11	0.25	5	0.06	4.53	0.13	0.28	5	0.01	···	···	···	···
Cu I	2.61	···	···	1	-0.64	2.48	···	···	1	-0.61	2.24	0.10	10	-0.68
La II	0.45	···	···	1	0.43	0.39	···	···	1	0.28	···	···	···	···
Mg I	6.97	0.11	0.22	4	0.39	6.76	0.11	0.22	4	0.35	6.62	0.09	12	0.38
Mn I	3.82	0.17	0.49	8	-0.62	3.60	0.20	0.56	8	-0.66	3.58	0.10	12	-0.52
Na I	5.51	···	···	1	0.29	5.40	···	···	1	0.35	5.04	0.21	12	0.16
Nd II	0.98	···	···	1	0.64	0.90	···	···	1	0.47	···	···	···	···
Ni I	5.16	0.05	0.18	12	-0.11	5.04	0.05	0.17	12	-0.06	4.86	0.05	12	-0.08
Sc I	2.00	···	···	1	-0.10	1.75	···	···	1	-0.17	···	···	···	···
Sc II	2.17	0.12	0.21	3	0.23	2.13	0.11	0.19	3	0.10	1.68	0.11	12	-0.05
Si I	6.71	0.12	0.30	6	0.16	6.69	0.12	0.29	6	0.31	6.58	0.09	8	0.36
Ti I	4.31	0.08	0.28	14	0.36	4.06	0.07	0.27	14	0.28	3.96	0.08	12	0.36
Ti II	4.34	0.09	0.35	16	0.55	4.32	0.09	0.35	16	0.44	···	···	···	···
V I	3.05	···	···	1	0.00	2.84	···	···	1	-0.03	2.65	0.04	12	-0.06
Y II	1.10	0.02	0.02	2	0.00	1.08	0.00	0.00	2	-0.107	···	···	···	···
Zr I	2.40	···	···	1	0.76	2.16	···	···	1	0.69	···	···	···	···
Zr II	3.26	···	···	1	1.78	3.18	···	···	1	1.61	···	···	···	···

Table 3.11. NGC 362's abundances. See Table 3.10 for a description of the table's contents.

	Photometric CMD Analysis					Theoretical SSP Analysis					Standard Stellar Analysis			
Species	$log\,\epsilon(X)$	σ_{mean}	σ	N_{lines}	[X/Fe]	$log\,\epsilon(X)$	σ_{mean}	σ	N_{lines}	[X/Fe]	$log\,\epsilon(X)$	σ	N_{stars}	[X/Fe]
Fe I	6.54	0.03	0.23	71	-0.96	6.43	0.02	0.21	70	-1.07	6.42	0.10	141	-1.08
Fe II	6.19	0.11	0.25	5	-1.31	6.26	0.11	0.24	5	-1.24	6.33	0.11	110	-1.17
Al I	6.07	···	···	1	0.67	5.99	···	···	1	0.69	5.77	0.52	18	0.48
Ba II	1.34	0.09	0.16	3	0.14	1.22	0.10	0.16	3	0.30	···	···	···	···
Ca I	5.67	0.11	0.34	9	0.32	5.53	0.11	0.32	9	0.30	5.45	0.08	19	0.22
Co I	4.32	0.25	0.35	2	0.37	4.23	0.25	0.35	2	0.38	···	···	···	···
Cr I	4.67	0.15	0.30	4	-0.01	4.49	0.13	0.27	4	-0.08	4.55	0.09	19	-0.01
Cu I	2.80	···	···	1	-0.45	2.72	···	···	1	-0.42	···	···	···	···
Mg I	6.61	···	···	1	0.04	6.43	···	···	1	-0.03	6.61	0.15	19	0.16
Mn I	4.27	0.16	0.33	4	-0.16	4.16	0.15	0.30	4	-0.16	3.92	0.09	19	-0.39
Nd II	1.24	···	···	1	1.10	1.21	···	···	1	1.00	···	···	···	···
Ni I	5.15	0.09	0.28	10	-0.12	5.09	0.09	0.29	10	-0.06	5.07	0.06	19	-0.08
Sc II	2.40	0.14	0.19	2	0.66	2.40	0.13	0.18	2	0.59	1.95	0.10	19	0.07
Si I	6.82	0.06	0.11	3	0.27	6.84	0.06	0.11	3	0.41	6.75	0.08	19	0.32
Ti I	4.20	0.10	0.28	7	0.27	4.00	0.11	0.29	7	0.17	4.17	0.07	19	0.34
Ti II	4.32	0.24	0.63	7	0.73	4.30	0.23	0.61	7	0.64	4.13	0.13	18	0.40
V I	2.76	···	···	1	-0.27	2.53	···	···	1	-0.40	2.87	0.11	19	-0.05
Y II	0.47	···	···	1	-0.43	0.47	···	···	1	-0.50	···	···	···	···

Table 3.12. NGC 2808's abundances. See Table 3.10 for a description of the table's contents.

	Photometric CMD Analysis					Theoretical SSP Analysis					Standard Stellar Analysis			
Species	$log\,\epsilon(X)$	σ_{mean}	σ	N_{lines}	[X/Fe]	$log\,\epsilon(X)$	σ_{mean}	σ	N_{lines}	[X/Fe]	$log\,\epsilon(X)$	σ	N_{stars}	[X/Fe]
Fe I	5.66	0.04	0.28	61	-1.83	5.85	0.03	0.25	59	-1.65	5.79	0.13	10	-1.71
Fe II	5.82	0.09	0.20	5	-1.68	5.81	0.09	0.19	5	-1.69	···	···	···	···
Ba II	0.81	0.11	0.16	2	0.32	0.95	0.08	0.13	3	0.46	···	···	···	···
Ca I	4.91	0.13	0.47	14	0.43	5.04	0.13	0.47	14	0.38	4.86	0.16	10	0.27
Cr I	3.84	0.21	0.42	4	0.03	4.03	0.19	0.39	4	0.04	3.96	0.30	4	0.03
Mg I	6.46	0.21	0.37	3	0.76	6.46	0.17	0.29	3	0.58	···	···	···	···
Mn I	3.39	0.09	0.12	2	-0.17	3.57	0.05	0.07	2	-0.18	···	···	···	···
Ni I	4.50	0.16	0.36	5	0.10	4.71	0.17	0.39	5	0.12	4.47	0.18	10	-0.05
Sc II	1.84	0.26	0.44	3	0.47	1.90	0.22	0.39	3	0.54	···	···	···	···
Si I	6.16	0.11	0.15	2	0.48	6.22	0.11	0.15	2	0.36	···	···	···	···
Ti I	3.72	0.18	0.53	9	0.65	3.94	0.17	0.51	9	0.68	3.37	0.34	9	0.19
Ti II	3.74	0.07	0.24	11	0.52	3.72	0.09	0.30	12	0.51	3.76	0.12	6	0.58
Zr II	2.35	···	···	1	1.43	2.35	···	···	1	1.48	···	···	···	···

Table 3.13. NGC 6093's abundances. See Table 3.10 for a description of the table's contents.

	Photometric CMD Analysis					Theoretical SSP Analysis					Standard Stellar Analysis			
Species	$log\,\epsilon(X)$	σ_{mean}	σ	N_{lines}	[X/Fe]	$log\,\epsilon(X)$	σ_{mean}	σ	N_{lines}	[X/Fe]	$log\,\epsilon(X)$	σ	N_{stars}	[X/Fe]
Fe I	7.08	0.05	0.35	44	-0.42	7.03	0.06	0.37	46	-0.47	7.10	0.04	7	-0.40
Fe II	7.05	0.06	0.13	5	-0.45	7.38	0.06	0.14	5	-0.12	7.12	0.09	7	-0.38
Al I	6.69	···	···	1	0.74	6.56	···	···	1	0.65	6.72	0.25	7	0.75
Ba II	2.31	0.49	0.70	2	0.58	2.29	0.49	0.69	2	0.24	1.90	0.12	7	0.11
Ca I	5.70	···	···	1	-0.19	5.53	···	···	1	-0.31	5.89	0.06	7	-0.02
Co I	4.65	···	···	1	0.15	4.57	···	···	1	0.12	4.52	0.09	7	0.00
Cr I	5.43	0.07	0.10	2	0.21	5.22	0.04	0.05	2	0.05	5.20	0.09	7	-0.04
Mn I	4.88	0.08	0.15	3	-0.08	4.77	0.10	0.18	3	-0.15	4.65	0.05	7	-0.34
Ni I	5.70	0.12	0.36	8	-0.11	5.69	0.12	0.34	8	-0.07	5.87	0.06	7	0.04
Sc I	2.14	···	···	1	-0.49	1.60	···	···	1	-0.98	···	···	···	···
Sc II	2.47	0.22	0.31	2	-0.13	2.56	0.26	0.36	2	-0.37	2.74	0.08	7	0.07
Si I	7.48	0.16	0.23	2	0.39	7.59	0.16	0.22	2	0.55	7.41	0.12	7	0.30
Ti I	4.64	0.23	0.46	4	0.16	4.34	0.26	0.51	4	-0.09	4.93	0.07	7	0.43
Ti II	5.23	0.15	0.21	2	0.78	5.36	0.14	0.19	2	0.58	4.93	0.14	7	0.41
Y II	2.25	···	···	1	0.48	2.34	···	···	1	0.25	···	···	···	···

Table 3.14. NGC 6388's abundances. See Table 3.10 for a description of the table's contents.

	Photometric CMD Analysis					Theoretical SSP Analysis					Standard Stellar Analysis			
Species	$log\,\epsilon(X)$	σ_{mean}	σ	N_{lines}	[X/Fe]	$log\,\epsilon(X)$	σ_{mean}	σ	N_{lines}	[X/Fe]	$log\,\epsilon(X)$	σ	N_{stars}	[X/Fe]
Fe I	5.52	0.03	0.25	71	-1.98	5.46	0.03	0.22	60	-2.04	5.48	0.03	6	-2.02
Fe II	5.40	0.07	0.21	8	-2.10	5.23	0.07	0.20	8	-2.27	5.50	0.07	6	-2.00
Ba II	0.30	0.10	0.22	5	0.23	0.10	0.13	0.29	5	0.20	-0.04	0.13	18	-0.22
Ca I	4.59	0.09	0.22	6	0.26	4.59	0.09	0.23	6	0.32	4.56	0.09	16	0.28
Ce II	2.76	···	···	1	3.28	2.36	···	···	1	3.05	···	···	···	···
Co I	3.46	···	···	1	0.52	3.22	···	···	1	0.34	···	···	···	···
Cr I	3.22	0.26	0.52	4	-0.44	3.21	0.26	0.51	4	-0.40	···	···	···	···
Mg I	5.44	0.13	0.22	3	-0.12	5.29	0.09	0.15	3	-0.20	5.51	0.11	8	0.00
Mn I	2.67	0.05	0.07	2	-0.74	2.43	0.03	0.05	2	-0.92	···	···	···	···
Ni I	4.66	0.16	0.39	6	0.40	4.66	0.17	0.41	6	0.47	···	···	···	···
Sc II	1.58	0.28	0.40	2	0.62	1.26	0.07	0.10	2	0.48	···	···	···	···
Ti I	3.71	0.42	0.84	4	0.79	3.71	0.44	0.87	4	0.85	3.46	0.15	13	0.58
Ti II	3.46	0.10	0.39	15	0.65	3.17	0.09	0.36	15	0.54	···	···	···	···
V I	3.76	···	···	1	1.74	3.83	···	···	1	1.87	···	···	···	···
Y II	3.11	···	···	1	2.99	2.99	···	···	1	3.05	···	···	···	···
Zr I	3.30	···	···	1	2.69	3.36	···	···	1	2.80	···	···	···	···
Zr II	1.34	···	···	1	0.84	1.10	···	···	1	0.78	···	···	···	···

Table 3.15. NGC 6397's abundances. See Table 3.10 for a description of the table's contents.

	Photometric CMD Analysis					Theoretical SSP Analysis					Standard Stellar Analysis			
Species	$log\,\epsilon(X)$	σ_{mean}	σ	N_{lines}	[X/Fe]	$log\,\epsilon(X)$	σ_{mean}	σ	N_{lines}	[X/Fe]	$log\,\epsilon(X)$	σ	N_{stars}	[X/Fe]
Fe I	6.15	0.02	0.22	100	-1.35	5.91	0.02	0.22	98	-1.59	5.99	0.02	8	-1.51
Fe II	6.33	0.07	0.21	9	-1.17	6.07	0.07	0.21	9	-1.43	5.95	0.10	8	-1.55
Al I	5.71	···	···	1	0.68	5.56	···	···	1	0.78	5.12	0.50	29	0.26
Ba II	1.25	0.06	0.11	3	0.25	0.85	0.06	0.10	3	0.11	0.82	0.08	18	0.20
Ca I	5.38	0.05	0.22	21	0.42	5.22	0.05	0.23	21	0.50	5.04	0.20	11	0.24
Ce II	0.26	···	···	1	-0.15	-0.07	···	···	1	-0.22	···	···	···	···
Co I	4.22	···	···	1	0.64	3.84	···	···	1	0.51	···	···	···	···
Cr I	4.46	0.14	0.31	5	0.16	4.16	0.15	0.34	5	0.12	4.16	0.17	3	0.03
Cu I	2.19	···	···	1	-0.68	1.88	···	···	1	-0.74	···	···	···	···
Eu II	-0.14	···	···	1	0.51	-0.42	···	···	1	0.49	-0.52	0.11	28	0.52
Mg I	6.69	0.19	0.37	4	0.50	6.54	0.17	0.34	4	0.60	6.02	0.17	18	0.00
Mn I	3.78	0.18	0.48	7	-0.26	3.49	0.18	0.47	7	-0.30	3.23	0.06	15	-0.65
Na I	5.12	···	···	1	0.29	4.96	···	···	1	0.38	5.02	0.31	36	0.36
Nd II	0.07	···	···	1	-0.21	-0.24	···	···	1	-0.26	···	···	···	···
Ni I	4.78	0.06	0.18	9	-0.10	4.55	0.09	0.29	11	-0.09	4.54	0.11	11	-0.17
Sc II	2.37	0.28	0.48	3	0.49	2.01	0.26	0.45	3	0.39	···	···	···	···
Si I	6.80	0.16	0.36	5	0.64	6.72	0.16	0.36	5	0.80	···	···	···	···
Ti I	4.00	0.09	0.35	16	0.45	3.64	0.09	0.38	16	0.33	3.56	0.33	8	0.18
Ti II	4.40	0.08	0.36	21	0.67	4.08	0.08	0.36	21	0.61	3.80	0.18	8	0.45
V I	2.47	···	···	1	-0.18	2.19	···	···	1	-0.22	···	···	···	···
Y I	3.32	···	···	1	2.45	2.79	···	···	1	2.17	···	···	···	···
Y II	1.52	0.05	0.08	2	0.48	1.09	0.09	0.13	2	0.31	0.75	0.10	18	0.09
Zr II	2.03	···	···	1	0.61	1.63	···	···	1	0.47	···	···	···	···

Table 3.16. NGC 6752's abundances. See Table 3.10 for a description of the table's contents.

3.4 Abundances for all other Elements

With the model atmospheres fully determined from the Fe line analysis, ILABUNDS is used to analyze the lines measured for all other elements. These solutions converge quickly as the atmospheres do not need to be adjusted during this stage. The elements analyzed are listed in Table 2.4 for each cluster. The quality of each line is indicated by the *A*, *B*, *C* ranking system, as described in Chapter 2. All lines ranked *A* or *B* are used to compute the final mean abundance for an element, as there are typically not enough lines to allow a statistical rejection of outliers. The final mean abundances for each cluster are listed in the left-hand columns of Tables 3.10 through 3.16.

3.5 Abundance Results from Photometric CMDs

The accuracy of the abundance analysis method is empirically assessed by comparing its abundance results to the abundance results obtained from the standard stellar analysis of individual cluster stars, which are available in the literature. For each cluster, a set of published stellar abundances was assembled and averaged together in order to create mean reference abundances. These literature sources, and the averaging method used to combine them, are discussed in Appendix B. The final mean stellar abundances are listed in the right-hand columns of Tables 3.10 through 3.16.

A direct comparison between this chapter's [Fe/H] results and the mean stellar [Fe/H] results is shown in Figure 3.12, where a perfect agreement would result in all data points lying on a 1:1 equivalence line. Linear least-squares fits are used to both identify any statistical uncertainties and any systematic offsets between the abundance analysis method's Fe I and Fe II metallicities as compared to the results from individual stars. Allowing both the slopes and intercepts of the best-fit lines to vary, the reduced-χ^2 values for the fits are 0.49 and 1.09 for Fe I and Fe II solutions, respectively, with y-intercepts of +0.02 *dex* and −0.09 *dex*, and small slopes of 0.95 and 0.89, respectively. If the slopes of the Fe I and Fe II lines are constrained to 1.0, the reduced-χ^2 values are 0.43 and 1.01, respectively, and the y-intercepts are +0.09 *dex*

and +0.02 *dex*, respectively. As the lines with constrained and unconstrained slopes are similar in reduced-χ^2 values, the simpler, constrained slope lines are adopted as the relationship between the method's metallicities and the literature's metallicities. These constrained slope lines also have the advantage that their y-intercepts can be interpreted as the analysis method's systematic offsets from the 1:1 equivalence line. Furthermore, the RMS deviations for the data around the constrained slope lines can be attributed to the statistical uncertainties for the analysis method's metallicities. These statistical uncertainties are 0.16 *dex* and 0.20 *dex* for the Fe I and Fe II derived metallicities, respectively, and they are displayed in the residual plot shown in Figure 3.12's lower panel.

Note in this comparison that no errors have been assigned to the published stellar abundances. To illustrate the uncertainty that does exist in these results, the average standard deviation of the published stellar abundances is $\sim$ 0.06 *dex* for [Fe/H] from Fe I and $\sim$ 0.09 *dex* for [Fe/H] from Fe II. If the total statistical uncertainty in Figure 3.12's metallicity comparison is a quadratic combination of statistical errors in all results, then a better estimate of the abundance analysis method's statistical uncertainties are 0.15 *dex* and 0.18 *dex*, respectively. Therefore, the statistical uncertainties in the published stellar abundances do not appreciably contribute to the previously calculated uncertainties. Regardless, both the Fe I and Fe II metallicities have statistical uncertainties of $\sim$0.2 dex, which render their small systematic offsets (+0.09 *dex* and +0.02 *dex*) insignificant.

The internal accuracy of the abundance analysis method to measure all available elemental abundances on a cluster-by-cluster basis can also be investigated. The empirical comparison between the method's abundance results for each cluster and their individual stellar abundances are shown in Figures 3.13 and 3.14. Here, the same strategy employed for the metallicities in Figure 3.12 are used to assess these internal accuracies. The upper panels of the figures display the abundances from the IL spectra analysis method ($log\,\epsilon(\mathrm{X})_{\mathrm{Photo}}$) compared to the abundances obtained from individual stars ($log\,\epsilon(\mathrm{X})_{\mathrm{Lit}}$). Linear least-squares fits with slopes that are both unconstrained and constrained to 1.0 were applied to each cluster's neutral and singularly ionized

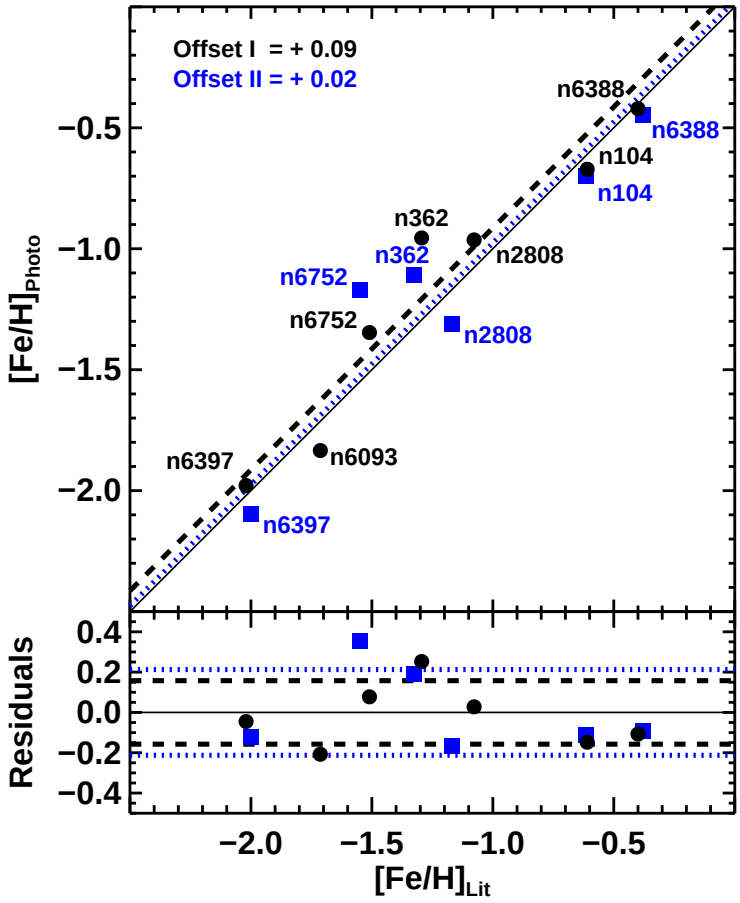

Figure 3.12. The abundance analysis method's accuracy in determining the metallicity of a cluster, when using each cluster's photometric CMD to define its stellar atmospheres. *Upper Panel*: $[Fe/H]_{Photo}$ corresponds to metallicities derived using the IL spectra abundance analysis method, while $[Fe/H]_{Lit}$ corresponds to metallicities derived from standard stellar abundance analyses in the literature. These $[Fe/H]_{Lit}$ values serve as fiducial metallicities against which the accuracy of the method's $[Fe/H]_{Photo}$ values are determined. The black solid line corresponds to a line of 1:1 equivalence between $[Fe/H]_{Photo}$ and $[Fe/H]_{Lit}$; therefore, any deviations from this line are attributed to errors in $[Fe/H]_{Photo}$. As discussed in the text, linear best-fit lines with slopes constrained to 1.0 are adopted to represent the relationship between $[Fe/H]_{Photo}$ and $[Fe/H]_{Lit}$. Black circles and blue squares depict [Fe/H] derived from Fe I and Fe II lines, respectively. The black dashed line and blue dotted line denote the linear best-fit lines for the Fe I and Fe II data, respectively. Based on the y-intercept offsets from the 1:1 line, $[Fe/H]_{Photo}$ has an average systematic offset from the published metallicities of +0.09 *dex* and +0.02 *dex* for Fe I and Fe II, respectively. *Lower Panel*: The *y-axis* corresponds to the residuals of the upper panel's metallicities with respect to their best-fit lines. Black circles and blue squares depict these residuals for Fe I and Fe II, respectively. The horizontal black dashed lines and blue dotted lines correspond to the ±1 RMS deviation scatter of the upper panel's Fe I and Fe II based metallicities around their corresponding best-fit lines, respectively. These RMS deviations are 0.16 *dex* and 0.20 *dex* for Fe I and Fe II, respectively. Therefore, $[Fe/H]_{Photo}$ has an average statistical uncertainty of 0.16 *dex* and 0.21 *dex* for the Fe I and Fe II based metallicities, respectively.

species. As with the metallicities in Figure 3.12, the fits with constrained slopes produce similar reduced-χ^2 values as the fits with unconstrained slopes. Therefore, the simpler fits with constrained slopes were adopted to represent the functional relationship between $log\,\epsilon(\mathrm{X})_{\mathrm{Photo}}$ and $log\,\epsilon(\mathrm{X})_{\mathrm{Lit}}$.

Again, the intercepts for the best-fit lines with constrained slopes are attributed to be the systematic offsets for the clusters' IL spectra abundance solutions, and the RMS deviations of the data around these lines are attributed to be the statistical uncertainties for the solutions. The numerical values for these systematic offsets and statistical uncertainties are listed in the captions of Figures 3.13 and 3.14. To determine which clusters have meaningful systematic offsets, the magnitudes of their offsets are compared to the magnitudes of their statistical uncertainties. Clusters NGC 362 and NGC 6752 both have meaningful systematic offsets equal to $\sim +0.3$ *dex* for their neutral species, and meaningful offsets equal to $+0.4$ *dex* and $+0.6$ *dex*, respectively, for their singularly ionized species. All other clusters have offsets within the range of their statistical uncertainties. Using all seven clusters, the mean statistical uncertainties for the neutral and singularly ionized species are 0.17 ± 0.04 *dex* and 0.24 ± 0.08 *dex*, respectively, where the assigned errors are simply the standard deviations for the calculations. The small assigned errors for these mean uncertainties indicates that all seven clusters have fairly universal statistical uncertainties. The mean systematic offsets for the seven clusters' neutral and singularly ionized species are $+0.14 \pm 0.14$ *dex* and $+0.21 \pm 0.27$ *dex*, respectively, where the assigned errors are once again the standard deviations for the calculations. The fact that the mean systematic offsets are similar to their assigned errors indicates that the IL spectra abundance results do not suffer from a single systematic offset that is universal for all the clusters, but instead are dominated by only NGC 362's and NGC 6752's offsets.

In an attempt to reduce any systematic abundance offsets through self-calibration, the abundance data is replotted in [X/Fe] format. Under ideal circumstances, this format produces self-calibration because any systematic offset shared by Fe and the other element in the ratio will logarithmically subtract out of the expression. Figures 3.15 and 3.16 show the abundance data in [X/Fe] format. Comparing these

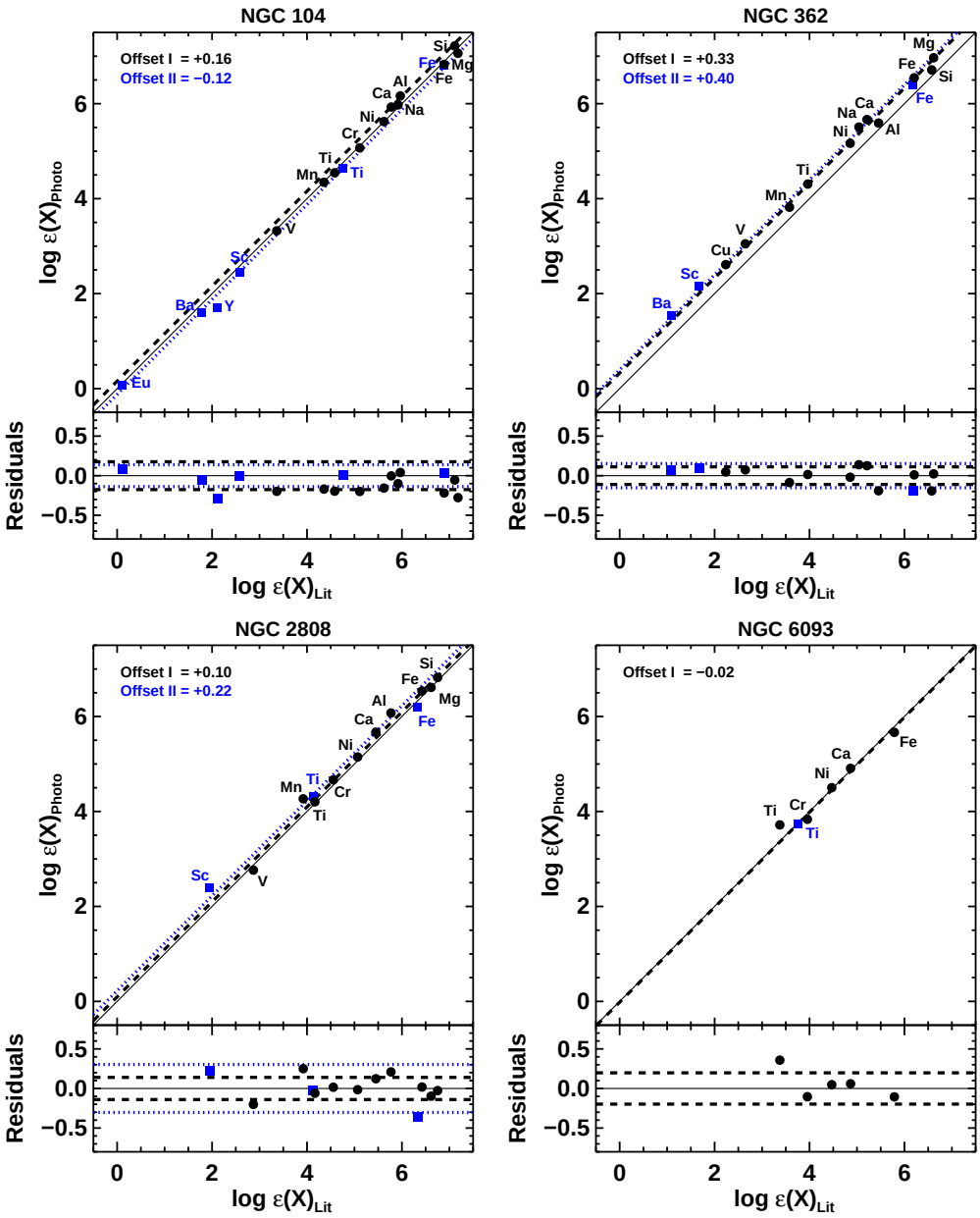

Figure 3.13. The abundance analysis method's internal accuracy in determining all the $log\,\epsilon(X)$ abundances for clusters NGC 104, NGC 362, NGC 2808, and NGC 6093, when using each cluster's photometric CMD to define its stellar atmospheres. All plotting conventions and data analysis match those used for the metallicities in Figure 3.12, except that the y-axis and x-axis of each plot's upper panel now correspond to its species' $log\,\epsilon(X)_{\rm Photo}$ and $log\,\epsilon(X)_{\rm Lit}$ abundances, respectively. *Upper Panels*: Based on the y-intercepts of their best-fit lines, the neutral species of NGC 104, NGC 362, NGC 2808, and NGC 6093 have average systematic abundance offsets of +0.16, +0.33, +0.10, and −0.02 *dex*, respectively. Likewise, the singularly ionized species of NGC 104, NGC 362, and NGC 2808 have average systematic offsets of −0.12, +0.40, and +0.22 *dex*, respectively. *Lower Panels*: Based on the RMS deviation of their neutral species abundances around their best-fit lines, NGC 104, NGC 362, NGC 2808, and NGC 6093 have average statistical uncertainties of 0.17, 0.11, 0.14, and 0.20 *dex*, respectively. Likewise, the singularly ionized species of NGC 104, NGC 362, and NGC 2808 have average statistical uncertainties of 0.14, 0.15, ad 0.30 *dex*, respectively.

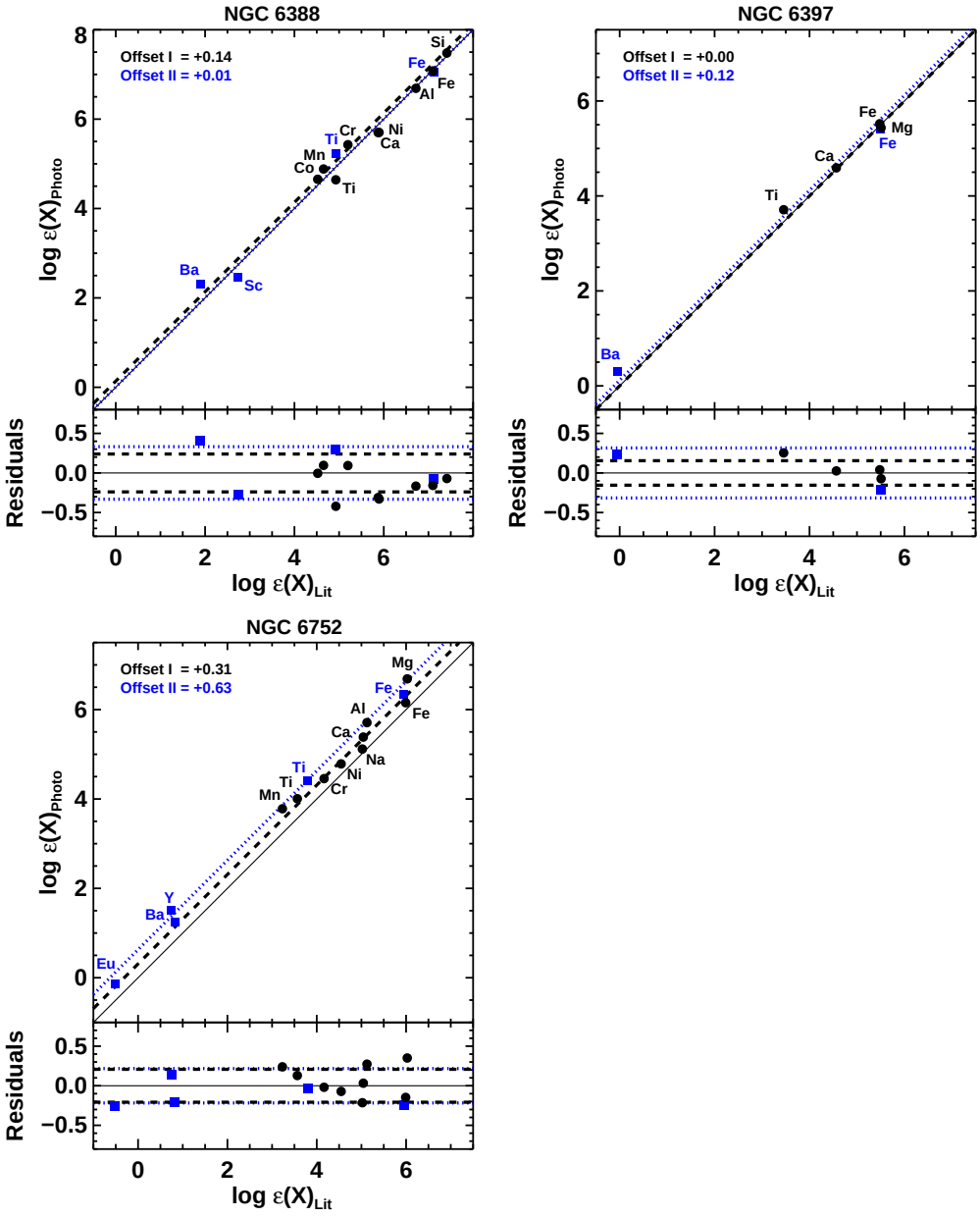

Figure 3.14. The abundance analysis method's internal accuracy in determining all the $log\,\epsilon(X)$ abundances for clusters NGC 6388, NGC 6397, and NGC 6752, when using each cluster's photometric CMD to define its stellar atmospheres. See Figure 3.13 for a description of the plotting conventions and data analysis. *Upper Panels*: The neutral species of NGC 6388, NGC 6397 and NGC 6752 have average systematic offsets of +0.14, 0.00, and +0.31 *dex*, respectively. Likewise, the singularly ionized species of NGC 6388, NGC 6397 and NGC 6752 have average systematic abundance offsets of +0.01, +0.12, and +0.63 *dex*, respectively. *Lower Panels*: The neutral species of NGC 6388, NGC 6397 and NGC 6752 have average statistical uncertainties of 0.24, 0.15, and 0.21 *dex*, respectively. Likewise, the singularly ionized species of NGC 6388, NGC 6397 and NGC 6752 have average statistical uncertainties of 0.33, 0.32, and 0.22 *dex*, respectively.

figures with their $log\,\epsilon$(X) counterparts (Figures 3.13 and 3.14) reveals that four of the seven clusters (NGC 362, NGC 2808, NGC 6388, NGC 6752) show noticeable improvement in their neutral species' [X/Fe] offsets compared to their $log\,\epsilon$(X) offsets. The offsets for NGC 2808, NGC 6388, and NGC 6752 all shrink by $\sim$0.1 *dex*, while NGC 362 shrinks by $\sim$0.3 *dex*. Meanwhile, the neutral species for NGC 104 and NGC 6397 have [X/Fe] offsets similar to their $log\,\epsilon$(X) counterparts, while NGC 6093's offset grows by $\sim$0.1 dex. As for the clusters' singularly ionized species, NGC 104, NGC 362, and NGC 6752 have [X/Fe] offsets that shrink by 0.05, 0.14, and 0.43 *dex*, respectively, while the offsets of NGC 2808 and NGC 6388 increase by 0.04 and 0.18 *dex*. Conducting similar comparisons between the statistical uncertainties shown in the [X/Fe] and $log\,\epsilon$(X) figures reveals that they generally remain at $\sim$0.2 *dex* regardless of the plotting method used, as would be expected for a self-calibration method.

The average [X/Fe] systematic offsets for all of the elements is quite small for most of the clusters. Typical offsets between the IL results and those from individual stars are in the range 0–0.1 *dex* for neutral species. Note that there are not enough ionized elements measured in these clusters to identify a "typical" offset for ionized elements, however the offset between the IL and individual star results assembled here is around +0.2 *dex*. For NGC 2808, there is a notably larger offset (+0.5 *dex*) in $[Ti/Fe]_{II}$ and $[Sc/Fe]_{II}$ between the IL results and those from stars. This is due to a combination of high Ti II and Sc II abundances and a low Fe II abundance, the cause of which is not obvious, but may have to do with the particularly strong blue HB for this cluster. Again, note that there is no consistent offset for the clusters in this sample between the IL results and those obtained from individual stars for the clusters.

Lastly, the accuracy of the abundance analysis can be investigated on an element-by-element basis. Figures 3.17 through 3.19 display $log\,\epsilon(X)_{Photo}$ versus $log\,\epsilon(X)_{Lit}$ for all elements that both have abundances measured in three or more clusters and possess stellar abundances in the literature. These elements include the Fe-peak elements Cr, Mn, Ni, Sc, and V displayed in Figure 3.17; the α-elements Ca, Mg, Si, and Ti displayed in Figure 3.18; the light-elements Al and Na displayed in Figure 3.19;

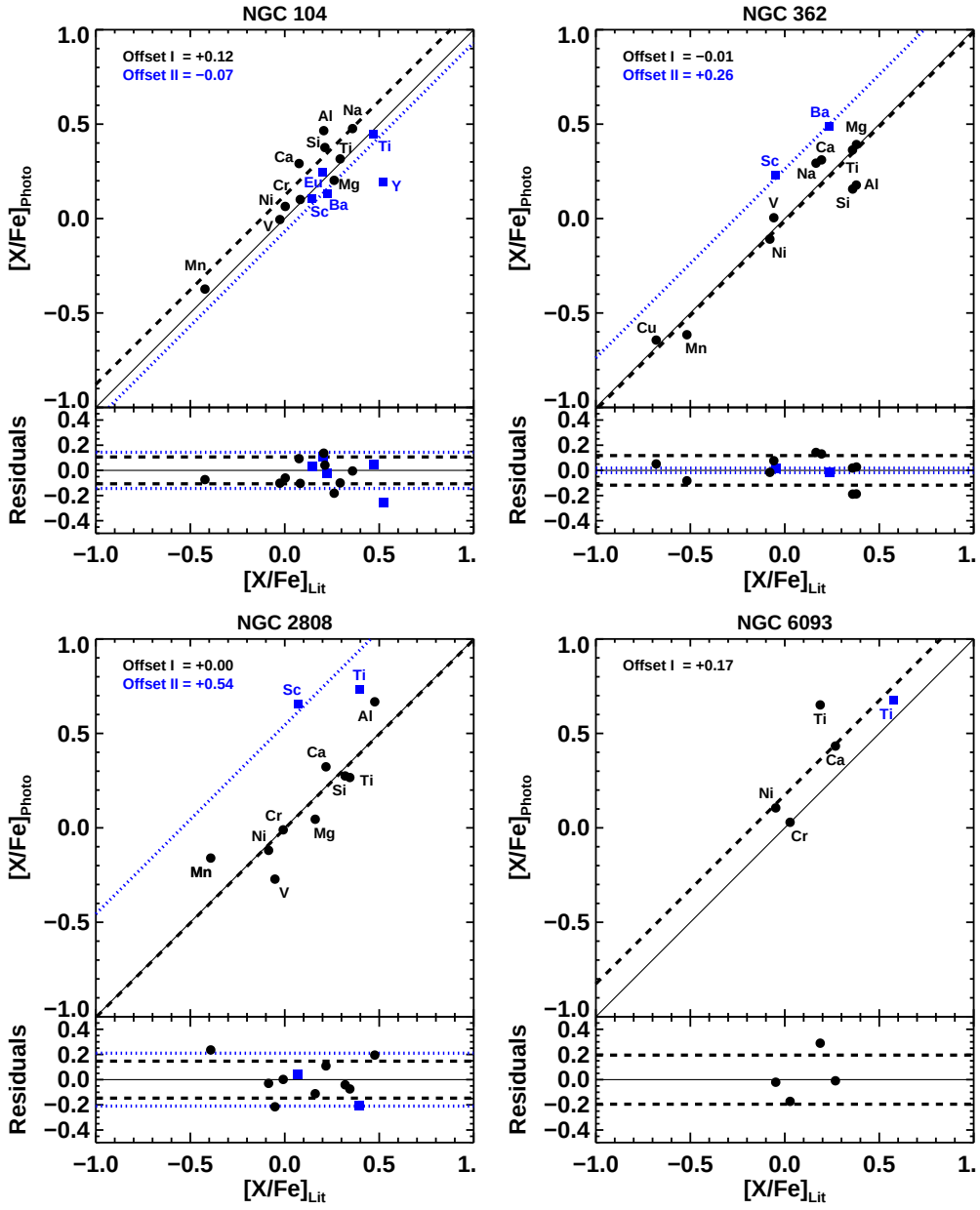

Figure 3.15. The abundance analysis method's internal accuracy in determining all the [X/Fe] abundance ratios for clusters NGC 104, NGC 362, NGC 2808, and NGC 6093, when using each cluster's photometric CMD to define its stellar atmospheres. All plotting conventions and data analysis match those used for the metallicities in Figure 3.12, except that the y-axis and x-axis of each plot's upper panel now correspond to its species' $[X/Fe]_{Photo}$ and $[X/Fe]_{Lit}$ abundance ratios, respectively. *Upper Panels*: Based on the y-intercepts of their best-fit lines, the neutral species of NGC 104, NGC 362, NGC 2808, and NGC 6093 have average systematic abundance offsets of +0.12, −0.01, 0.00, and +0.17 *dex*, respectively. Likewise, the singularly ionized species of NGC 104, NGC 362, and NGC 2808 have average systematic abundance offsets of −0.07, +0.26, and +0.54 *dex*, respectively. *Lower Panels*: Based on the RMS deviation of their neutral species abundances around their best-fit lines, NGC 104, NGC 362, NGC 2808, and NGC 6093 have average statistical uncertainties of 0.11, 0.12, 0.16, and 0.20 *dex*, respectively. Likewise, the singularly ionized species of NGC 104, NGC 362, and NGC 2808 have average statistical uncertainties of 0.14, 0.02, ad 0.21 *dex*, respectively.

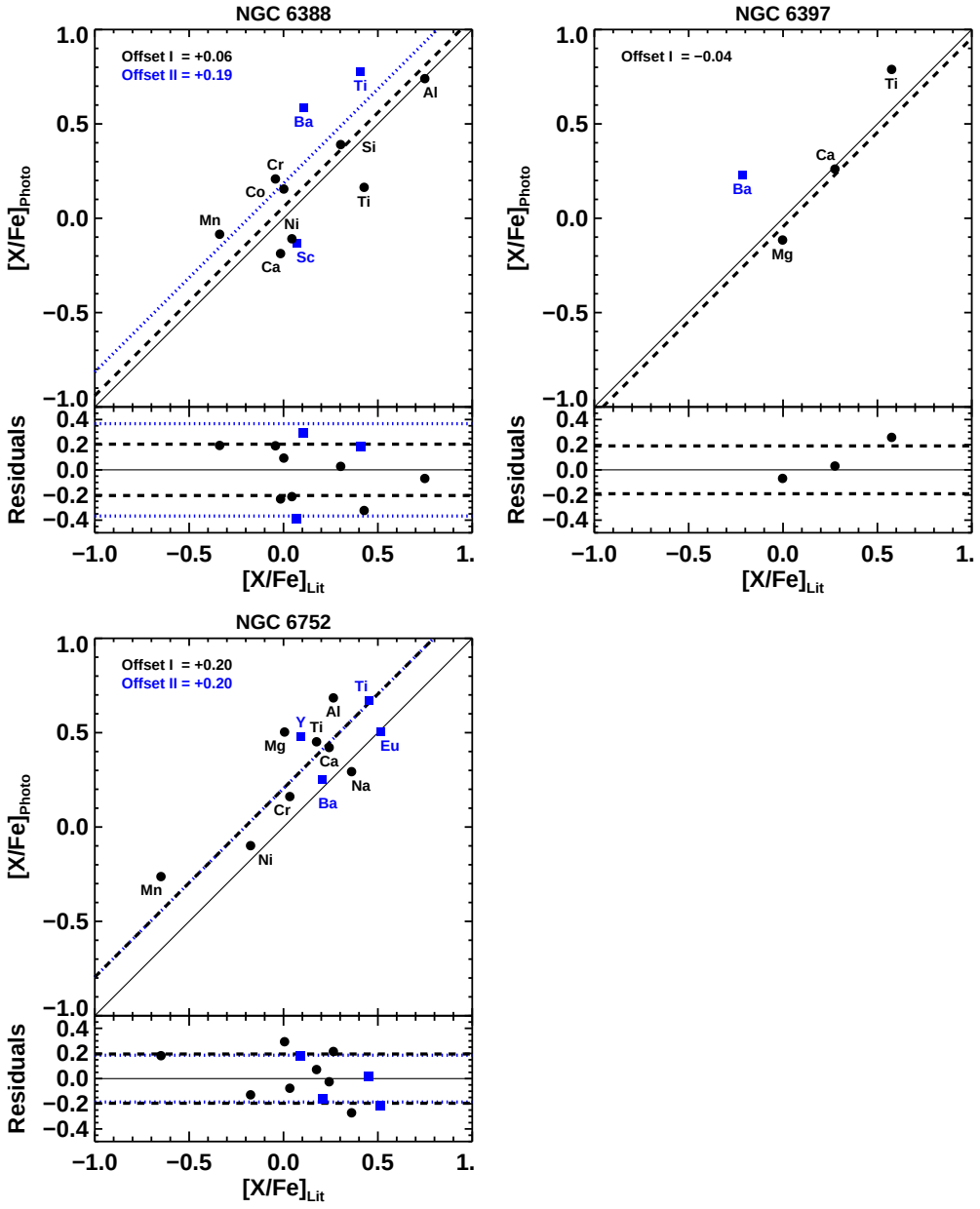

Figure 3.16. The abundance analysis method's internal accuracy in determining all the [X/Fe] abundance ratios for clusters NGC 6388, NGC 6397, and NGC 6752, when using each cluster's photometric CMD to define its stellar atmospheres. See Figure 3.15 for a description of the plotting conventions and data analysis. *Upper Panels*: The neutral species of NGC 6388, NGC 6397 and NGC 6752 have average systematic abundance offsets of +0.06, −0.04, and +0.20 *dex*, respectively. Likewise, the singularly ionized species of NGC 6388 and NGC 6752 have average systematic abundance offsets of +0.19 and +0.20 *dex*, respectively. *Lower Panels*: The neutral species of NGC 6388, NGC 6397 and NGC 6752 have average statistical uncertainties of 0.20, 0.19, and 0.20 *dex*, respectively. Likewise, the singularly ionized species of NGC 6388 and NGC 6752 have average statistical uncertainties of 0.37 and 0.18 *dex*, respectively.

and the neutron-capture element Ba, which is also displayed in Figure 3.19. Note that any *real* differences in the abundances between stars and the integrated light, such as would be expected for Mg, Al, and Na due to intra-cluster variations (see Colucci et al. 2009) should average out if enough stars are included.

Once again the simpler fits with constrained slopes are adopted to represent the functional relationship between the IL spectra abundances and the literature abundances. The intercepts of the fits are attributed to be the abundance analysis method's systematic offsets for the various species' abundances, and the RMS deviation around these fits is attributed to be the analysis method's statistical uncertainties. Of all the measured elements, only Mn and Si possess systematic offsets that are larger than their statistical uncertainties, but this is only on the order of 0.05 *dex*. The mean systematic offsets for all the Fe-peak elements, α-elements, and light-elements are $+0.19 \pm 0.06$ *dex*, $+0.11 \pm 0.07$ *dex*, and $+0.21 \pm 0.00$ *dex*, respectively, and their mean statistical uncertainties are $+0.26 \pm 0.10$ *dex*, $+0.24 \pm 0.12$ *dex*, and $+0.23 \pm 0.00$ *dex*, respectively.

In general, this chapter's analysis concludes that the [Fe/H] results from the IL analysis, when using the given knowledge of the stellar populations that contribute to the clusters' light, have systematic errors less than 0.1 *dex*, and [X/Fe] results that are also better than 0.1 *dex*, on average. As will be discussed in the next chapter, however, the uncertainties in the reddening corrections and photometric errors prevent this chapter's analysis from being conducted with "perfect" knowledge of the contributing stars. It is likely that systematic errors in the temperatures of the stars (derived from photometry) do affect the results when analyzing the spectra with observed photometry.

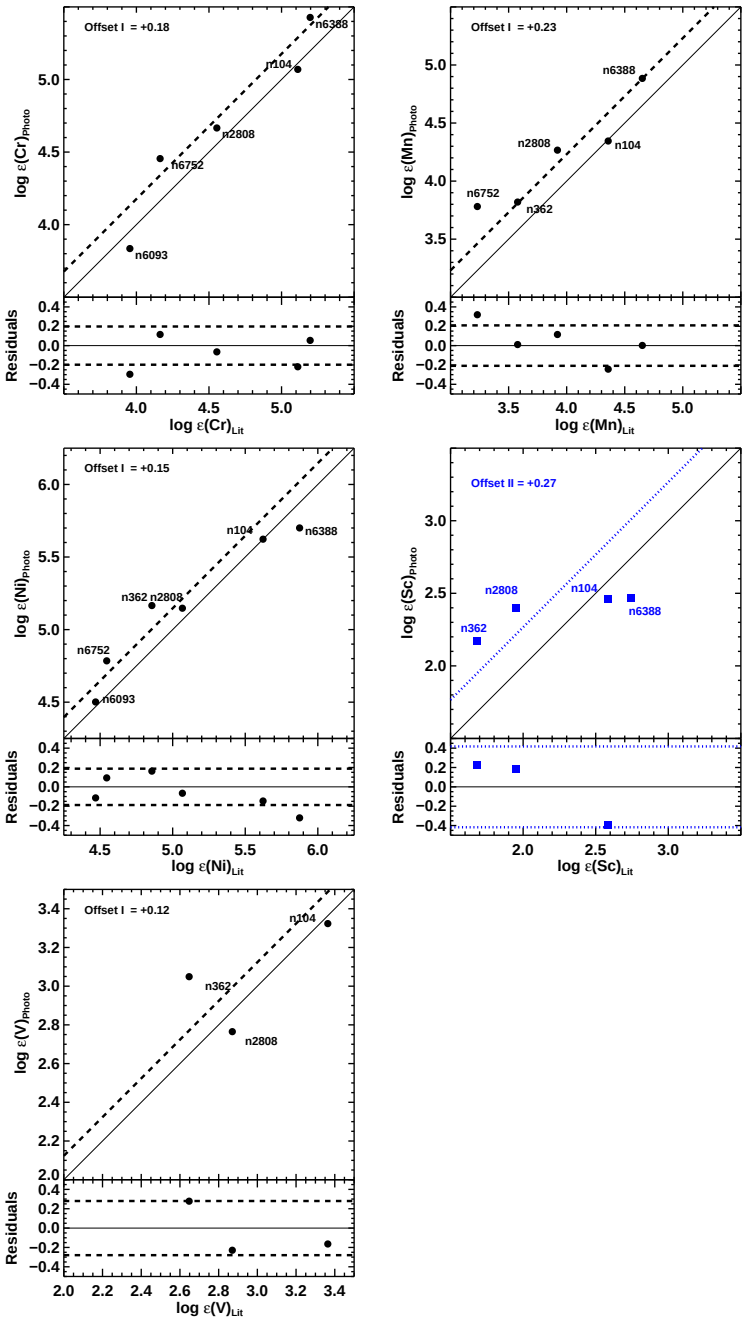

Figure 3.17. The abundance analysis method's global accuracy in determining the abundances of various Fe-peak elements, when using each cluster's photometric CMD to define its stellar atmospheres. All plotting conventions and data analysis match those used for the metallicities in Figure 3.12, except that the y-axis and x-axis of each plot's upper panel now correspond to its species' $log\,\epsilon(X)_{\rm Photo}$ and $log\,\epsilon(X)_{\rm Photo}$ abundances, respectively. From left-to-right, row 1 depicts Cr and Mn; row 2 depicts Ni and Sc; row 3 depicts V. *Upper Panels*: Cr I, Mn I, Ni I, Sc II, and V I have systematic abundance offsets of +0.18, +0.23, +0.15, +0.27, and +0.12 *dex*, respectively. *Lower Panels*: Cr I, Mn I, Ni I, Sc II, and V I have statistical uncertainties of 0.20, 0.21, 0.19, 0.42, and 0.28 *dex*, respectively.

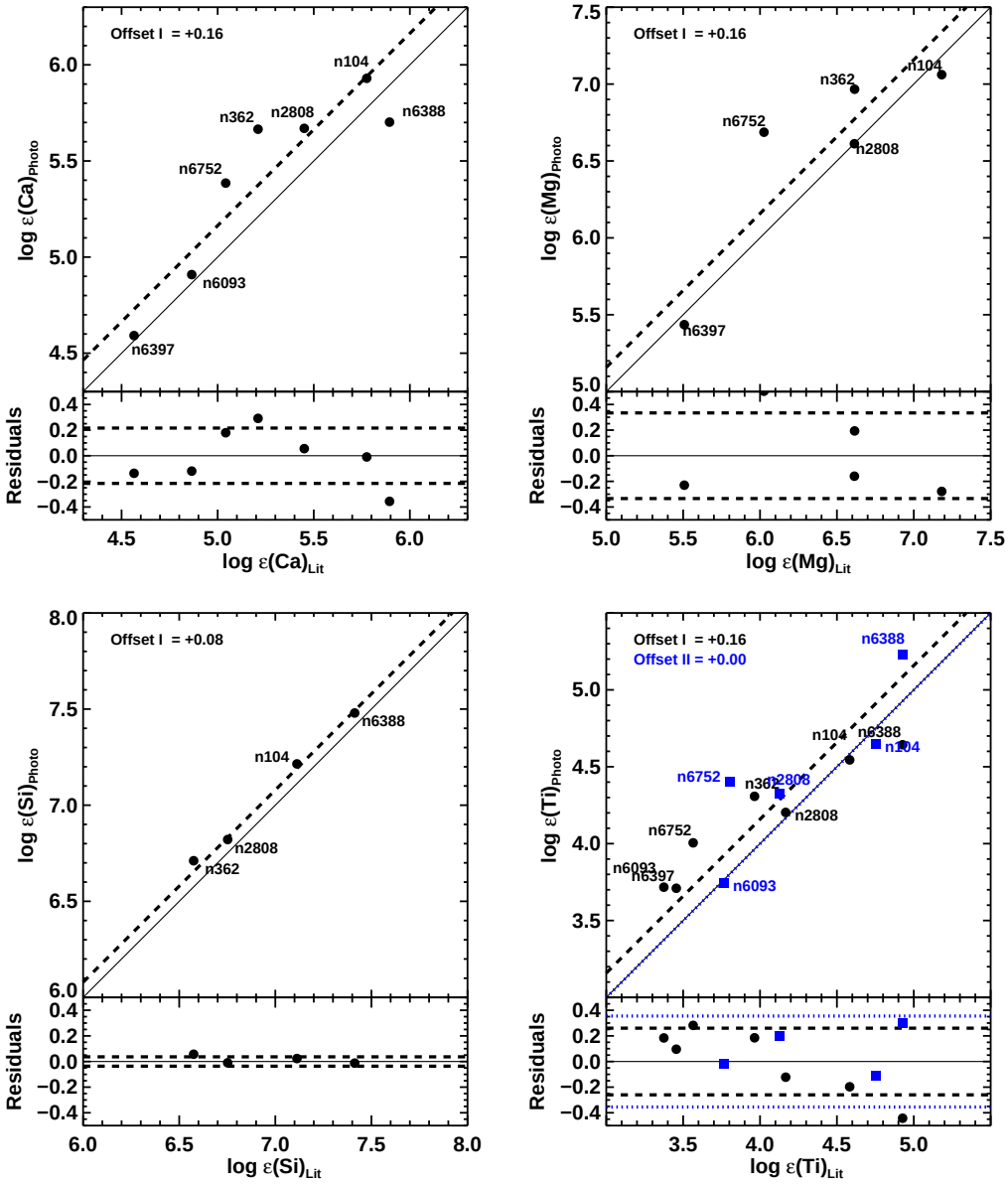

Figure 3.18. The abundance analysis method's global accuracy in determining the abundances of various α-elements, when using each cluster's photometric CMD to define its stellar atmospheres. All plotting conventions and data analysis match those used for the Fe-peak abundances in Figure 3.17. From left-to-right, row 1 depicts Ca and Mg, while row 2 depicts Si and Ti. *Upper Panels*: Ca I, Mg I, Si I, Ti I and Ti II have systematic abundance offsets of +0.16, +0.16, +0.08, +0.16, and 0.00 *dex*, respectively. *Lower Panels*: Ca I, Mg I, Si I, Ti I and Ti II have statistical uncertainties of 0.22, 0.33, 0.04, 0.26, and 0.35 *dex*, respectively.

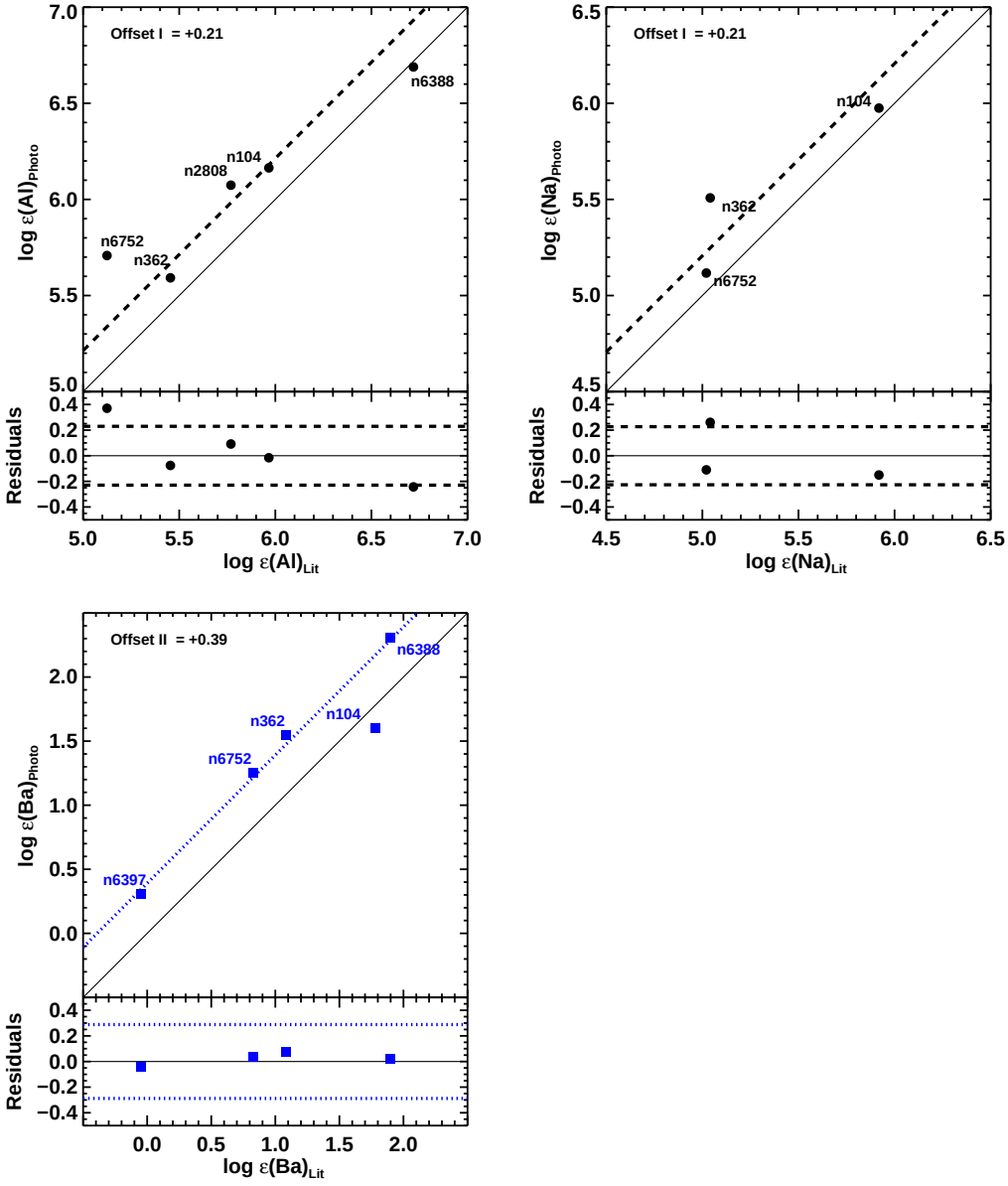

Figure 3.19. The abundance analysis method's global accuracy in determining the abundances of two light-elements and one n-capture element, when using each cluster's photometric CMD to define its stellar atmospheres. All plotting conventions and data analysis match those used for the Fe-peak abundances in Figure 3.17. From left-to-right, row 1 depicts the light-elements Al and Na, while row 2 depicts the n-capture element Ba. *Upper Panels*: Al I, Na I, and Ba II have systematic abundance offsets of +0.21, +0.21, and +0.39 *dex*, respectively. *Lower Panels*: Al I, Na I, and Ba II have statistical uncertainties of 0.23, 0.23, and 0.29 *dex*, respectively.

CHAPTER 4

Theoretical SSP Analysis

As the final test and demonstration of this dissertation's abundance analysis method, this chapter closely follows the analysis steps intended for real, unresolved, extragalactic GCs by using theoretical SSPs instead of observed photometry. First, using no *a priori* knowledge of the training set clusters' real stellar populations, age-metallicity grids of theoretical SSPs are created for the training set clusters by populating isochrones with enough stars to match the observed flux from each cluster's scanned region. Each populated isochrone in the grid consists of stars with precisely known atmospheric parameters, which allows for easy construction of fully-defined model atmospheres. Second, in order to determine which SSP best matches a cluster's unknown stellar population, the analysis method systematically adopts an SSP from the cluster's grid, synthesizes light-weighted EWs for all the Fe lines in the cluster's IL spectrum until the observed and synthesized Fe line EWs converge, and then applies the physical condition that the converged [Fe/H] must equal the [Fe/H] of that SSP's original isochrone. This procedure results in a locus of several potentially valid SSPs in the grid. Third, the analysis method imposes the physical constraint that the final, best SSP should result in synthesized Fe I line abundances that are stable over the full range of EP, EW, and wavelength. Once the best SSP is determined, it can be used to perform light-weighted line synthesis on the clusters' non-Fe line EWs in order to obtain their abundances.

This chapter is organized as follows. § 4.1 discusses the creation of the theoretical SSP grids for the training set clusters. In § 4.3, the methods used to search the SSP grids for each cluster's best matching SSP are discussed. This search also results in the determination of each cluster's metallicity. In § 4.4, the stellar properties of

the best matching SSPs are discussed. In § 4.5, the best matching SSPs are used to derive the clusters' non-Fe abundances. In § 4.6, the systematic and statistical errors for the abundance results are determined.

4.1 Construction of Theoretical SSPs

Several research groups are currently producing stellar evolution tracks that could potentially be used to create SSPs for this dissertation's abundance analysis method. These are obviously ongoing efforts and have been compared and reviewed in the literature several times. For a recent review, see Gallart et al. (2003). For the purposes of the analysis method, it is important that the stellar evolution tracks both reproduce realistic SSPs, and cover a wide range in age, metallicity, and relative abundance distributions (e.g. [α/Fe]) in order to provide a broad enough grid for the analysis of unknown GC systems. After extensive testing with the models from the Padova[1] (Girardi et al. 2000) and Teramo[2] groups, the Teramo group's "BaSTI" isochrones (Pietrinferni et al. 2004, 2006; Cordier et al. 2007) were chosen for two general reasons. First, the abundance solutions were not found to be sensitive to any one particular group's set of isochrones. And second, the BaSTI grids cover a broader range in stellar parameter space and provide more alternative treatments for detailed, stellar evolution considerations (e.g. mass loss, convective overshooting, extended AGBs, etc.).

Several different implementations of BaSTI isochrones are available. After some initial testing, the versions selected are those that incorporate the latest application of Teramo group's FRANEC code (Degl'Innocenti et al. 2008), with the code's options of α-element enhancement (Weiss et al. 1995), no convective overshooting, the low-temperature opacities of (Ferguson et al. 2005), extended asymptotic giant branches (Iben & Truran 1978), and a Reimers' (1975) mass-loss parameter of 0.2. The age-metallicty grid available for these options consists of 63 ages, that span a range of 0.03 to 19.0 Gyr, and 11 heavy element mass fractions (Z), that span from 0.0001

[1] http://pleiadi.pd.astro.it/

[2] http://albione.oa-teramo.inaf.it/

to 0.0400. A subset of these isochrones were chosen with ages of 1.0, 2.0, 3.0, 5.0, 7.0, 10.0, 13.0, and 15.0 Gyr, and all 11 available values of Z (0.0001, 0.0003, 0.0006, 0.0010, 0.0020, 0.0040, 0.0080, 0.0100, 0.0198, 0.0300, and 0.0400). Therefore, the grids of isochrones for the training set clusters consist of 88 isochrones that uniformly sample an age-metallicity parameter space of 1 to 15 Gyr in age and 0.0001 to 0.0400 in Z.

The BaSTI isochrones themselves provide the user with the initial mass, current mass, T_{eff}, L, M_V, and eight colors for all the stellar types in the isochrones. To transform the isochrones into theoretical SSPs, they were populated with stars using the IMF of Kroupa (2001). To do so, the IMF was first discretized so that it could be applied to the isochrones as a function of their initial stellar masses. The application of this IMF then requires low-mass cut-offs, high-mass cut-offs, and normalizations for each cluster. After some testing, it was decided that the IMF requires a low-mass cut-off near 0.7 $\mathcal{M}_{\odot}$ in order to account for mass segregation within the centers of the clusters' scanned regions (e.g. Baumgardt & Makino 2003). Note, though, that the effects of not including this low-mass cut-off are actually quite mild due to the minimal amount of flux that these low-mass stars contribute to the stellar population. For the high-mass limit, the mass of each isochrone's highest mass stellar type was used. Finally, for the IMF's normalizations, the total amount of V-band flux observed within the clusters' scanned regions were used, which are discussed in more detail below.

To calculate the total amount of V-band flux observed within each cluster's scanned region, the Trager et al. (1995) catalog of Galactic GC surface-brightness profiles was used. This catalog contains V-band surface-brightness profiles for Galactic GCs that were culled from several published sources, brought to a uniform magnitude scale, and then fit with Chebyshev polynomials (Trager et al. 1995). The raw surface-brightness data and polynomial fits for the training set clusters are shown in Figures 4.1 and 4.2. To calculate the amount of flux emitted from the scanned regions, the Chebyshev surface-brightness profiles were integrated over a circular area that contained an areal coverage equivalent to the clusters' actual 32×32 $arcsec^2$

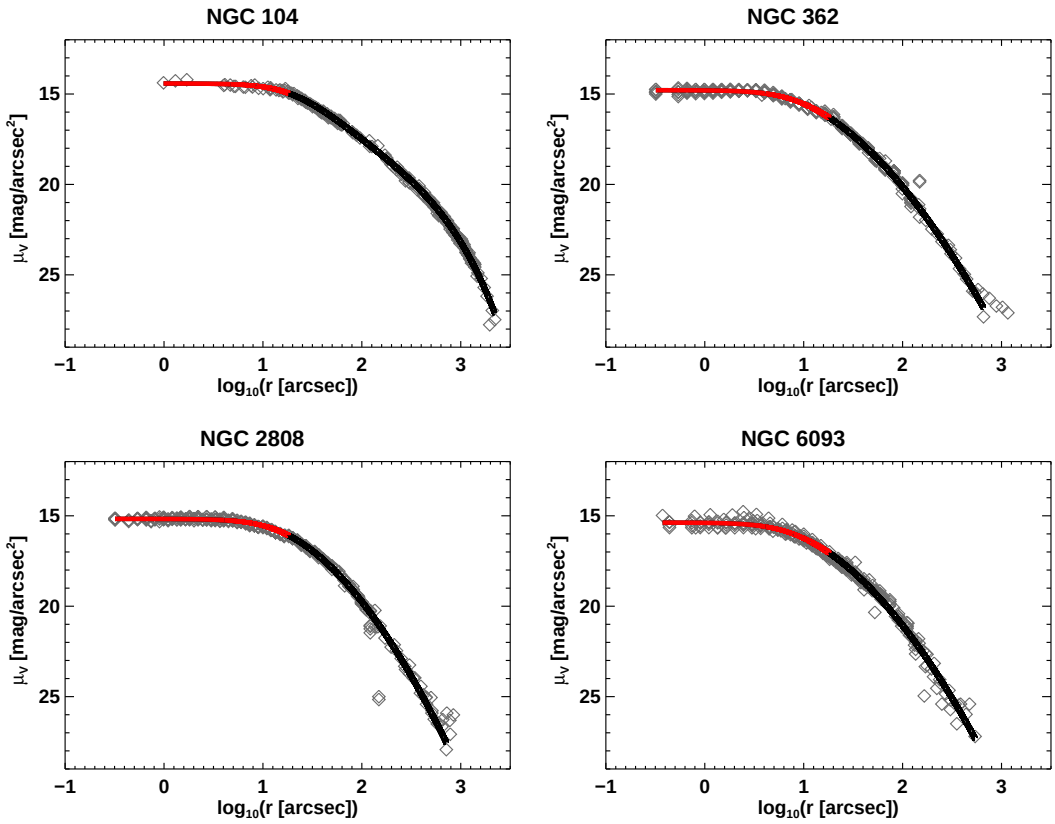

Figure 4.1. Surface-brightness profiles for NGC 104, NGC 362, NGC 2808, and NGC 6093. Light-grey diamonds depict observed surface-brightness data that have been culled from several published sources and then brought to a uniform magnitude scale by Trager et al. (1995). The black-and-red solid lines correspond to Chebyshev polynomial fits to the surface-brightness data performed by Trager et al. (1995). The red sections of the Chebyshev fits correspond to the radius of a circle with the equivalent areal coverage as each clusters' 32×32 $arcsec^2$ scanned region. This radius is equal to $\pi^{-0.5}32''$. Note that the scanned regions sample the majority of each cluster's core region. The fraction of V-band flux contained within these scanned regions is listed in Table 4.1.

scanned regions. This circle has a radius of $\pi^{-0.5}$ 32", and is depicted in Figures 4.1 and 4.2 as the inner red segment of each cluster's Chebyshev polynomial. The final calculated fraction of each cluster's total V-band flux contained within its scanned region is listed in Table 4.1.

4.2 Atmospheric Parameters for the Theoretical SSPs

Model atmospheres for the stars in each cluster's 88 isochrone-based SSPs were produced using the same basic methods outlined for the photometry in § 3.1. One major advantage, though, is that the isochrones directly provide theoretically pristine values

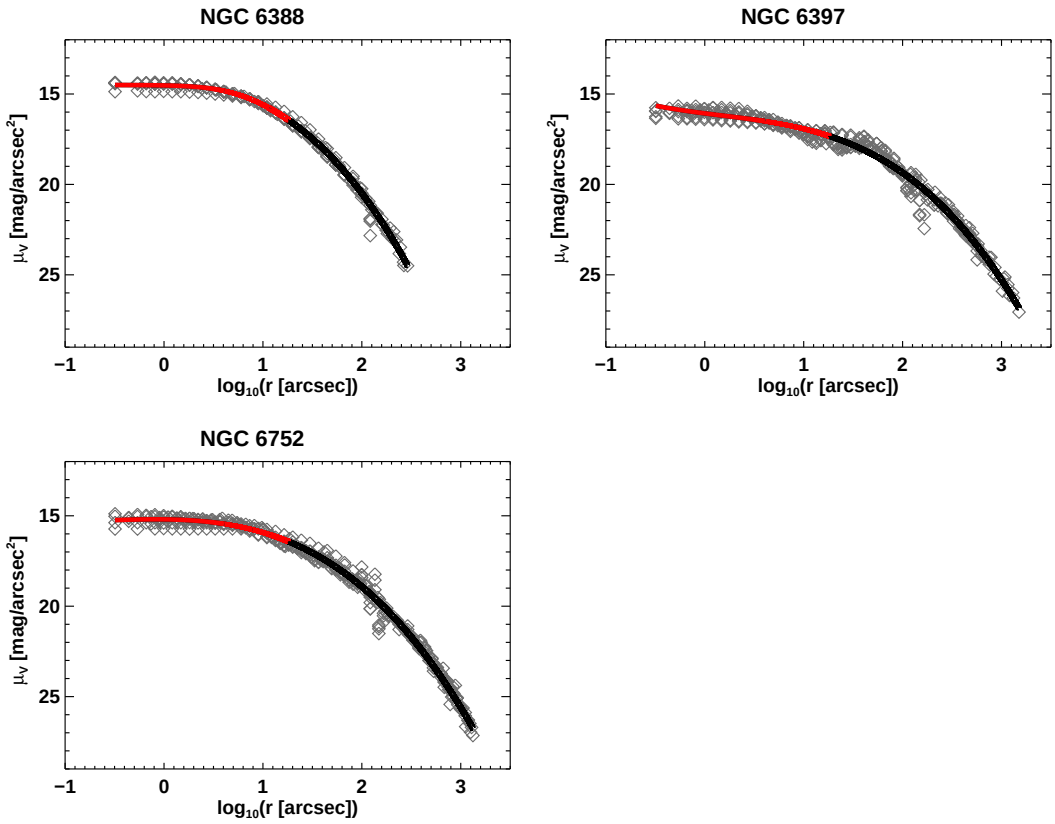

Figure 4.2. Surface-brightness profiles for NGC 6388, NGC 6397 and NGC 6752. See Figure 4.1 for available explanations.

Cluster	Flux Frac.
NGC 104	0.052
NGC 362	0.20
NGC 2808	0.17
NGC 6093	0.25
NGC 6388	0.27
NGC 6397	0.032
NGC 6752	0.059

Table 4.1. The flux contributions from the training set clusters' scanned regions. The "Flux Frac." column lists the V-band flux emitted from each cluster's scanned region normalized using the total amount of V-band flux emitted from the entire cluster.

for the stellar T_{eff}, L, M_V, colors, masses, and [M/H] values. Therefore, the only parameters that needed to be calculated were $log(g_\star)$, R, and ξ_v. These parameters were calculated using Equations 3.1, 3.5, and 3.4, respectively. Next, each SSP's stellar population was binned by M_V in order to define ∼28 representative average stellar types, where each bin consists of ∼3.5% of the population's V-band flux. These average stellar types were then assigned the flux-weighted stellar parameters from all the stars within their bins. The atmospheric parameters for these ∼28 average stellar types define the model atmospheres used for that SSP's line synthesis analysis.

4.3 Finding the Best Matching SSPs

With model atmospheres defined for each SSP's ∼28 average stellar types, Fe line synthesis can be conducted for each cluster as described in § 3.3. The only difference, though, is that the analysis must be sequentially carried out for all 88 SSPs in each cluster's age-metallicity grid of SSPs, which yields 88 potential [Fe/H] solutions for a cluster. In more detail, the analysis for a single SSP proceeds as follows. Each Fe line observed in a cluster's IL spectrum is synthesized by adjusting the [Fe/H] value of the selected SSP's model atmospheres, until the synthesized, light-weighted EW matches the measured EW for the line. This is done for all the Fe lines measured for a cluster, and the final list of synthesized Fe line abundances are then averaged together using the σ-clipping routine discussed in § 3.3 to determine the final mean [Fe/H] value obtained from the selected SSP. Note that if the initial [Fe/H] value for the SSP is inconsistent with the final [Fe/H] solution determined from the Fe line synthesis, then the SSP is a poor match for the cluster. From this criterion alone, a handful of potentially viable SSPs for each cluster are determined. The [Fe/H] solutions obtained for all 88 SSPs, both consistent and inconsistent, are plotted in Figures 4.3 and 4.4.

Each plot in these figures shows the metallicity used to calculate the SSP (the "input" [Fe/H]) on the *x-axis* and the [Fe/H] values derived from the synthesis of the Fe lines (the "output" [Fe/H]) on the *y-axis*. The synthesized metallicities based on Fe I lines are displayed as circles, while those based on Fe II lines are displayed as "X's".

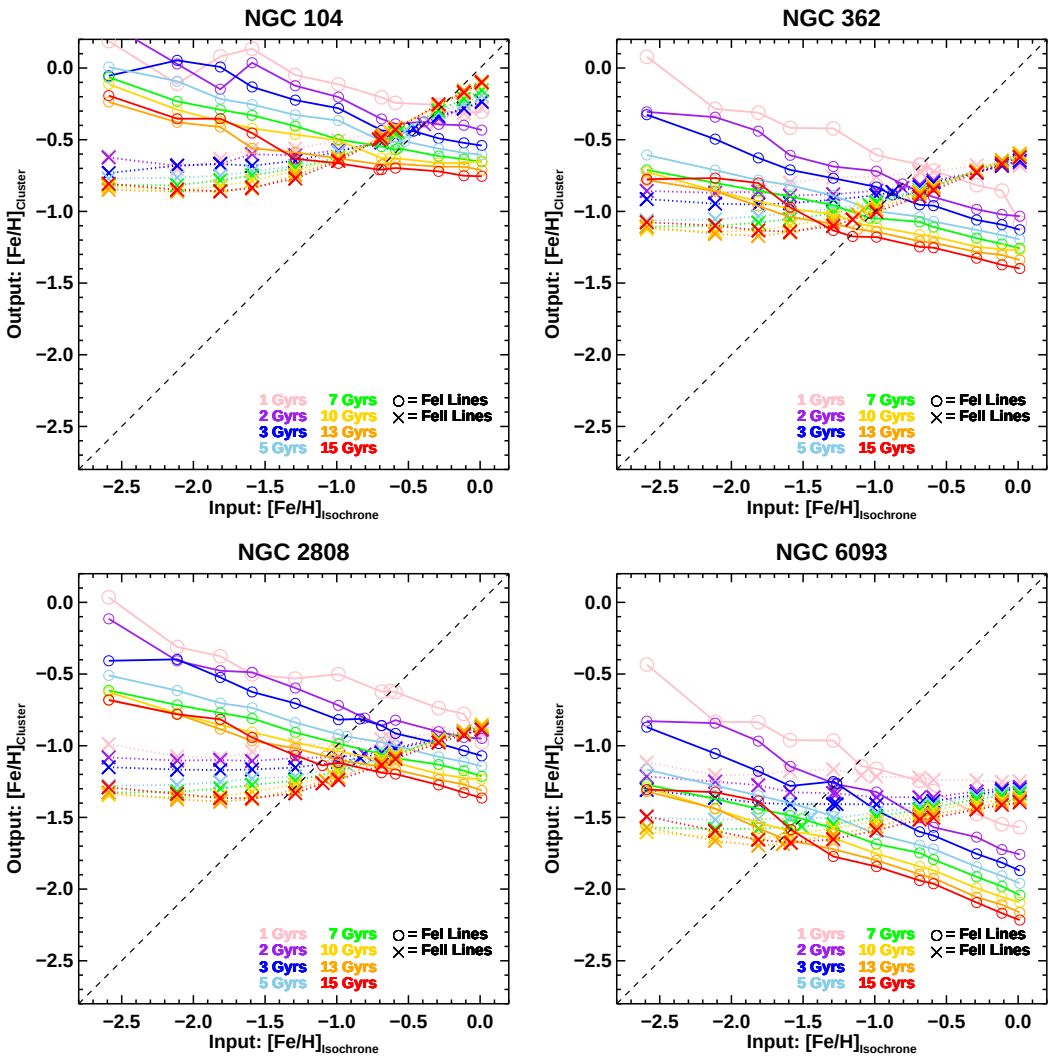

Figure 4.3. All possible metallicity solutions for NGC 104, NGC 362, NGC 2808, and NGC 6093 that result when the abundance analysis method analyzes all possible theoretical SSPs. The output [Fe/H] solutions are plotted on the *y-axes*, while the [Fe/H] of the input theoretical SSPs are plotted on the *x-axes*. Circles and "X's" depict the [Fe/H] values from Fe I and Fe II lines, respectively. Physically valid solutions are located on the dashed 1:1 equivalence line.

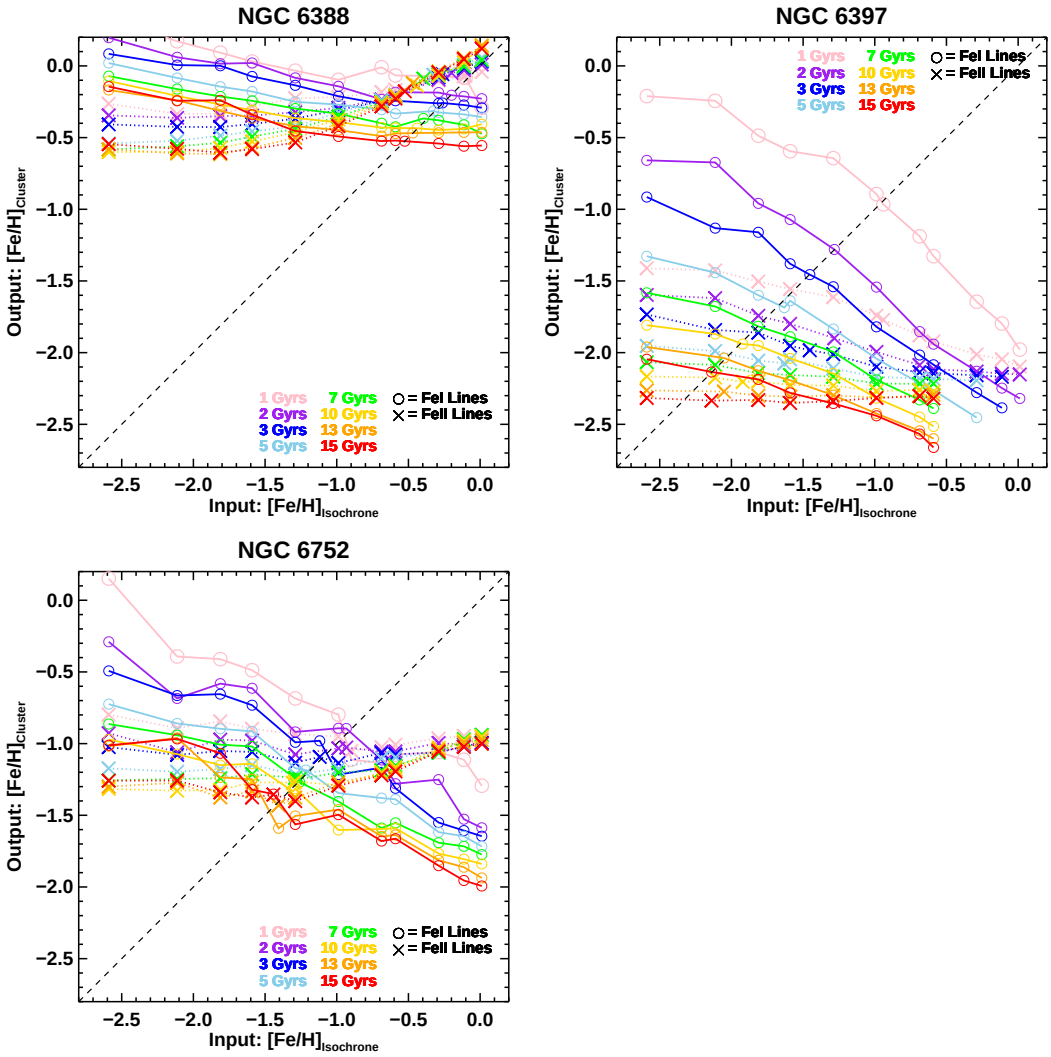

Figure 4.4. All possible metallicity solutions for NGC 6388, NGC 6397, and NGC 6752 that result when the abundance analysis method analyzes all possible theoretical SSPs. See Figure 4.3 for available explanations.

Each synthesized metallicity is color-coded according to the age of its corresponding SSP. Solid and dotted lines respectively connect Fe I and Fe II synthesized metallicities produced by SSPs of the same age. These lines of constant age are well behaved and almost universally monotonic as a function of the SSP metallicities. The self-consistent solutions (i.e. where the "input" and "output" [Fe/H] values are consistent with each other) are those which lie on the diagonal 1:1 line. Note that the solutions for Fe I and Fe II are consistently different. This is potentially due to departures from ionization equilibrium, as discussed in Kraft & Ivans (2003). For this reason, and because the Fe I results are based on 7-10 times as many lines as the Fe II results, making them statistically more robust, only Fe I solutions are used here to select the appropriate SSP solutions. Therefore, a single self-consistent age-metallicity solution exists for each of the 8 possible SSP ages, based on where Fe I's constant age lines cross the 1:1 line. Note, however, that both Fe I and Fe II are used in the following sections, when [X/Fe] abundance ratios are computed; Fe I and Fe II are used in the abundance ratios for neutral and singularly ionized species, respectively, as is typically done when presenting abundance measurements for single stars. This normalization ideally removes any existing offset between neutral and ionized species.

Because the diagonal 1:1 line intersects each constant-age line between two solutions in the set of 88-isochrones, new isochrones were interpolated to obtain isochrones that exactly correspond to the most-appropriate age-metallicity solutions. The isochrone interpolations followed the prescription recommended by Pietrinferni et al. (2006). These interpolation steps are: (i.) select an intersection point, (ii.) select all 11 available Z valued isochrones that match that intersection point's age, (iii.) match together the stellar types of the 11 isochrones, (iv.) quadratical fit their stellar parameters as a function of their isochrones' metallicity, (v.) use the quadratic fits to interpolate values of the stellar parameters that correspond to the intersection point's metallicity. These interpolated isochrones are then converted into SSPs and model atmospheres using the methods discussed in § 4.1 and § 4.2, respectively. Finally, the interpolated SSPs are processed through the Fe line synthesis analysis. As expected, the solutions for these SSPs are such that the input and output [Fe/H] agree, and

they lie on the 1:1 line in Figures 4.3 and 4.4.

Each cluster's 8 potential SSP solutions are all plotted in Figures 4.5 and 4.6 as CMDs that overlap their cluster's scanned region CMD. Note that the 8 potential SSP solutions for each cluster are quite similar to their cluster's observed CMD, but vary in the location of their turn-off points along the cluster's main sequence, which is obviously a function of the cluster age. Note that in some solutions it appears that a young SSP is approximating a strong blue horizontal branch.

To select the single, best-fitting SSP from the 8 potential matches, the stability of the [Fe/H] solutions as a function excitation potential (EP), wavelength (λ), and reduced EWs (reduced EW $\equiv \log(\mathrm{EW}/\lambda)$ are used. These diagnostics, discussed in Chapter 3 (see § 3.3), are commonly used in standard stellar abundance analysis to diagnose problems with, and tune, the physical parameters of a model atmosphere used in the analysis of a single star's spectrum. Here, as the stellar parameters are given completely by the SSPs, these diagnostics are used to identify the most appropriate SSP for each cluster. The best-fitting SSP should simply show the weakest correlation between the [Fe/H] solutions for Fe I and Fe II lines and the parameters of the lines. Linear least squares fits between [Fe/H] and these parameters are used to identify and quantify the strength of any existing correlations. Plots illustrating the behavior of the Fe abundances with EP, wavelength, and reduced EW are shown in Figures 4.7 through 4.20 for all clusters and all 8 of their potential SSP solutions. From these plots, 5 diagnostics are obtained: the slope of [Fe/H] with EP, wavelength, and reduced EW, and the standard deviation of the [Fe/H] solution for Fe I lines and Fe II lines. Note that the average number of Fe I lines that have calculated abundances is 74, while on average only 7 Fe II lines are available in these clusters. Consequently, all statistics from the Fe I lines are more useful.

For any one of these diagnostics, there is not a statistically significant difference between the quality of the solution from SSPs within a range of 5 $Gyrs$. For example, the slope of the [Fe/H] vs. EP relationship in Figure 4.10 for NGC 362 looks essentially the same for SSPs between ages 10 and 15 $Gyrs$. However, while the difference in these diagnostics may be small over a wide range in SSP age, they are found to

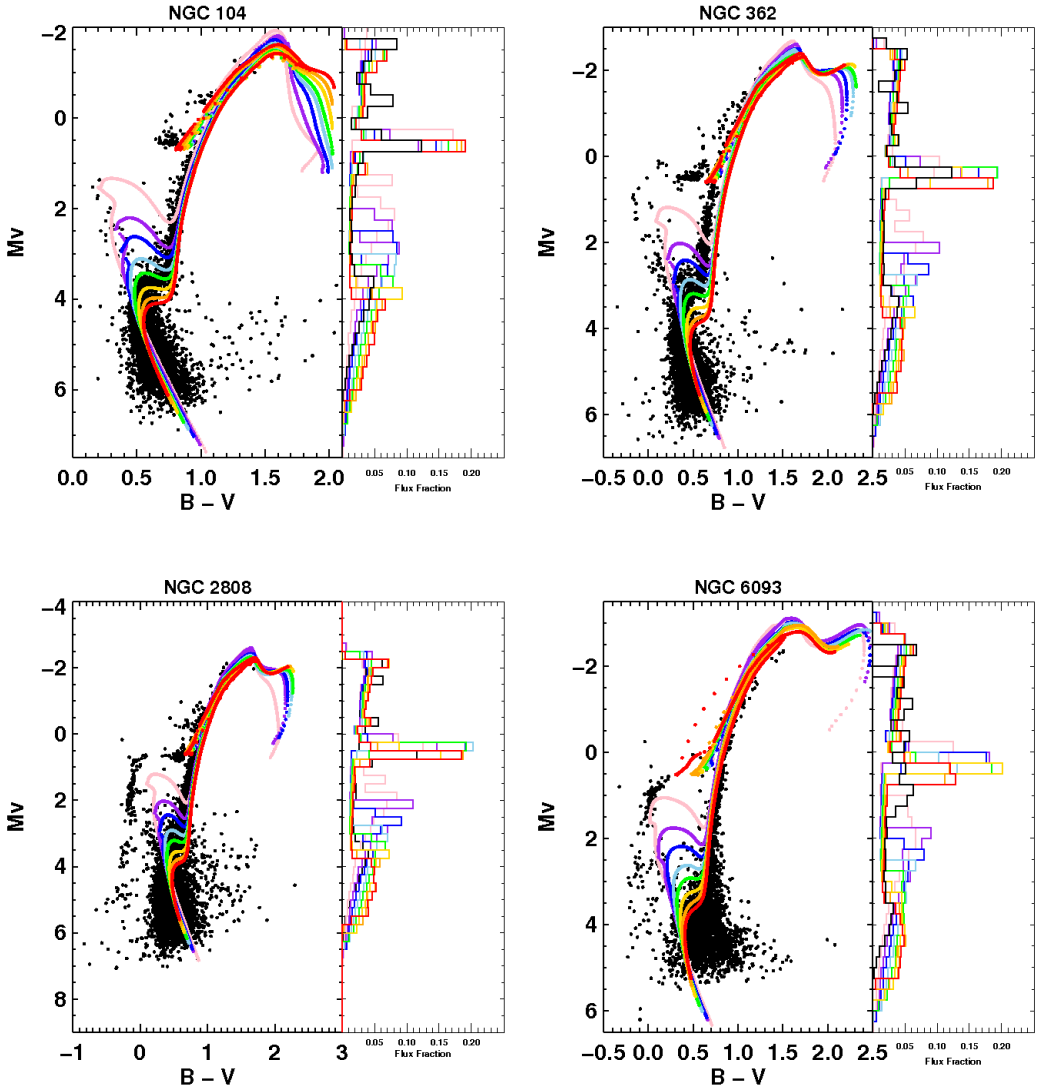

Figure 4.5. CMDs of the 8 potential SSP solutions for NGC 104, NGC 362, NGC 2808, and NGC 6093 that result when the abundance analysis method analyzes all possible SSPs. Each plot's left panel displays its cluster's 8 potential theoretical SSP solutions, in CMD format, along with the photometric CMD of the cluster's scanned region (black dots). These SSPs correspond to the intersection points of Figure 4.3's constant age lines with the 1:1 metallicity lines. The colors pink, purple, blue, light-blue, green, yellow, orange, and red correspond to SSP ages of approximately 1, 2, 3, 5, 7, 10, 13, and 15 *Gyr*, respectively. *Right Panels*: Each plot's right panel displays the luminosity functions of its photometric CMD (black line) and its cluster's 8 potential theoretical SSP solutions (colored lines). The *y-axes* display the absolute V-band magnitudes of the CMDs, binned by 0.25 magnitudes, while the *x-axes* display the fractional V-band flux of the CMDs. Each luminosity function is normalized using the total amount of V-band flux emitted from its cluster's scanned region. Therefore, the flux fractions displayed for the theoretical luminosity functions are in the same units as the photometric luminosity functions, which allows for direct comparisons between them.

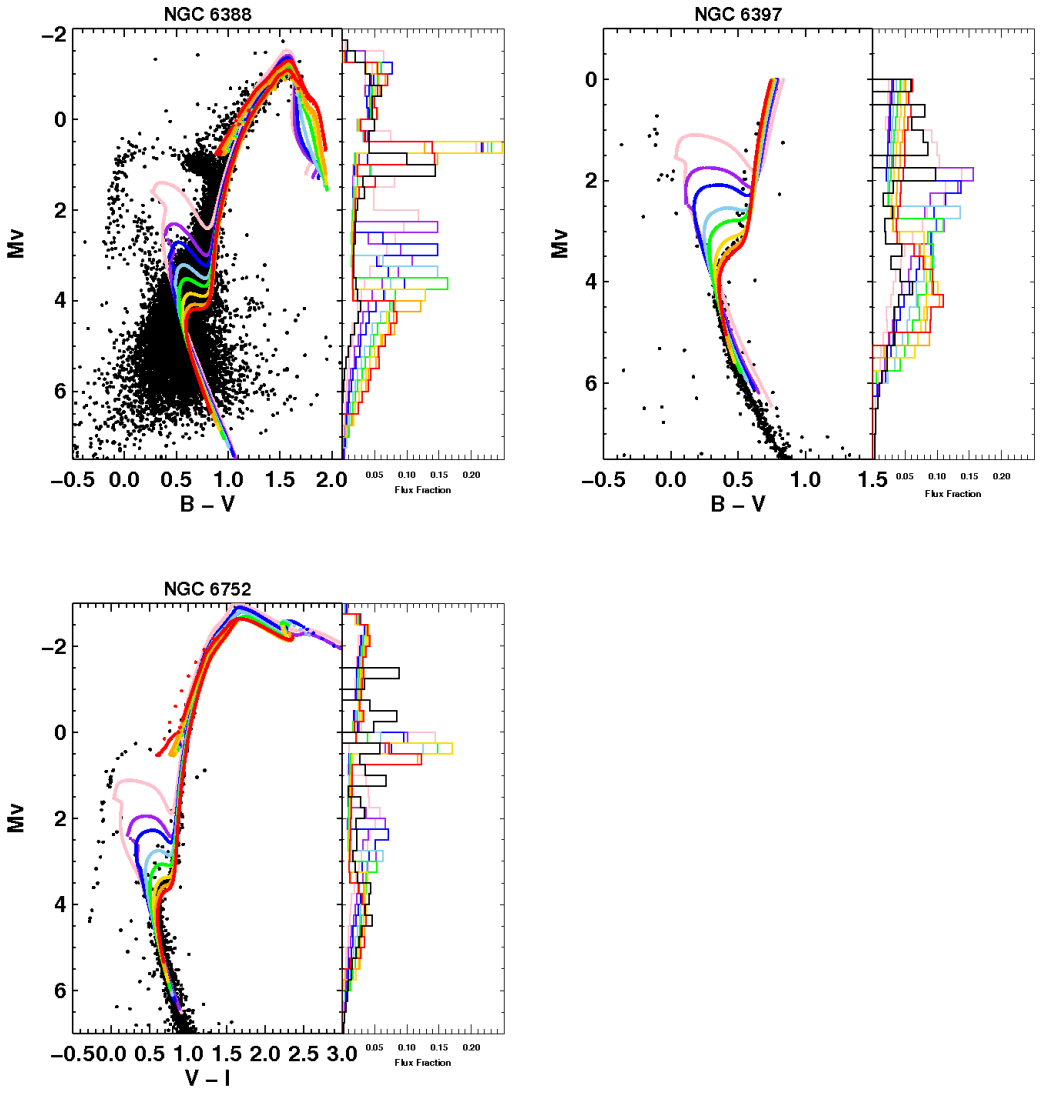

Figure 4.6. CMDs of the 8 potential SSP solutions for NGC 6388, NGC 6397, and NGC 6752 that result when the abundance analysis method analyzes all possible SSPs. See Figure 4.24 for available explanations.

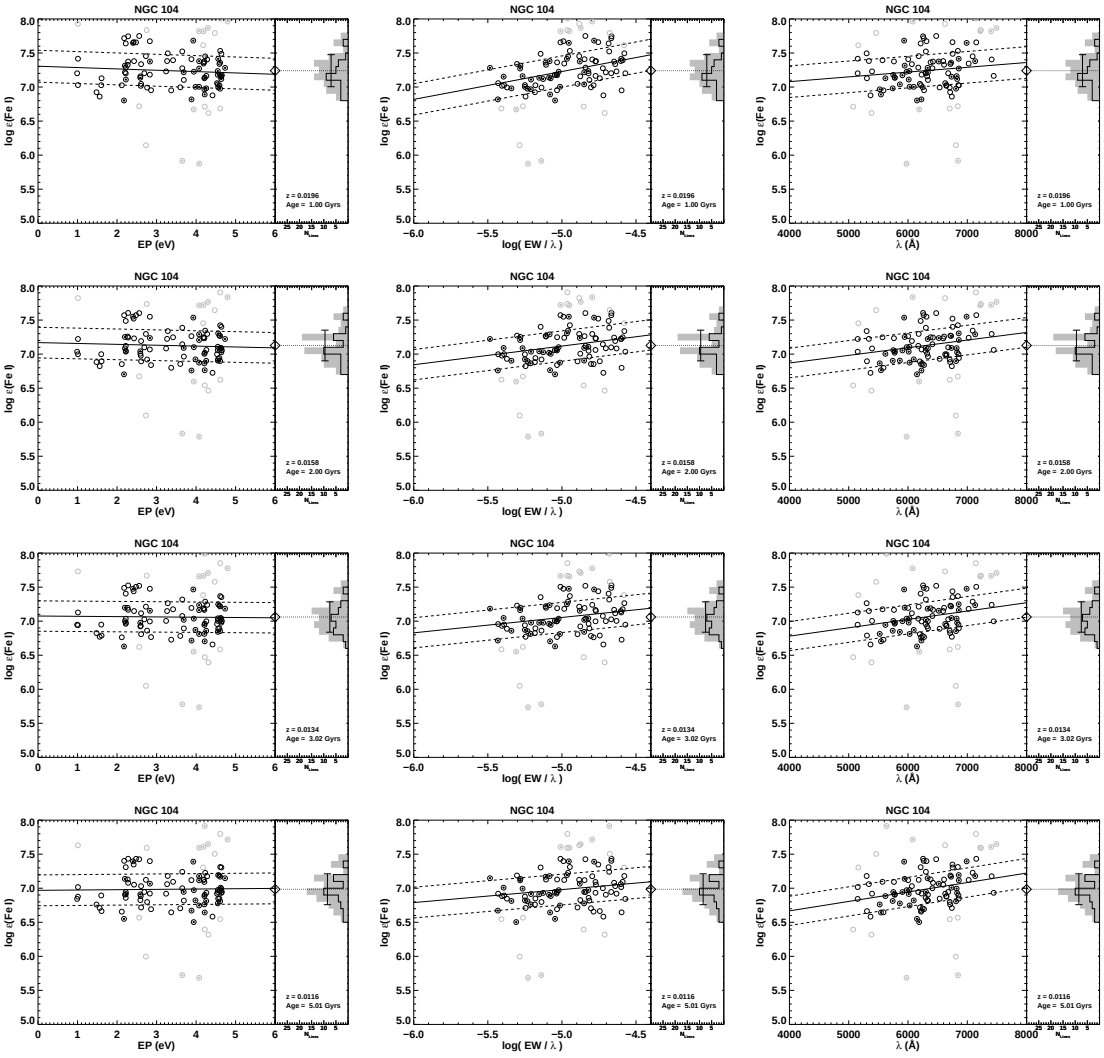

Figure 4.7. Fe line abundances synthesized from the IL spectra of NGC 104 using its 1, 2, 3, 5 *Gyr* potential SSP solutions to define its set of model atmospheres. These plots are listed, from top-to-bottom, in order of increasing age. All plotting conventions and notations follow those used in Figure 3.10.

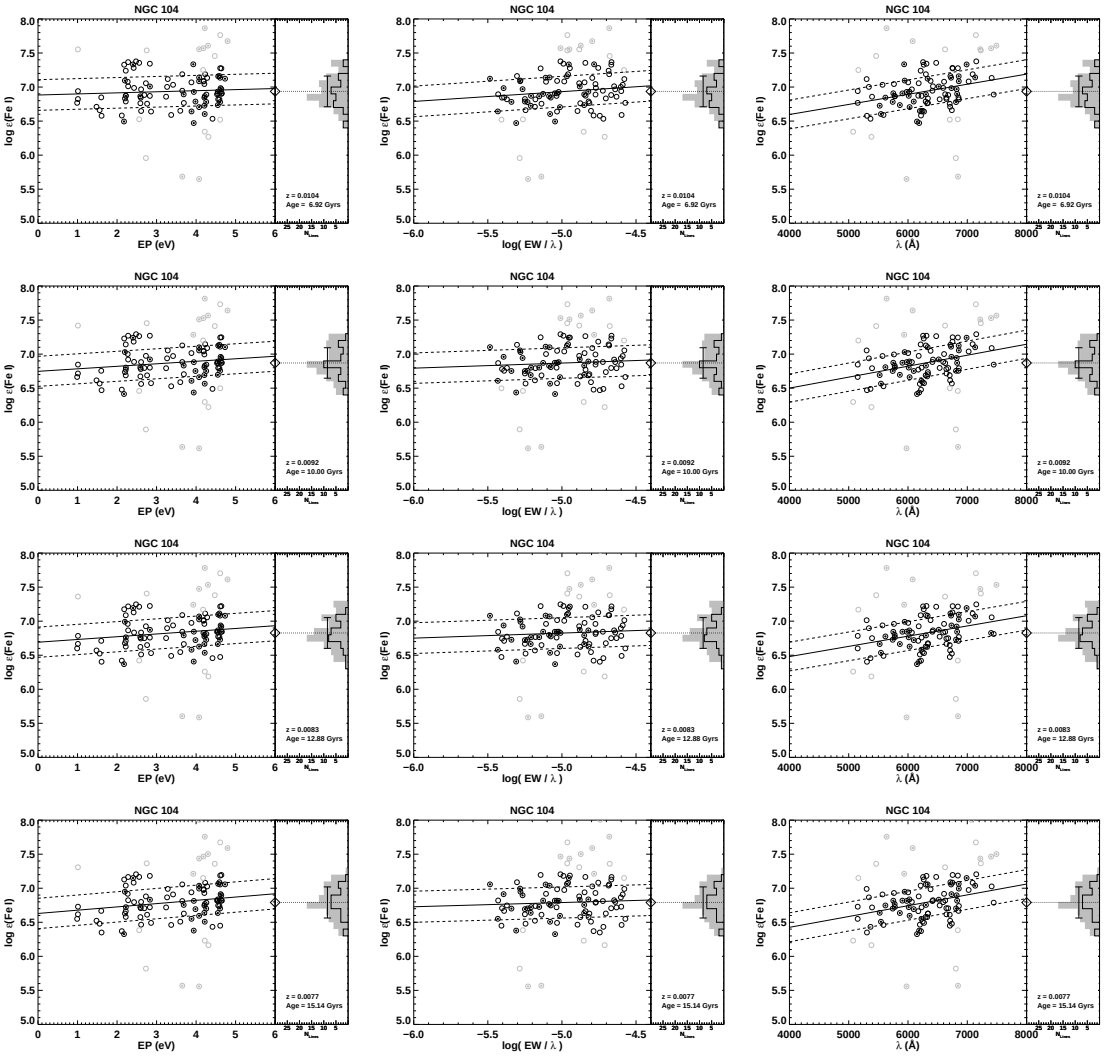

Figure 4.8. Fe line abundances synthesized from the IL spectra of NGC 104 using its 7, 10, 13, and 15 *Gyr* potential SSP solutions to define its set of model atmospheres. These plots are listed, from top-to-bottom, in order of increasing age. All plotting conventions and notations follow those used in Figure 3.10.

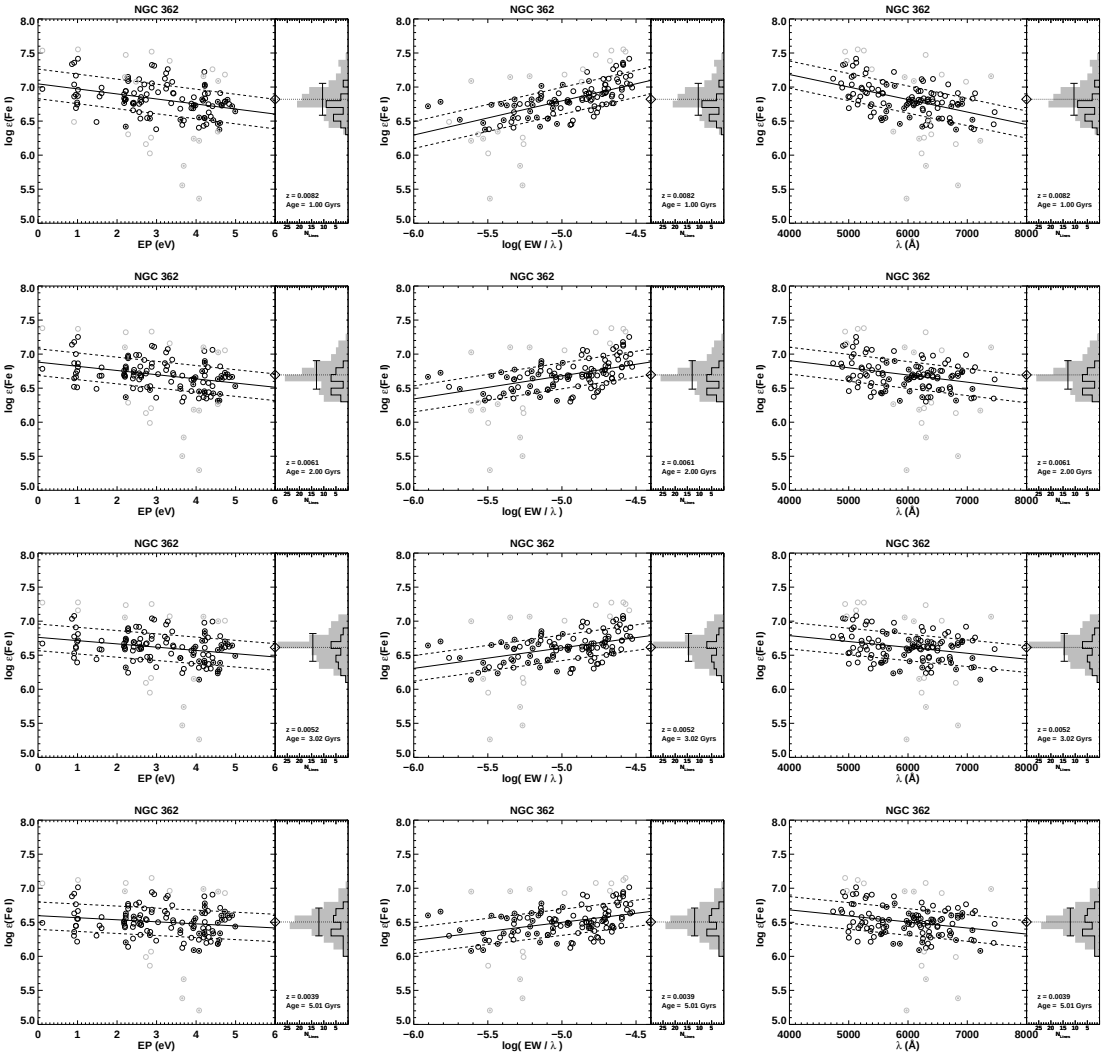

Figure 4.9. Fe line abundances synthesized from the IL spectra of NGC 362 using its 1, 2, 3, 5 *Gyr* potential SSP solutions to define its set of model atmospheres. These plots are listed, from top-to-bottom, in order of increasing age. All plotting conventions and notations follow those used in Figure 3.10.

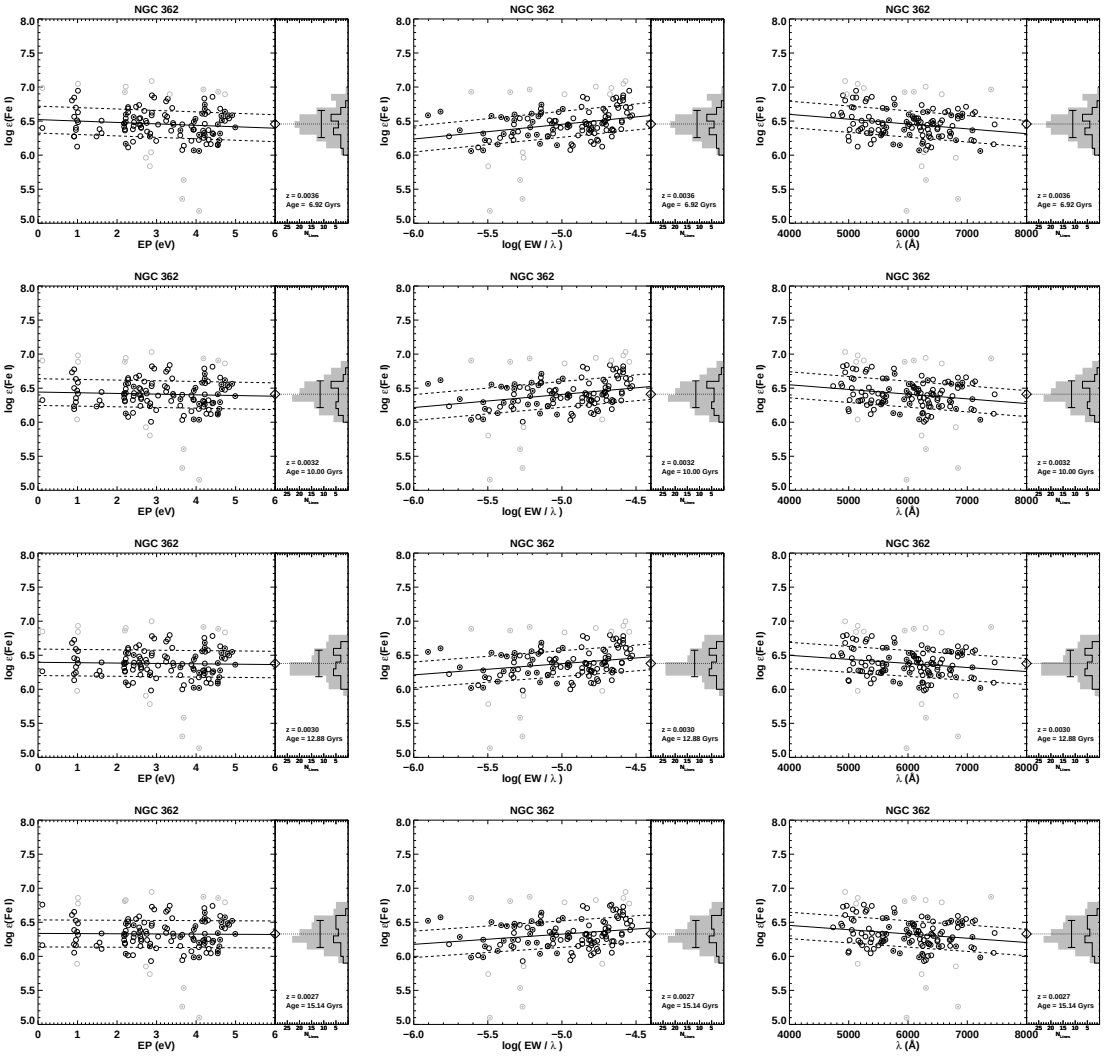

Figure 4.10. Fe line abundances synthesized from the IL spectra of NGC 362 using its 7, 10, 13, and 15 *Gyr* potential SSP solutions to define its set of model atmospheres. These plots are listed, from top-to-bottom, in order of increasing age. All plotting conventions and notations follow those used in Figure 3.10.

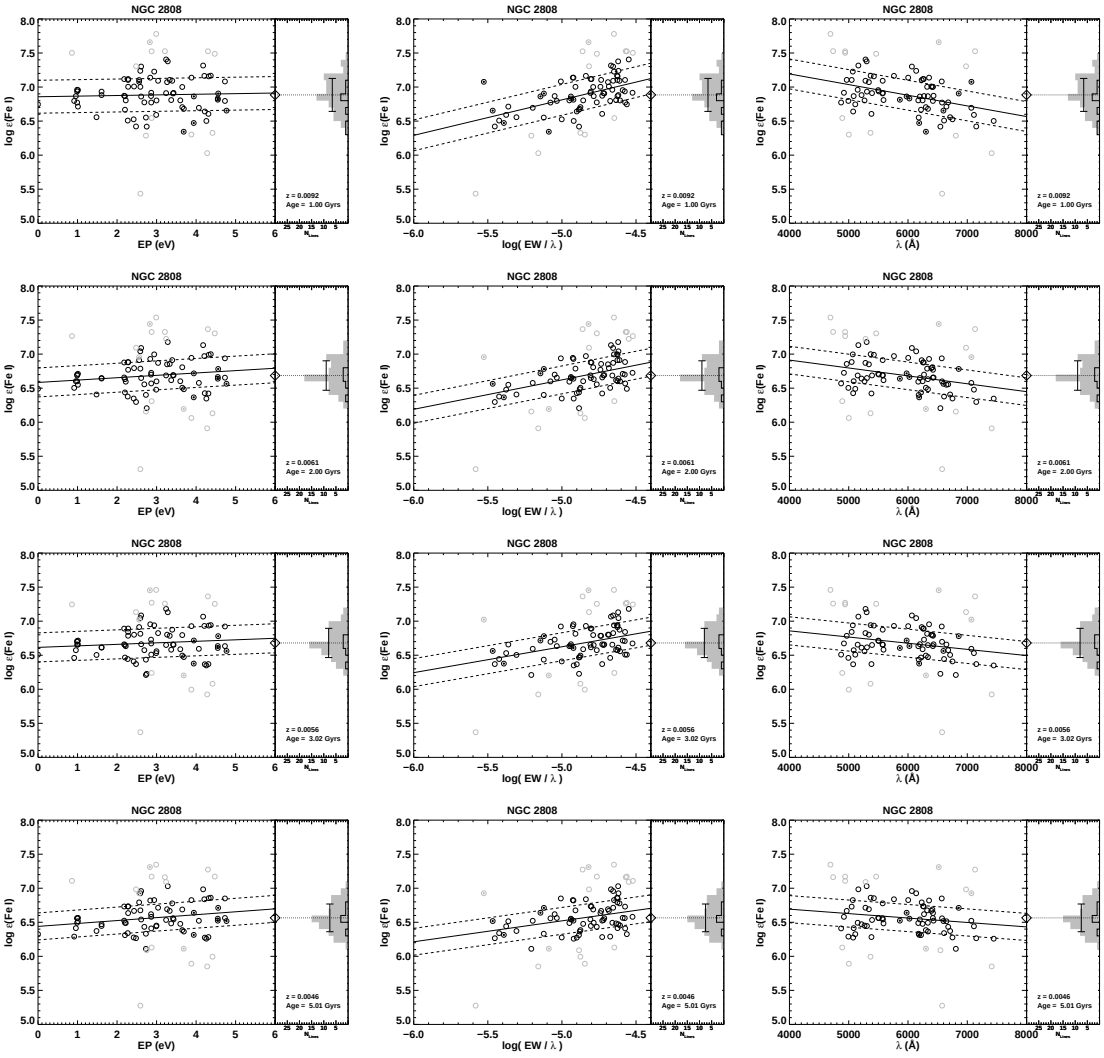

Figure 4.11. Fe line abundances synthesized from the IL spectra of NGC 2808 using its 1, 2, 3, 5 *Gyr* potential SSP solutions to define its set of model atmospheres. These plots are listed, from top-to-bottom, in order of increasing age. All plotting conventions and notations follow those used in Figure 3.10.

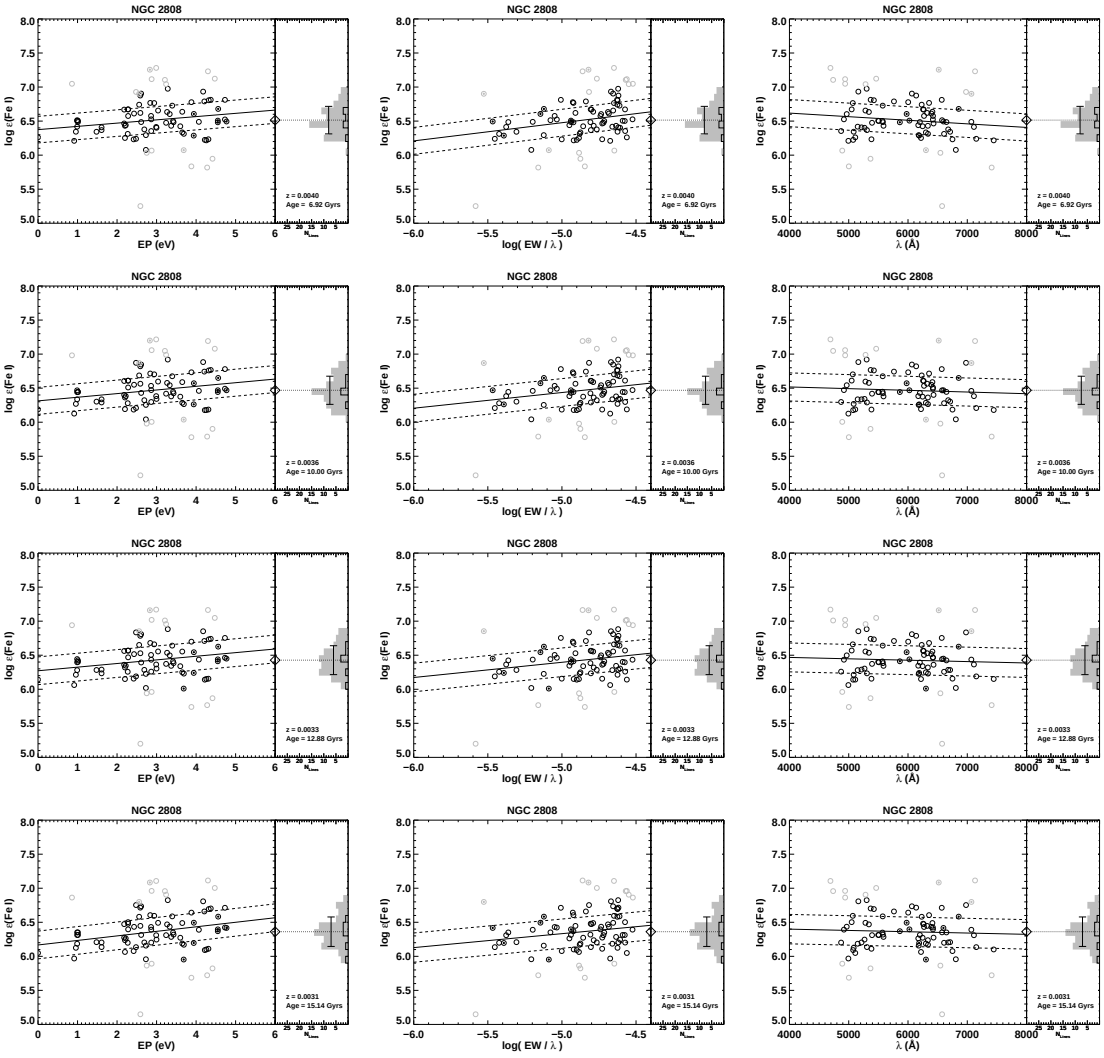

Figure 4.12. Fe line abundances synthesized from the IL spectra of NGC 2808 using its 7, 10, 13, and 15 *Gyr* potential SSP solutions to define its set of model atmospheres. These plots are listed, from top-to-bottom, in order of increasing age. All plotting conventions and notations follow those used in Figure 3.10.

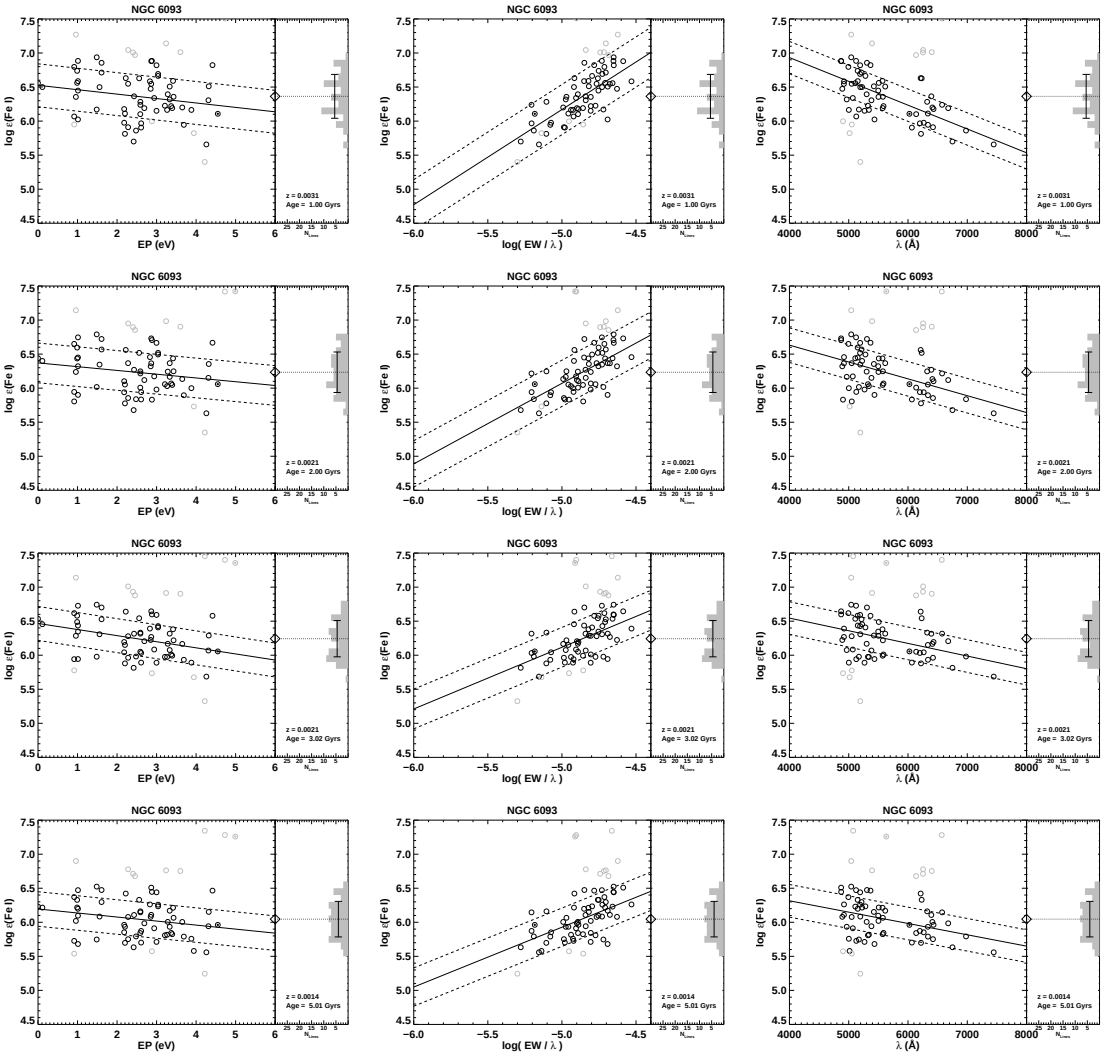

Figure 4.13. Fe line abundances synthesized from the IL spectra of NGC 6093 using its 1, 2, 3, 5 *Gyr* potential SSP solutions to define its set of model atmospheres. These plots are listed, from top-to-bottom, in order of increasing age. All plotting conventions and notations follow those used in Figure 3.10.

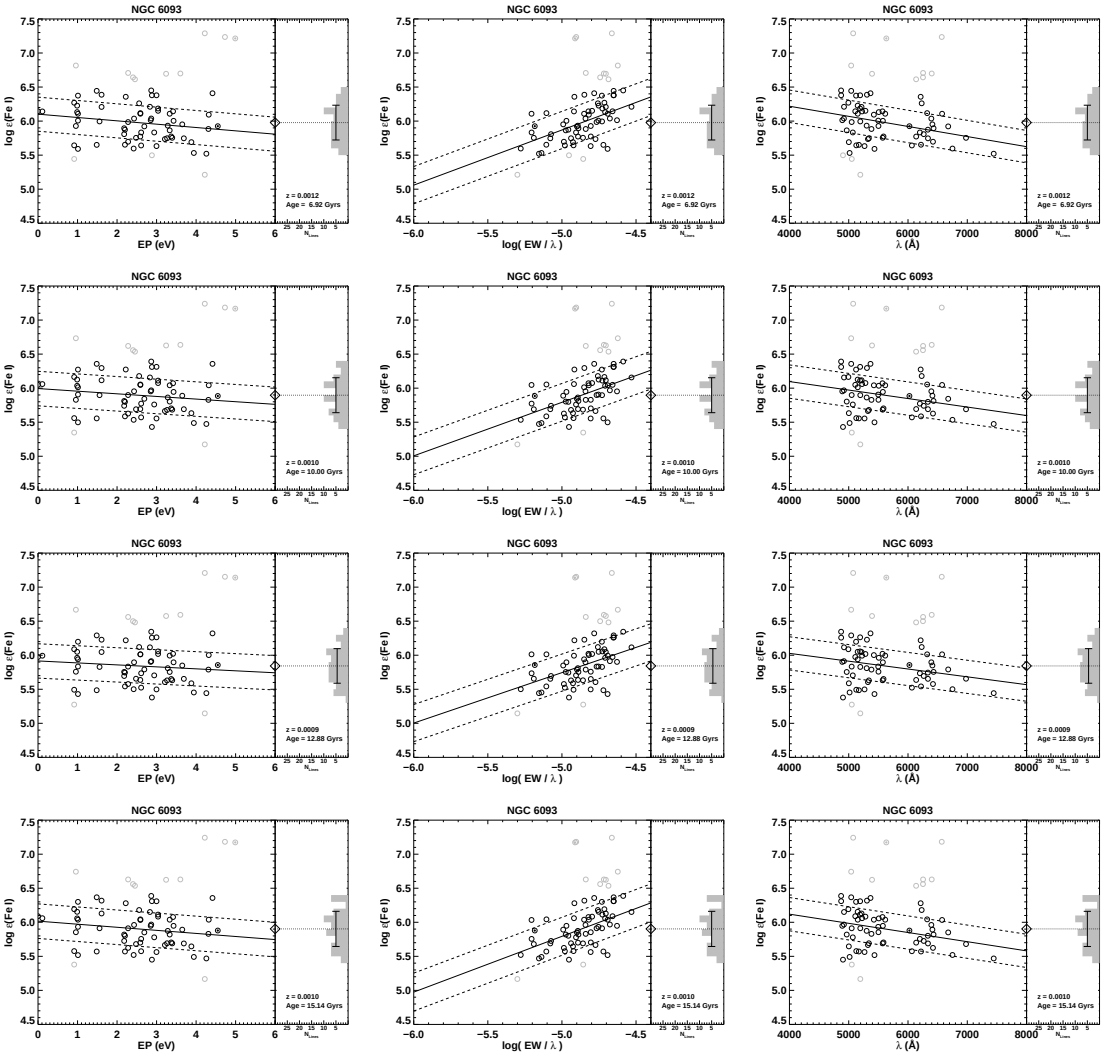

Figure 4.14. Fe line abundances synthesized from the IL spectra of NGC 6093 using its 7, 10, 13, and 15 *Gyr* potential SSP solutions to define its set of model atmospheres. These plots are listed, from top-to-bottom, in order of increasing age. All plotting conventions and notations follow those used in Figure 3.10.

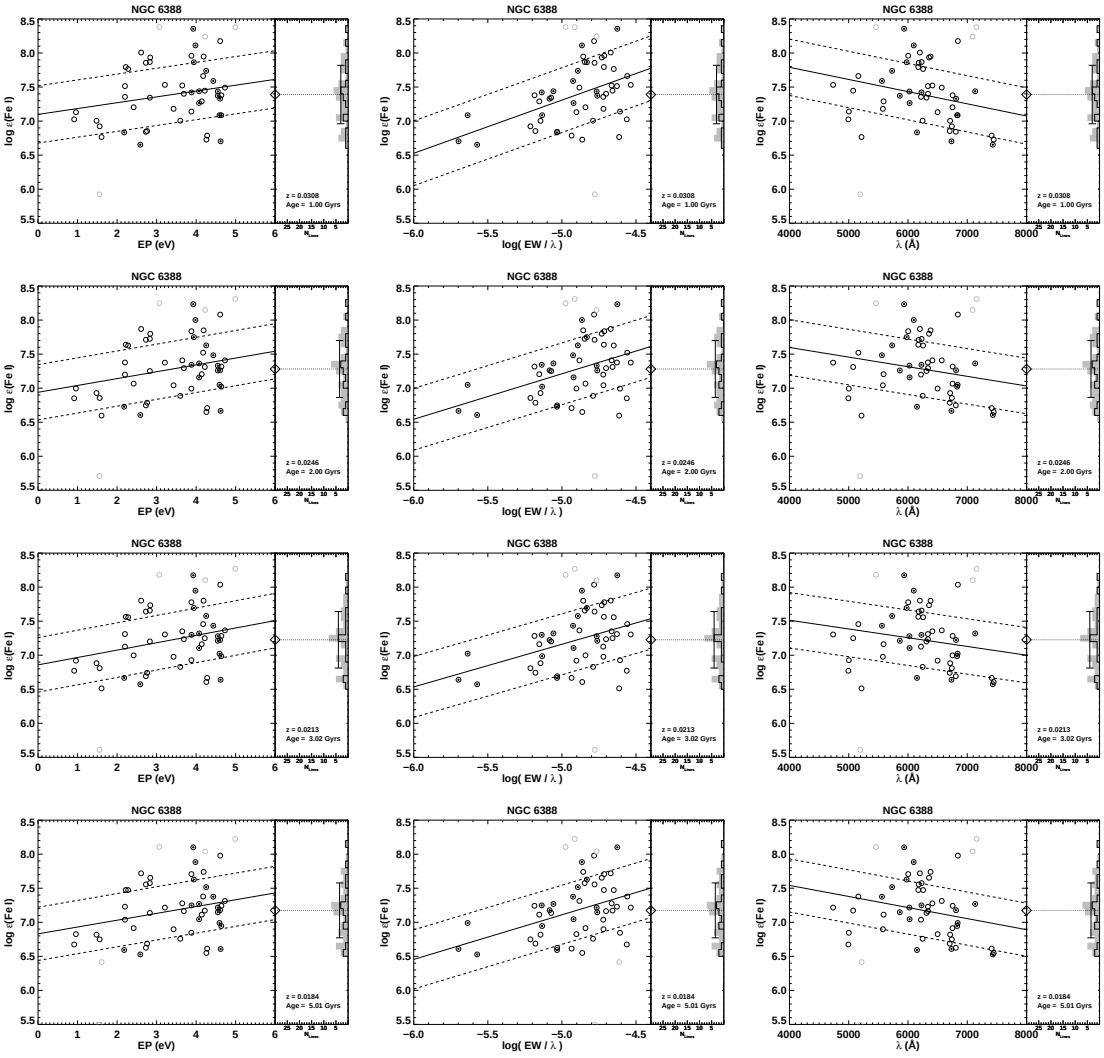

Figure 4.15. Fe line abundances synthesized from the IL spectra of NGC 6388 using its 1, 2, 3, 5 *Gyr* potential SSP solutions to define its set of model atmospheres. These plots are listed, from top-to-bottom, in order of increasing age. All plotting conventions and notations follow those used in Figure 3.10.

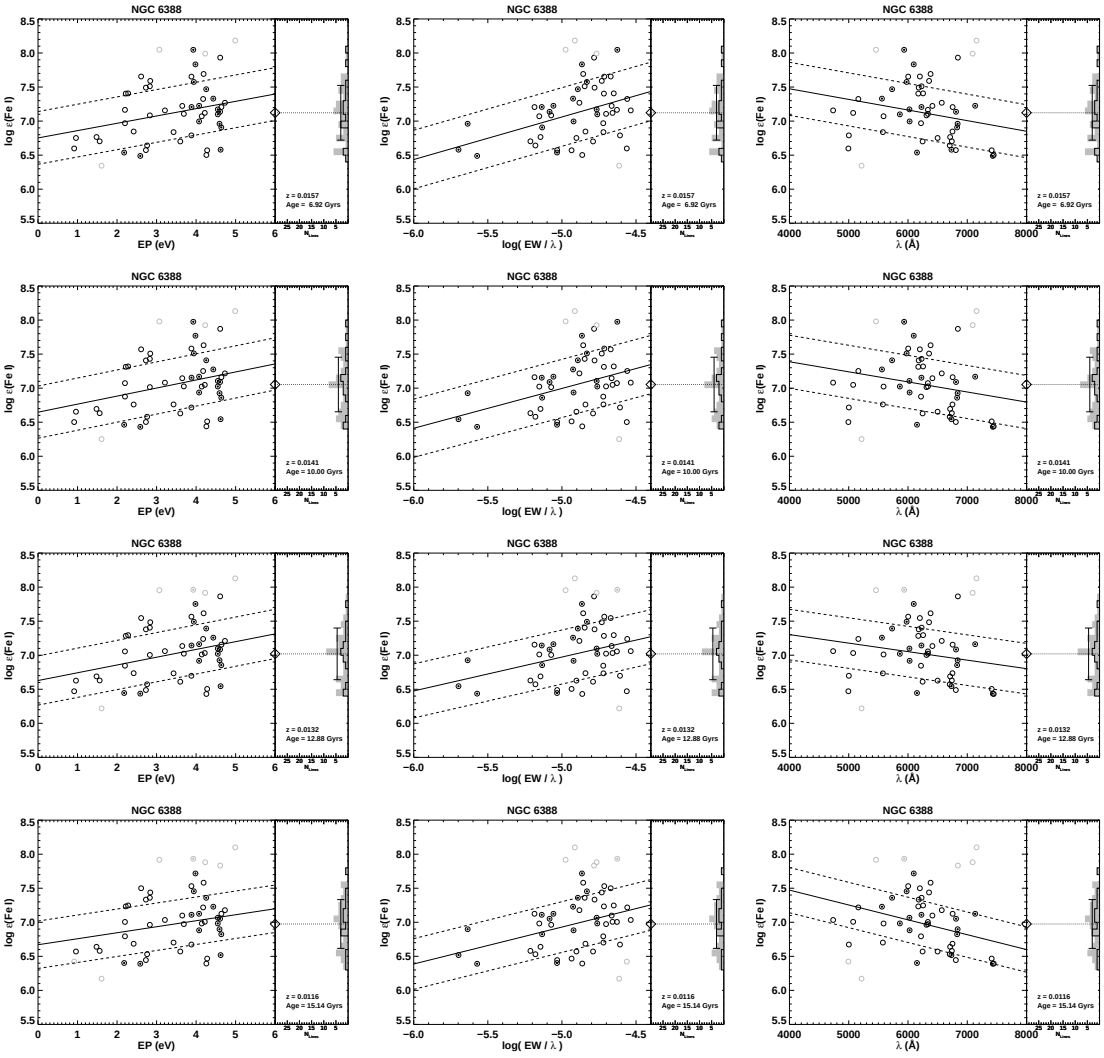

Figure 4.16. Fe line abundances synthesized from the IL spectra of NGC 6388 using its 7, 10, 13, and 15 *Gyr* potential SSP solutions to define its set of model atmospheres. These plots are listed, from top-to-bottom, in order of increasing age. All plotting conventions and notations follow those used in Figure 3.10.

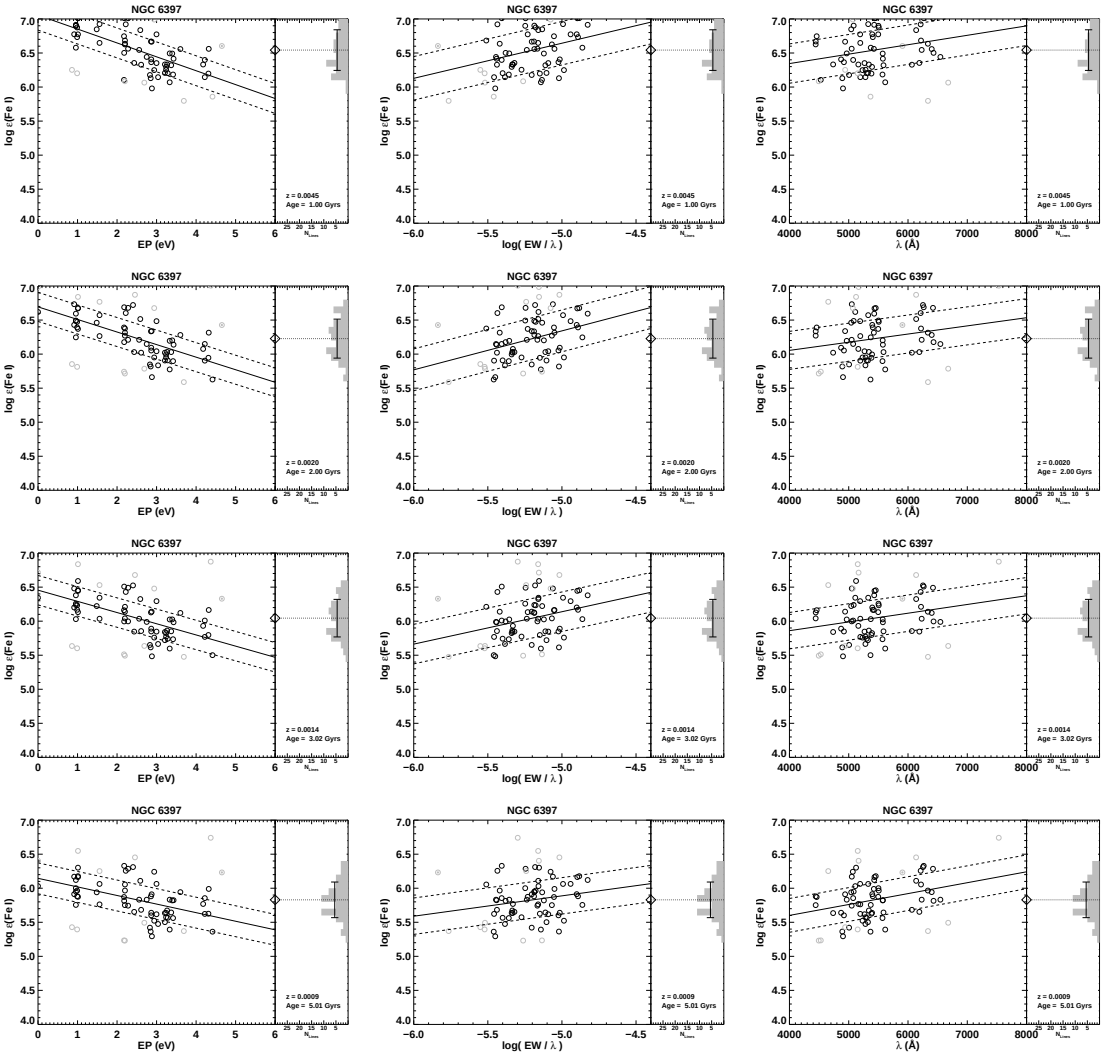

Figure 4.17. Fe line abundances synthesized from the IL spectra of NGC 6397 using its 1, 2, 3, 5 *Gyr* potential SSP solutions to define its set of model atmospheres. These plots are listed, from top-to-bottom, in order of increasing age. All plotting conventions and notations follow those used in Figure 3.10.

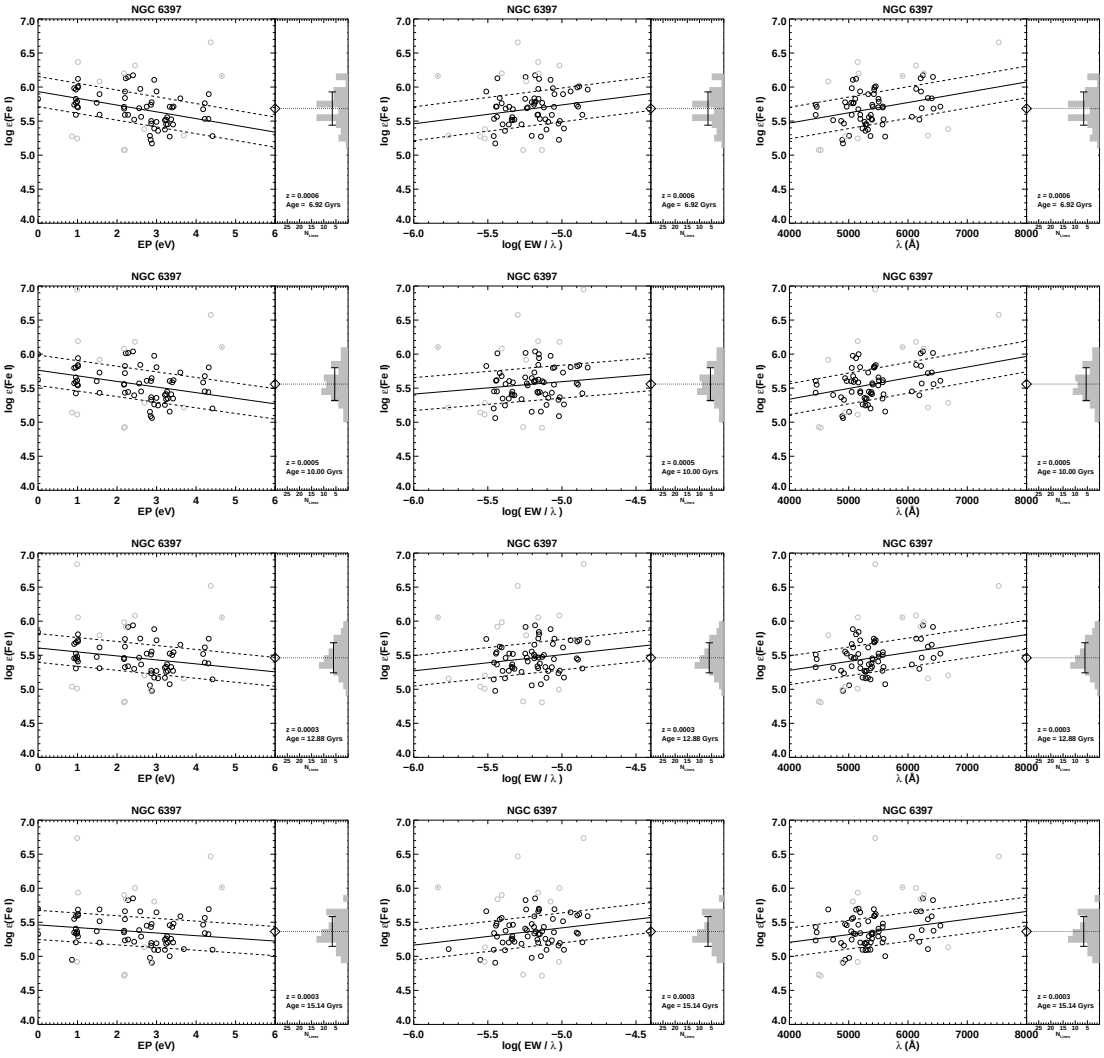

Figure 4.18. Fe line abundances synthesized from the IL spectra of NGC 6397 using its 7, 10, 13, and 15 *Gyr* potential SSP solutions to define its set of model atmospheres. These plots are listed, from top-to-bottom, in order of increasing age. All plotting conventions and notations follow those used in Figure 3.10.

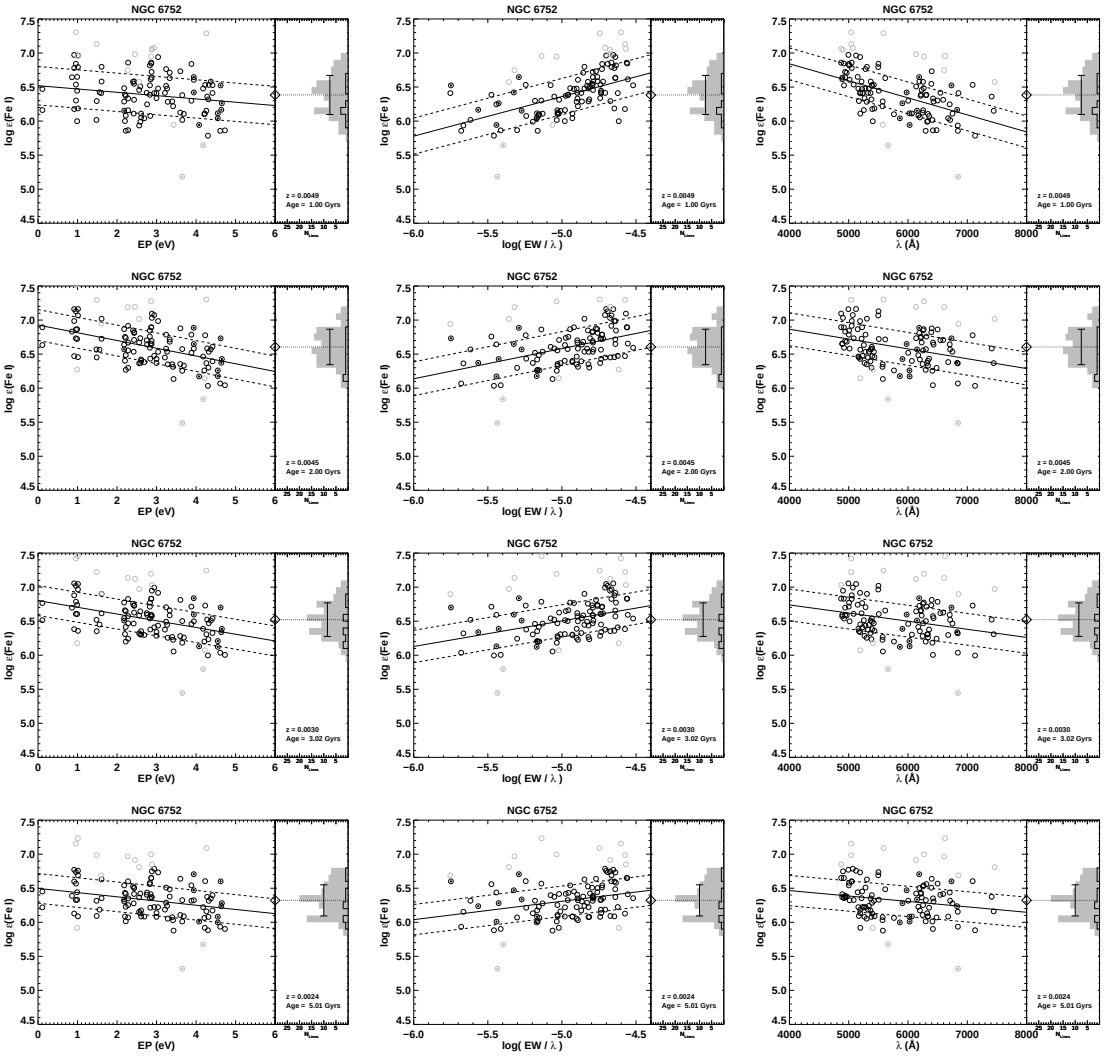

Figure 4.19. Fe line abundances synthesized from the IL spectra of NGC 6752 using its 1, 2, 3, 5 *Gyr* potential SSP solutions to define its set of model atmospheres. These plots are listed, from top-to-bottom, in order of increasing age. All plotting conventions and notations follow those used in Figure 3.10.

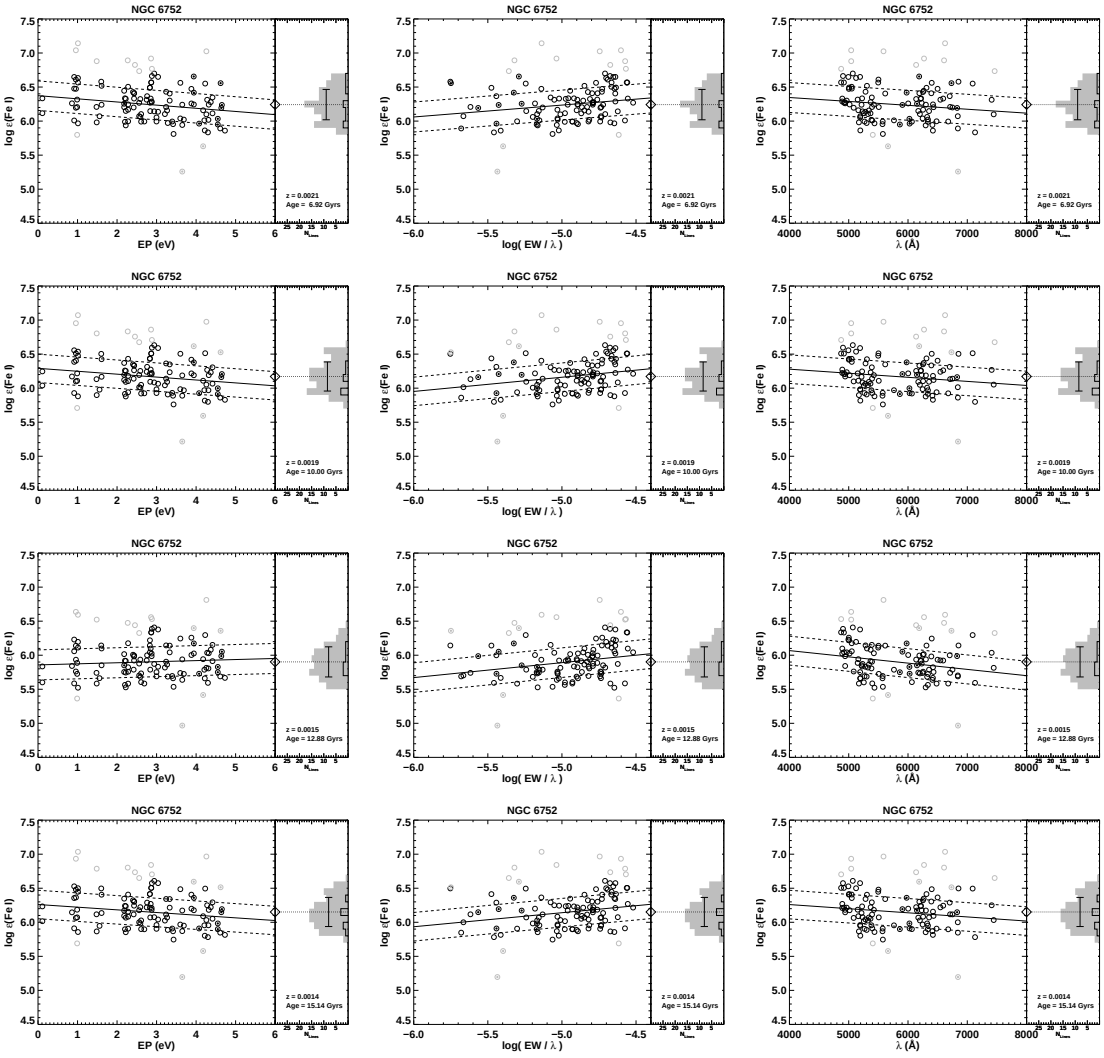

Figure 4.20. Fe line abundances synthesized from the IL spectra of NGC 6752 using its 7, 10, 13, and 15 *Gyr* potential SSP solutions to define its set of model atmospheres. These plots are listed, from top-to-bottom, in order of increasing age. All plotting conventions and notations follow those used in Figure 3.10.

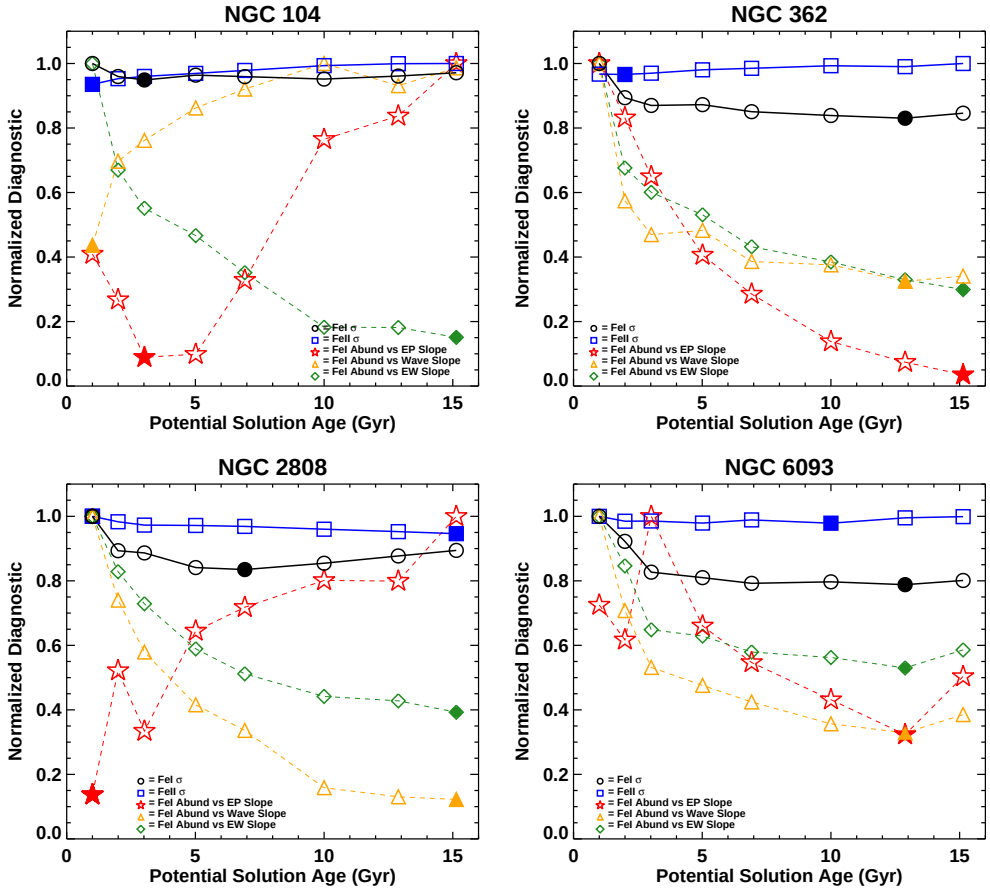

Figure 4.21. Fe line abundance diagnostics for NGC 104, NGC 362, NGC 2808, and NGC 6093. All diagnostics are normalized to their maximum values so that they can be shown on the same scale. The five diagnostic quantities are: (i.) the σ of the Fe I line abundances, (ii.) the σ of the Fe II line abundances, (iii.) the slope in $log\,\epsilon$(Fe I) vs. EP, (iv.) the slope in $log\,\epsilon$(Fe I) vs. wavelength, and (v.) the slope in $log\,\epsilon$(Fe I) vs. EW. Black circles, blue squares, red stars, orange triangles, and green diamonds depict the diagnostic quantities (i.), (ii.), (iii.), (iv.), and (v.), respectively. Filled symbols represent the diagnostics' global minima.

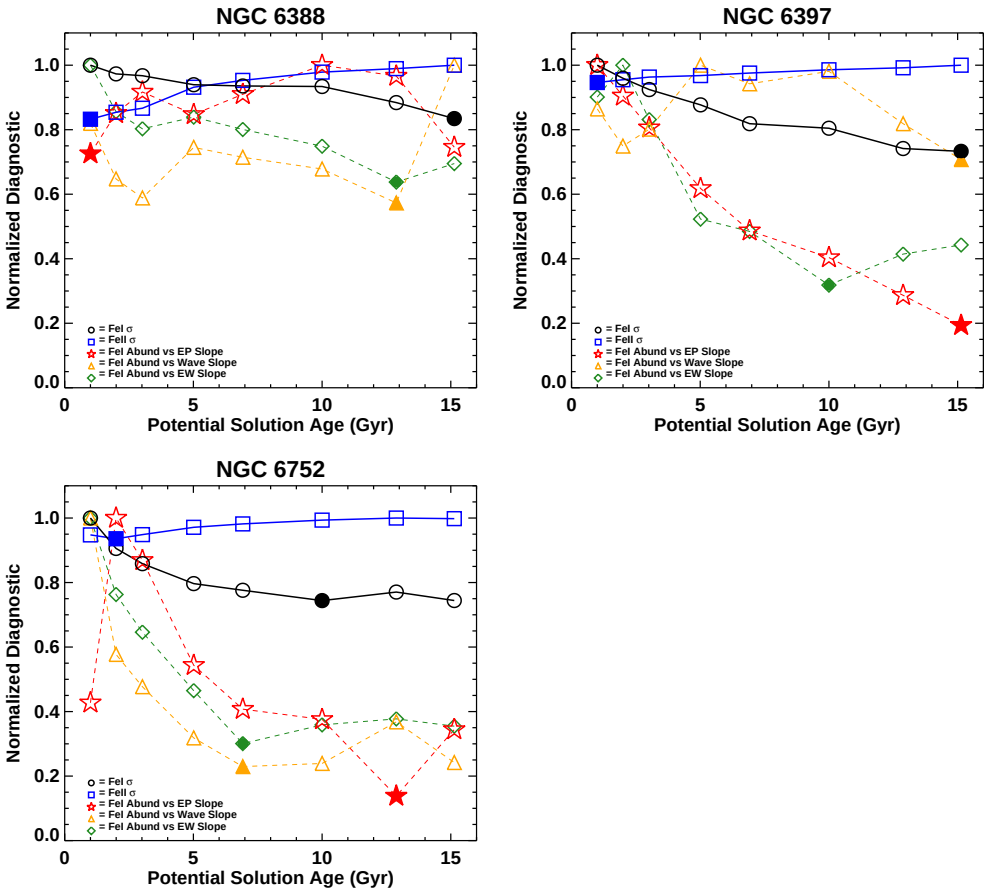

Figure 4.22. Fe line abundance diagnostics for NGC 6388, NGC 6397, and NGC 6752. See Figure 4.21 for available explanations.

change monotonically with age, and are strongly correlated with each other. This suggests that there is clearly a preferred SSP age and [Fe/H] range for each GC. To see this more clearly, these diagnostics are plotted in Figures 4.21 and 4.22. These plots show all five diagnostics as a function SSP age for the 8 SSPs that match the original selection criterion ("input" and "output" metallicities being self-consistent; see above). In the figures for NGC 362, NGC 2808, NGC 6093, NGC 6397, and NGC 6752, it is clear that all five diagnostics simultaneously imply that better solutions are obtained for older SSPs (at least older than ages >7 $Gyrs$). The only two clusters were the conclusions might be considered inconclusive are NGC 104 and NGC 6388; these are discussed further below. As the MW clusters are known to be old, these diagnostics would seem to be identifying an accurate age *range*. While a few of the clusters show global minima for several of the diagnostics at the oldest available SSP age, the statistical preferences for the 15 Gyr SSP over the 10 Gyr SSP is weak in most cases. This is not surprising because the SSPs themselves change very little over this range in age (see Figures 4.5 and 4.6). For any one cluster, it is found that the SSPs in age ranges of 5 $Gyrs$ (e.g. 10−15 $Gyrs$ or 7−13 $Gyrs$), give acceptable solutions. Finer ranges in age are difficult to statistically identify.

In the remaining cases where the diagnostics in Figures 4.21 and 4.22 are not *all* monotonically decreasing towards older ages (NGC 104, NGC 2808, NGC 6388), closer inspection still allows for the identification of the best-fitting SSP. First, because the EP diagnostic is sensitive to stellar temperature, it is clear from the plots in Figures 4.5 and 4.6 that this diagnostic will show a dip (smaller slope) at small SSP ages when there is a blue horizontal branch in the cluster that contributes hot stars. This is because young SSPs will add stars that mimic this hotter temperature population. This is notable in the diagnostics for NGC 2808 and NGC 6388, which have strong blue HBs and have global minima in EP at small ages, but also in NGC 6093 and NGC 6752, which show small local minima in the EP diagnostic at young ages, even though they have a global minimum for old ages. This temperature sensitivity for the slope of Fe solutions with EP is expected (see discussions above), however it seems to make this EP diagnostic less reliable at distinguishing between the

pre-selected, 8 SSPs than one might expect. Among the remaining diagnostics, while small changes in any single value are not statistically significant, strong changes do seem to be good indicators of the best fitting SSP; all of the clusters show a consistent, if broad, minimum in 3 or 4 of the remaining diagnostics EW, λ, and Fe I and Fe II standard deviation at ages 10–15 $Gyrs$. The reduced EW appears to be the single most reliable indicator of a best SSP match for these old clusters.

The only clusters for which the diagnostics require more discussion are NGC 104 and NGC 6388. First it is noted that for both of these clusters, the EW diagnostic does show a global minimum in the range 13-15 Gyr. For NGC 6388, the diagnostics for Fe I standard deviation and λ also reach a global minimum in this range, so that the preferred SSP age range for this cluster is also "old" (10-15 Gyr), even though the diagnostics do not change very much over the full range of ages. It is also noted for this cluster that the [Fe/H] solutions from Fe I and Fe II have standard deviations that are by far the largest for the training set sample because this is the most metal-rich and highest velocity dispersion cluster in the sample; therefore, it both has relatively strong lines and more line blending than in the other clusters. These large standard deviations make the slope diagnostics less reliable, which makes any statistical difference between this cluster's different SSP solutions the smallest within the training set sample (see Figures 4.15 and 4.16). Given these characteristics, it is somewhat reassuring that it is possible to identify an age preference consistent with the known properties of NGC 6388. For NGC 104, once again, the EW diagnostic clearly identifies the best SSP as the oldest (15 $Gyrs$). Like NGC 6388, NGC 104 is also relatively metal-rich, and has high standard deviations for its Fe line abundances, however no other problems are obvious. For NGC 104, as for the others, an acceptable age range of 10-15 Gyr is identified, but note that while this is the preferred range, it is not strongly constrained.

In order to select which of the SSPs in the "old" 10-15 Gyr range should be selected as the single best SSP for each cluster, the analysis method's mean synthesized metallicities from each cluster's 8 SSPs are plotted in Figure 4.23. The first striking feature to note from this figure is that most of the synthesized, output metallicities

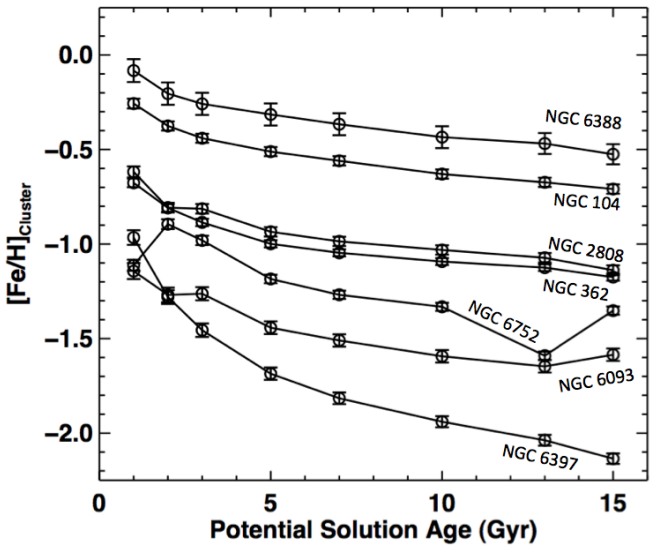

Figure 4.23. Synthesized metallicities from each cluster's 8 potential SSP solutions plotted against SSP age. Note that the synthesized metallicities remain essentially constant to within a range of $\sim$0.1 *dex* for SSPs older than 7 *Gyr*.

essentially asymptotically approach a single metallicity value as the input SSPs become older. For example, once the input SSPs become older than 5 *Gyr*, the output metallicities stay constrained around a metallicity ranger of around 0.2 *dex*, and then once the SSPs become older than 7 *Gyr*, this metallicity range shrinks to around 0.1 *dex*. Therefore, whichever specific, "old" SSP solution is chosen for a cluster ends up having little impact on the abundance results for the cluster's abundance analysis. The physical explanation for why the abundance results are insensitive to which old SSP is chosen is because the stellar populations for old GCs themselves asymptotically approach the same characteristic composition of stellar phases. This evolution towards uniformity can be easily seen back in Figures 4.5 and 4.6. Therefore, out of the "old" 10-15 *Gyr* acceptable SSP range, previously determined using the Fe line abundance diagnostics above, the middle 13 *Gyr* SSP is chosen as the best-matching SSP for each cluster.

4.4 Stellar Properties for the Best Matching SSPs

The best-fitting SSP adopted for each cluster is the one in the middle of the acceptable age range ($\sim$ 13 Gyrs). Before discussing the abundance analysis results obtained from the these best SSPs, the agreement between each best SSP and its cluster's observed CMD is investigated in Figures 4.24 and 4.25. In six of the seven cases, the selected SSPs match the location of the main sequence of the CMD quite well. The only exception is NGC 362, which is $\sim$0.15 magnitudes too red. These successful SSP matches are noteworthy, because they were selected purely spectroscopically based on Fe line abundance analysis. The luminosity functions, shown on the right in these plots, are also interesting. In general, the selected SSPs are quite well matched to the observed CMD with minor exceptions, most notably the main sequence of NGC 6388, and the red giant branches of NGC 6752 and NGC 6397, which are likely due to the low mass and poorly sampled scan regions of these clusters. The overall closeness of each cluster's photometric and SSP luminosity functions demonstrate that the methods used to create and search the grids of SSPs are able to produce and find SSPs that approximate the true GC stellar populations closely enough to obtain accurate abundances. Next, recall that the SSPs were simplified for the line abundance calculations by binning them into $\sim$28 representative average stellar types (see § 4.2). For completeness, these average stellar types are shown in Figures 4.26 and 4.27 for the best matching SSPs. The stellar parameters corresponding to these average stellar types are listed for each cluster in Tables 4.2 through 4.8.

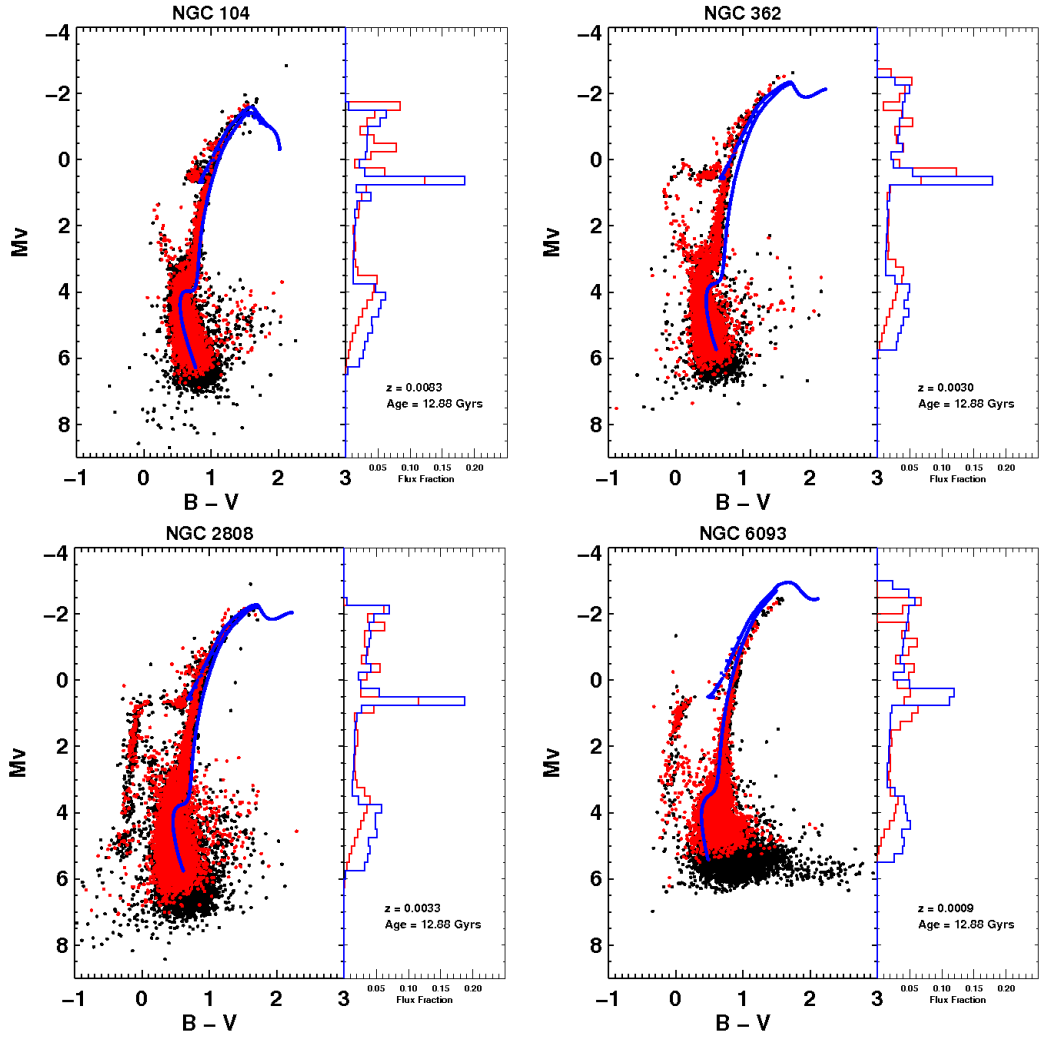

Figure 4.24. The best 13 *Gyr* SSPs compared with the photometric CMDs of NGC 104, NGC 362, NGC 2808, and NGC 6093. *Left Panels*: Red and black dots correspond to stars located inside and outside of each cluster's scanned region, respectively. The blue lines are comprised of the stars in the theoretical SSPs. The Z metallicity and age of each cluster's theoretical SSP is displayed in the lower right-hand corner of its plot. *Right Panels*: Each plot's right panel displays the luminosity functions of its CMD and SSP. The *y-axes* display the absolute V-band magnitudes of the CMDs, binned by 0.25 magnitudes, while the *x-axes* display the fractional V-band flux of the CMDs. The red lines and the blue lines correspond to each cluster's CMD luminosity function and its SSP luminosity function, respectively. Each cluster's CMD and SSP luminosity functions were normalized using the total amount of V-band flux emitted from the CMD stars located inside the cluster's scanned region.

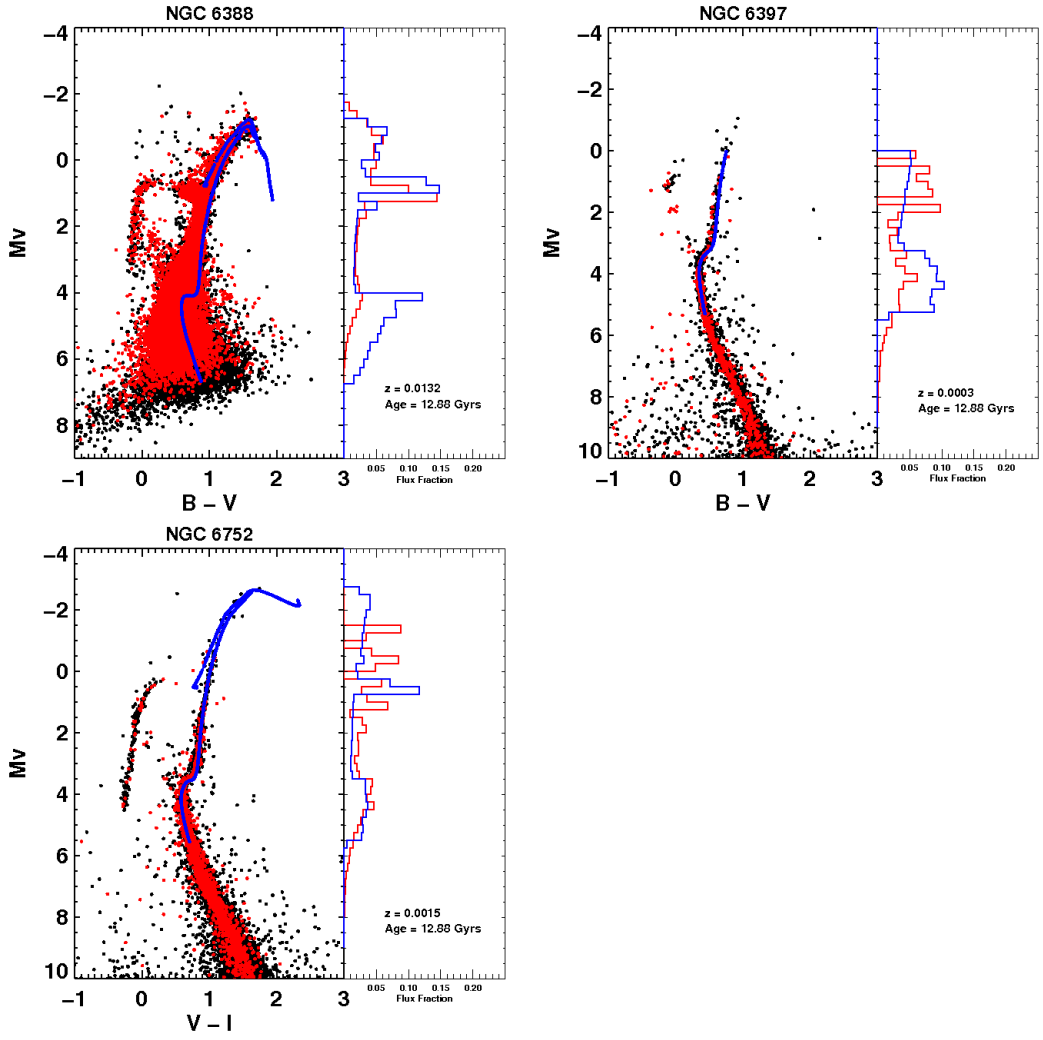

Figure 4.25. The best 13 *Gyr* SSPs compared with the photometric CMDs of NGC 6388, NGC 6397, and NGC 6752. See Figure 4.24 for available explanations.

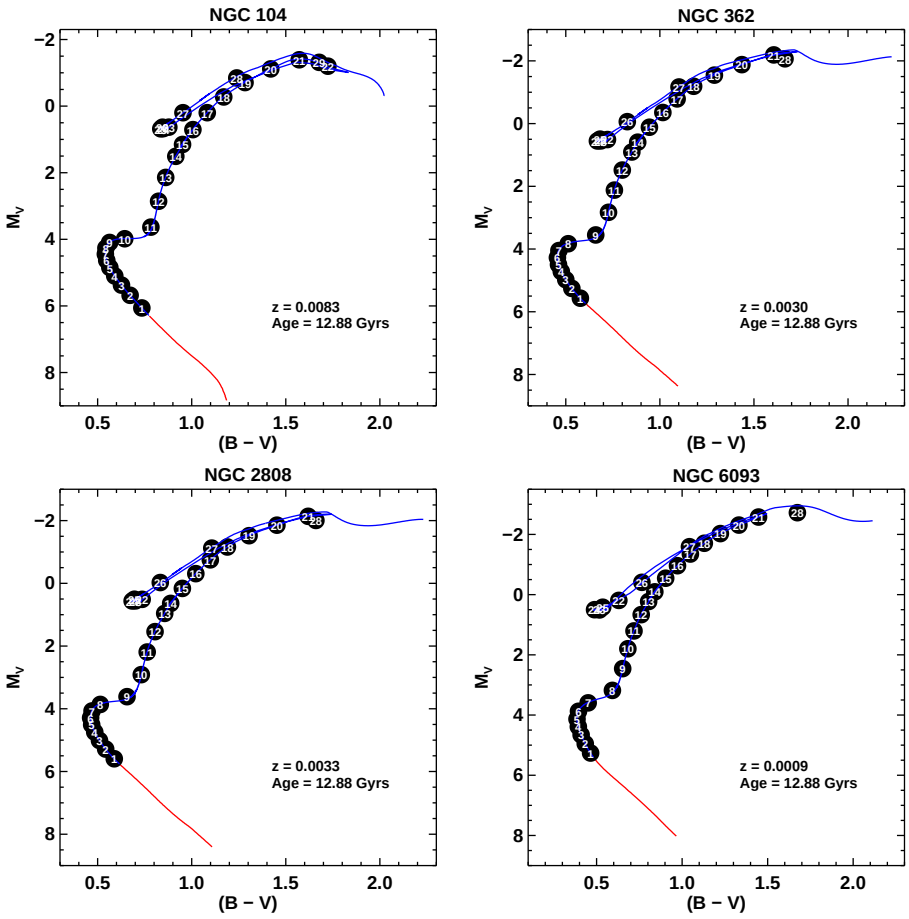

Figure 4.26. The conversion of the best 13 *Gyr* SSPs for NGC 104, NGC 362, NGC 2808, and NGC 6093 into ∼28 representative average stellar types. The Z metallicity and age of the SSP analyzed is displayed in the lower right-hand corner of its plot. The blue-and-red lines are comprised of the theoretical SSPs' stars plotted as CMDs. The lower red segments are comprised of low-mass stars that were cut to account for mass segregation inside the scanned regions. Stars were grouped into CMD segments that contain ∼3.5% of the total V-band flux within the SSP. Each numbered black dot represents the flux-weighted average color and magnitude location for all the stars contained within its segment. The enclosed stars also have flux-weighted average T_{eff}, $log(g_\star)$, R, and ξ_v calculated for them. These parameters are listed in Tables 4.2 through 4.8.

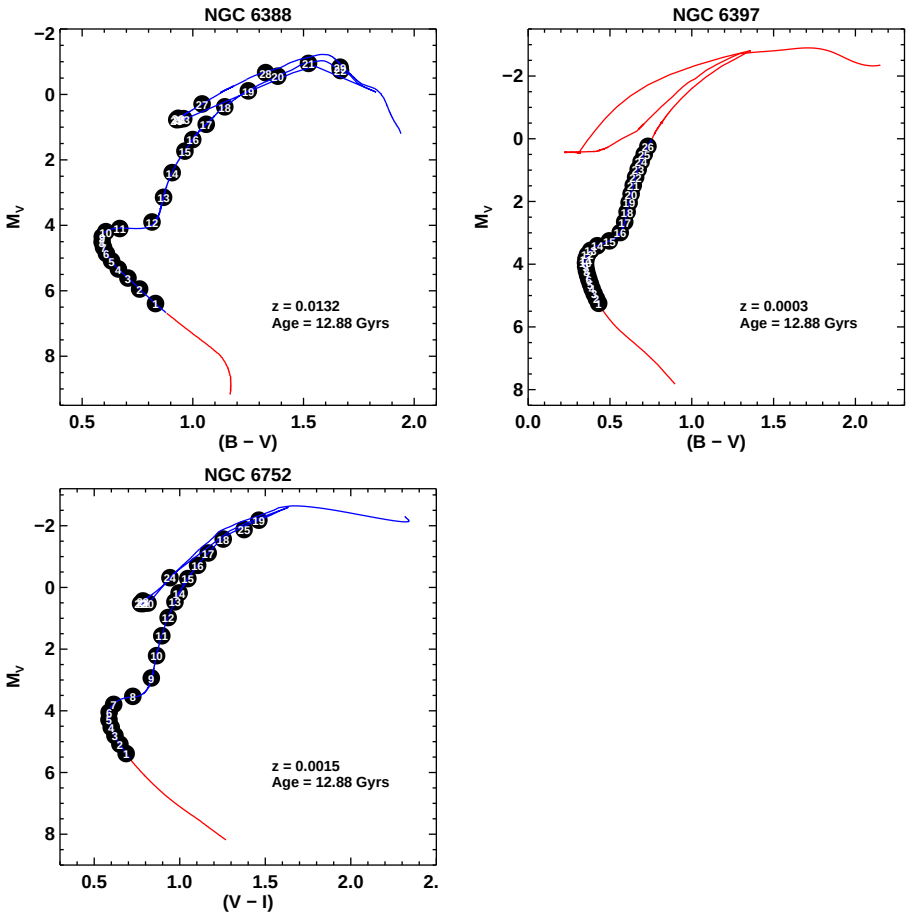

Figure 4.27. The conversion of the best 13 *Gyr* SSPs for NGC 6388, NGC 6397, and NGC 6752 into ∼28 representative average stellar types. The upper red segment of NGC 6397's SSP is comprised of bright stars ($M_V \leq 0$) that were cut in order to account for the lack of high-luminosity RGB stars within its scanned region. See Figure 4.26 for available explanations.

Box	$\langle M_v \rangle$ (mag)	$\langle (B-V) \rangle$ (mag)	T_{eff} (K)	$log(g_\star)$ $(log(cgs))$	ξ_v $(km\ s^{-1})$	R $(R_\odot)$	N_{stars}	Flux Frac.
1	6.061	0.735	5271	4.581	0.97	0.72	3355	0.0367
2	5.681	0.673	5488	4.538	0.98	0.77	2283	0.0355
3	5.375	0.627	5648	4.491	0.99	0.83	1830	0.0377
4	5.101	0.591	5773	4.438	1.00	0.89	1451	0.0386
5	4.848	0.565	5866	4.379	1.01	0.97	1126	0.0378
6	4.633	0.548	5924	4.320	1.03	1.04	869	0.0356
7	4.445	0.541	5948	4.259	1.04	1.13	749	0.0365
8	4.263	0.544	5932	4.187	1.05	1.24	618	0.0356
9	4.094	0.564	5853	4.099	1.07	1.38	525	0.0353
10	3.983	0.644	5570	3.955	1.10	1.63	473	0.0353
11	3.634	0.783	5127	3.636	1.17	2.38	347	0.0350
12	2.857	0.824	5018	3.277	1.25	3.60	170	0.0351
13	2.141	0.862	4932	2.950	1.32	5.25	88	0.0352
14	1.507	0.915	4815	2.637	1.38	7.52	49	0.0352
15	1.151	0.951	4742	2.455	1.42	9.24	35	0.0351
16	0.706	1.006	4632	2.214	1.47	12.24	23	0.0353
17	0.197	1.083	4481	1.917	1.54	17.21	14	0.0351
18	-0.275	1.170	4322	1.620	1.60	24.20	9	0.0352
19	-0.707	1.283	4154	1.313	1.67	34.38	6	0.0360
20	-1.117	1.420	3972	0.989	1.73	49.68	4	0.0350
21	-1.391	1.571	3765	0.637	1.81	74.04	3	0.0350
22	-1.199	1.724	3525	0.221	1.90	117.34	2	0.0216
23	0.632	0.878	4949	2.302	1.45	10.77	22	0.0353
24	0.676	0.849	5013	2.354	1.44	9.74	22	0.0351
25	0.682	0.836	5046	2.372	1.44	9.54	23	0.0354
26	0.633	0.845	5025	2.342	1.45	9.87	22	0.0351
27	0.198	0.953	4792	2.044	1.51	14.46	15	0.0352
28	-0.846	1.239	4256	1.281	1.67	34.63	6	0.0354
29	-1.314	1.677	3628	0.319	1.88	109.57	2	0.0153

Table 4.2. NGC 104's representative average stellar types as derived from its from its best 13 Gyr SSP. The "Box" column lists the labels assigned to the regions used to convert the SSP into its $\sim$28 average stellar types. These locations are shown in Figure 4.26. For each average stellar type: the "$\langle M_V \rangle$" column lists the flux-weighted average M_V magnitude; the "$\langle (B-V) \rangle$" column lists the flux-weighted average $(B-V)$ color; the "T_{eff}" column lists the effective temperature; the "$log(g_\star)$" column lists the surface gravity; the "ξ_v" column lists the microturbulent velocity; the "R" column lists the radius; the "N_{stars}" column lists the number of stars represented by each average stellar type; and the "Flux Frac." column lists the amount of flux that each average stellar type's N_{stars} stars emit, normalized to the total flux of the SSP.

Box	$\langle M_v \rangle$ (mag)	$\langle (B-V) \rangle$ (mag)	T_{eff} (K)	$log(g_\star)$ $(log(cgs))$	ξ_v $(km\ s^{-1})$	R $(R_\odot)$	N_{stars}	Flux Frac.
1	5.568	0.577	5736	4.553	0.98	0.74	3400	0.037
2	5.255	0.532	5898	4.497	0.99	0.80	2512	0.036
3	4.977	0.500	6019	4.436	1.00	0.87	1966	0.037
4	4.720	0.476	6110	4.371	1.01	0.95	1496	0.035
5	4.496	0.461	6168	4.306	1.03	1.03	1230	0.036
6	4.274	0.455	6186	4.230	1.04	1.14	988	0.035
7	4.048	0.463	6139	4.131	1.07	1.28	835	0.037
8	3.831	0.513	5926	3.982	1.10	1.53	659	0.035
9	3.551	0.659	5411	3.690	1.16	2.17	510	0.035
10	2.829	0.727	5194	3.315	1.24	3.34	266	0.035
11	2.121	0.758	5105	2.995	1.31	4.83	137	0.035
12	1.481	0.800	5001	2.691	1.37	6.85	78	0.036
13	0.906	0.851	4885	2.405	1.43	9.51	46	0.036
14	0.593	0.882	4819	2.245	1.47	11.40	33	0.035
15	0.116	0.944	4694	1.986	1.52	15.38	22	0.035
16	-0.354	1.016	4558	1.717	1.58	20.92	14	0.035
17	-0.788	1.092	4420	1.456	1.63	28.20	9	0.035
18	-1.190	1.179	4279	1.195	1.69	37.97	6	0.036
19	-1.546	1.290	4129	0.927	1.75	51.42	5	0.035
20	-1.880	1.436	3964	0.641	1.81	70.79	4	0.037
21	-2.190	1.605	3799	0.341	1.87	98.46	3	0.038
22	0.509	0.721	5225	2.352	1.44	9.88	31	0.035
23	0.552	0.686	5306	2.406	1.43	8.90	32	0.035
24	0.554	0.668	5352	2.425	1.43	8.70	32	0.035
25	0.496	0.682	5319	2.388	1.44	9.08	30	0.035
26	-0.061	0.827	4987	2.011	1.52	14.56	19	0.035
27	-1.167	1.102	4452	1.269	1.67	33.76	7	0.035
28	-2.066	1.665	3759	0.240	1.89	117.16	2	0.028

Table 4.3. NGC 362's representative average stellar types as derived from its best 13 *Gyr* SSP. See Table 4.2 for available explanations.

Box	$\langle M_v \rangle$ (mag)	$\langle (B-V) \rangle$ (mag)	T_{eff} (K)	$log(g_\star)$ $(log(cgs))$	ξ_v $(km\ s^{-1})$	R $(R_\odot)$	N_{stars}	Flux Frac.
1	5.594	0.588	5704	4.555	0.98	0.74	5873	0.036
2	5.284	0.543	5867	4.500	0.99	0.80	4340	0.036
3	5.011	0.510	5988	4.441	1.00	0.87	3397	0.036
4	4.744	0.485	6084	4.375	1.01	0.95	2900	0.039
5	4.509	0.468	6145	4.308	1.03	1.03	2128	0.036
6	4.288	0.463	6163	4.231	1.04	1.14	1732	0.036
7	4.070	0.470	6120	4.137	1.06	1.28	1391	0.035
8	3.861	0.514	5933	3.999	1.09	1.50	1156	0.035
9	3.614	0.656	5431	3.725	1.15	2.09	923	0.035
10	2.912	0.732	5189	3.348	1.23	3.22	489	0.035
11	2.190	0.763	5100	3.022	1.30	4.69	254	0.036
12	1.541	0.805	4996	2.715	1.37	6.68	139	0.036
13	0.958	0.856	4878	2.424	1.43	9.32	84	0.037
14	0.640	0.888	4811	2.262	1.46	11.21	59	0.035
15	0.162	0.950	4687	2.003	1.52	15.13	38	0.035
16	-0.309	1.022	4549	1.732	1.58	20.61	25	0.035
17	-0.749	1.099	4408	1.466	1.63	27.96	17	0.036
18	-1.159	1.190	4262	1.197	1.69	37.97	12	0.036
19	-1.520	1.305	4108	0.921	1.75	51.88	8	0.036
20	-1.855	1.453	3942	0.636	1.81	71.42	6	0.035
21	-2.137	1.619	3776	0.335	1.87	99.36	5	0.037
22	0.510	0.737	5196	2.342	1.45	10.08	53	0.035
23	0.559	0.701	5277	2.399	1.43	8.99	55	0.035
24	0.562	0.683	5322	2.419	1.43	8.78	55	0.035
25	0.506	0.696	5294	2.384	1.44	9.14	52	0.035
26	-0.026	0.833	4981	2.025	1.51	14.36	34	0.035
27	-1.123	1.107	4444	1.284	1.67	33.27	12	0.035
28	-2.005	1.660	3756	0.262	1.89	115.11	4	0.028

Table 4.4. NGC 2808's representative average stellar types as derived from its best 13 *Gyr* SSP. See Table 4.2 for available explanations.

Box	$\langle M_v \rangle$ (mag)	$\langle (B-V) \rangle$ (mag)	T_{eff} (K)	$log(g_\star)$ $(log(cgs))$	ξ_v $(km\ s^{-1})$	R $(R_\odot)$	N_{stars}	Flux Frac.
1	5.262	0.465	6092	4.531	0.98	0.76	2268	0.036
2	4.953	0.434	6235	4.463	1.00	0.83	1767	0.037
3	4.659	0.410	6351	4.390	1.01	0.92	1340	0.037
4	4.387	0.393	6433	4.314	1.03	1.01	1056	0.038
5	4.134	0.386	6464	4.229	1.04	1.12	784	0.035
6	3.875	0.394	6400	4.113	1.07	1.29	640	0.036
7	3.595	0.451	6097	3.914	1.11	1.63	479	0.035
8	3.181	0.592	5518	3.557	1.19	2.48	330	0.035
9	2.458	0.653	5314	3.193	1.27	3.77	171	0.035
10	1.798	0.683	5220	2.891	1.33	5.33	92	0.035
11	1.206	0.719	5123	2.614	1.39	7.33	53	0.035
12	0.665	0.761	5022	2.352	1.44	9.90	33	0.036
13	0.229	0.804	4930	2.134	1.49	12.68	21	0.035
14	-0.093	0.840	4859	1.969	1.53	15.35	16	0.035
15	-0.545	0.904	4746	1.728	1.58	20.24	10	0.035
16	-0.961	0.973	4633	1.495	1.63	26.38	7	0.036
17	-1.349	1.048	4519	1.268	1.67	34.16	5	0.036
18	-1.706	1.130	4407	1.047	1.72	43.83	4	0.036
19	-2.028	1.224	4291	0.828	1.77	56.06	3	0.036
20	-2.310	1.332	4171	0.605	1.82	71.70	2	0.036
21	-2.577	1.447	4061	0.387	1.86	90.78	2	0.035
22	0.192	0.630	5392	2.264	1.46	13.12	24	0.035
23	0.508	0.517	5668	2.509	1.41	7.80	28	0.035
24	0.501	0.488	5782	2.547	1.40	7.47	28	0.035
25	0.419	0.536	5625	2.456	1.42	8.30	25	0.035
26	-0.408	0.765	5050	1.885	1.54	16.62	13	0.035
27	-1.592	1.043	4565	1.152	1.70	38.23	4	0.035
28	-2.722	1.674	3859	0.068	1.93	134.82	1	0.035

Table 4.5. NGC 6093's representative average stellar types as derived from its best 13 *Gyr* SSP. See Table 4.2 for available explanations.

Box	$\langle M_v \rangle$ (mag)	$\langle (B-V) \rangle$ (mag)	T_{eff} (K)	$log(g_\star)$ $(log(cgs))$	ξ_v $(km\ s^{-1})$	R $(R_\odot)$	N_{stars}	Flux Frac.
1	6.390	0.831	5000	4.587	0.97	0.72	20503	0.036
2	5.947	0.760	5237	4.546	0.98	0.77	13593	0.036
3	5.611	0.707	5420	4.507	0.99	0.82	9838	0.036
4	5.333	0.664	5568	4.467	0.99	0.87	7879	0.037
5	5.087	0.633	5673	4.419	1.00	0.93	6209	0.036
6	4.862	0.610	5752	4.367	1.02	1.00	5330	0.038
7	4.672	0.596	5800	4.315	1.03	1.07	4091	0.035
8	4.509	0.590	5820	4.263	1.04	1.14	3513	0.035
9	4.346	0.591	5812	4.201	1.05	1.24	3211	0.037
10	4.193	0.607	5754	4.124	1.07	1.36	2736	0.037
11	4.098	0.670	5538	4.009	1.09	1.56	2433	0.036
12	3.898	0.816	5082	3.738	1.15	2.16	2018	0.035
13	3.143	0.868	4947	3.373	1.23	3.28	1026	0.035
14	2.390	0.907	4868	3.034	1.30	4.86	505	0.035
15	1.731	0.964	4749	2.707	1.37	7.08	276	0.035
16	1.379	1.000	4680	2.527	1.41	8.67	196	0.035
17	0.912	1.060	4561	2.268	1.46	11.73	130	0.035
18	0.379	1.144	4401	1.951	1.53	16.90	80	0.036
19	-0.110	1.251	4227	1.627	1.60	24.51	51	0.035
20	-0.558	1.383	4037	1.283	1.67	36.33	33	0.035
21	-0.949	1.522	3824	0.908	1.75	55.78	24	0.036
22	-0.732	1.667	3522	0.396	1.86	101.02	23	0.028
23	0.741	0.959	4815	2.298	1.46	10.60	110	0.035
24	0.762	0.940	4858	2.330	1.45	10.23	111	0.035
25	0.772	0.927	4887	2.348	1.45	10.01	112	0.035
26	0.729	0.934	4875	2.325	1.45	10.28	108	0.035
27	0.290	1.042	4652	2.020	1.51	15.18	76	0.035
28	-0.666	1.329	4144	1.278	1.67	35.58	31	0.036
29	-0.833	1.665	3571	0.400	1.86	101.48	6	0.008

Table 4.6. NGC 6388's representative average stellar types as derived from its best 13 *Gyr* SSP. See Table 4.2 for available explanations.

Box	$\langle M_v \rangle$ (mag)	$\langle (B-V) \rangle$ (mag)	T_{eff} (K)	$log(g_\star)$ $(log(cgs))$	ξ_v $(km\ s^{-1})$	R $(R_\odot)$	N_{stars}	Flux Frac.
1	5.247	0.431	6215	4.550	0.98	0.74	79	0.035
2	5.099	0.417	6287	4.518	0.98	0.77	76	0.039
3	4.940	0.403	6361	4.482	0.99	0.81	74	0.044
4	4.784	0.391	6428	4.446	1.00	0.85	58	0.039
5	4.631	0.380	6489	4.407	1.01	0.89	56	0.044
6	4.486	0.371	6541	4.368	1.02	0.94	41	0.037
7	4.353	0.363	6582	4.331	1.02	0.98	40	0.041
8	4.211	0.356	6619	4.289	1.03	1.04	40	0.046
9	4.071	0.352	6640	4.243	1.04	1.10	28	0.037
10	3.952	0.350	6639	4.198	1.05	1.16	25	0.036
11	3.829	0.354	6610	4.144	1.06	1.24	22	0.036
12	3.699	0.362	6545	4.076	1.08	1.34	20	0.036
13	3.560	0.382	6414	3.985	1.10	1.49	17	0.035
14	3.412	0.422	6174	3.855	1.12	1.73	15	0.035
15	3.256	0.496	5805	3.675	1.16	2.14	12	0.035
16	2.991	0.563	5538	3.478	1.20	2.68	10	0.035
17	2.650	0.590	5435	3.304	1.24	3.28	7	0.035
18	2.332	0.605	5380	3.157	1.27	3.88	5	0.035
19	2.037	0.617	5336	3.023	1.30	4.53	4	0.035
20	1.756	0.629	5295	2.895	1.33	5.25	3	0.035
21	1.484	0.642	5254	2.770	1.36	6.07	2	0.037
22	1.226	0.657	5213	2.650	1.38	6.96	2	0.035
23	0.976	0.672	5171	2.533	1.41	7.97	2	0.037
24	0.729	0.690	5126	2.415	1.43	9.12	1	0.038
25	0.492	0.709	5083	2.301	1.46	10.40	1	0.036
26	0.242	0.732	5034	2.179	1.48	11.97	1	0.046

Table 4.7. NGC 6397's representative average stellar types as derived from its best 13 *Gyr* SSP. See Table 4.2 for available explanations.

Box	$\langle M_v \rangle$ (mag)	$\langle (B-V) \rangle$ (mag)	T_{eff} (K)	$log(g_\star)$ $(log(cgs))$	ξ_v $(km\ s^{-1})$	R $(R_\odot)$	N_{stars}	Flux Frac.
1	5.386	0.515	5915	4.532	0.98	0.76	423	0.037
2	5.081	0.477	6067	4.471	0.99	0.83	310	0.035
3	4.804	0.448	6189	4.407	1.01	0.90	240	0.035
4	4.536	0.427	6282	4.337	1.02	0.98	203	0.038
5	4.288	0.416	6332	4.260	1.04	1.08	150	0.036
6	4.044	0.416	6318	4.165	1.06	1.22	119	0.036
7	3.792	0.436	6194	4.032	1.09	1.43	94	0.035
8	3.531	0.546	5728	3.780	1.14	1.93	74	0.035
9	2.935	0.667	5321	3.395	1.22	3.01	43	0.035
10	2.212	0.701	5215	3.064	1.29	4.40	22	0.036
11	1.567	0.736	5118	2.766	1.36	6.21	12	0.035
12	0.977	0.780	5010	2.481	1.42	8.61	7	0.036
13	0.467	0.829	4902	2.224	1.47	11.54	4	0.035
14	0.177	0.860	4839	2.076	1.50	13.68	3	0.035
15	-0.286	0.923	4720	1.826	1.56	18.23	2	0.035
16	-0.717	0.993	4598	1.582	1.61	24.09	1	0.035
17	-1.117	1.067	4475	1.344	1.66	31.59	1	0.035
18	-1.569	1.170	4323	1.055	1.72	43.96	1	0.052
19	-2.180	1.398	4057	0.574	1.82	76.10	1	0.090
20	0.507	0.634	5370	2.402	1.43	8.92	4	0.035
21	0.523	0.599	5460	2.445	1.42	8.44	4	0.035
22	0.522	0.580	5511	2.464	1.42	8.26	5	0.035
23	0.437	0.602	5466	2.411	1.43	8.77	4	0.035
24	-0.316	0.802	5001	1.906	1.54	16.30	2	0.035
25	-1.876	1.290	4242	0.782	1.78	67.50	1	0.061

Table 4.8. NGC 6752's representative average stellar types as derived from its best 13 *Gyr* SSP. See Table 4.2 for available explanations.

4.5 Abundances from the Best Matching SSPs

For convenience, the the Fe-line diagnostics and metallicity solutions for all of the clusters' best 13 *Gyr* SSPs are shown in Figures 4.28 and 4.29. The final Fe I and Fe II mean abundances determined from analyzing each cluster's best SSP can be found in the center columns of Tables 3.10 through 3.16.

These SSPs are also used to analyze all of the non-Fe elements with measured EWs following the same procedure used for Fe lines. Abundances for these non-Fe species can be found in the middle columns of Tables 3.10 through 3.16.

4.6 Accuracy of Analysis using the Best Matching SSPs

The accuracy of the abundance analysis method, when using the best 13 *Gyr* SSPs to define each cluster's model atmospheres, is empirically assessed by comparing its abundance results with standard stellar abundances from the literature. Recall that these standard stellar abundances were introduced in § 3.5 and that they are defined in Appendix B.

First, the metallicities determined from the abundance analysis method's application on the 13 *Gyr* SSPs are directly compared with the standard stellar metallicities. This comparison is shown in Figure 4.30, where a perfect agreement would result in all data points lying on a 1:1 equivalence line. Within the figure, linear least-squares data fitting is used to identify any statistical uncertainties and systematic offsets between the abundance analysis method's Fe I and Fe II metallicity solutions as compared to the results from individual stars. Allowing both the slopes and intercepts of the best-fit lines to vary, the reduced-χ^2 values for the fits are 0.21 and 0.71 for Fe I and Fe II solutions, respectively, with y-intercepts (-0.03 *dex* and $+0.37$ *dex*, respectively) and small slopes (0.97 and 1.24, respectively). If the slopes of the Fe I and Fe II lines are constrained to 1.0, the reduced-χ^2 values are 0.18 and 1.21, respectively, and the y-intercepts are $+0.01$ *dex* and $+0.11$ *dex*, respectively. As the lines with constrained and unconstrained slopes are similar in reduced-χ^2 values, the simpler, more intuitive solutions that use constrained slopes are adopted as the relationship be-

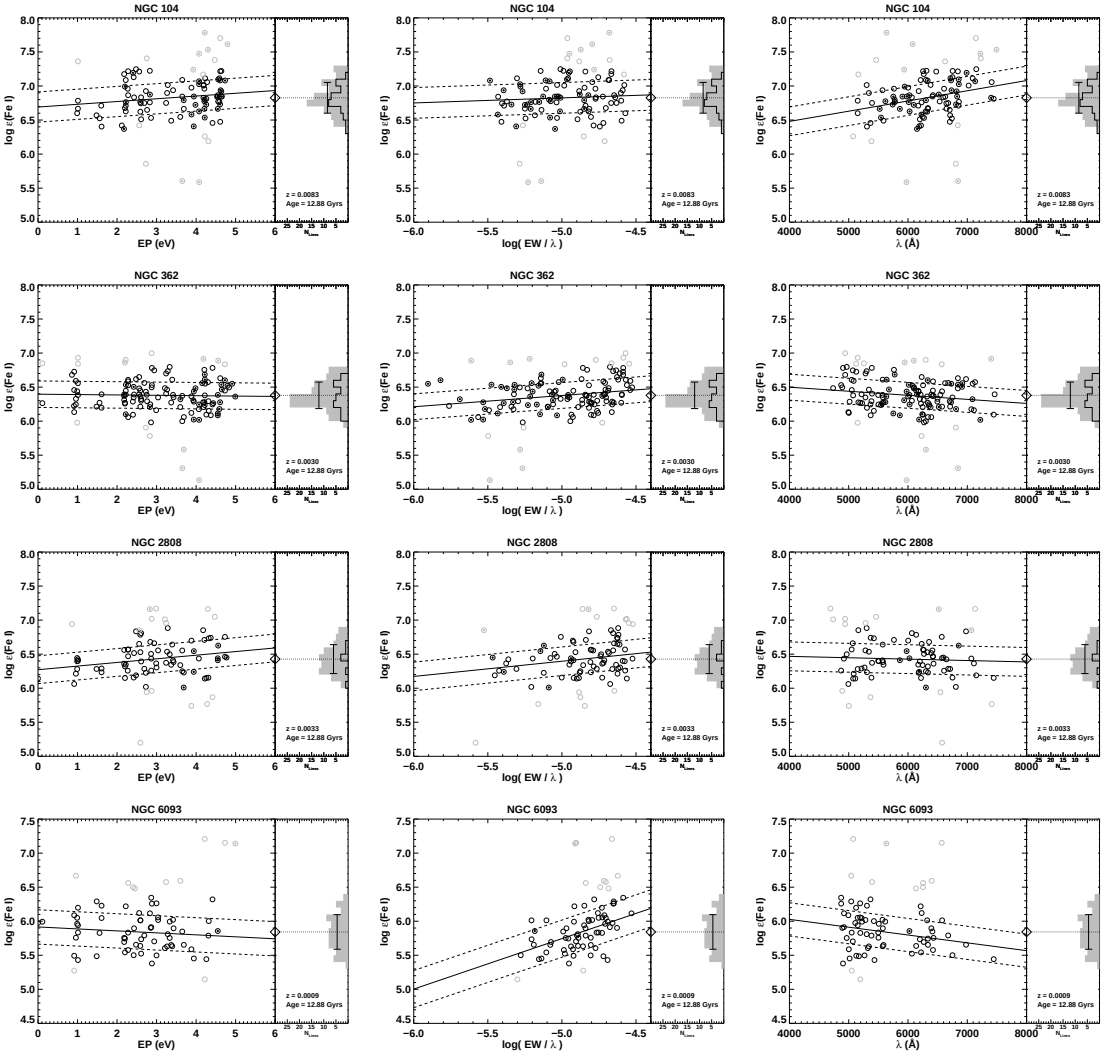

Figure 4.28. Fe line abundances synthesized from the IL spectra of NGC 104, NGC 362, NGC 2808, and NGC 6093, when using each cluster's 13 *Gyr* theoretical SSP to define its set of model atmospheres. All plotting conventions and notations follow those used in Figure 3.10.

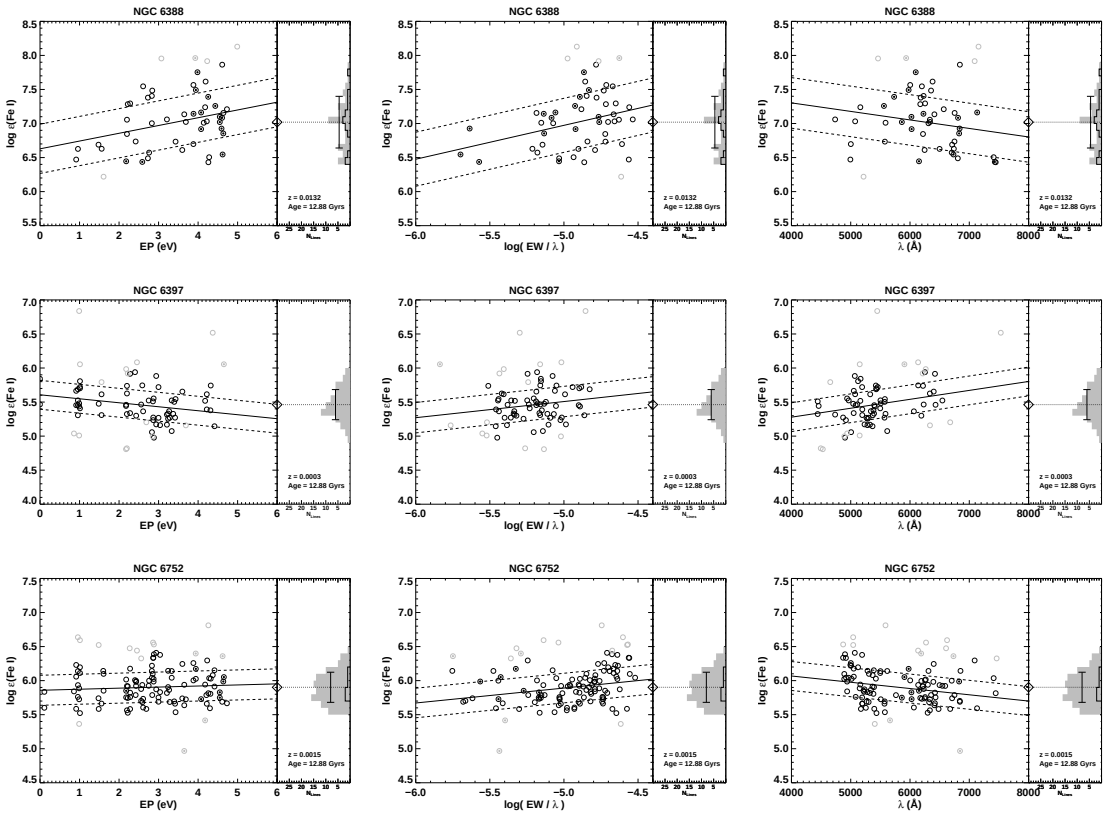

Figure 4.29. Fe line abundances synthesized from the IL spectra of NGC 6388, NGC 6397, and NGC 6752, when using each cluster's 13 Gyr theoretical SSP to define its set of model atmospheres. All plotting conventions and notations follow those used in Figure 3.10.

tween the method's metallicities and the literature's metallicities. These constrained slope best-fit lines also have the advantage that their y-intercepts can be naturally interpreted as the analysis method's systematic offsets from the 1:1 equivalence line. Furthermore, the RMS deviations for the data around the constrained best-fit lines can be attributed to the statistical uncertainties for the analysis method's metallicities. These statistical uncertainties are 0.09 *dex* and 0.22 *dex* for the Fe I and Fe II derived metallicities, respectively, and they are displayed in the residual plot shown in Figure 4.30's lower panel.

It is very interesting to note that the accuracy of the solution in [Fe/H] from Fe I lines is actually *better* from the SSP analysis than for the analysis based on the observed photometry of the clusters in Chapter 3. The obvious conclusion is that stellar atmospheres obtained from a well-matched SSP are more accurate than those calculated from the observed photometry. Notice that this does imply that the best-fitting SSPs that were identified by the method outlined in the previous sections are, indeed, a good match to the true SSPs of the clusters. It also implies that the stellar atmospheres obtained from observed photometry are not ideal. There are several possible explanations for this. First, the photometry itself will unavoidably suffer from non-negligible observational errors in such crowded fields and also suffer from small conversion errors between the HST and the Johnson-Cousins magnitude systems. The width of the main sequences of the photometric CMDs (see Figures 3.3 and 3.4) are a good indication of these observational errors, as they should ideally be quite narrow. Unrecognized binary stars may also complicate these errors, as well as differential reddening. Also, the reddening corrections applied are not perfect, particularly for NGC 362 (see Figure 4.24), so that there may be some small overall temperature errors. Lastly, some errors are likely accrued in converting from the observed parameters to the physical parameters of the stellar atmospheres.

The internal accuracy of the abundance analysis method to measure all available elemental abundances on a cluster-by-cluster basis is also investigated. The empirical comparison between the method's abundance results for each cluster and their standard stellar abundances are shown in Figures 4.31 and 4.32. Here, the same

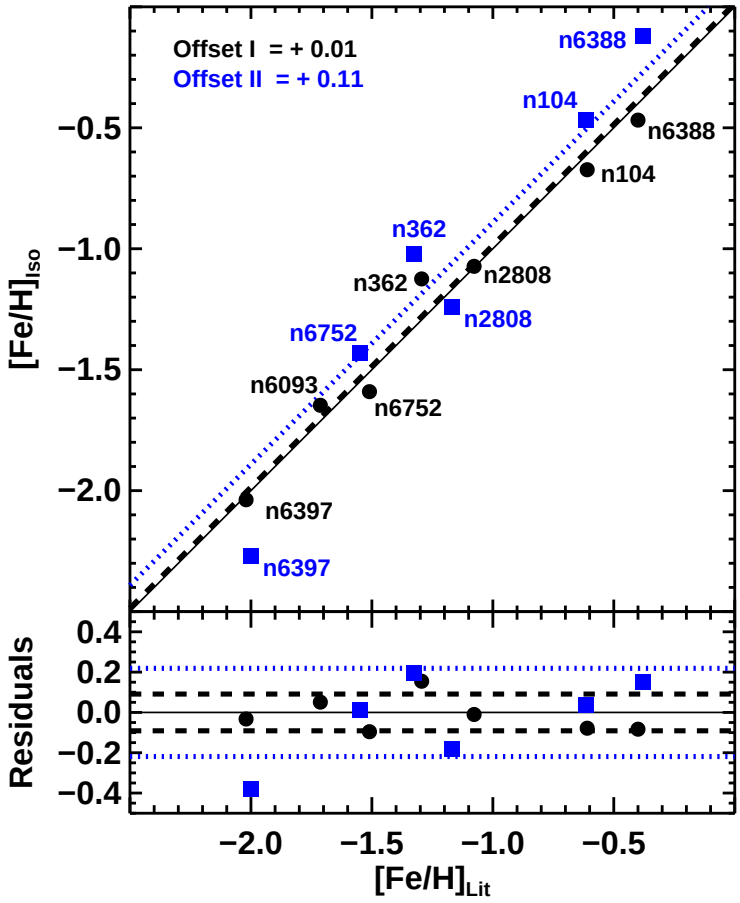

Figure 4.30. The abundance analysis method's accuracy in determining the metallicity of a cluster, when using each cluster's best 13 *Gyr* SSP to define its stellar atmospheres. *Upper Panel*: $[Fe/H]_{Iso}$ corresponds to metallicities derived using the IL spectra abundance analysis method, while $[Fe/H]_{Lit}$ corresponds to metallicities derived from standard stellar abundance analyses in the literature. These $[Fe/H]_{Lit}$ values serve as fiducial metallicities against which the accuracy of the method's $[Fe/H]_{Iso}$ values are determined. The black solid line corresponds to a line of 1:1 equivalence between $[Fe/H]_{Iso}$ and $[Fe/H]_{Lit}$; therefore, any deviations from this line are attributed to errors in $[Fe/H]_{Iso}$. As discussed in the text, linear best-fit lines with slopes constrained to 1.0 are adopted to represent the relationship between $[Fe/H]_{Iso}$ and $[Fe/H]_{Lit}$. Black circles and blue squares depict [Fe/H] derived from Fe I and Fe II lines, respectively. The black dashed line and blue dotted line denote the linear best-fit lines for the Fe I and Fe II data, respectively. Based on the y-intercept offsets from the 1:1 line, $[Fe/H]_{Iso}$ has an average systematic offset from the published metallicities of +0.01 *dex* and +0.11 *dex* for Fe I and Fe II, respectively. *Lower Panel*: The *y-axis* corresponds to the residuals of the upper panel's metallicities with respect to their best-fit lines. Black circles and solid squares depict these residuals for Fe I and Fe II, respectively. The horizontal black dashed lines and blue dotted lines correspond to the ±1 RMS deviation scatter of the upper panel's Fe I and Fe II based metallicities around their corresponding best-fit lines, respectively. These RMS deviations are 0.09 *dex* and 0.22 *dex* for Fe I and Fe II, respectively. Therefore, $[Fe/H]_{Iso}$ has an average statistical uncertainty of 0.09 *dex* and 0.22 *dex* for the Fe I and Fe II based metallicities, respectively.

strategy employed for the metallicities in Figure 4.30 are used to assess these internal accuracies. The upper panels of the figures display the abundances from the IL spectra abundance analysis method when using the 13 *Gyr* SSPs ($log\,\epsilon(\mathrm{X})_{\mathrm{Iso}}$) compared to the abundances obtained from individual stars ($log\,\epsilon(\mathrm{X})_{\mathrm{Lit}}$). Linear least-squares fits with slopes that are both unconstrained and constrained to 1.0 were applied to each cluster's neutral and singularly ionized species. As with the metallicities in Figure 4.30, the fits with constrained slopes produce similar reduced-χ^2 values as the fits with unconstrained slopes. Therefore, the simpler fits with constrained slopes are adopted to represent the functional relationship between $log\,\epsilon(\mathrm{X})_{\mathrm{Iso}}$ and $log\,\epsilon(\mathrm{X})_{\mathrm{Lit}}$.

Again, the intercepts for the best-fit lines with constrained slopes are attributed to be the systematic offsets for the clusters' IL spectra abundance solutions, and the RMS deviations of the data around these lines are attributed to be the statistical uncertainties for the solutions. The numerical values for these systematic offsets and statistical uncertainties are listed in the captions of Figures 4.31 and 4.32 and also in Table 4.9. To determine which clusters have meaningful systematic offsets, the magnitudes of their offsets are compared to the magnitudes of their statistical uncertainties. NGC 362 has a meaningful systematic offset equal to $\sim +0.2$ *dex* for its neutral species, and a meaningful offset equal to $+0.4$ *dex*, for its singularly ionized species. All other clusters have offsets within the range of their statistical uncertainties. Using all seven clusters, the mean statistical uncertainties for the neutral and singularly ionized species are 0.20 ± 0.06 *dex* and 0.21 ± 0.10 *dex*, respectively, where the assigned errors are simply the standard deviations for the calculations. The small assigned errors for these mean uncertainties indicates that all seven clusters have fairly universal statistical uncertainties. The mean systematic offsets for the seven clusters' neutral and singularly ionized species are $+0.07 \pm 0.09$ *dex* and $+0.15 \pm 0.19$ *dex*, respectively, where the assigned errors are once again the standard deviations for the calculations. The fact that the mean systematic offsets are similar to their assigned errors indicates that the IL spectra abundance results do not suffer from a single systematic offset that is universal for all the clusters, but instead are dominated by NGC 362's offsets.

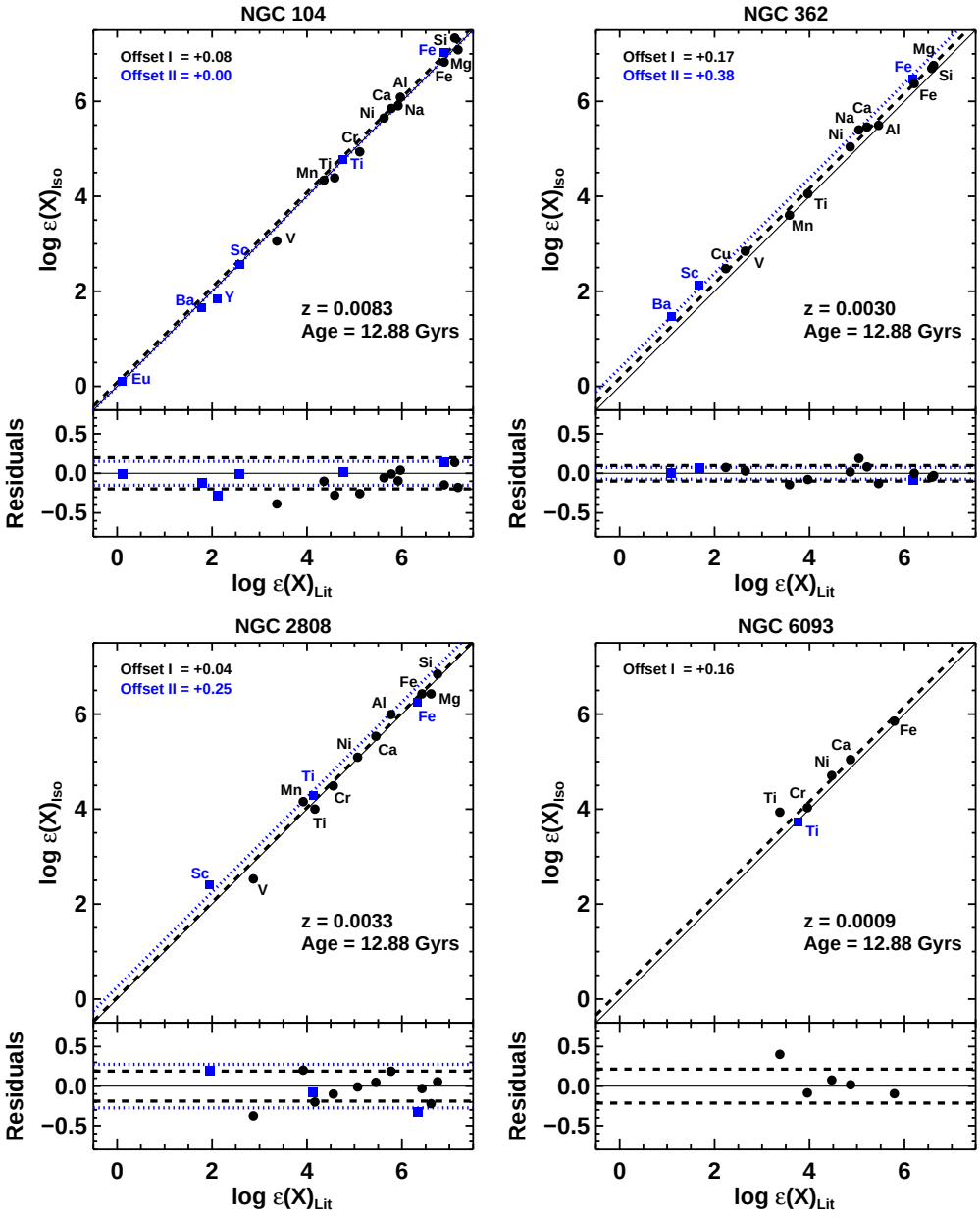

Figure 4.31. The abundance analysis method's internal accuracy in determining all the $log\,\epsilon(X)$ abundances for clusters NGC 104, NGC 362, NGC 2808, and NGC 6093, when using each cluster's best 13 *Gyr* SSP to define its stellar atmospheres. All plotting conventions and data analysis match those used for the metallicities in Figure 4.30, except that the y-axis and x-axis of each plot's upper panel now correspond to its species' $log\,\epsilon(X)_{\rm Iso}$ and $log\,\epsilon(X)_{\rm Lit}$ abundances, respectively. *Upper Panels*: The neutral species of NGC 104, NGC 362, NGC 2808, and NGC 6093 have average systematic abundance offsets of +0.08, +0.17, +0.04, and +0.16 *dex*, respectively. Likewise, the singularly ionized species of NGC 104, NGC 362, and NGC 2808 have average systematic offsets of 0.00, +0.38, and +0.25 *dex*, respectively. *Lower Panels*: The neutral species of NGC 104, NGC 362, NGC 2808, and NGC 6093 have average statistical uncertainties of 0.20, 0.10, 0.19, and 0.21 *dex*, respectively. Likewise, the singularly ionized species of NGC 104, NGC 362, and NGC 2808 have average statistical uncertainties of 0.15, 0.07, ad 0.28 *dex*, respectively.

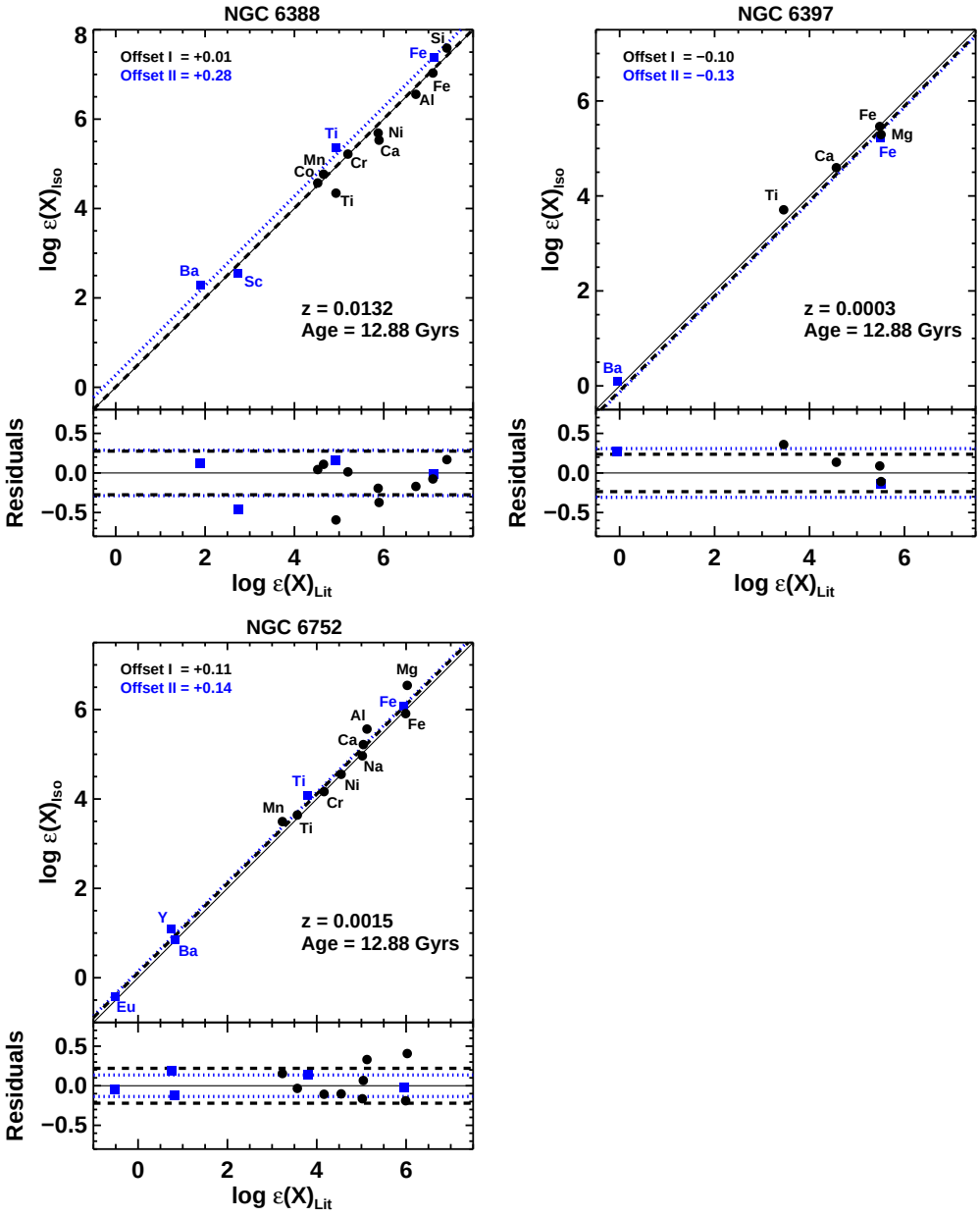

Figure 4.32. The abundance analysis method's internal accuracy in determining all the $log\,\epsilon(X)$ abundances for clusters NGC 6388, NGC 6397, and NGC 6752, when using each cluster's best 13 *Gyr* SSP to define its stellar atmospheres. See Figure 4.31 for a description of the plotting conventions and data analysis. *Upper Panels*: The neutral species of NGC 6388, NGC 6397 and NGC 6752 have average systematic abundance offsets of +0.01, −0.10, and +0.11 *dex*, respectively. Likewise, the singularly ionized species of NGC 6388, NGC 6397 and NGC 6752 have average systematic abundance offsets of +0.28, −0.13, and +0.14 *dex*, respectively. The neutral species of NGC 6388, NGC 6397 and NGC 6752 have average statistical uncertainties of 0.28, 0.24, and 0.22 *dex*, respectively. Likewise, the singularly ionized species of NGC 6388, NGC 6397 and NGC 6752 have average statistical uncertainties of 0.29, 0.31, and 0.14 *dex*, respectively.

Cluster	Ion.	Systematic (dex)	Statistical (dex)
NGC 104	I	$+0.08 \pm 0.05$	0.20
NGC 362	I	$+0.17 \pm 0.08$	0.10
NGC 2808	I	$+0.04 \pm 0.07$	0.19
NGC 6093	I	$+0.16 \pm 0.16$	0.21
NGC 6388	I	$+0.01 \pm 0.05$	0.28
NGC 6397	I	-0.10 ± 0.11	0.24
NGC 6752	I	$+0.11 \pm 0.10$	0.22
Mean	I	$+0.07 \pm 0.09$	0.20 ± 0.06
NGC 104	II	0.00 ± 0.08	0.15
NGC 362	II	$+0.38 \pm 0.11$	0.07
NGC 2808	II	$+0.25 \pm 0.14$	0.28
NGC 6388	II	$+0.28 \pm 0.11$	0.29
NGC 6397	II	-0.13 ± 0.16	0.31
NGC 6752	II	$+0.14 \pm 0.07$	0.14
Mean	II	$+0.15 \pm 0.19$	0.21 ± 0.10

Table 4.9. The abundance analysis method's estimated $log\,\epsilon(X)_{\rm Iso}$ uncertainties per training set cluster, when using each cluster's best 13 Gyr SSP to define its stellar atmospheres. For a graphical interpretation, see Figures 4.31 and 4.32. Systematic offsets are equivalent to the intercepts of the clusters' $log\,\epsilon(X)_{\rm Iso}$ versus $log\,\epsilon(X)_{\rm Lit}$ linear best-fit lines with slopes constrained to 1.0, and their quoted errors are equivalent to the fitting process' formal standard deviations for the intercepts. Statistical uncertainties are equivalent to the RMS deviations of the clusters' abundance data around their respective $log\,\epsilon(X)_{\rm Iso}$ versus $log\,\epsilon(X)_{\rm Lit}$ linear best-fit lines with constrained slopes. The mean systematic offset is the mean of all the clusters' systematic offsets, and its quoted error is their standard deviation. The mean statistical uncertainty is the mean of all the clusters' statistical uncertainties, and its quoted error is their standard deviation.

In an attempt to reduce any systematic offsets through self-calibration, the abundance data is replotted in [X/Fe] abundance ratio format. Figures 4.33 and 4.34 show the abundance data in [X/Fe] format. Comparing these figures with their $log\,\epsilon(\mathrm{X})$ counterparts (Figures 4.31 and 4.32) reveals that NGC 362 shows a noticeable improvement in its neutral species' [X/Fe] offset compared to its $log\,\epsilon(\mathrm{X})$ offset, but NGC 6752 shows a larger offset. The offset for NGC 362 shrinks by 0.17 *dex*, while NGC 6752 grows by 0.14 *dex*. As for the clusters' singularly ionized species, NGC 362, NGC 6388, and NGC 6752 have [X/Fe] offsets that shrink by 0.27, 0.27, and 0.08 *dex*, respectively, while the offsets of NGC 104 and NGC 2808 increase by -0.19 and 0.22 *dex*. Conducting similar comparisons between the statistical uncertainties shown in the [X/Fe] and $log\,\epsilon(\mathrm{X})$ figures reveals that they generally remain at $\sim$0.2 *dex*.

Lastly, the accuracy of the abundance analysis can be investigated on an element-by-element basis. Figures 4.35 through 4.37 display $log\,\epsilon(\mathrm{X})_{\mathrm{Iso}}$ versus $log\,\epsilon(\mathrm{X})_{\mathrm{Lit}}$ for all elements that have abundances measured in three or more clusters and possess stellar abundances in the literature. These elements include the Fe-peak elements Cr, Mn, Ni, Sc, and V displayed in Figure 4.35; the α-elements Ca, Mg, Si, and Ti displayed in Figure 4.36; the light-elements Al and Na displayed in Figure 4.37; and the neutron-capture element Ba, which is also displayed in Figure 4.37.

Once again the simpler fits with constrained slopes are adopted to represent the functional relationship between the IL spectra abundances and the literature abundances. The intercepts of the fits are attributed to be the abundance analysis method's systematic offsets for the various species' abundances, and the RMS deviation around these fits is attributed to be the analysis method's statistical uncertainties. The numerical values for these systematic offsets and statistical uncertainties are listed in the captions of Figures 4.35 through 4.37 and also in Table 4.9. Of all the measured elements, only Si possesses a systematic offset that is larger than its statistical uncertainties, but this is only on the order of 0.06 *dex*. The mean systematic offsets for all the Fe-peak elements, α-elements, and light-elements are $+0.08 \pm 0.12$ *dex*, $+0.04 \pm 0.09$ *dex*, and $+0.11 \pm 0.01$ *dex*, respectively, and their mean sta-

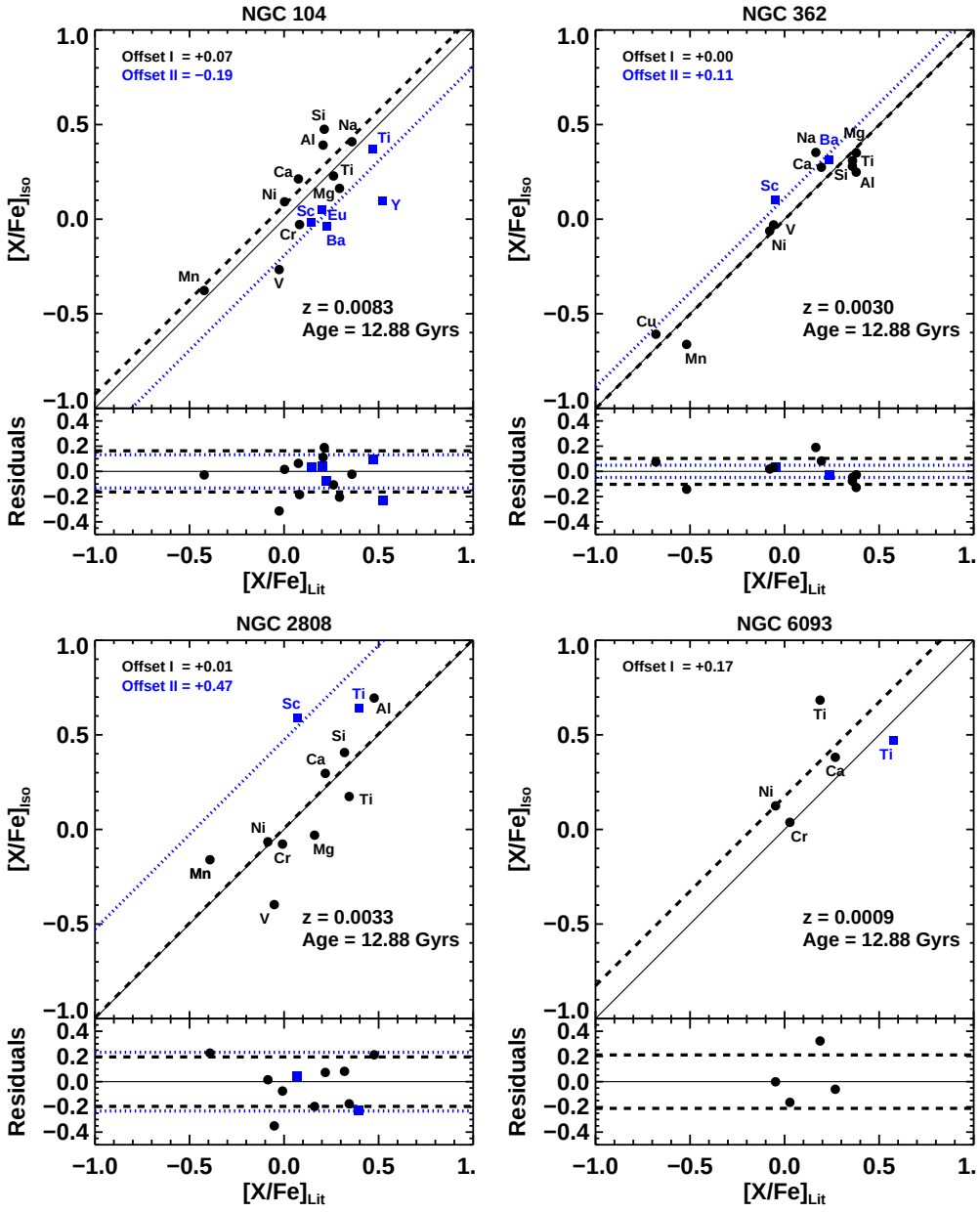

Figure 4.33. The abundance analysis method's internal accuracy in determining all the [X/Fe] abundance ratios for clusters NGC 104, NGC 362, NGC 2808, and NGC 6093, when using each cluster's best 13 *Gyr* SSP to define its stellar atmospheres. All plotting conventions and notations match those used for the metallicities in Figure 4.30, except that the y-axis and x-axis of each plot's upper panel now correspond to its species' $[X/Fe]_{Iso}$ and $[X/Fe]_{Lit}$ abundance ratios, respectively. *Upper Panels*: The neutral species of NGC 104, NGC 362, NGC 2808, and NGC 6093 have average systematic abundance offsets of +0.07, 0.00, +0.01, and +0.17 *dex*, respectively. Likewise, the singularly ionized species of NGC 104, NGC 362, and NGC 2808 have average systematic abundance offsets of −0.19, +0.11, and +0.47 *dex*, respectively. *Lower Panels*: The neutral species of NGC 104, NGC 362, NGC 2808, and NGC 6093 have average statistical uncertainties of 0.16, 0.10, 0.20, and 0.21 *dex*, respectively. Likewise, the singularly ionized species of NGC 104, NGC 362, and NGC 2808 have average statistical uncertainties of 0.13, 0.05, and 0.23 *dex*, respectively.

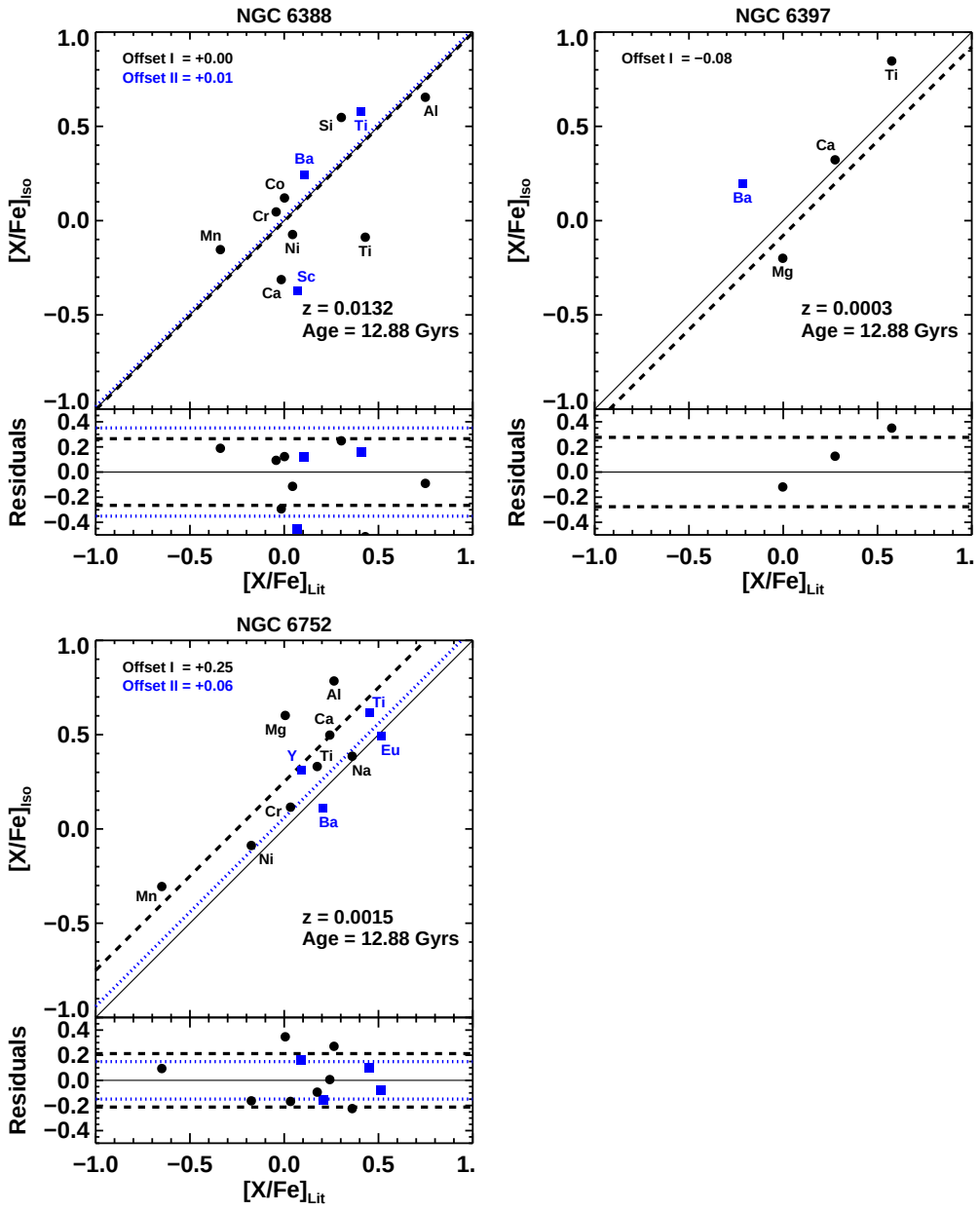

Figure 4.34. The abundance analysis method's internal accuracy in determining all the [X/Fe] abundance ratios for clusters NGC 6388, NGC 6397, and NGC 6752, when using each cluster's best 13 *Gyr* SSP to define its stellar atmospheres. See Figure 4.33 for a description of the plotting conventions and data analysis. *Upper Panels*: The neutral species of NGC 6388, NGC 6397 and NGC 6752 have average systematic abundance offsets of 0.00, −0.08, and +0.25 *dex*, respectively. Likewise, the singularly ionized species of NGC 6388 and NGC 6752 have average systematic abundance offsets of +0.01 and +0.06 *dex*, respectively. *Lower Panels*: The neutral species of NGC 6388, NGC 6397 and NGC 6752 have average statistical uncertainties of 0.26, 0.28, and 0.21 *dex*, respectively. Likewise, the singularly ionized species of NGC 6388 and NGC 6752 have average statistical uncertainties of 0.35 and 0.15 *dex*, respectively.

Species	Systematic (dex)	Statistical (dex)
Fe I	$+0.01 \pm 0.09$	0.09
Fe II	$+0.11 \pm 0.08$	0.22
Fe-Peak Elements		
Cr I	$+0.01 \pm 0.05$	0.10
Mn I	$+0.12 \pm 0.13$	0.12
Ni I	$+0.08 \pm 0.10$	0.15
Sc II	$+0.30 \pm 0.11$	0.35
V I	-0.08 ± 0.24	0.31
Mean	$+0.08 \pm 0.12$	0.19 ± 0.10
α-Elements		
Ca I	$+0.05 \pm 0.10$	0.20
Mg I	-0.07 ± 0.10	0.32
Si I	$+0.12 \pm 0.09$	0.06
Ti I	-0.03 ± 0.14	0.37
Ti II	$+0.13 \pm 0.08$	0.19
Mean	$+0.04 \pm 0.09$	0.23 ± 0.12
Light Elements		
Al I	$+0.12 \pm 0.05$	0.22
Na I	$+0.10 \pm 0.26$	0.23
Mean	$+0.11 \pm 0.01$	0.22 ± 0.01
n-Capture Element		
Ba II	$+0.11 \pm 0.08$	0.23
Mean Total	$+0.07 \pm 0.10$	0.21 ± 0.10

Table 4.10. The abundance analysis method's estimated $log\,\epsilon(X)_{\rm Iso}$ uncertainties per elemental species, when using each cluster's best 13 *Gyr* SSP to define its stellar atmospheres. Graphical interpretations are displayed in Figures 4.35 through 4.37. Note that the only species listed are those that possess $log\,\epsilon(X)_{\rm Iso} - log\,\epsilon(X)_{\rm Lit}$ abundance pairs for three or more clusters. Systematic offsets are equivalent to the intercepts of the species' $log\,\epsilon(X)_{\rm Iso}$ versus $log\,\epsilon(X)_{\rm Lit}$ linear best-fit lines with slopes constrained to 1.0, and their quoted errors are equivalent to the fitting process' formal standard deviations for the intercepts. Statistical uncertainties are equivalent to the RMS deviations of the species' abundance data around their respective $log\,\epsilon(X)_{\rm Iso}$ versus $log\,\epsilon(X)_{\rm Lit}$ linear best-fit lines with constrained slopes. The mean systematic offset is the mean of all the species' systematic offsets, and its quoted error is their standard deviation. The mean statistical uncertainty is the mean of all the species' statistical uncertainties, and its quoted error is their standard deviation.

tistical uncertainties are $+0.19 \pm 0.10$ dex, $+0.23 \pm 0.12$ dex, and $+0.22 \pm 0.01$ dex, respectively.

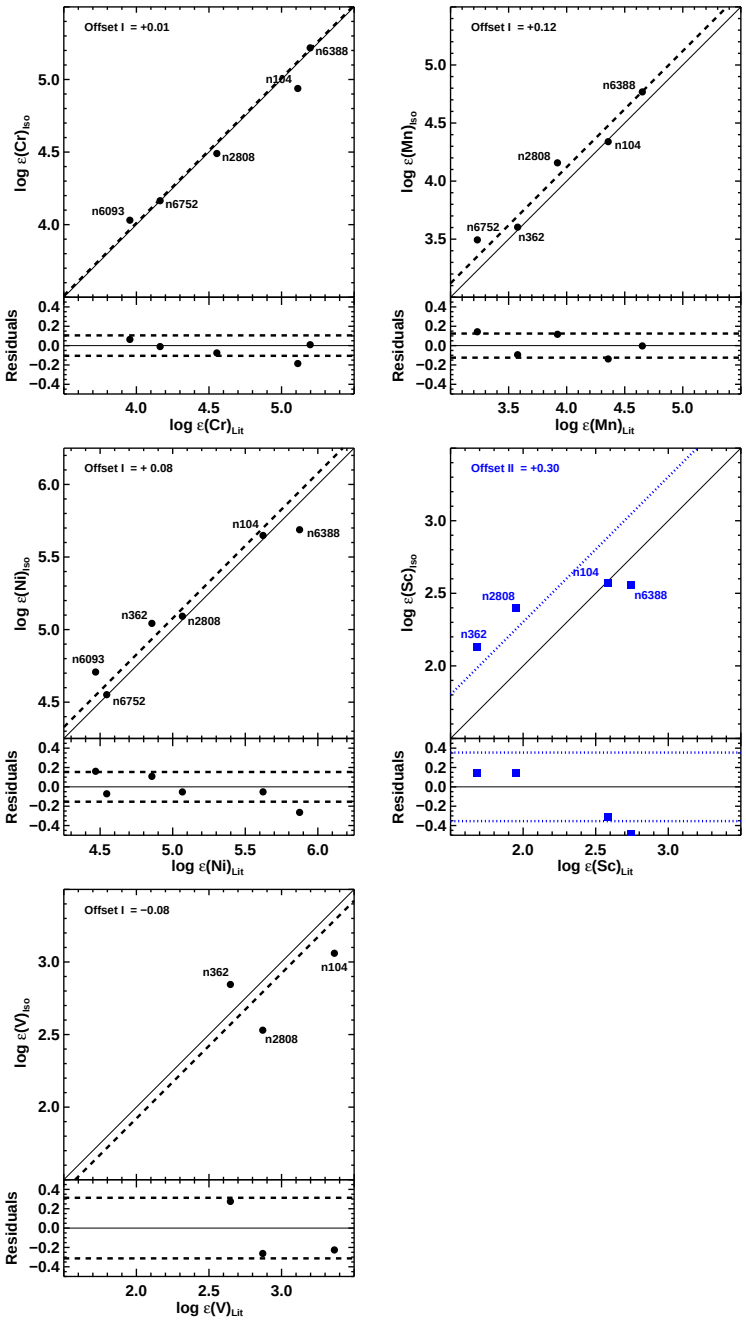

Figure 4.35. The abundance analysis method's global accuracy in determining the abundances of various Fe-peak elements, when using each cluster's best 13 *Gyr* SSP to define its stellar atmospheres. All plotting conventions and data analysis match those used for the metallicities in Figure 4.30, except that the y-axis and x-axis of each plot's upper panel now correspond to its species' $log\,\epsilon(X)_{\rm Iso}$ and $log\,\epsilon(X)_{\rm Lit}$ abundances, respectively. From left-to-right, row 1 depicts Cr and Mn; row 2 depicts Ni and Sc; row 3 depicts V. *Upper Panels*: Cr I, Mn I, Ni I, Sc II, and V I have systematic abundance offsets of +0.01, +0.12, +0.08, +0.30, and −0.08 *dex*, respectively. *Lower Panels*: Cr I, Mn I, Ni I, Sc II, and V I have statistical uncertainties of 0.10, 0.12, 0.15, 0.35, and 0.31 *dex*, respectively.

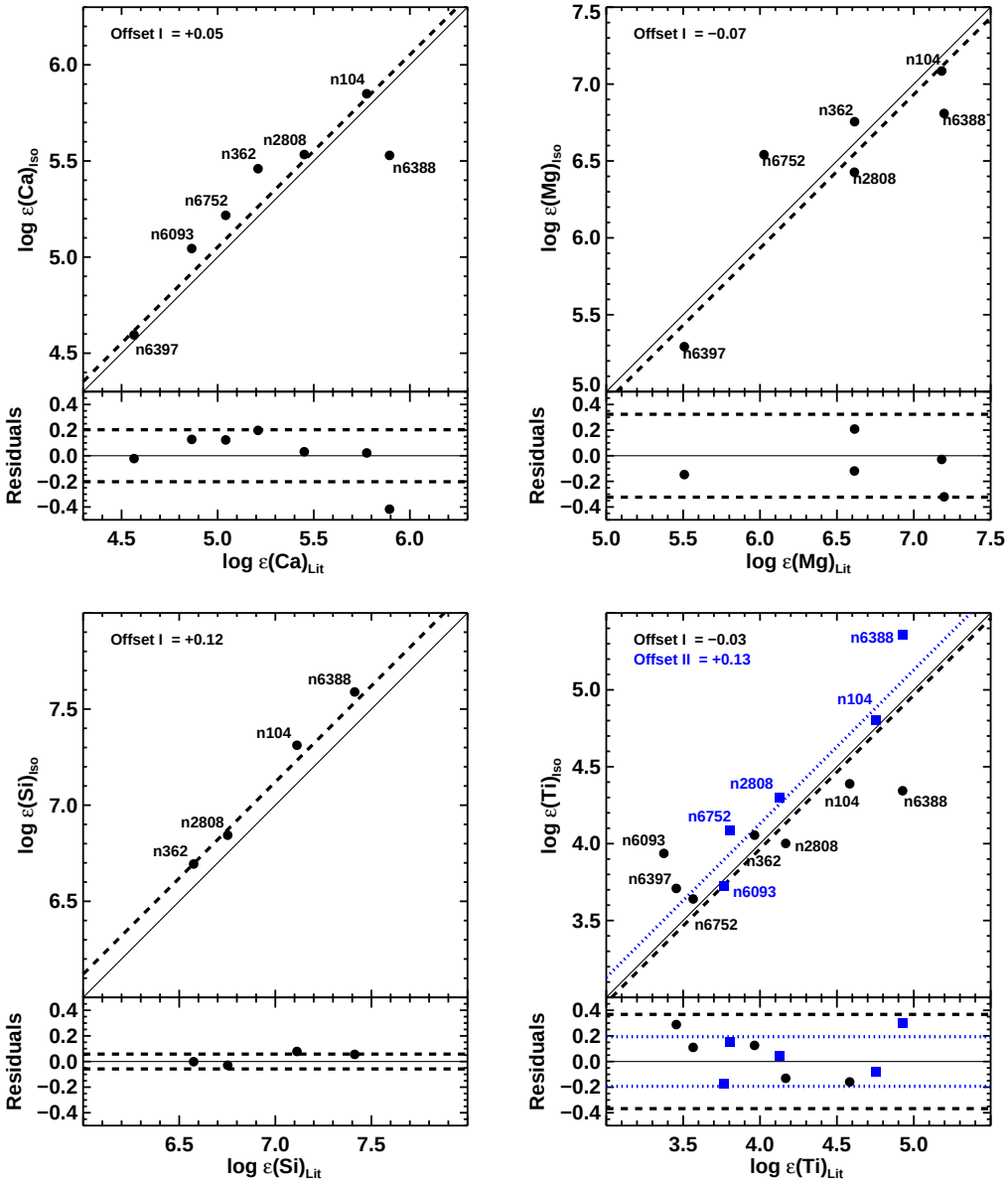

Figure 4.36. The abundance analysis method's global accuracy in determining the abundances of various α-elements, when using each cluster's best 13 *Gyr* SSP to define its stellar atmospheres. All plotting conventions and data analysis match those used for the Fe-peak abundances in Figure 4.35. From left-to-right, row 1 depicts Ca and Mg, while row 2 depicts Si and Ti. *Upper Panels*: Ca I, Mg I, Si I, Ti I and Ti II have systematic abundance offsets of +0.05, −0.07, +0.12, −0.03, and +0.03 *dex*, respectively. *Lower Panels*: Ca I, Mg I, Si I, Ti I and Ti II have statistical uncertainties of 0.20, 0.32, 0.06, 0.38, and 0.19 *dex*, respectively.

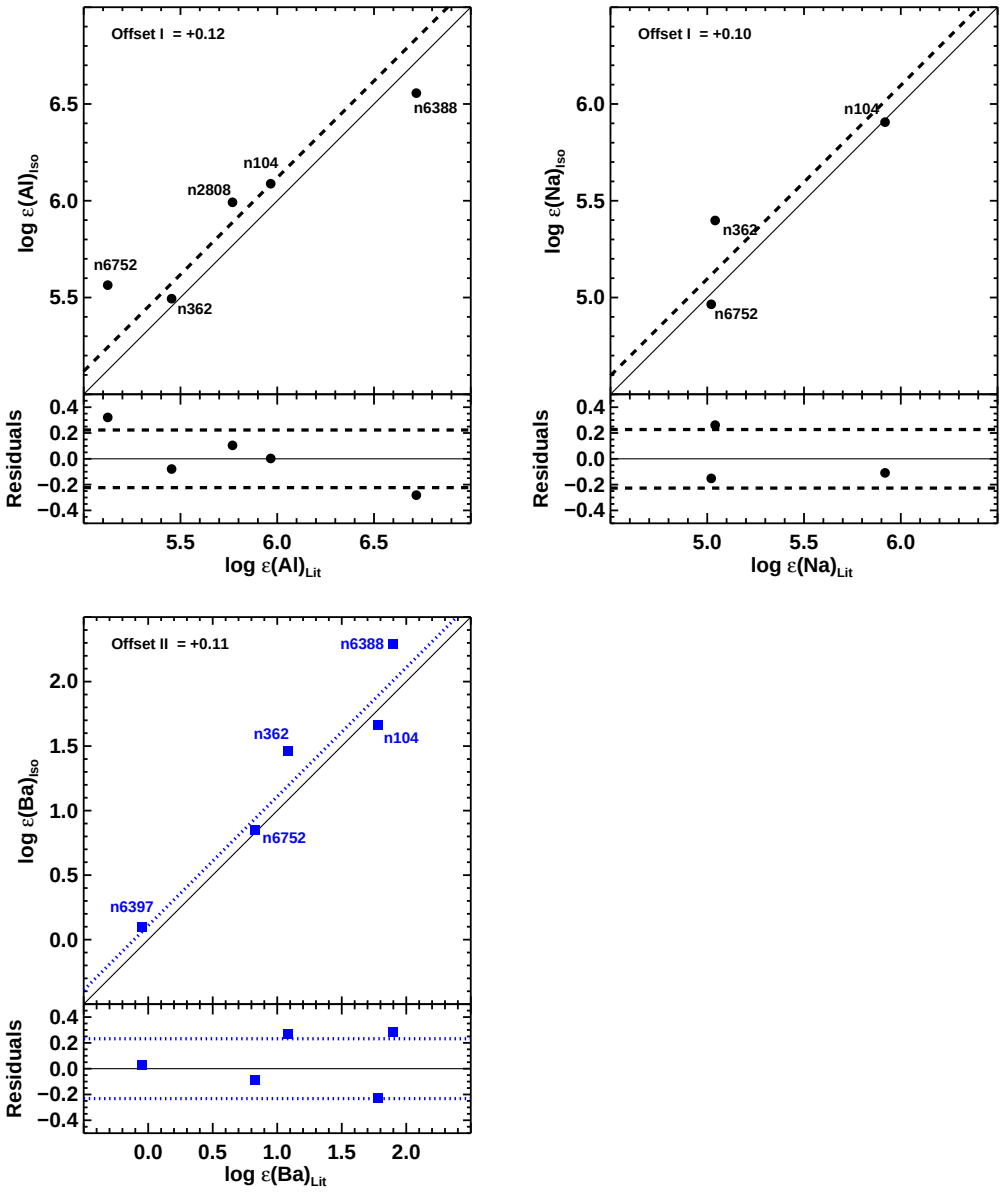

Figure 4.37. The abundance analysis method's global accuracy in determining the abundances of two light-elements and one n-capture element, when using each cluster's best 13 *Gyr* SSP to define its stellar atmospheres. All plotting conventions and data analysis match those used for the Fe-peak abundances in Figure 4.35. From left-to-right, row 1 depicts the light-elements Al and Na, while row 2 depicts the n-capture element Ba. *Upper Panels*: Al I, Na I, and Ba II have systematic abundance offsets of +0.12, +0.10, and +0.11 *dex*, respectively. *Lower Panels*: Al I, Na I, and Ba II have statistical uncertainties of 0.22, 0.23, and 0.23 *dex*, respectively.

CHAPTER 5

Conclusions

This dissertation has demonstrated that detailed abundances can be derived from the IL spectra of extragalactic GCs with an accuracy and precision that are competitive with standard stellar abundance analysis. This accuracy and precision is fully quantified in Tables 4.9 and 4.10. The IL spectra analysis produces abundances that are on average only < 0.1 *dex* larger than the abundances from standard stellar analysis. These abundances also have statistical uncertainties on average of ~ 0.2 *dex*. Note that this quoted uncertainty represents the uncertainty in an entire sample of measured abundances, not the uncertainty in the mean. These accuracies are further placed into perspective when realizing that standard stellar analysis produces abundances with accuracies on the order of $\lesssim 0.15$ *dex* (see, e.g., Tables B.1 through B.7).

In terms of cluster age constraints, the analysis method is capable of isolating a GC's age to within a range of 5 *Gyr*. For old GCs, this age constraint is enough to select SSPs solutions that all produce abundance results within $\sim$0.1 *dex* of each other. This insensitivity to which old SSP is selected is due to the self-similarity of old GC stellar systems. Work on a training set of young and intermediate age clusters in the LMC shows similar accuracy in constraining abundances and better resolution in age, as CMDs change more rapidly in those age intervals.

As an example of the kind of abundance information that can be obtained from extragalactic GCs using this method, Figure 5.1 plots [α/Fe] versus [Fe/H] for the training set clusters. Here, the characteristic α-element enrichment plateau for metal-poor stars is clearly seen using the abundance results determined from the 13 *Gyr* SSP analysis. Similar plots for the Fe-peak elements, neutron-capture elements, and

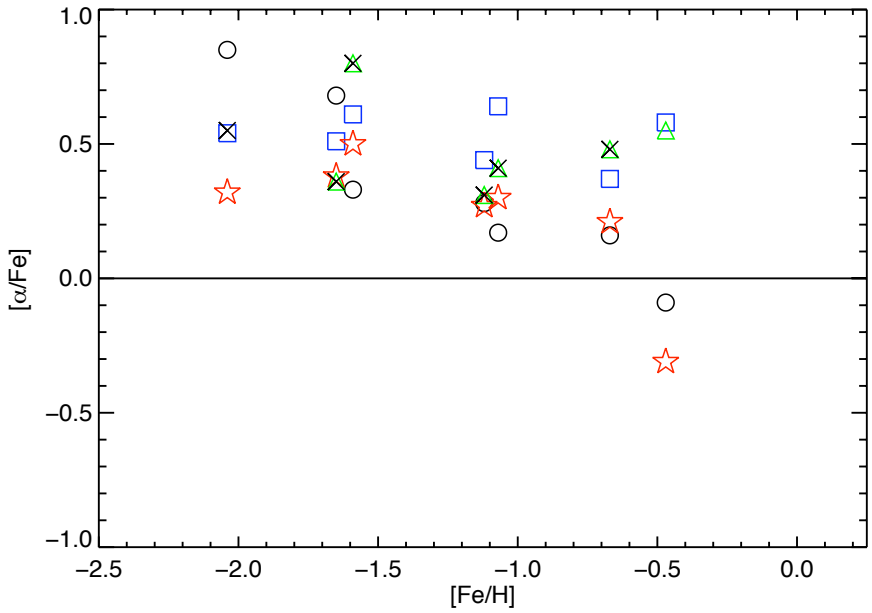

Figure 5.1. [α/Fe] versus [Fe/H] abundance ratio trend for the training set clusters, when using their best 13 *Gyr* SSPs to define their stellar atmospheres. Black circles are $[Ti/Fe]_I$. Blue squares are $[Ti/Fe]_{II}$. Red stars are $[Ca/Fe]_I$. Green triangles are $[Si/Fe]_I$. Black X's are $[Mg/Fe]_I$.

light-elements can also be constructed. Normally, for extragalactic GC systems, this level of detailed abundance investigation is not possible. Instead, only metallicity distributions can usually be constructed. Therefore, once this method is systematically applied to extragalactic GC systems (e.g. Colucci et al. 2009), it will provide many more avenues for observationally constraining the formation histories of GCs and their host galaxies.

In order to quantify the distances to which this IL analysis can be applied, the method's signal-to-noise requirements are considered. The basis for this analysis is the signal-to-noise model for echelle spectroscopes documented in Schroeder (2000) (*Equation 17.3.3*). This model takes as inputs the source magnitude, the telescope diameter, the sky brightness, the exposure time, and several instrument specific parameters. Here, the sky brightness is set equal to 22 $mag\ arcsec^{-2}$, the source magnitude is rewritten in terms of distance and absolute magnitude, the telescope diameter and exposure times are left as variables, and the instrument specific parameter values are adopted from the generic values recommended by Schroeder (2000). The param-

	1 hr		6 hr		10 hr	
D (m)	d_{dim} (Mpc)	d_{bright} (Mpc)	d_{dim} (Mpc)	d_{bright} (Mpc)	d_{dim} (Mpc)	d_{bright} (Mpc)
10	0.5	2.5	1	6	1.5	7.5
30	1.5	7	3.5	17	4.5	22
42	2	10	5	24	6	31

Table 5.1. GC distances with signal-to-noise of 50. "D" is the telescope diameter. "d_{dim}" and "d_{bright}" are the distances for GCs with $M_V = -6.5\ mag$ and $M_V = -9.5\ mag$, respectively. The hours refer to the total integration time on the clusters.

eter space investigated consists of GCs with $-9.5\ mag \leq M_V \leq -6.5\ mag$, telescopes with diameters of 10 m, 30 m, and 42 m, and exposure times of 1 hr, 6 hr, and 10 hr.

Figure 5.2 shows the signal-to-noise obtainable within the investigated parameter space. From top-to-bottom, the plots correspond to a 1 hr, 6 hr, and 10 hr exposure, respectively. The green diagonally hatched, blue diagonally hatched, and red horizontally hatched areas correspond to the 10 m, 30 m, and 42 m telescope, respectively. The upper limits for each area correspond to observing a $M_V = -9.5\ mag$ GC, while the lower limits correspond to observing a $M_V = -6.5\ mag$ GC. Because the measurement of elemental absorption lines becomes increasing difficult below a signal-to-noise of ~ 50, a horizontal reference line is placed across the plot at this value. Based on this signal-to-noise requirement, the observation distances for GCs with brightnesses between $-9.5\ mag \leq M_V \leq -6.5\ mag$ are listed in Table 5.1.

From the table, it is clear that current 10 m class telescopes can observe all the GCs in and around the Local Group. The most obvious target is Andromeda's GC system (e.g. Colucci et al. 2009), which has approximately 450 ± 100 GCs (Battistini et al. 1993). Other natural targets include M33, LMC, SMC, Fornax, Sagittarius, NGC 147, NGC 185, and NGC 205. Because the brightest GCs can be seen out to $\sim 6 - 7\ Mpc$ with 10 m telescopes, the GC systems around many galaxies within galaxy groups M81, Centaurus A, NGC 4736, Sculptor, and NGC 5457 can also be observed (see Table 5.2).

Upcoming 30 m (i.e. GMT and TMT) and 42 m (i.e. ELT) class telescopes will dramatically increase the distances, and hence the number of GC systems, that the analysis method can probe. For example, these telescopes can observe essentially all

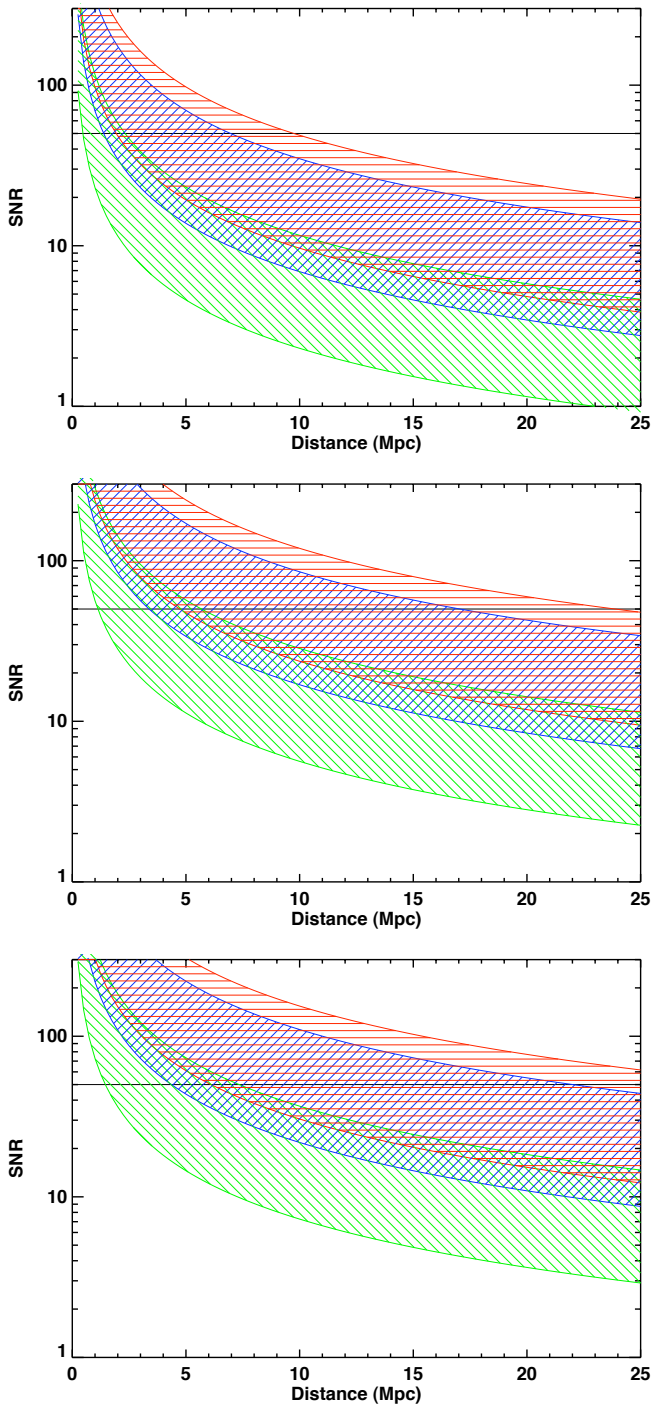

Figure 5.2. Signal-to-noise as a function of GC distance. See the text for details.

GCs out to 4.5 Mpc and 6 Mpc, respectively, and the brightest GCs out to 22 Mpc and 31 Mpc, respectively. Such large distances allow for the observation of essentially all the GC systems in the observationally important Virgo and Fornax galaxy clusters. Numerous galaxy groups will also fall within the range of observations (see Table 5.2). Ideally, when equipped with efficient, multi-slit spectrographs, these future telescopes will be able to observe entire GC systems within the course of a few nights of observation time. When this avalanche of spectroscopic data is analyzed, it will result in detailed abundance histories for entire extragalactic GC systems in numerous galaxy environments. This wealth of information will represent an important contribution to GC and galaxy formation research, and perhaps contribute several unexpected results.

Name	N_{gal}	RA (B1950) $(h:m:s)$	Dec (B1950) $(d:m:s)$	Distance (Mpc)
		Clusters		
Virgo	> 1175	12 28 17.6	+12 40 02	16.5
Fornax	> 235	03 36 34.1	−35 36 47	19.3
		Groups		
Local	23	...	...	< 1
M81	9	09 51 45.3	+69 18 13	2.9
Centaurus A	10	13 29 26.5	−30 31 36	3.6
NGC 4736	16	12 24 56.3	+38 25 49	3.9
Sculptor	13	00 12 53.0	−32 14 12	4.6
NGC 5457	8	14 02 21.0	+54 38 43	5.1
NGC 5194	7	13 26 26.6	+47 11 05	7.6
NGC 4258	21	12 27 57.8	+43 30 06	7.8
IC 2233	6	08 10 05.4	+49 41 23	8.6
Leo I	12	10 44 34.7	+13 19 19	10.3
Coma I	27	12 19 49.2	+30 12 18	10.4
NGC 3175	10	10 01 47.5	−28 17 27	11.3
NGC 4217	6	12 13 58.1	+47 19 14	11.4
NGC 925	6	02 26 18.0	+34 18 52	11.6
NGC 4151	16	12 04 52.3	+43 17 24	12.5
NGC 5033	8	13 09 32.2	+36 25 28	13.1
NGC 1448	16	03 53 28.5	−44 42 15	13.2
NGC 3507	13	10 52 08.8	+17 36 42	14.0
NGC 1672	11	04 52 08.0	−59 53 12	14.5
NGC 3607	16	11 16 31.9	+18 11 27	14.6
Ursa Major	54	11 49 20.1	+52 15 40	14.6
NGC 5364	7	13 52 28.0	+05 27 11	14.9
Dorado	12	04 15 57.5	−55 58 45	15.9
NGC 2442	6	07 36 33.0	−69 15 54	15.9
NGC 4699	40	12 52 44.0	−07 42 58	16.4
NGC 1532	7	04 10 10.2	−32 40 00	17.2
NGC 3190	7	10 15 02.0	+22 07 26	17.4
NGC 3414	6	10 48 16.3	+28 18 34	19.1
NGC 4036	11	11 37 23.4	+59 02 08	19.1
NGC 5566	6	14 18 28.7	+03 34 52	19.6
NGC 4038	14	11 55 11.5	−18 47 54	20.0
NGC 988	11	02 38 00.0	−08 02 44	20.3
NGC 5506	6	14 08 20.5	−02 37 37	20.6
NGC 3732	6	11 40 27.5	−09 49 30	20.8
NGC 3923	11	11 46 41.4	−28 01 00	21.5
NGC 5084	6	13 17 52.0	−21 13 09	22.0
PGC 71001	10	23 15 54.0	−42 42 51	22.1
Eridanus	48	03 35 21.0	−21 30 42	22.2
NGC 5846	13	15 03 28.8	+01 53 57	22.2
NGC 3813	6	11 35 44.9	+35 32 43	22.4
NGC 908	6	02 20 12.5	−21 15 22	22.5
NGC 3430	7	10 47 09.0	+33 14 45	22.5
NGC 936	6	02 25 22.3	−01 22 36	22.8
NGC 5638	6	14 27 19.5	+03 26 41	22.8
NGC 5746	12	14 38 24.4	+00 25 49	23.2
NGC 2708	7	08 53 05.3	−02 52 36	23.3
NGC 1255	6	03 17 03.0	−25 57 53	23.7
NGC 2967	7	09 45 09.7	+00 51 15	23.9
PGC 70090	10	22 54 38.0	−36 37 20	24.6
NGC 720	6	01 48 46.5	−13 56 30	24.8
NGC 4589	9	12 41 42.0	+73 54 00	26.0
NGC 5061	10	13 17 19.5	−26 51 36	26.0
NGC 4105	20	12 04 08.0	−29 43 12	26.1
NGC 3642	9	11 17 39.0	+58 03 21	26.4
NGC 4291	10	12 08 40.0	+76 06 19	26.7
NGC 5485	7	14 03 29.7	+55 20 25	27.1
PGC 68165	8	22 11 19.0	−46 12 15	27.3
NGC 584	8	01 29 43.9	−07 15 48	27.8
NGC 5322	9	13 53 05.2	+59 59 16	28.0
NGC 3665	6	11 20 36.4	+38 35 13	28.7

Table 5.2. Potential target galaxy clusters and groups. The data for the galaxy clusters and galaxy groups come from Jordán et al. (2007) and Giuricin et al. (2000), respectively.

APPENDIX A

ILABUNDS' Line Abundance Determination Algorithms

A.1 Fe Line Abundance Algorithm

The following lists ILABUNDS' Fe line abundance determination algorithm.

1. Determine the initial $[Fe/H]_{atmos}$ value to use for the ∼28 model atmospheres that correspond to the cluster's ∼28 representative average stellar types:

(a) If the abundance analysis is using photometric CMDs to define the cluster's model atmospheres, then the user provides a guessed $[Fe/H]_{atmos}$ value.

(b) If the abundance analysis is using theoretical SSPs to define the cluster's model atmospheres, then $[Fe/H]_{atmos}$ is set equal to $[Fe/H]_{SSP}$.

2. ILABUNDS interpolates a model atmosphere for each stellar type's combination of T_{eff}, $log(g_{\star})$, ξ_v, and $[Fe/H]_{atmos}$.

3. ILABUNDS picks an Fe line equivalent width, EW_{obs}, from a list containing all the Fe line EWs that were measured within the cluster's IL spectrum.

4. ILABUNDS uses $[Fe/H]_{atmos}$ as the initial guess for the Fe line's abundance, $log\,\epsilon(Fe)_{line}$.

5. MOOG synthesizes the Fe line individually for all ∼28 stellar types using the Fe line's known λ, EP, $log(gf)$, and guessed $log\,\epsilon(Fe)_{line}$ value.

6. ILABUNDS computes the flux-weighted equivalent width, $(\overline{EW})$, that results from the superposition of all the stars represented by the ∼28 average stellar

types by using Equation 3.6.

7. ILABUNDS compares EW_{obs} to $\overline{EW}$:

(a) If $\mathrm{EW}_{obs} = \overline{EW}$ and:

(i.) EW_{obs} is the last Fe line EW in the cluster's list of Fe line EWs, then ILABUNDS stores that Fe line's abundance and proceeds to **Step 8**.

(ii.) EW_{obs} is *not* the last Fe line EW in the cluster's list of Fe line EWs, then ILABUNDS stores that Fe line's abundance and loops back to **Step 3**.

(b) If $\mathrm{EW}_{obs} \neq \overline{EW}$, then ILABUNDS guesses a new $log\,\epsilon(\mathrm{Fe})_{line}$ value and returns to **Step 5**.

8. ILABUNDS computes the mean metallicity, $[\mathrm{Fe/H}]_{mean}$, implied by all the Fe lines' $log\,\epsilon(\mathrm{Fe})_{line}$ values.

9. ILABUNDS compares $[\mathrm{Fe/H}]_{mean}$ to $[\mathrm{Fe/H}]_{atmos}$:

(a) If $[\mathrm{Fe/H}]_{mean} = [\mathrm{Fe/H}]_{atmos}$, then ILABUNDS proceeds to **Step 10**.

(b) If $[\mathrm{Fe/H}]_{mean} \neq [\mathrm{Fe/H}]_{atmos}$, then ILABUNDS guesses a new $[\mathrm{Fe/H}]_{atmos}$ to be equal to $[\mathrm{Fe/H}]_{mean}$ and then loops back to **Step 2**.

10. ILABUNDS concludes that the best calulated metallicity for the cluster is $[\mathrm{Fe/H}]_{mean}$, and then prints out each Fe line's $log\,\epsilon(\mathrm{Fe})_{line}$ value for the user to analyze later outside of the ILABUNDS program.

When using an initial guess of $[\mathrm{Fe/H}]_{atmos} = -1.0\ dex$ in Step 1 for photometric CMD based analysis, ILABUNDS typically needs only two loops through the algorithm before it reaches a $[\mathrm{Fe/H}]_{mean} = [\mathrm{Fe/H}]_{atmos}$ convergence in Step 10. When running on a standard desktop PC, it typically takes ILABUNDS $\sim$3.5 minutes to complete one loop through the algorithm, and therefore $\sim$7 minutes to reach the [Fe/H] convergence.

When using an initial guess of $[\mathrm{Fe/H}]_{atmos} = [\mathrm{Fe/H}]_{SSP}$ in Step 1 for theoretical SSP based analysis, ILABUNDS typically needs two loops through the algorithm before it reaches a $[\mathrm{Fe/H}]_{mean} = [\mathrm{Fe/H}]_{atmos}$ convergence in Step 10. Each loop through the algorithm typically takes ∼3.5 minutes to complete, and, therefore, ∼7 minutes to reach a metallicity convergence. Because ILABUNDS must be applied to all 88 SSPs in a cluster's age-metallicity grid, it typically takes ∼10.3 hours to complete the Fe line abundance analysis for an entire grid of SSPs.

A.2 Non-Fe Line Abundance Algorithm

The following lists ILABUNDS' non-Fe line abundance determination algorithm.

1. ILABUNDS uses $[\mathrm{Fe/H}]_{atmos} = [\mathrm{Fe/H}]_{mean}$ for the cluster's ∼28 model atmospheres, where $[\mathrm{Fe/H}]_{mean}$ was determined during the Fe line abundance stage of the abundance analysis method (see Algorithm A.1).

2. ILABUNDS interpolates a model atmosphere for each stellar type's combination of T_{eff}, $log(g_{\star})$, ξ_v, and $[\mathrm{Fe/H}]_{atmos}$.

3. ILABUNDS picks a non-Fe line equivalent width, EW_{obs}, from a list containing all the non-Fe line EWs that were measured within the cluster's IL spectrum.

4. ILABUNDS guesses the non-Fe line's abundance, $log\,\epsilon(\mathrm{X})_{line}$.

5. MOOG synthesizes the non-Fe line individually for all ∼28 stellar types using the non-Fe line's known λ, EP, $log(gf)$, and guessed $log\,\epsilon(\mathrm{X})_{line}$ value.

6. ILABUNDS computes the flux-weighted equivalent width, $(\overline{EW})$, that results from the superposition of all the stars represented by the ∼28 stellar types by using Equation 3.6.

7. ILABUNDS compares EW_{obs} to $\overline{EW}$:

(a) If $\mathrm{EW}_{obs} = \overline{EW}$ and:

(i.) EW_{obs} is the last non-Fe line EW in the cluster's list of non-Fe line EWs, then ILABUNDS stores that non-Fe line's abundance and proceeds to **Step 8**.

(ii.) EW_{obs} is *not* the last non-Fe line EW in the cluster's list of non-Fe line EWs, then ILABUNDS stores that non-Fe line's abundance and loops back to **Step 3**.

(b) If $\mathrm{EW}_{obs} \neq \overline{EW}$, then ILABUNDS guesses a new $log\,\epsilon(\mathrm{X})_{line}$ and returns to **Step 5**.

8. ILABUNDS prints out each non-Fe line's $log\,\epsilon(\mathrm{X})_{line}$ value for the user to analyze later outside of the ILABUNDS program.

APPENDIX B

Reference Stellar Abundances from the Literature

For each training set cluster, standard stellar abundanaces were culled from published sources in the literature. This literature search concentrated on abundances published between the years 2000 and 2007. The collected abundances were then brought into $log\,\epsilon$(X) format. When a cluster had a species abundance that was measured by more than one literature source, the abundances were averaged together. Tables B.1 through B.7 list the resultant stellar abundances and their literature sources.

Elem.	Ion.	$log\,\epsilon(X)$ (dex)	σ_{mean} (dex)	σ (dex)	N_{stars}	Ref.
Al	I	5.97	0.04	0.16	16	1, 3
Ba	II	1.78	0.03	0.07	6	1, 13
Ca	I	5.78	0.02	0.06	16	1, 3
C	I	7.66	0.04	0.14	12	5
Cr	I	5.11	0.02	0.07	11	3
Cr	II	5.09	0.05	0.18	12	3
Eu	II	0.11	0.04	0.14	13	1, 13, 19
Fe	I	6.89	0.01	0.04	24	1, 3, 14, 19
Fe	II	6.89	0.02	0.08	24	1, 3, 14, 19
La	II	0.82	0.05	0.16	11	1, 19
Mg	I	7.18	0.03	0.10	14	1, 3
Mn	I	4.36	0.03	0.12	12	3
Na	I	5.92	0.08	0.37	23	1, 3, 19
Nd	II	1.32	0.03	0.09	7	19
Ni	I	5.62	0.04	0.14	12	3
N	I	7.70	0.18	0.62	12	5
O	I	8.46	0.06	0.24	14	1, 3
Sc	II	2.58	0.04	0.15	12	3
Si	I	7.11	0.03	0.14	16	1, 3
Sr	II	2.56	0.04	0.05	2	13
Ti	I	4.58	0.02	0.10	16	1, 3
Ti	II	4.76	0.04	0.15	15	1, 3
V	I	3.36	0.03	0.08	10	3
Y	I	2.28	0.06	0.17	7	19
Y	II	2.12	0.12	0.36	9	13, 19
Zn	II	4.10	0.04	0.14	11	3
Zr	I	2.36	0.14	0.46	11	1, 19
Zr	II	2.59	0.06	0.15	7	19

Table B.1. NGC 104's standard stellar abundances from the literature. The "$log\,\epsilon(X)$" column lists the average stellar abundance for the various species. The σ_{mean} column equals the standard deviation of the mean stellar abundances in $log\,\epsilon(X)$ form. The σ column equals the standard deviation of the entire sample of stellar abundances in $log\,\epsilon(X)$ form. The N_{stars} column lists the number of stars used to compute the average $log\,\epsilon(X)$ abundance. The "Ref." column lists the literature sources for the stellar abundances. The references are: [1]: Alves-Brito et al. (2005); [2]: Carretta et al. (2003); [3]: Carretta et al. (2004b); [4]: Carretta, Bragaglia, & Cacciari (2004a); [5]: Carretta et al. (2005); [6]: Carretta (2006); [7]: Carretta et al. (2006); [8]: Carretta et al. (2007); [9]: Castilho et al. (2000); [10]: Cavallo, Suntzeff, & Pilachowski (2004); [11]: Gratton et al. (2001); [12]: James et al. (2004a); [13]: James et al. (2004b); [14]: Kraft & Ivans (2003); [15]: Pace et al. (2006); [16]: Shetrone & Keane (2000); [17]: Simmerer et al. (2003); [18]: Sobeck et al. (2006); [19]: Wylie et al. (2006); [20]: Yong et al. (2005).

Elem.	Ion.	$log\,\epsilon(X)$ (dex)	σ_{mean} (dex)	σ (dex)	N_{stars}	Ref.
Al	I	5.45	0.07	0.24	12	16
Ba	II	1.08	0.06	0.22	12	16
Ca	I	5.21	0.02	0.07	12	16
Cu	I	2.24	0.03	0.10	10	17
Eu	II	-0.24	0.03	0.09	12	16
Fe	I	6.20	0.01	0.03	7	14
Fe	II	6.18	0.03	0.07	7	14
Mg	I	6.62	0.03	0.09	12	16
Mn	I	3.58	0.03	0.10	12	18
Na	I	5.04	0.06	0.21	12	16
Ni	I	4.86	0.02	0.05	12	16
O	I	7.65	0.06	0.19	12	16
Sc	II	1.68	0.03	0.11	12	16
Si	I	6.58	0.03	0.09	8	16
Ti	I	3.96	0.02	0.08	12	16
V	I	2.65	0.01	0.04	12	16

Table B.2. NGC 362's standard stellar abundances from the literature. See Table B.1 for available explanations.

Elem.	Ion.	$log\,\epsilon(X)$ (dex)	σ_{mean} (dex)	σ (dex)	N_{stars}	Ref.
Al	I	5.77	0.12	0.52	18	6
Ca	I	5.45	0.02	0.08	19	6
Cr	I	4.55	0.02	0.09	19	6
Cr	II	4.67	0.03	0.11	18	6
Fe	I	6.42	0.01	0.10	141	4, 7
Fe	II	6.33	0.01	0.11	110	4, 7
Mg	I	6.61	0.03	0.15	19	6
Mn	I	3.92	0.02	0.09	19	6
Na	I	5.40	0.02	0.28	222	2, 4, 7
Ni	I	5.07	0.01	0.06	19	6
O	I	7.66	0.04	0.38	110	4, 7
Sc	II	1.95	0.02	0.10	19	6
Si	I	6.75	0.02	0.08	19	6
Ti	I	4.17	0.02	0.07	19	6
Ti	II	4.13	0.03	0.13	18	6
V	I	2.87	0.02	0.11	19	6

Table B.3. NGC 2808's standard stellar abundances from the literature. See Table B.1 for available explanations.

Elem.	Ion.	$log\,\epsilon(X)$ (dex)	σ_{mean} (dex)	σ (dex)	N_{stars}	Ref.
Al	I	5.10	0.13	0.41	10	10
Ca	I	4.86	0.05	0.16	10	10
Cr	I	3.96	0.15	0.30	4	10
Eu	II	-0.42	0.03	0.09	10	10
Fe	I	5.79	0.04	0.13	10	10
La	II	-0.17	0.06	0.16	8	10
Ni	I	4.47	0.06	0.18	10	10
Ti	I	3.37	0.12	0.34	9	10
Ti	II	3.76	0.05	0.12	6	10

Table B.4. NGC 6093's standard stellar abundances from the literature. See Table B.1 for available explanations.

Elem.	Ion.	$log\,\epsilon(X)$ (dex)	σ_{mean} (dex)	σ (dex)	N_{stars}	Ref.
Al	I	6.72	0.09	0.25	7	8
Ba	I	1.90	0.04	0.12	7	8
Ca	I	5.89	0.02	0.06	7	8
Ce	II	0.84	0.06	0.17	7	8
Co	I	4.52	0.04	0.09	7	8
Cr	I	5.20	0.04	0.09	7	8
Eu	I	0.36	0.04	0.11	7	8
Fe	I	7.10	0.01	0.04	7	8
Fe	II	7.12	0.03	0.09	7	8
La	II	1.14	0.04	0.11	7	8
Mg	I	7.20	0.02	0.04	7	8
Mn	I	4.65	0.02	0.05	7	8
Na	I	6.37	0.05	0.14	7	8
Ni	I	5.87	0.02	0.06	7	8
O	I	8.02	0.07	0.18	7	8
Sc	II	2.74	0.03	0.08	7	8
Si	I	7.41	0.05	0.12	7	8
Ti	I	4.93	0.03	0.07	7	8
Ti	II	4.93	0.05	0.14	7	8
V	I	3.92	0.03	0.08	7	8
Y	I	1.64	0.06	0.17	7	8
Zr	I	1.99	0.04	0.12	7	8
Zr	II	1.96	0.07	0.19	7	8

Table B.5. NGC 6388's standard stellar abundances from the literature. See Table B.1 for available explanations.

Elem.	Ion.	$log\,\epsilon(X)$ (dex)	σ_{mean} (dex)	σ (dex)	N_{stars}	Ref.
Al	I	4.69	0.04	0.10	8	11
Ba	II	-0.04	0.03	0.13	18	9, 13
Ca	I	4.56	0.02	0.09	16	9
Eu	II	-1.13	0.03	0.04	2	13
Fe	I	5.48	0.01	0.03	6	14
Fe	II	5.50	0.03	0.07	6	14
Mg	I	5.51	0.04	0.11	8	11
Na	I	4.51	0.17	0.87	27	5, 9, 11
O	I	6.98	0.03	0.13	24	5, 9, 11
Si	I	5.78	0.05	0.11	5	9
Sr	II	0.80	0.01	0.01	2	13
Ti	I	3.46	0.04	0.15	13	9
Y	II	0.02	0.08	0.20	7	13, 9

Table B.6. NGC 6397's standard stellar abundances from the literature. See Table B.1 for available explanations.

Elem.	Ion.	$log\,\epsilon(X)$ (dex)	σ_{mean} (dex)	σ (dex)	N_{stars}	Ref.
Al	I	5.12	0.09	0.50	29	10, 11
Ba	II	0.82	0.02	0.08	18	12
Ca	I	5.04	0.06	0.20	11	10
Cr	I	4.16	0.10	0.17	3	10
Eu	II	-0.52	0.02	0.11	28	10, 12
Fe	I	5.99	0.01	0.02	8	14
Fe	II	5.95	0.04	0.10	8	14
La	II	-0.23	0.06	0.15	7	10
Mg	I	6.02	0.04	0.17	18	11
Mn	I	3.23	0.02	0.06	15	18
Na	I	5.02	0.05	0.31	36	5, 11
Ni	I	4.54	0.03	0.11	11	10
O	I	7.51	0.06	0.29	24	5, 11
Sr	II	1.49	0.04	0.17	18	12
Ti	I	3.56	0.12	0.33	8	10
Ti	II	3.80	0.06	0.18	8	10
Y	II	0.75	0.02	0.10	18	12

Table B.7. NGC 6752's standard stellar abundances from the literature. See Table B.1 for available explanations.

BIBLIOGRAPHY

Aerts, C., Thoul, A., Daszyńska, J., et al. 2003, Science, 300, 1926

Alonso, A., Arribas, S., & Martínez-Roger, C. 1999, A&AS, 140, 261

Alves-Brito, A., Barbuy, B., Ortolani, S., et al. 2005, A&A, 435, 657

Anders, E. & Ebihara, M. 1982, Geochim. Cosmochim. Acta, 46, 2363

Anders, E. & Grevesse, N. 1989, Geochim. Cosmochim. Acta, 53, 197

Aoki, W., Ryan, S. G., Norris, J. E., et al. 2002, ApJ, 580, 1149

Armandroff, T. E. & Zinn, R. 1988, AJ, 96, 92

Arnett, D. 1996, Supernovae and nucleosynthesis. an investigation of the history of matter, from the Big Bang to the present (Princeton, NJ: Princeton University Press)

Arnett, D. 2004, in Origin and Evolution of the Elements, ed. A. McWilliam & M. Rauch, 12–26

Arp, H. & Sandage, A. 1985, AJ, 90, 1163

Ashman, K. M. & Bird, C. M. 1993, AJ, 106, 2281

Ashman, K. M. & Zepf, S. E. 1992, ApJ, 384, 50

Ashman, K. M. & Zepf, S. E. 1998, Globular Cluster Systems (Cambridge: Cambridge University Press)

Asplund, M., Grevesse, N., & Sauval, A. J. 2005, in Astronomical Society of the Pacific Conference Series, Vol. 336, Cosmic Abundances as Records of Stellar Evolution and Nucleosynthesis, ed. T. G. Barnes, III & F. N. Bash, 25

Asplund, M., Grevesse, N., Sauval, A. J., Allende Prieto, C., & Kiselman, D. 2004, A&A, 417, 751

Barth, A. J., Ho, L. C., Filippenko, A. V., & Sargent, W. L. 1995, AJ, 110, 1009

Basu, S. & Antia, H. M. 2004, ApJ, 606, L85

Battistini, P. L., Bonoli, F., Casavecchia, M., et al. 1993, A&A, 272, 77

Baum, E. M., Knox, H. D., & Miller, T. R., eds. 2002, Nuclides and Isotopes (New York: Knolls Atomic Power Laboratory, Inc.)

Baumgardt, H. & Makino, J. 2003, MNRAS, 340, 227

Beasley, M. A., Baugh, C. M., Forbes, D. A., Sharples, R. M., & Frenk, C. S. 2002, MNRAS, 333, 383

Bekki, K., Yahagi, H., Nagashima, M., & Forbes, D. A. 2008, MNRAS, 387, 1131

Bensby, T., Feltzing, S., & Lundström, I. 2003, A&A, 410, 527

Bensby, T., Feltzing, S., Lundström, I., & Ilyin, I. 2005, A&A, 433, 185

Bertelli, G., Nasi, E., Girardi, L., et al. 2003, AJ, 125, 770

Bessell, M. S., Brett, J. M., Scholz, M., & Wood, P. R. 1991, A&AS, 89, 335

Bessell, M. S., Brett, J. M., Wood, P. R., & Scholz, M. 1989, A&AS, 77, 1

Binney, J. & Tremaine, S. 1987, Galactic dynamics (Princeton, NJ: Princeton University Press)

Bloecker, T. 1995, A&A, 297, 727

Böhm-Vitense, E. 1958, Zeitschrift fur Astrophysik, 46, 108

Bono, G., Castellani, V., & Marconi, M. 2002, ApJ, 565, L83

Bowen, G. H. & Willson, L. A. 1991, ApJ, 375, L53

Brodie, J. P. & Huchra, J. P. 1991, ApJ, 379, 157

Brodie, J. P., Schroder, L. L., Huchra, J. P., et al. 1998, AJ, 116, 691

Brodie, J. P. & Strader, J. 2006, ARA&A, 44, 193

Burbidge, E. M., Burbidge, G. R., Fowler, W. A., & Hoyle, F. 1957, Reviews of Modern Physics, 29, 547

Burkert, A. & Ruiz-Lapuente, P. 1997, ApJ, 480, 297

Burstein, D. 1987, in Nearly Normal Galaxies. From the Planck Time to the Present, ed. S. M. Faber, 47–56

Burstein, D., Faber, S. M., Gaskell, C. M., & Krumm, N. 1984, ApJ, 287, 586

Busso, G., Cassisi, S., Piotto, G., et al. 2007, A&A, 474, 105

Buta, R., Crocker, D. A., & Byrd, G. G. 1999, AJ, 118, 2071

Calzetti, D., Meurer, G. R., Bohlin, R. C., et al. 1997, AJ, 114, 1834

Cameron, A. G. W. 2001, ApJ, 562, 456

Cannon, R. D., Croke, B. F. W., Bell, R. A., Hesser, J. E., & Stathakis, R. A. 1998, MNRAS, 298, 601

Carbon, D. F., Romanishin, W., Langer, G. E., et al. 1982, ApJS, 49, 207

Cariulo, P., Degl'Innocenti, S., & Castellani, V. 2004, A&A, 421, 1121

Carlson, M. N., Holtzman, J. A., Watson, A. M., et al. 1998, AJ, 115, 1778

Carraro, G., Bertelli, G., Bressan, A., & Chiosi, C. 1993, A&AS, 101, 381

Carraro, G., Zinn, R., & Moni Bidin, C. 2007, A&A, 466, 181

Carretta, E. 2006, AJ, 131, 1766

Carretta, E., Bragaglia, A., & Cacciari, C. 2004a, ApJ, 610, L25

Carretta, E., Bragaglia, A., Cacciari, C., & Rossetti, E. 2003, A&A, 410, 143

Carretta, E., Bragaglia, A., Gratton, R. G., et al. 2006, A&A, 450, 523

Carretta, E., Bragaglia, A., Gratton, R. G., et al. 2007, A&A, 464, 967

Carretta, E. & Gratton, R. G. 1997, A&AS, 121, 95

Carretta, E., Gratton, R. G., Bragaglia, A., Bonifacio, P., & Pasquini, L. 2004b, A&A, 416, 925

Carretta, E., Gratton, R. G., Clementini, G., & Fusi Pecci, F. 2000, ApJ, 533, 215

Carretta, E., Gratton, R. G., Lucatello, S., Bragaglia, A., & Bonifacio, P. 2005, A&A, 433, 597

Castelli, F. & Kurucz, R. L. 2004, ArXiv Astrophysics e-prints

Castilho, B. V., Pasquini, L., Allen, D. M., Barbuy, B., & Molaro, P. 2000, A&A, 361, 92

Cavallo, R. M., Suntzeff, N. B., & Pilachowski, C. A. 2004, AJ, 127, 3411

Chiosi, C., Bertelli, G., & Bressan, A. 1992, ARA&A, 30, 235

Coc, A., Vangioni-Flam, E., Descouvemont, P., Adahchour, A., & Angulo, C. 2004, ApJ, 600, 544

Cohen, J. G. 2004, AJ, 127, 1545

Cole, S., Lacey, C. G., Baugh, C. M., & Frenk, C. S. 2000, MNRAS, 319, 168

Colucci, J. E., Bernstein, R. A., Cameron, S., McWilliam, A., & Cohen, J. G. 2009, ArXiv e-prints

Conti, P. S. & Vacca, W. D. 1994, ApJ, 423, L97+

Cordier, D., Lebreton, Y., Goupil, M.-J., et al. 2002, A&A, 392, 169

Cordier, D., Pietrinferni, A., Cassisi, S., & Salaris, M. 2007, AJ, 133, 468

Côté, P., Marzke, R. O., & West, M. J. 1998, ApJ, 501, 554

Côté, P., McLaughlin, D. E., Cohen, J. G., & Blakeslee, J. P. 2003, ApJ, 591, 850

Côté, P., McLaughlin, D. E., Hanes, D. A., et al. 2001, ApJ, 559, 828

Cottrell, P. L. & Sneden, C. 1986, A&A, 161, 314

Couture, J., Harris, W. E., & Allwright, J. W. B. 1990, ApJS, 73, 671

Cowan, J. J., Sneden, C., Burles, S., et al. 2002, ApJ, 572, 861

Cox, A. N., ed. 2000, Allen's astrophysical quantities (New York: Springer)

Da Costa, G. S. & Armandroff, T. E. 1995, AJ, 109, 2533

Daniel, S. A., Latham, D. W., Mathieu, R. D., & Twarog, B. A. 1994, PASP, 106, 281

D'Antona, F., Gratton, R., & Chieffi, A. 1983, Memorie della Societa Astronomica Italiana, 54, 173

Day, R. W., Lambert, D. L., & Sneden, C. 1973, ApJ, 185, 213

de Grijs, R., O'Connell, R. W., & Gallagher, III, J. S. 2000, in ESA Special Publication, Vol. 445, Star Formation from the Small to the Large Scale, ed. F. Favata, A. Kaas, & A. Wilson, 43

de Marchi, G., Clampin, M., Greggio, L., et al. 1997, ApJ, 479, L27+

de Vega, H. J., Sánchez, N., & Combes, F. 1996, Nature, 383, 56

Degl'Innocenti, S., Prada Moroni, P. G., Marconi, M., & Ruoppo, A. 2008, Ap&SS, 316, 25

Demarque, P., Sarajedini, A., & Guo, X.-J. 1994, ApJ, 426, 165

Denissenkov, P. A. & Denissenkova, S. N. 1990, Sov. Astron. Lett., 16, 642

Denissenkov, P. A. & VandenBerg, D. A. 2003, ApJ, 593, 509

Dickens, R. J. 1972, MNRAS, 157, 281

Duncan, R. C., Shapiro, S. L., & Wasserman, I. 1986, ApJ, 309, 141

Dupret, M.-A., Thoul, A., Scuflaire, R., et al. 2004, A&A, 415, 251

Eddington, A. S. 1926, The Internal Constitution of the Stars (Cambridge: Cambridge University Press)

Eggen, O. J., Lynden-Bell, D., & Sandage, A. R. 1962, ApJ, 136, 748

Elmegreen, B. C. 2004, in Astronomical Society of the Pacific Conference Series, Vol. 322, The Formation and Evolution of Massive Young Star Clusters, ed. H. J. G. L. M. Lamers, L. J. Smith, & A. Nota, 277

Elmegreen, B. G. 2009, in Globular Clusters - Guides to Galaxies, ed. T. Richtler & S. Larsen, 87

Elmegreen, B. G. & Efremov, Y. N. 1997, ApJ, 480, 235

Elmegreen, B. G. & Elmegreen, D. M. 2001, AJ, 121, 1507

Elmegreen, B. G. & Scalo, J. 2004, ARA&A, 42, 211

Elson, R., Hut, P., & Inagaki, S. 1987, ARA&A, 25, 565

Falgarone, E. & Phillips, T. G. 1991, in IAU Symposium, Vol. 147, Fragmentation of Molecular Clouds and Star Formation, ed. E. Falgarone, F. Boulanger, & G. Duvert, 119

Fall, S. M. & Zhang, Q. 2001, ApJ, 561, 751

Feltzing, S., Primas, F., & Johnson, R. A. 2009, A&A, 493, 913

Ferguson, J. W., Alexander, D. R., Allard, F., et al. 2005, ApJ, 623, 585

Ferraro, F. R., Valenti, E., Straniero, O., & Origlia, L. 2006, ApJ, 642, 225

Forbes, D. A., Brodie, J. P., & Grillmair, C. J. 1997, AJ, 113, 1652

Forbes, D. A. & Forte, J. C. 2001, MNRAS, 322, 257

Forbes, D. A. & Hau, G. K. T. 2000, MNRAS, 312, 703

Freeman, K. & Bland-Hawthorn, J. 2002, ARA&A, 40, 487

Freiburghaus, C., Rosswog, S., & Thielemann, F.-K. 1999, ApJ, 525, L121

Freytag, B. & Salaris, M. 1999, ApJ, 513, L49

Fulbright, J. P. 2002, AJ, 123, 404

Fulbright, J. P., McWilliam, A., & Rich, R. M. 2006, ApJ, 636, 821

Gallart, C., Zoccali, M., & Aparicio, A. 2005, ARA&A, 43, 387

Gallart, C., Zoccali, M., Bertelli, G., et al. 2003, AJ, 125, 742

Gebhardt, K. & Kissler-Patig, M. 1999, AJ, 118, 1526

Geisler, D. & Forte, J. C. 1990, ApJ, 350, L5

Gilbert, A. M., Graham, J. R., McLean, I. S., et al. 2000, in Astronomical Society of the Pacific Conference Series, Vol. 211, Massive Stellar Clusters, ed. A. Lançon & C. M. Boily, 101

Gilroy, K. K. & Brown, J. A. 1991, ApJ, 371, 578

Girardi, L., Bressan, A., Bertelli, G., & Chiosi, C. 2000, A&AS, 141, 371

Giuricin, G., Marinoni, C., Ceriani, L., & Pisani, A. 2000, ApJ, 543, 178

Gnedin, O. Y., Lee, H. M., & Ostriker, J. P. 1999, ApJ, 522, 935

Gnedin, O. Y. & Ostriker, J. P. 1997, ApJ, 474, 223

Goeppert-Mayer, M. & Jensen, J. H. D. 1955, Elementary theory of nuclear shell structure (New York: Wiley)

Gratton, R., Sneden, C., & Carretta, E. 2004, ARA&A, 42, 385

Gratton, R. G., Bonifacio, P., Bragaglia, A., et al. 2001, A&A, 369, 87

Gratton, R. G., Bragaglia, A., Carretta, E., et al. 2003, A&A, 408, 529

Gratton, R. G. & Sneden, C. 1994, A&A, 287, 927

Gray, D. F. 2008, The Observation and Analysis of Stellar Photospheres (Cambridge: Cambridge University Press)

Grevesse, N., Asplund, M., & Sauval, A. J. 2007, Space Science Reviews, 130, 105

Grevesse, N. & Noels, A. 1993, in Origin and Evolution of the Elements, ed. S. Kubono & T. Kajino, 15–25

Grevesse, N. & Sauval, A. J. 1998, Space Science Reviews, 85, 161

Habing, H. J. 1996, A&A Rev., 7, 97

Harris, W. E. 1996, AJ, 112, 1487

Harris, W. E. 2001, in Saas-Fee Advanced Course 28: Star Clusters, ed. L. Labhardt & B. Binggeli (New York: Springer), 223–395

Harris, W. E. & Pudritz, R. E. 1994, ApJ, 429, 177

Heggie, D. & Hut, P. 2003, The Gravitational Million-Body Problem: A Multidisciplinary Approach to Star Cluster Dynamics (Cambridge: Cambridge University Press)

Hill, V., Plez, B., Cayrel, R., et al. 2002, A&A, 387, 560

Hillebrandt, W. & Niemeyer, J. C. 2000, ARA&A, 38, 191

Ho, L. C. & Filippenko, A. V. 1996, ApJ, 472, 600

Hollowell, D. & Iben, I. J. 1989, ApJ, 340, 966

Holtzman, J. A., Faber, S. M., Shaya, E. J., et al. 1992, AJ, 103, 691

Holtzman, J. A., Watson, A. M., Mould, J. R., et al. 1996, AJ, 112, 416

Hoyle, F. 1946, MNRAS, 106, 343

Ibata, R. A., Gilmore, G., & Irwin, M. J. 1994, Nature, 370, 194

Iben, I. & Renzini, A. 1984, Phys. Lett., 105, 329

Iben, Jr., I. 1974, ARA&A, 12, 215

Iben, Jr., I. & Renzini, A. 1983, ARA&A, 21, 271

Iben, Jr., I. & Truran, J. W. 1978, ApJ, 220, 980

Iben, I. J. 1967, ARA&A, 5, 571

Iwamoto, K., Brachwitz, F., Nomoto, K., et al. 1999, ApJS, 125, 439

Izotov, Y. I. & Thuan, T. X. 2004, ApJ, 602, 200

James, G., François, P., Bonifacio, P., et al. 2004a, A&A, 414, 1071

James, G., François, P., Bonifacio, P., et al. 2004b, A&A, 427, 825

Johnson, K. E. & Conti, P. S. 2000, AJ, 119, 2146

Johnson, K. E., Vacca, W. D., Leitherer, C., Conti, P. S., & Lipscy, S. J. 1999, AJ, 117, 1708

Jordán, A., Blakeslee, J. P., Côté, P., et al. 2007, ApJS, 169, 213

Jordi, C., Figueras, F., Carrasco, J. M., Tautvaisiene, G., & Castelli, F. 2002, UB-PWG-008, 008

Kasparova, A. V. & Zasov, A. V. 2008, Astronomy Letters, 34, 152

Keller, S. C. & Wood, P. R. 2002, ApJ, 578, 144

Kennicutt, Jr., R. C. 1998, ApJ, 498, 541

Kennicutt, Jr., R. C. & Chu, Y.-H. 1988, AJ, 95, 720

King, I. R. 1966, AJ, 71, 64

Kirby, E. N., Guhathakurta, P., & Sneden, C. 2008, ApJ, 682, 1217

Klypin, A., Kravtsov, A. V., Valenzuela, O., & Prada, F. 1999, ApJ, 522, 82

Kobayashi, C., Umeda, H., Nomoto, K., Tominaga, N., & Ohkubo, T. 2006, ApJ, 653, 1145

Kozhurina-Platais, V., Demarque, P., Platais, I., Orosz, J. A., & Barnes, S. 1997, AJ, 113, 1045

Kraft, R. P. 1994, PASP, 106, 553

Kraft, R. P. & Ivans, I. I. 2003, PASP, 115, 143

Kraft, R. P., Sneden, C., Smith, G. H., et al. 1997, AJ, 113, 279

Krauss, L. M. & Chaboyer, B. 2003, Science, 299, 65

Kravtsov, A. V. & Gnedin, O. Y. 2005, ApJ, 623, 650

Kroupa, P. 2001, MNRAS, 322, 231

Kundu, A. & Whitmore, B. C. 2001, AJ, 121, 2950

Kupka, F. G., Ryabchikova, T. A., Piskunov, N. E., Stempels, H. C., & Weiss, W. W. 2000, Baltic Astronomy, 9, 590

Lada, C. J. & Lada, E. A. 2003, ARA&A, 41, 57

Langer, G. E., Hoffman, R., & Sneden, C. 1993, PASP, 105, 301

Langer, G. E., Suntzeff, N. B., & Kraft, R. P. 1992, PASP, 104, 523

Larsen, S. S., Brodie, J. P., Huchra, J. P., Forbes, D. A., & Grillmair, C. J. 2001, AJ, 121, 2974

Larsen, S. S. & Richtler, T. 1999, A&A, 345, 59

Lattimer, J. M. & Schramm, D. N. 1974, ApJ, 192, L145

LeBlanc, J. M. & Wilson, J. R. 1970, ApJ, 161, 541

Leckrone, D. 2001, in Encyclopedia of Astronomy and Astrophysics, ed. P. Murdin

Lee, Y.-W. 1990, ApJ, 363, 159

Lodders, K. 2003, ApJ, 591, 1220

Lucatello, S., Gratton, R., Cohen, J. G., et al. 2003, AJ, 125, 875

Luridiana, V., Peimbert, A., Peimbert, M., & Cerviño, M. 2003, ApJ, 592, 846

Maeder, A. & Mermilliod, J. C. 1981, A&A, 93, 136

Maeder, A. & Meynet, G. 1989, A&A, 210, 155

Marigo, P. 2001, A&A, 370, 194

Mashonkina, L. & Gehren, T. 2000, A&A, 364, 249

Mashonkina, L. & Gehren, T. 2001, A&A, 376, 232

Mashonkina, L., Gehren, T., & Bikmaev, I. 1999, A&A, 343, 519

Matteucci, F. & Recchi, S. 2001, ApJ, 558, 351

Mazzitelli, I. 1979, A&A, 79, 251

McLaughlin, D. E. & Pudritz, R. E. 1996, ApJ, 457, 578

McWilliam, A. 1997, ARA&A, 35, 503

McWilliam, A. & Bernstein, R. A. 2008, ApJ, 684, 326

McWilliam, A., Preston, G. W., Sneden, C., & Shectman, S. 1995, AJ, 109, 2736

McWilliam, A. & Rich, R. M. 1994, ApJS, 91, 749

Meléndez, J. 2004, ApJ, 615, 1042

Mengel, S., Lehnert, M. D., Thatte, N., & Genzel, R. 2000, in Astronomical Society of the Pacific Conference Series, Vol. 211, Massive Stellar Clusters, ed. A. Lançon & C. M. Boily, 96

Meurer, G. R., Freeman, K. C., Dopita, M. A., & Cacciari, C. 1992, AJ, 103, 60

Meurer, G. R., Heckman, T. M., Leitherer, C., et al. 1995, AJ, 110, 2665

Miller, B. W., Whitmore, B. C., Schweizer, F., & Fall, S. M. 1997, AJ, 114, 2381

Minniti, D. 1995, AJ, 109, 1663

Moore, B., Ghigna, S., Governato, F., et al. 1999, ApJ, 524, L19

Moretti, A., Piotto, G., Arcidiacono, C., et al. 2009, A&A, 493, 539

Nakamura, T., Umeda, H., Nomoto, K., Thielemann, F.-K., & Burrows, A. 1999, ApJ, 517, 193

Nakasato, N., Mori, M., & Nomoto, K. 2000, ApJ, 535, 776

Navarro, J. F., Frenk, C. S., & White, S. D. M. 1997, ApJ, 490, 493

Nordstroem, B., Andersen, J., & Andersen, M. I. 1997, A&A, 322, 460

Norris, J., Cottrell, P. L., Freeman, K. C., & Da Costa, G. S. 1981, ApJ, 244, 205

O'Connell, R. W., Gallagher, III, J. S., & Hunter, D. A. 1994, ApJ, 433, 65

O'Connell, R. W., Gallagher, III, J. S., Hunter, D. A., & Colley, W. N. 1995, ApJ, 446, L1+

Oestlin, G., Bergvall, N., & Roennback, J. 1998, A&A, 335, 85

Olive, K. A., Steigman, G., & Skillman, E. D. 1997, ApJ, 483, 788

Osborn, W. 1971, The Observatory, 91, 223

Ostriker, J. P., Spitzer, L. J., & Chevalier, R. A. 1972, ApJ, 176, L51+

Pace, G., Recio-Blanco, A., Piotto, G., & Momany, Y. 2006, A&A, 452, 493

Pagel, B. E. J. 1997, Nucleosynthesis and Chemical Evolution of Galaxies (Cambridge: Cambridge University Press)

Palmieri, R., Piotto, G., Saviane, I., Girardi, L., & Castellani, V. 2002, A&A, 392, 115

Perrett, K. M., Stiff, D. A., Hanes, D. A., & Bridges, T. J. 2003, ApJ, 589, 790

Pietrinferni, A., Cassisi, S., Salaris, M., & Castelli, F. 2004, ApJ, 612, 168

Pietrinferni, A., Cassisi, S., Salaris, M., & Castelli, F. 2006, ApJ, 642, 797

Piotto, G. 2009, in IAU Symposium, Vol. 258, IAU Symposium, ed. E. E. Mamajek, D. R. Soderblom, & R. F. G. Wyse, 233–244

Piotto, G., Bedin, L. R., Anderson, J., et al. 2007, ApJ, 661, L53

Piotto, G., King, I. R., Djorgovski, S. G., et al. 2002, A&A, 391, 945

Prandtl, L. 1952, Essentials of Fluid Dynamics (London: Blackie)

Pryor, C. & Meylan, G. 1993, in Astronomical Society of the Pacific Conference Series, Vol. 50, Structure and Dynamics of Globular Clusters, ed. S. G. Djorgovski & G. Meylan, 357

Puzia, T. H., Saglia, R. P., Kissler-Patig, M., et al. 2002, A&A, 395, 45

Qian, Y.-Z. 2000, ApJ, 534, L67

Reimers, D. 1975, Memoires of the Societe Royale des Sciences de Liege, 8, 369

Renzini, A. & Fusi Pecci, F. 1988, ARA&A, 26, 199

Renzini, A. & Voli, M. 1981, A&A, 94, 175

Ribas, I., Jordi, C., & Giménez, Á. 2000, MNRAS, 318, L55

Robinson, F. J., Demarque, P., Li, L. H., et al. 2004, MNRAS, 347, 1208

Rutledge, G. A., Hesser, J. E., & Stetson, P. B. 1997, PASP, 109, 907

Rutten, R. J. 2003, Radiative Transfer in Stellar Atmospheres, Lecture Notes (Utrecht: Utrecht University)

Saad, S. M. & Lee, S.-G. 2001, Journal of Korean Astronomical Society, 34, 99

Salaris, M. & Cassisi, S. 2005, Evolution of Stars and Stellar Populations (West Sussex, England: John Wiley & Sons, Ltd)

Salaris, M., Chieffi, A., & Straniero, O. 1993, ApJ, 414, 580

Salpeter, E. E. 1955, ApJ, 121, 161

Sandage, A. & Tammann, G. A. 2006, ARA&A, 44, 93

Santos, M. R. 2003, in Extragalactic Globular Cluster Systems, ed. M. Kissler-Patig, 348

Sarajedini, A., Bedin, L. R., Chaboyer, B., et al. 2007, AJ, 133, 1658

Schechter, P. 1976, ApJ, 203, 297

Schmidt, M. 1959, ApJ, 129, 243

Schroder, K.-P., Pols, O. R., & Eggleton, P. P. 1997, MNRAS, 285, 696

Schroder, L. L., Brodie, J. P., Kissler-Patig, M., Huchra, J. P., & Phillips, A. C. 2002, AJ, 123, 2473

Schroeder, D. J. 2000, Astronomical optics (San Diego, CA: Academic Press, Inc)

Schwarzschild, K. 1906, Gttingen Nachr., 41

Schweizer, F. 1987, in Nearly Normal Galaxies. From the Planck Time to the Present, ed. S. M. Faber, 18–25

Schweizer, F., Miller, B. W., Whitmore, B. C., & Fall, S. M. 1996, AJ, 112, 1839

Searle, L. & Zinn, R. 1978, ApJ, 225, 357

Shetrone, M. D. & Keane, M. J. 2000, AJ, 119, 840

Simmerer, J., Sneden, C., Ivans, I. I., et al. 2003, AJ, 125, 2018

Simon, J. D. & Geha, M. 2007, ApJ, 670, 313

Smartt, S. J. 2009, ArXiv e-prints

Smith, G. H. 1987, PASP, 99, 67

Smith, L. J. & Gallagher, III, J. S. 2000, in Astronomical Society of the Pacific Conference Series, Vol. 211, Massive Stellar Clusters, ed. A. Lançon & C. M. Boily, 90

Sneden, C. 1973, ApJ, 184, 839

Sneden, C., Cowan, J. J., Lawler, J. E., et al. 2003, ApJ, 591, 936

Sneden, C., Ivans, I. I., & Fulbright, J. P. 2004, in Origin and Evolution of the Elements, ed. A. McWilliam & M. Rauch, 170–185

Sneden, C., McWilliam, A., Preston, G. W., et al. 1996, ApJ, 467, 819

Sneden, C., Pilachowski, C. A., & Vandenberg, D. A. 1986, ApJ, 311, 826

Sobeck, J. S., Ivans, I. I., Simmerer, J. A., et al. 2006, AJ, 131, 2949

Spitzer, L. 1987, Dynamical evolution of globular clusters (Princeton, NJ: Princeton University Press)

Spitzer, L. J. & Thuan, T. X. 1972, ApJ, 175, 31

Stothers, R. B. 1991, ApJ, 383, 820

Stothers, R. B. & Chin, C.-W. 1991, ApJ, 374, 288

Straniero, O., Gallino, R., Busso, M., et al. 1995, ApJ, 440, L85

Susa, H. & Umemura, M. 2004, ApJ, 600, 1

Sweigart, A. V. 1983, ApJ, 273, 795

Symbalisty, E. M. D., Schramm, D. N., & Wilson, J. R. 1985, ApJ, 291, L11

Thielemann, F. K. 2001, in Encyclopedia of Astronomy and Astrophysics, ed. P. Murdin

Thoul, A., Jorissen, A., Goriely, S., et al. 2002, A&A, 383, 491

Toomre, A. & Toomre, J. 1972, ApJ, 178, 623

Trager, S. C., King, I. R., & Djorgovski, S. 1995, AJ, 109, 218

Trager, S. C., Worthey, G., Faber, S. M., Burstein, D., & Gonzalez, J. J. 1998, ApJS, 116, 1

Tripicco, M. J. & Bell, R. A. 1995, AJ, 110, 3035

Umeda, H. & Nomoto, K. 2005, ApJ, 619, 427

van den Hoek, L. B. & Groenewegen, M. A. T. 1997, A&AS, 123, 305

Van Eck, S., Goriely, S., Jorissen, A., & Plez, B. 2003, A&A, 404, 291

Vandenberg, D. A. 1983, ApJS, 51, 29

Vandenberg, D. A., Bolte, M., & Stetson, P. B. 1996, ARA&A, 34, 461

Vassiliadis, E. & Wood, P. R. 1993, ApJ, 413, 641

Ventura, P., D'Antona, F., Mazzitelli, I., & Gratton, R. 2001, ApJ, 550, L65

Wallerstein, G., Iben, I. J., Parker, P., et al. 1997, Reviews of Modern Physics, 69, 995

Watson, A. M., Gallagher, III, J. S., Holtzman, J. A., et al. 1996, AJ, 112, 534

Weiss, A., Peletier, R. F., & Matteucci, F. 1995, A&A, 296, 73

West, M. J., Côté, P., Marzke, R. O., & Jordán, A. 2004, Nature, 427, 31

White, R. E. & Shawl, S. J. 1987, ApJ, 317, 246

White, S. D. M. & Frenk, C. S. 1991, ApJ, 379, 52

White, S. D. M. & Rees, M. J. 1978, MNRAS, 183, 341

Whitmore, B. 2003, in Extragalactic Globular Cluster Systems, ed. M. Kissler-Patig, 336

Whitmore, B. C. 2000, ArXiv Astrophysics e-prints

Whitmore, B. C. & Schweizer, F. 1995, AJ, 109, 960

Whitmore, B. C., Schweizer, F., Leitherer, C., Borne, K., & Robert, C. 1993, AJ, 106, 1354

Whitmore, B. C., Zhang, Q., Leitherer, C., et al. 1999, AJ, 118, 1551

Willson, L. A. 2000, ARA&A, 38, 573

Winkler, H. 1997, MNRAS, 287, 481

Woo, J.-H., Gallart, C., Demarque, P., Yi, S., & Zoccali, M. 2003, AJ, 125, 754

Woosley, S. E., Arnett, W. D., & Clayton, D. D. 1973, ApJS, 26, 231

Woosley, S. E., Heger, A., & Weaver, T. A. 2002, Reviews of Modern Physics, 74, 1015

Woosley, S. E. & Weaver, T. A. 1995, ApJS, 101, 181

Worthey, G. 1994, ApJS, 95, 107

Worthey, G., Faber, S. M., Gonzalez, J. J., & Burstein, D. 1994, ApJS, 94, 687

Worthey, G. & Ottaviani, D. L. 1997, ApJS, 111, 377

Wylie, E. C., Cottrell, P. L., Sneden, C. A., & Lattanzio, J. C. 2006, ApJ, 649, 248

Yong, D., Grundahl, F., Nissen, P. E., Jensen, H. R., & Lambert, D. L. 2005, A&A, 438, 875

Zepf, S. E. & Ashman, K. M. 1993, MNRAS, 264, 611

Zepf, S. E., Ashman, K. M., English, J., Freeman, K. C., & Sharples, R. M. 1999, AJ, 118, 752

Zepf, S. E., Beasley, M. A., Bridges, T. J., et al. 2000, AJ, 120, 2928

Zepf, S. E., Carter, D., Sharples, R. M., & Ashman, K. 1995, ApJ, 445, L19

Zinn, R. 1985, ApJ, 293, 424

Zinn, R. & West, M. J. 1984, ApJS, 55, 45